ORNL-6853

ornl

OAK RIDGE NATIONAL LABORATORY

LOCKHEED MARTIN

The Mass Transfer Dynamics of Gaseous Methyl-Iodide Adsorption by Silver-Exchanged Sodium Mordenite

R. T. Jubin

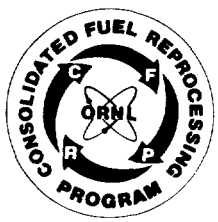

MANAGED BY
LOCKHEED MARTIN ENERGY SYSTEMS, INC.
FOR THE UNITED STATES
DEPARTMENT OF ENERGY

UCN-13673 (36 6-95)

THE MASS TRANSFER DYNAMICS OF GASEOUS METHYL-IODIDE ADSORPTION BY SILVER-EXCHANGED SODIUM MORDENITE

A Dissertation

Presented for the

Doctor of Philosophy

Degree

The University of Tennessee, Knoxville

Robert Thomas Jubin

December 1994

DEDICATION

This work is dedicated to two generations of my family...

First to my parents, who instilled in me the desire to learn

and

Second to my children, for whom the future waits.

ACKNOWLEDGMENTS

I would like to express my appreciation for the support and facilities provided by Oak Ridge National Laboratory (ORNL), operated by Martin Marietta Energy Systems, Inc., under U.S. Government contract DE-AC05-84OR21400 for the Department of Energy and within ORNL, the Robotics and Process Systems Division under the direction of Joseph Herndon. I must also thank the Process Systems section and Kenneth Plummer for the help they provided to carry out the basic research associated with this study.

The help and guidance rendered by my major professor, Dr. Robert M. Counce, and my entire committee are deeply appreciated. In addition, John David Randolph is recognized for his technical expertise in the laboratory, assistance in conducting the experiments, and for his words of encouragement when most needed. I also wish to thank Jeff Collins, who, as a co-op student, helped to set up the laboratory equipment and prepare the initial version of the software used in data collection. Lisa Kyker is deeply thanked for her efforts in the final typing and proofreading of this document.

I also wish to thank my loving and persistent wife for her strength, support, gentle prodding, and most importantly, patience through the many peaks and valleys experienced over the years while I was in graduate school. And finally, I am unable to find adequate words to express my appreciation for the understanding and undying love of my children for their often distracted father.

ABSTRACT

The adsorption of methyl iodide onto hydrogen-reduced silver-exchanged mordenite (Ag°Z) was studied. The removal of organic iodides from off-gas streams is an important step in controlling the release of radioactive iodine to the environment during the treatment of radioactive wastes or the processing of some irradiated materials. Nine well accepted mass transfer models were evaluated for their ability to adequately explain the observed CH_3I uptake behavior onto the Ag°Z. Linear and multidimensional regression techniques were utilized in the estimation of the diffusion constants and other model parameters which then permitted the selection of an appropriate mass transfer model.

While a number of studies have been conducted to evaluate the loading of both elemental and methyl iodide on silver-exchanged mordenite, these previous studies focused primarily on the macro scale (deep-bed) while evaluating the material under a broad range of process conditions and contaminants for total bed loading at the time of breakthrough. A few studies evaluated equilibrium or maximum loading. Thus, to date, only bulk loading data exist for the adsorption of CH_3I onto Ag°Z. Hence this is believed to be the first study to quantify the controlling mass transfer mechanisms of this process.

It can be concluded from the analysis of the experimental data obtained by the "single-pellet" type experiments and for the process conditions used in this study that the overall mass transfer rate associated with the adsorption of CH_3I onto Ag°Z is affected by both micropore and macropore diffusion. The macropore diffusion rate was significantly faster than the micropore diffusion, resulting in a two-step adsorption behavior which was adequately modeled by a bimodal pore distribution model. The micropore diffusivity was determined to be on the order of 2×10^{-14} cm^2/s. The system was also shown to be isothermal under all conditions of this study. Two other conclusions were also obtained. First, the gas film resistance to mass transfer for the 1/16- and 1/8-in.-diam Ag°Z pellets can be ignored under the conditions used in this study. Finally, it was shown that by decreasing the water vapor content of the feed gas, the chemical reaction rate appeared to become the initial rate-limiting factor for the mass transfer.

TABLE OF CONTENTS

CHAPTER PAGE

CHAPTER PAGE

CHAPTER PAGE

LIST OF TABLES

TABLE PAGE

TABLE PAGE

TABLE PAGE

LIST OF FIGURES

FIGURE PAGE

FIGURE PAGE

FIGURE PAGE

FIGURE PAGE

LIST OF SYMBOLS

a = constant in Eq. (2.16)
B_{12} = constant in Eq. (2.53)
b = constant in Eq. (2.16); stoichiometric coefficient for B
C = concentration (g/cm^3)
C_p = heat capacity (cal/g°K) or (kJ/kg°K)
c = constant
D = combined diffusivity in Eq. (2.31)
D_{AB} = molecular diffusion coefficient (cm^2/s)
D_c = intercrystalline or micropore diffusivity (cm^2/s)
D_e = ash layer diffusion coefficient (cm^2/s)
D_k = Knudsen diffusion coefficient (cm^2/s)
D_p = pore or macropore diffusivity (cm^2/s)
D_{pf} = equivalent diffusivity for Poiseuille flow
D_s = diffusivity of 'A' in solid pellet (cm^2/s)
D_∞ = pre-exponential factor in Arrhenius expression for D
E = activation energy (cal/mol)
E_d = diffusional activation energy (cal/mol)
E_r = removal coefficient (1/cm)
f = fraction of the molecules striking the surface of a pore wall
G = mass flow rate (g/s*cm^2)
g_c = conversion factor
ΔH = Enthalpy change on adsorption (cal/mol)
H = relative humidity (%)
h_m = heat transfer coefficient (cal/cm^2 s °K)
K = Boltzmann's constant in Eq. (4.1)
K^* = Henry's law constant based on q/C (cm)
k_f = thermal conductivity (cal/cm s °K) or (W/m°K)
k_g = gas film mass transfer coefficient (cm/s)
k_o = constant in Eq. (2.28)
k_s = reaction rate constant for the gas solid reaction (cm/s)
k_v = volume reaction rate constant for Eq. (2.52) (cm^3/mol^{n-1} s)
k_∞ = pre-exponential factor in Arrhenius expression for k_s
L = volume to external area (cm)
l = bed depth (cm)
M = molecular weight (g/mol)

m_t = mass adsorbed at time t
m_∞ = mass adsorbed at time $t \rightarrow \infty$
N = moles
N_{Da} = Damköhler number ($k_s r_a / D_p$)
N_{Nu} = Nusselt number ($h_m(2r_a)/k_f$)
N_{Sc} = Schmidt number ($\mu / D_{AB}\rho_{air}$)
N_{Sh} = Sherwood number ($k_g(2r_a)/D_{AB}$)
N_{Re} = Reynolds number ($G(2r_a)/\mu$)
P_t = the total pressure (atm)
p = root to transcendental equations
q = adsorbed phase concentration (g/cm^3)
R = gas constant
R^2 = coefficient of determination
r_a = pellet radius (cm)
r_c = pellet core radius (cm)
r_i = particle radius (cm)
r_p = pore radius (cm)
r_{pa} = macropore radius (cm)
r_{pm} = mesopore radius (cm)
r_{pi} = micropore radius (cm)
r_v = volume rate of conversion in Eq. (2.52) (mol/cm^3 s)
S = surface area (m^2/g) or (m^2/cm^3)
T = temperature (°C or °K)
T_c = critical temperature (°K)
t = time (s)
V = particle volume (cm^3)
V_c = critical volume (cm^3/g mol)
v = face velocity (cm/s)
W_1 = constant in Eq. (2.53)
W_2 = constant in Eq. (2.53)
X = conversion
z = constant

Greek Symbols:

α = ratio of diffusional time constants $(D_c/r_i^2)/(D_p/r_a^2)$
α' = ratio of time constants for heat transfer and diffusion $(h_m S/C_p)/(D_c/r_i^2)$
β = parameter defined by Eq. (2.63)
β' = parameter defined by Eq. (2.68)
ξ = constant in Eq. (5.5)
ε = void fraction in bed

ε_p = porosity of pellet
ε_{AB} = Lennard Jones constant (ε_{AB}/K has units of °K)
λ = mean free path (cm)
μ = viscosity (poise)
θ = dimensionless time defined in Eq. (2.54)
ϕ = Thiele modulus defined in Eq. (2.55)
τ = tortuosity factor
ρ = density (g/cm^3)
ρ_B = molar density of B (gmol/cm^3)
ρ_p = bulk pellet density(g/cm^3)
σ = standard deviation
σ_{AB} = force constant in Lennard-Jones potential function (Å)
Ω_{AB} = collision integral
ζ = constant in Eq. (2.53)

Subscripts:

A = component A (generally CH_3I)
B = component B (generally silver, but in the D_{AB} term is air)
eff = effective value
ex = external
f = final or film in Eqs. (2.80) and (2.81)
g = bulk gas phase
i = instantaneous
0 = initial
s = surface

Superscripts:

° = metallic form of silver

Other Symbols and Notations:

$\bar{}$ = average value

1. INTRODUCTION

Iodine-129 is a naturally occurring radioactive isotope continually arising from several sources, including the spontaneous fission of uranium and the interaction of cosmic rays with xenon in the atmosphere. Through these and other natural pathways, about 10 mg is produced annually (Pence and Staples, 1974). Of all of the radioactive iodine isotopes, I^{129} has the longest half-life, 1.6×10^7 years, and as a result it accumulates in the biosphere. Pence and Staples (1974) reported the estimated accumulation as of 1940 to be 2×10^5 g. Today, however, the largest annual source term for I^{129} is the fission process in nuclear reactors.

The I^{129} generation rate in light-water reactors (LWR) power reactor fuel is about 4.4×10^{10} Bq/GW(e) year (Burger and Burns, 1979). In other terms, a single LWR produces 234 g of I^{129} based on a uranium burnup of 30,000 MWd/t (Burger, 1977). If this spent fuel undergoes aqueous processing, it is estimated that approximately 99% of the fission product iodine will be volatilized into the process off-gas systems (Burger and Scheele, 1983). In the designs of most aqueous processing facilities, the off-gas from the shearing and dissolution steps is combined into a single gas stream commonly referred to as the dissolver off-gas (DOG). Burger and Burns (1979) estimated that (1) this stream contains >90% of the iodine contained in the fuel and (2) the combined off-gas streams from the other process vessels, the vessel off-gas (VOG), contain a smaller fraction of the

total iodine (<10%). But, depending on the chemical processing steps used and the material being processed, a portion of the total iodine was expected to form nonvolatile iodine compounds which would leave the process in the high-level liquid waste, which must ultimately be processed. Currently there are no plans for any reprocessing of spent commercial power reactor fuel in the United States, but there is a significant quantity of radioactive wastes containing I^{129} stored at various sites throughout the U.S. Department of Energy (DOE) complex. This waste, which accumulated over the past 4 to 5 decades, originated from the processing of nuclear materials by numerous methods. Currently over 100 million gal of high- and low-level waste generated primarily from weapons material production are stored in 332 underground tanks (U.S. Department of Energy, Office of Environmental Management, 1994). These tanks contain organic material as well as numerous radionuclides including cesium, strontium, technetium, and iodine, in addition to transuranics such as plutonium and americium. These wastes, which may be liquid, solid, or sludge, are also alkaline in nature and high in sodium and nitrate. McKay et al. (1982) show significant variation in the fractions of the iodine reporting to the aqueous or sludge wastes from operation in several countries. The aqueous/sludge fractions ranged from less than 1% to as high as 94.5%. The treatment of these wastes may result in the potential for the evolution of gaseous radioiodine, which would require the treatment of the off-gas streams. Processes currently under evaluation involve both dissolution of the sludges from the tanks and high-temperature operations such as calcination and vitrification, all of which can result in the release of iodine.

The requirements for the retention of iodine or exposure limits to workers and the general population are contained in numerous federal, state, and local laws. Pertinent federal regulations include the Code of Federal Regulations (CFR) 10 CFR 20 (National Archives of the United States, 1994), 40 CFR 190 (National Archives of the United States, 1993), and 40 CFR 191 (National Archives of the United States, 1993). In 40 CFR 190, release limits to the environment from the LWR fuel cycle are stated by the Environmental Protection Agency for certain radionuclides. For I^{129} the limit is 1.9×10^8 Bq/GW(e)year. The 40 CFR 191 addresses the environmental radiation protection standards for the management and disposal of spent nuclear fuel and high-level and transuranic wastes.

Various technologies have been studied and developed over the past 3 to 4 decades to control the discharge of iodine to the environment. Liquid scrubbing systems utilizing caustic, nitric acid, or nitric acid and mercury have been developed (Pence and Staples, 1974). The use of solid adsorbents has also been investigated for the main removal system or as back-up or polishing systems following one of the liquid scrubbing systems. The materials studied include silver-exchanged zeolites, silver-impregnated alumina silicates, and macroreticular resins.

One of the promising solid sorbent technologies for the removal and retention of iodine in terms of performance and simplicity is the adsorption on hydrogen-reduced silver mordenite (Ag°Z). This form of the sorbent has been reported by several researchers [Thomas et al. (1977), Jubin (1980, 1982), and Scheele et al. (1983)] to be more effective

in trapping I_2 and CH_3I than the ionic silver mordenite (AgZ). The mordenite structure is also more resistant to acid vapors than is the faujasite-type zeolite, which has also been studied as an iodine adsorbent material. This higher acid resistance tends to make the material more suitable for use in a gas stream potentially containing nitric acid vapors and NO_x compounds.

While a number of studies have been conducted to evaluate the loading of both elemental and methyl iodide on silver-exchanged mordenite, these studies focused primarily on the macro scale (deep-bed) while evaluating the material under a broad range of process conditions and contaminants for total bed loading at the time of breakthrough. A few studies have evaluated equilibrium or maximum loading capacities of the AgZ or Ag°Z. In general terms, only bulk loading data appear to exist in the literature for the adsorption of CH_3I onto AgZ or Ag°Z.

The ultimate objective of this study was to expand the understanding of the gaseous methyl iodide trapping on hydrogen-reduced silver mordenite. The specific objective was to provide sufficient insight into the adsorption process to allow the determination of the primary controlling mechanisms and diffusion and/or reaction coefficients associated with the process. This was accomplished through the use of well established fundamental mass transfer mechanisms and models for adsorption in addition to the relevant chemical reaction principles.

The results obtained from this analysis can aid in the optimization of operating conditions and equipment design for such an adsorption process. In addition, the results

are available for use in the development of a deep-bed model which would be valuable in the prediction of the performance of process equipment.

2. LITERATURE REVIEW

2.1 PREVIOUS IODINE ADSORPTION STUDIES ON ZEOLITES

Maeck et al. (1968) performed an initial scoping study on the use of organic and inorganic adsorbers for removing iodine from gas streams. In this study, over 70 different materials or variations of materials were tested for I_2 and CH_3I retention. The results of this study indicated that a faujasite-type zeolite material, Linde molecular sieve 13X, which had been converted to the silver form (AgX), was highly effective at removing both I_2 and CH_3I over a wide range of test conditions.

Staples et al. (1976) proposed that the two obvious mechanisms of physisorption and chemisorption were responsible for iodine loading on the metal-exchanged zeolites. The data presented in their paper indicated that the extent to which either or both of these mechanisms occurred was related to the cation that was exchanged for the sodium in the original zeolite substrate (see Table 2.1). They considered that the quantity of iodine remaining on the bed following an air purge of up to 120 h to be chemisorbed.

The study of silver-exchanged mordenites was begun by Thomas et al. (1977) as an outgrowth of the development work on metal-exchanged zeolites. One of the key objectives of this effort was to identify a material that could be repeatedly regenerated. This required a substrate with a high thermal stability as well as good chemical stability in

Table 2.1: Adsorption limits for metal-exchanged zeolites at 150°C.[a]

	Iodine loading (mg of I_2 per gram of bed)[b]		
Absorbent	Saturated	Physisorbed	Chemisorbed
NaX	364	334	30
AgX	349	135	214
PbX	179	153	26
CdX	374	329	45

[a]Source: Staples et al., 1976.

[b]Based on dry weights of 0.61 g/cm^3 for NaX, 0.71 g/cm^3 for CdX, 0.85 g/cm^3 for AgX, and 0.85 g/cm^3 for PbX.

a potentially acidic vapor stream. Literature from the Norton Company (Norton, 1976) suggested that compared to X- and Y-type zeolites, the Norton Zeolon™ (Trademark of the Norton Company) family of zeolites possessed superior acid-resistant characteristics.

Jubin (1980), in a series of tests using an eight-run fractional 2^n factorial-designed experiment, identified the significant process parameters affecting the adsorption of CH_3I on silver-exchanged mordenite. The experimental design method used in that study was described by Murphy (1977). One of the significant factors affecting the loading was the pretreatment method of the silver-exchanged zeolite prior to the exposure to CH_3I. This factor had been previously identified for elemental iodine by Thomas et al. (1978). The pretreatment of the silver-exchanged mordenite will be discussed in more detail in Sect. 2.2.2. The process of interest involved the exposure of the silver-exchanged mordenite to the hydrogen gas stream to reduce the silver to the metallic form. In the following discussions, the ionic form of silver is denoted as Ag and the metallic form of silver is denoted as Ag°.

The tests conducted by Jubin (1980) involved deep beds of AgZ or Ag°Z. The bed was divided into segments with stainless steel screen spacers. All tests were conducted using CH_3I with a CH_3I^{131} tracer to facilitate the determination of the quantity of iodine loaded on each bed segment. The loading process was terminated when the CH_3I decontamination factor (DF) dropped below 1000. The DF was defined as the ratio of inlet gas concentration to the outlet gas concentration. Loading results were presented for bed segment 1, the inlet segment. The data indicated that pretreatment with 4.5% hydrogen instead of air improved the loading of the bed segment. Higher loading was also noted for the 25 to 40°C dew point than for a –54°C dew point and for the 200°C furnace temperature over the 150°C furnace temperature. The effects of NO, NO_2 and CH_3I concentration were of the same order of magnitude as the experimental error and interaction effect; thus no significant trends were identified for these process parameters.

Jubin (1982) continued to evaluate the effects of water vapor and bed temperature as well as the silver content of the mordenite. It was also noted that with the increased loadings observed with higher bed temperature, the length of bed required to contain the mass transfer zone (MTZ) also increased. At 150°C, for both the dry and humidified gas stream, the MTZ was estimated to be 5 to 7.5 cm based on the identification of a saturation zone in which two or more bed segments of the test bed had virtually the same iodine loading. At 200°C the MTZ was over 10 cm and thus was not contained in the shorter 10-cm-deep beds used in this second test program. Figure 2.1 shows the loading of the first bed segment as a function of temperature and moisture in the gas stream.

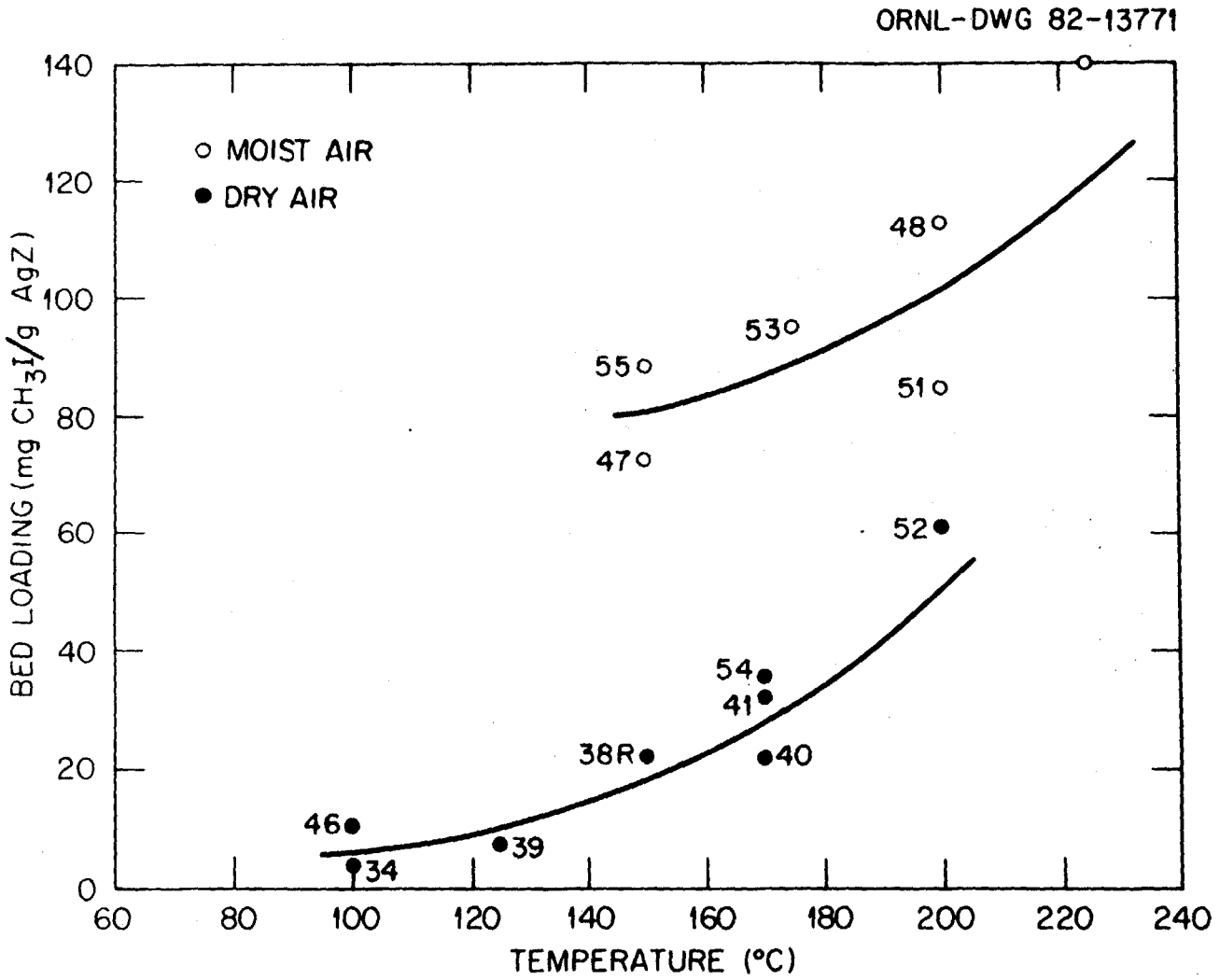

Figure 2.1. CH_3I loading at breakthrough on the first of four 2.54-cm deep beds as a function of temperature and carrier gas water vapor content. Note: Numbers located next to data points are original run identifiers.

Since the MTZ at 200°C was longer than the total sorbent depth, the saturation zone for these tests had not formed when the run was terminated due to the effluent DF reaching the desired endpoint. Thus higher bed loadings associated with the saturation zone could be expected under the test conditions used had the total sorbent depth been greater to allow the formation of such a zone or if the runs had been continued even though the minimum acceptable DF had been reached.

It was also noted (Jubin, 1982) that AgZ made from a NaZ produced in the Brian, Texas, facility rather than the Stow, Ohio, plant exhibited CH_3I breakthroughs at lower loadings.

At the same time Jubin was conducting his work at Oak Ridge National Laboratory (ORNL), Burger, Scheele, and other team members were also working at Pacific Northwest Laboratories on silver-exchanged mordenite. These two efforts produced complementary results. Scheele et al. (1983) also reported improved effectiveness in iodine adsorption on AgZ following hydrogen pretreatment. Variations in the overall performance of the material varied with changes in operating parameters. They reported that 20- to 40-mesh hydrogen pretreated silver-mordenite was a more effective trap than was 1/16-in. extrudate. At a water concentration of 4×10^{-6} mol/L, a significant reduction in trapping efficiency was noted. In these tests, a CH_3I inlet gas concentration of 1.3×10^{-5} mol/L was used. These studies also utilized deep beds. Analysis was done by taking gas samples as side streams after each 5- to 8-cm-thick bed segment. The gas

was analyzed by gas chromatography, and the integrated inlet CH_3I flow was used to obtain loading on each segment.

Later tests by Scheele and Burger (1987) showed that there was some movement of iodine in a deep bed during extended periods of standby operation in which only air at elevated temperature was passed through the bed. They indicated the bed stabilized at an iodine loading of about 4×10^{-7} mol/g AgZ. It was also reported that the hydrogen-pretreated silver-exchanged mordenite had a 30% lower loading capacity than the untreated material. The iodine loaded on the pretreated mordenite was less mobile than on the untreated mordenite.

All of these studies focused on the macroscale loading characteristics of the deep beds and did not evaluate the impact of the process variables on the diffusion and/or specific reactions occurring in the silver mordenite adsorbent on a microscale or single-pellet scale. Only the pretreatment method results lead to a relatively clear conclusion. The Ag°Z is preferred over AgZ, but even this is somewhat uncertain in that actual maximum loadings for silver mordenite prepared by both pretreatment methods were not done. The improved loading resulting from the other process variables could be accounted for through improvements in the diffusion rate or in the reaction rate, and the differentiation of these cannot be extracted from this data. Thus the need for the current analysis is established.

2.2 CHEMICAL REACTIONS

2.2.1 Silver/Iodine Reactions

In spite of numerous studies over the past 15 to 18 years, the precise chemical reactions involving elemental iodine and organic iodides on the silver-exchanged mordenite have not been fully explained. One starting point noted by Thomas et al. (1977) was that the silver contained in the mordenite structure existed in both the ionic and metallic states; thus the reactions considered must include both forms of silver.

Scheele et al. (1983) provided an extensive discussion on the competing reactions that may occur between the reactive compounds in the off-gas stream and the AgZ or Ag°Z. Of the reactions reported in their paper the following appeared to be the most relevant for this study:

$$Ag^{\circ} + \frac{1}{2}I_2(g) \leftrightarrow AgI \tag{2.1}$$

$$Ag_2O + I_2(g) \leftrightarrow 2AgI + \frac{1}{2}O_2 \tag{2.2}$$

$$AgNO_3 + \frac{1}{2}I_2 \leftrightarrow AgI + \frac{1}{2}O_2 + NO_2(g) \tag{2.3}$$

$$2Ag^{\circ} + 2CH_3I(g) \leftrightarrow 2AgI + C_2H_6(g) \tag{2.4}$$

$$Ag^{\circ} + CH_3I(g) + H_2O \leftrightarrow AgI + CH_3OH(g) + \frac{1}{2}H_2 \tag{2.5}$$

$$Ag^{\circ} + CH_3I(g) + CH_3OH(g) \leftrightarrow AgI + CH_3OCH_3(g) + \frac{1}{2}H_2 \tag{2.6}$$

$$Ag^{+}(ag) + CH_3I(g) + H_2O(g) \leftrightarrow AgI + CH_3OH(g) + H^{+}(ag) \tag{2.7}$$

$$Ag^{+}(ag) + CH_3I(g) + CH_3OH(g) \leftrightarrow AgI + CH_3OCH_3(g) + H^{+}(ag) \quad (2.8)$$

$$2\,Ag^{\circ} + I_2(g) + \frac{3}{2}O_2 \leftrightarrow AgI + AgIO_3 \quad (2.9)$$

$$Ag_2O + I_2(g) + O_2 \leftrightarrow AgI + AgIO_3 \quad (2.10)$$

Methanol and dimethyl ether were detected by Donner and Tamberg (1971, 1972) in the effluent from a bed of silver-exchanged type X zeolite through which CH_3I was passed. This appeared to correspond to the reactions defined by Eqs. (2.5) and (2.6).

If the silver exists as an oxide in the zeolite structure, potential reactions with elemental iodine include both Eqs. (2.2) and (2.10). Reactions defined by Eqs. (2.1), (2.4), (2.5), (2.6), and (2.9) apply following hydrogen reduction of the silver.

The reactions involving NO_x are ignored in this study in spite of their significance to the actual process streams. This simplification was done to make the analysis of the mass transfer more tractable.

2.2.2 Hydrogen Reduction of the Silver

Results of tests by Thomas et al. (1977), Jubin (1980, 1982), and others indicated that mordenite with the silver in the metallic state had a higher capacity for iodine chemisorption than when the silver was in the ionic state.

Beyer and Jacobs (1977) proposed the following reduction and oxidation stoichiometry to account for what was described as a reversible formation and disappearance of the metallic silver in the zeolite structure:

$$2Ag^{+} + H_2 \rightarrow 2Ag^{\circ} + 2H^{+} \tag{2.11}$$

$$2Ag^{\circ} + 2H^{+} + \frac{1}{2}O_2 \rightarrow 2Ag^{+} + H_2O \tag{2.12}$$

A second reaction similar to Eq. (2.11) was proposed by Thomas et al. (1977) for the hydrogen reduction step:

$$Ag_2O(s) + H_2(g) \rightarrow 2Ag^{\circ}(s) + H_2O(g). \tag{2.13}$$

The most notable difference between these two discussions on this subject is that Thomas et al. indicated that the reaction defined by Eq. (2.13) is irreversible.

Tsutsumi and Takahashi (1977) proposed the following reduction reaction which shows the role of the mordenite:

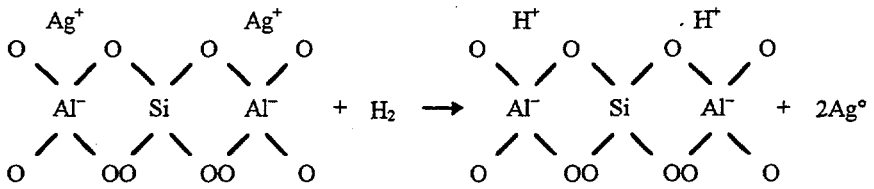

(2.14)

Aside from the higher reported loadings associated with the hydrogen pretreatment, there was little in the literature concerning chemical mechanisms involved as related to the iodine uptake. There were some limited observations made as an outgrowth of regeneration tests involving the use of either pure hydrogen or 4 to 5% hydrogen.

Thomas et al. (1977) reported a 60% decrease in the capacity of the silver mordenite following exposure to dry air at 100°C for 16 to 64 h with no subsequent hydrogen treatment. The equilibrium reaction

$$Ag_2O(s) \leftrightarrow 2Ag^{\circ}(s) + \frac{1}{2}O_2(g) \qquad (2.15)$$

was thought to have been involved. The reported free energy of this reaction is zero at 180°C. As the temperature is lowered, the formation of Ag_2O is favored. It was further proposed that hydrogen pretreatment could "permanently" protonate the oxygen atom associated with the silver cation via the irreversible reaction in Eq. (2.13) and thus assure that the silver was in the metallic state.

Additional information concerning the effects of H_2 was determined during studies of the regeneration potential of the iodine-loaded AgZ material. Jubin (1980) conducted tests at ORNL to confirm the previously reported regeneration potential of AgZ or Ag°Z. For safety reasons, these were the first tests to be conducted utilizing a dilute (4.5 vol%) stream of H_2 as the regeneration gas stream. The tests were also conducted in a stainless-steel filter housing while the previous work had been done in glass. Test results showed that less than 2% of the iodine originally loaded as CH_3I onto the Ag°Z remained following the regeneration step using a 4.5% H_2-95.5% Ar gas stream at 500°C. However, a significant loss in the subsequent loading capacity was observed following this regeneration treatment method.

The effects of the pretreatment of AgZ with 4.5% H_2-95.5% Ar at 200°C were examined by Jubin (1980) using X-ray diffraction analysis. The test results indicated that free silver or metallic silver was present in the material. Similar analysis of untreated material did not reveal the presence of free silver. This appeared to correspond to the reaction in Eqs. (2.11) or (2.13). Further examination of the Ag°Z material with a

scanning electron micrograph revealed nodules on the surface of the zeolite structure. These were suspected to be free silver. No nodules were detected on the untreated AgZ. The nodules were estimated to be on the order of 2000 Å based on measurements from the photomicrographs. Scanning the surface of the pellets indicated that the nodules were present on all surfaces and not localized. Induced electron fluorescence indicated a high concentration of silver in the nodules and that additional silver (i.e., silver not present in the nodules) still remains in the mordenite structure. These results are similar to those reported by Yates (1965), which also showed a high degree of mobility for the silver atoms.

In an attempt to identify a cause for the decreased loading capacity following regeneration, Jubin (1982) observed on scanning electron micrographs large (>8000 Å) silver nodules in the Ag°Z material that had undergone regeneration. For the regenerated material, a much stronger silver band was shown by X-ray diffraction than for the Ag°Z prior to regeneration. It was hypothesized that the reduced loading capacity was associated with the increased size and quantity of silver nodules and the probable simultaneous reduction in the number of readily available silver sites in the zeolite structure.

Jubin (1982) then conducted a series of tests to examine the possibility of the postregeneration loading efficiency being affected by the material of the filter housing material. This was accomplished by comparing the loading performance of material treated in glass with that of material treated in stainless steel. AgZ, treated in a glass column with 100% H_2 for 24 h at 500°C, was loaded with CH_3I to 54 mg/g at 200°C in

moist air. The CH_3I loading obtained was about 10 times higher than that following similar hydrogen treatment at 500°C in stainless steel. It was also noted that this loading following treatment in the glass column at 500°C was approximately half the loading achieved prior to breakthrough for Ag°Z under the same loading conditions following pretreatment with 4.5% H_2 at 200°C.

Beyer and Jacobs (1977) reported that when higher temperatures were used for hydrogen reduction, the intensity of the (111) diffraction of crystalline silver external to the zeolite increased. At the same time, the silver crystallite particle size also increased. It was also reported that this external silver phase disappeared following oxidation at sufficiently high temperatures. Some irreversibility of the system was noted following a second redox cycle at 643°K, when a small amount of silver remained between the zeolite crystallites.

Beyer and Jacobs (1977) also reported that the rate of reduction strongly depended on the iron impurity content of the zeolite material used. By studying a partially deironized material, they showed that the rate of reduction of silver ions decrease five-fold. Through the use of Arrhenius plots it was deduced that the reduction mechanism remained unchanged. They concluded that the reduction process may be a catalyzed process in which the hydrogen was probably activated on the iron.

Jubin (1982) concluded that the rapid formation of large silver nodules when treating AgZ in the stainless steel housing at high temperatures might be accounted for by this "activation" of the hydrogen by iron.

2.2.3 Relative Humidity

Consistent results have been obtained in the numerous studies on the effects of high relative humidity. In general, with increased humidity there was an observed decrease in the iodine removal efficiency. Maeck and Pence (1970) reported that CH_3I adsorption increased with temperature for a constant relative humidity.

Thomas et al. (1977) indicated that at a relatively high dew point (23°C) there was no significant effect on iodine loading by either hydrogen pretreatment or superficial face velocity.

Significant effects on the loading of "deep beds" were observed by Burger and Scheele (1981) with variations in water content of the carrier gas. These studies provided insight into the effects of very low relative humidity. At a constant retention factor of 100, about 2 to 5 times the quantity of CH_3I was loaded from a gas stream having a water vapor content of 5×10^{-4} mol/L compared to a gas stream containing 4×10^{-6} mol/L of H_2O. It was noted that even when the zeolites are in equilibrium with air containing 4×10^{-6} mol/L of H_2O, significant water is contained in the zeolite, but that "this water may not be as available for reaction as the more loosely bound water at higher content."

As noted is Sect. 2.1, Jubin (1980) observed higher loading for CH_3I on the AgZ or Ag°Z beds prior to breakthrough when the gas had a dew point of 25 to 40°C rather than –54°C. The loading achieved was 2 to 3 times higher with the higher water vapor content.

Shiomi et al. (1982) conducted a parametric study of the iodine removal efficiencies for charcoal and AgX. A mathematical expression for the removal efficiency was developed from the experimental data and mass transfer theory, which accounted for the effects of temperature between 20 and 90°C, relative humidity between 0 and 95%, and face velocity between 5 and 35 cm/s.

$$E_r = a\rho_{bulk} v^{-z} e^{(bT-cH)} \tag{2.16}$$

where:

E_r is the removal coefficient (1/cm),

ρ_{bulk} is the packing density (g/cm^3),

v is the face velocity (cm/s),

T is the temperature (°C),

H is the relative humidity (%), and

a, b, c, and z are constants.

Their study also reported that the uptake on AgX was controlled by the external fluid phase diffusion.

To summarize the reported effects of water vapor, the data indicate that some moderate water vapor content in the gas stream is required to provide high CH_3I removal efficiencies. Low efficiencies have been noted at high relative humidity and when the gas stream is very dry.

2.2.4 NO_x Reactions

Work by Thomas et al. (1977) indicated that the presence of 2% NO_2 in the feed gas stream resulted in a three-fold decrease in I_2 loading on AgX. There was also an interaction of water vapor with NO_2 noted on the iodine loading. In this case, with a constant 5% water vapor content in the feed gas stream, the iodine loading was reduced with the addition of 2% NO_2 at 100°C, but the loading was increased at 200°C with the same 2% NO_2 addition.

NO was reported by Murphy et al. (1977) to have a positive impact on iodine loading. NO_2, however, had a negative impact on the iodine loading in the absence of NO. They suggest this may be due to the equilibrium reaction:

$$2Ag^{\circ}(s) + NO_2(g) \leftrightarrow 2AgO(s) + NO(g) \qquad (2.17)$$

They reported that the reaction to convert the metal to the oxide form has a free energy of 6.3 kcal/mol at 150°C if any effects of the mordenite matrix are ignored. They went on to state that the formation of the oxide was thermodynamically unfavorable and would only occur in the absence of NO. Even then, in the presence of O_2, it was speculated that NO might also serve to hold the silver in the metallic state.

Structured experiments conducted by Jubin (1980, 1982) indicated similar results for both NO and NO_2.

2.3 MORDENITE STRUCTURE AND COMPOSITION

2.3.1 Structure

Obviously, one of the more important factors affecting the adsorption rate is the adsorbent itself. The zeolite structure is formed out of a primary tetrahedron building block composed of four oxygen atoms attached to a single silicon atom, $(SiO_4)^{4-}$ (Vaughan, 1988). Note that stoichiometrically, the primary building block is SiO_2 and is neutral in electrical charge but for purposes of visualization it is shown as $(SiO_4)^{4-}$. A variety of "secondary building units" (SBUs) can then be formed by joining these basic building units through the oxygen atoms located at the corners of the tetrahedron. The SBUs are classified into 16 primary types (Meier and Olson, 1992). The various zeolite crystal structures are formed, in turn, by connecting the SBUs to create the characteristic framework of a specific crystal. For example, consider Fig. 2.2. The SBUs shown in this figure are classified as S4R and S6R, single four and six rings respectively, may be combined to give Type A, Sodalite, or Faujasite (Types X and Y), depending on how the resulting cubo-octahedrons are connected (Vaughan, 1988). In addition, the possible substitution of other elements for the central silicon atom gives rise to other structural possibilities. The substitution of another cation for silicon is limited by the condition that it must not generate excessive strain when fitting into the location at the center of the four tetrahedron oxygen atoms. Further, the substitution process must be such that it produces an electrically neutral structure. For example, consider replacing the Si^{4+} in the neutral SiO_2 SBU with Al^{3+}. This results in a net negative charge on the three-dimensional zeolite

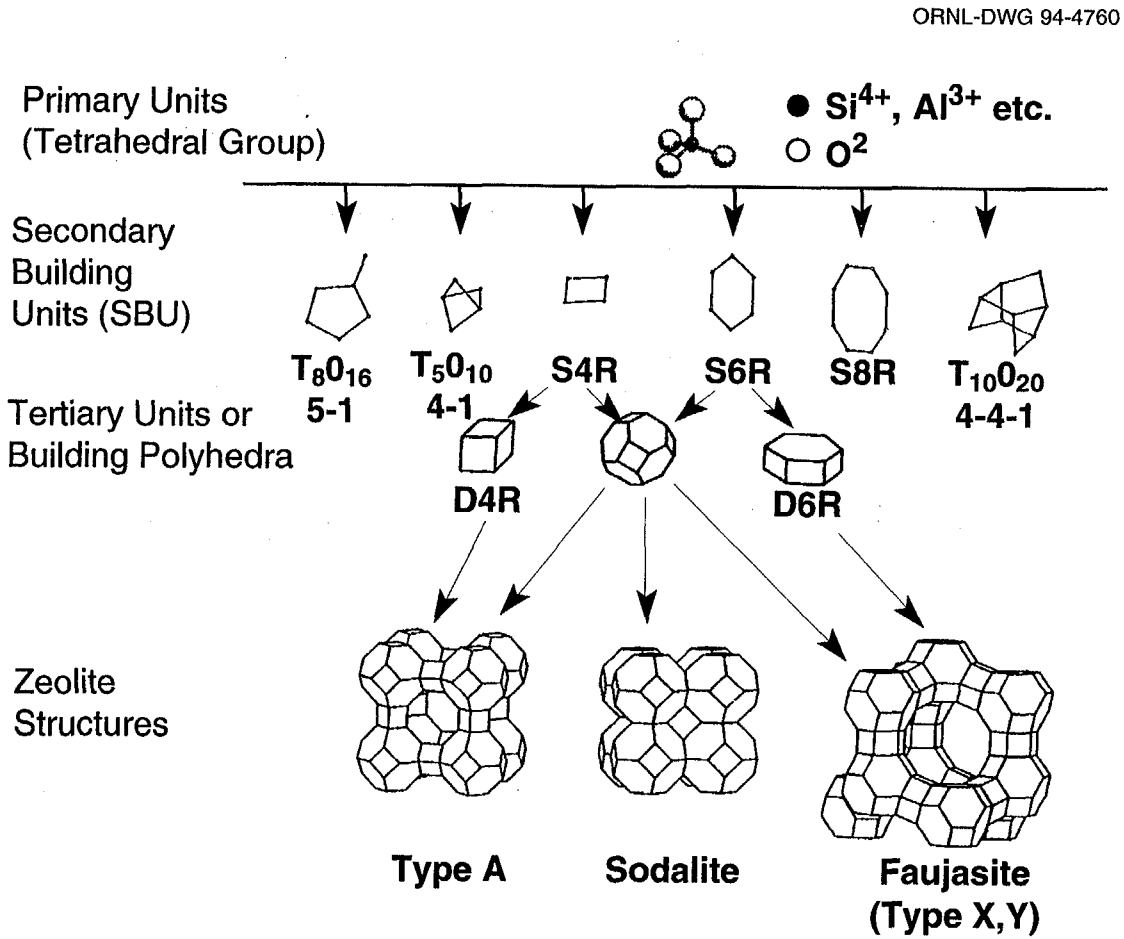

Figure 2.2. Building blocks of zeolites. Adapted from Figure 1, p. 25, and Figure 2, p. 26, D. E. W. Vaughan, "The Synthesis and Manufacture of Zeolites," *Chemical Engineering Progress*, Vol. 84, No. 2, p. 25–31, February 1988. Used with permission of the American Institute of Chemical Engineers.

"framework" formed by the mutual sharing of all the oxygen atoms in the primary tetrahedrons (Breck, 1974 and Vaughan, 1988). This must be compensated for by the addition of a "nonframework" cation such as Na^+ (Vaughan, 1988). This "nonframework" cation is more mobile than the Si or Al cations which are locked in the tetrahedron and can easily be exchanged for other cations such as H^+ or Ag^+. This capability is used in the preparation of the silver mordenite used in this study. Not counting the variations allowed by ion exchange of the nonframework cation, Meier and Olson (1992) identify 85 microporous zeolite-type material structure types.

In addition to classification of zeolites through the contained SBUs, the resultant structures can be divided into those containing one-, two-, or three-dimensional pore structures. Mordenite has a one-dimensional primary pore structure (see Fig. 2.3). Mordenite also contains a secondary pore structure which runs perpendicular to the primary channels (Meier and Olson 1992).

As just noted, the mordenite crystal structure contains two distinct sets of channels. The primary channels have dimensions of 6.7 × 7.0 Å [i.e., 7 Å in pore size and linked in plane by much smaller channels or pockets with openings of 3.6 Å (Breck, 1974)]. Literature from the Norton Company (1976) reports that the effective pore diameter to be 8 to 9 Å and that the specific surface area to be 400 to 450 m^2/g. Iodine or methyl iodide must pass through these pore openings to be sorbed. The kinetic diameter of the molecule controls the ability to enter the pores of the mordenite crystal. Scheele et al. (1983) indicated that I_2 has a kinetic diameter of 5 Å and estimated that CH_3I has a

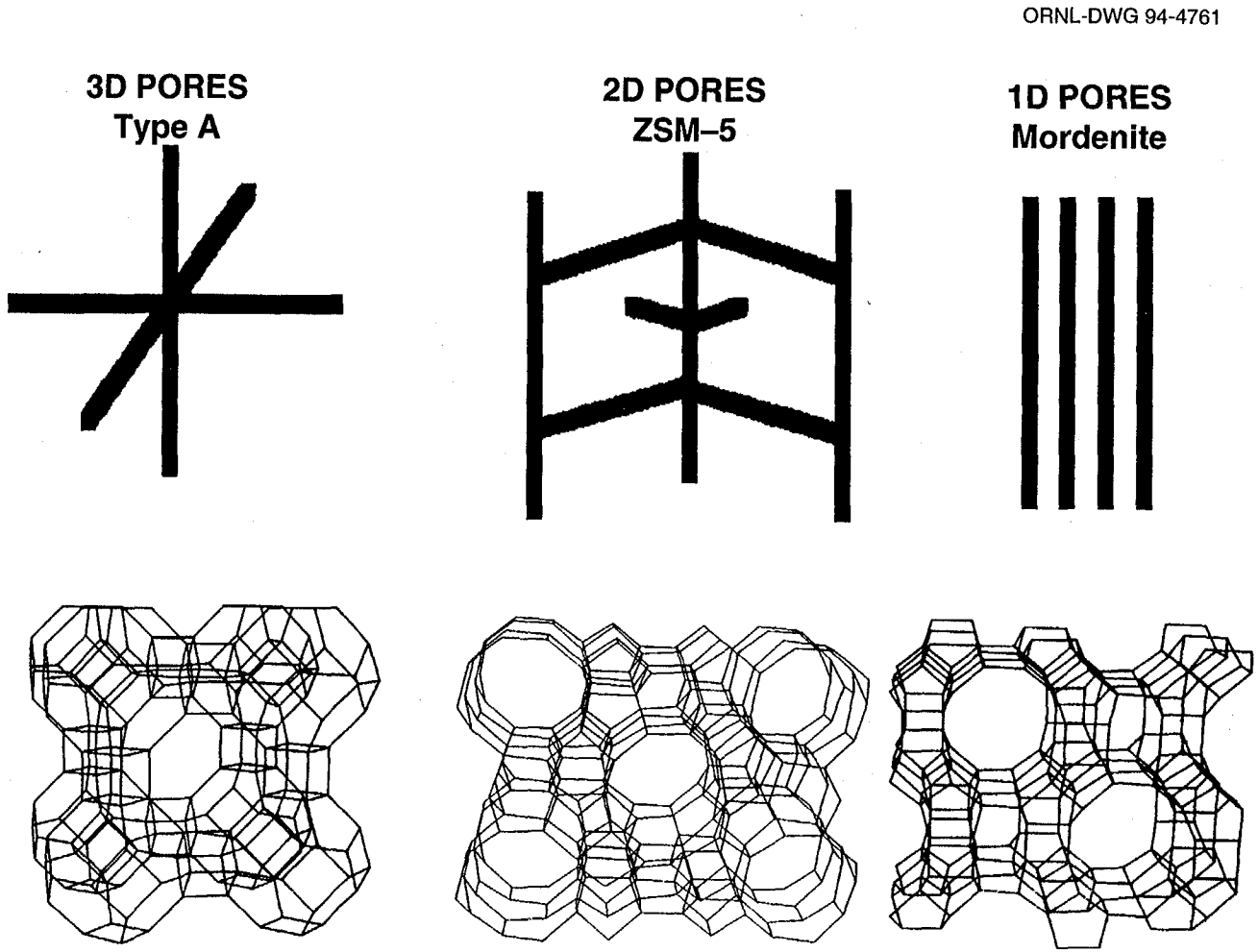

Figure 2.3. Pore structure of commercial zeolites. Redrawn after Figure 4, p. 27, D. E. W. Vaughan, "The Synthesis and Manufacture of Zeolites," *Chemical Engineering Progress*, Vol. 84, No. 2, p. 25–31, February 1988. Used with permission of the American Institute of Chemical Engineers.

kinetic diameter of ~6 Å. The effective pore size in AgZ could also be changed slightly by the exchange of the sodium cation for silver.

2.3.2 Composition

As might be expected, the physical properties of different types of zeolites vary with composition. Higher SiO_2:Al_2O_3 ratios result in harder and more acid resistant zeolite material but with a lower ion-exchange capability due to fewer nonframework cations. High chemical stability is also indicated by the high SiO_2:Al_2O_3 ratio. As noted in Sect. 2.1, a synthetic mordenite, a Norton Zeolon™, was chosen for continued iodine removal studies because of the desire for improved thermal stability during the regeneration process (Thomas et al., 1977). Breck (1974) gives the following structure for the sodium form of mordenites:

$$(Na_2O) * (Al_2O_3) * (SiO_2)_{10} * 6H_2O \qquad (2.18)$$

The synthetic sodium mordenite used in this study, as well as the studies conducted by Jubin (1980, 1982) and Burger and Scheele (1981), was initially produced and marketed by the Norton Company under the trade names Zeolon™ 100, Zeolon™ 200, and Zeolon™ 900. Other studies, Burger and Scheele (1982), Scheele et al. (1983), and Scheele and Burger (1987), were conducted using a material produced by the Ionex Corporation. The Ionex material is also produced from Norton Zeolon™, so the data should be comparable. In the late 1980's the rights/license for the production of the Zeolon™ molecular sieves was purchased by the PQ Corporation (Porey, 1993). A review by Vaughan (1988) on the synthesis and manufacture of zeolites indicated that, in addition

to the PQ Corporation, sodium mordenite was also produced by Union Carbide Corporation and Toyo Soda of Japan. Porey (1993) indicated that all of this the new material contained a silica binder whereas the original Norton mordenite was binderless.

2.4 DIFFUSION IN POROUS MEDIA

2.4.1 Diffusion in Zeolites

The process of physical adsorption in porous adsorbent material is generally extremely rapid according to Kärger and Ruthven (1992). As a result, in most cases, mass or heat transfer resistances are the controlling factors for the overall rate of adsorption.

Kärger and Ruthven (1992) provided an outstanding discussion on the diffusional resistances in zeolite pellets. What follows is a summary of that discussion as it applies to the problem at hand.

Kärger and Ruthven (1992) indicated that the pores can be classified in three broad categories based on their diameter. According to the International Union of Pure and Applied Chemistry (IUPAC) classification, pores with a diameter less than 20 Å are considered micropores while pores with a diameter greater than 500 Å are classified as macropores. The region between 20 and 500 Å is classified as mesopores.

The mass transport in each of these three size regions is controlled by different diffusion mechanisms (Kärger and Ruthven, 1992). In the macropores, interactions between the pore walls and the diffusing molecule are minor and generally bulk diffusion is observed. Typically, the macropore provides only limited adsorption capacity but may significantly impact the mass transfer rates. As the size of the pore decreases, the

interactions with the walls become increasingly important. In the mesopore region, diffusion control is generally associated with Knudsen diffusion; however, both surface diffusion and capillary effects may play significant roles. In the micropore region, surface forces are the most significant as the diffusion molecule interacts with the wall more frequently than with other diffusing molecules. This form of diffusion is also known as "intracrystalline" diffusion. Micropore diffusion is also quite different from the diffusion processes in either the macropore or mesopore regions in that it is an activated process.

Kärger and Ruthven, (1992) further indicate that the analysis of loading data obtained for zeolite crystals which are "sufficiently large" can generally be accomplished through the use of the simple single micropore diffusion resistance model. However, in the case of commercial pelleted adsorbents, there is often a continuous range of pore sizes which include micropores, mesopores, and macropores. This makes the analysis somewhat more difficult and, in many cases, only an average or effective diffusivity can be determined. The analysis of many commercially available zeolite adsorbents is a bit more tractable because these materials are formed from small microporous particles of the actual zeolite crystal to produce a macroporous pellet of a manageable size. This is often accomplished by the use of some type of binder material. In such pellets, the pore size distribution is reported to often exhibit a bimodal-type distribution. In this situation it is possible that the mass transport may be the controlled by macropore and/or micropore diffusion resistances.

There is also the possibility of external resistance from the gas film surrounding the adsorbent material which must be considered if the surrounding fluid consists of more than one component (Kärger and Ruthven, 1992). In all such cases, there will be a boundary layer or film in which the mass transfer will occur by molecular diffusion. The thickness of the film is a function of the hydrodynamic condition present in the system. The magnitude of this resistance may in some cases be controlling.

2.4.2 Molecular

In the adsorption process with pelletized zeolite molecular sieves there are two regions of interest in which molecular diffusion would appear to be important. The first is diffusion through the gas film surrounding the pellet and the second may be diffusion in the macropores. In the case of the diffusion through the gas film surrounding the pellet, the mass transfer can be represented by Fick's law (Yang, 1987):

$$Flux = k_g\left(C_s - C_g\right). \tag{2.19}$$

A similar situation exists in the macropores provided that they are large compared to the mean free path (Yang, 1987). In these cases, the principle interaction, or collisions, for the diffusing molecule is with other diffusing molecules. In this case there is minimal influence from the pore wall, and the diffusion process occurs by virtually the same mechanism as found for the bulk fluid. Therefore in the idealized case of a straight cylindrical pore, the molecular diffusivity, (D_{AB}), and the "pore diffusivity" are identical (Kärger and Ruthven, 1992). Yang (1987) states that a reasonable rule is that this situation is true if "the pore diameter is greater than ten times the mean free path."

The molecular diffusivity, D_{AB}, can be estimated using the Chapman-Enskog equation, (Bird et al., 1960):

$$D_{AB} = 0.0018583 \frac{T^{3/2}\left(\frac{1}{M_A}+\frac{1}{M_B}\right)^{1/2}}{P_t \sigma_{AB}^{\,2} \Omega_{AB}} \tag{2.20}$$

where:

T is the absolute temperature,

P_t is the total pressure,

M_A and M_B are the molecular weight of components A and B,

σ_{AB} is the force constant in Lennard-Jones potential function, and

Ω_{AB} is the collision integral.

To account for the nonideal pore structure, Lee (1976) describes the use of an effective diffusion coefficient. This is defined as

$$D_{AB,eff} = \frac{D_{AB}\varepsilon_p}{\tau}, \tag{2.21}$$

where ε_p is the void fraction or porosity of the pellet and τ is the tortuosity factor. The tortuosity factor was stated to be in the range of 3 to 7. This results in a decrease in the molecular diffusivity by a factor of 10 to 25.

Abbasi et al. (1983) suggested that for ordinary diffusion in porous solids where mercury porosimetry data was available τ can be estimated by:

$$\tau = \frac{1}{\varepsilon_p} + 1.196\frac{\sigma}{\bar{d}}, \tag{2.22}$$

where $\bar{d}$ and σ are the mean and standard deviation of the pore size respectively.

2.4.3 Knudsen Diffusion

For small pore diameters or low gas pressures, the frequency with which the diffusing molecules collide with the pore walls relative to each other increases as compared to the case of molecular diffusion. According to Ruthven (1984) the molecules that strike the pore walls are briefly adsorbed and then given off in a random direction. This diffusional process is often called "Knudsen" diffusion. Yang (1987) indicates that Knudsen diffusion "may be assumed" for values of $2r_p/\lambda$ less than 0.1, where r_p is the radius of the pore and λ is the mean free path of the gas molecules. For $0.1 < 2r_p/\lambda < 10$, a transition range exists in which both molecular and Knudsen diffusion are significant (Treybal, 1980).

To determine if Knudsen diffusion might be involved, the mean free path must be determined or estimated. The mean free path, λ, of the molecule can be estimated by the following relationship presented by Treybal (1980):

$$\lambda = \frac{3.2\,\mu}{P_t}\sqrt{\frac{RT}{2\pi g_c M_A}}. \tag{2.23}$$

The physical relationship for the Knudsen diffusivity may be derived from kinetic theory. One such derivation is detailed in the dissertation of Vaidyanathan (1971). For a long, straight capillary, the Knudsen diffusivity can be expressed by:

$$D_k = \frac{4\bar{r}_p}{3}\left(\frac{2}{\pi}\frac{RT}{M}\right)^{1/2}\left(\frac{2-f}{f}\right) = 9700\bar{r}_p\left(\frac{T}{M}\right)^{1/2}\left(\frac{2-f}{f}\right) \tag{2.24}$$

where:

f is the fraction of the molecules striking the surface of a pore wall,

$\bar{r}_p$ is the mean pore radius,

T is the temperature,

R is the gas constant; and

M is the molecular weight.

Vaidyanathan (1971) reported that typically a value of 1.0 is assigned to f but that values of (π/2) to (4/3) have also been recommended by various researchers. As noted, this expression is for a well defined structure and thus must be modified slightly to account for the nature of practical porous material.

If detailed pore volume distribution data are not available, the mean pore radius may be defined as:

$$\bar{r}_p = \frac{2\varepsilon_p}{S\rho_p}, \tag{2.25}$$

where:

S is the specific total surface area, (cm^2/g) and

ρ_p is the average bulk density or pellet density, (gm/cm^3).

An empirical factor referred to as tortuosity factor, τ, is then introduced to account for the irregularities of the internal structure. This factor must be determined experimentally. With these modifications, the effective Knudsen diffusion coefficient is given by

$$D_{k,eff} = \frac{4\varepsilon_p}{3\tau}\left(\frac{2\varepsilon_p}{S\rho_P}\right)\left(\frac{2}{\pi}\frac{RT}{M}\right)^{1/2} . \tag{2.26}$$

Simplifying yields:

$$D_{k,eff} = 19400\left(\frac{\varepsilon_p^2}{\tau S\rho_P}\right)\left(\frac{T}{M}\right)^{1/2} . \tag{2.27}$$

However if pore size data are available, the Knudsen diffusivity can be estimated in a similar manner as described for bulk or molecular diffusion by Abbasi et al., (1983). In their correlation the void fraction and tortuosity factor are lumped into a term k_o and the effective Knudsen diffusivity is given by:

$$D_{k,eff} = \frac{4}{3}\left(\frac{8RT}{\pi M}\right)^{1/2} k_o , \tag{2.28}$$

where k_o is correlated by

$$\frac{k_o}{\bar{d}} = 0.0093 + 0.1\varepsilon_p - 0.0181\frac{\sigma}{\bar{d}} , \tag{2.29}$$

$\bar{d}$ and σ in the above equation are the mean and standard deviation of the pore size respectively. If only the mean diameter is available, a less accurate form of Eq. (2.29) is:

$$\frac{k_o}{\bar{d}} = -0.0082 + 0.1\varepsilon_p . \tag{2.30}$$

In the transition region between molecular and Knudsen diffusion, the combined diffusivity can be estimated by the reciprocal addition rule if the mole fraction of component A is small. This yields:

$$\frac{1}{D} = \frac{1}{D_k} + \frac{1}{D_{AB}} \quad . \tag{2.31}$$

2.4.4 Poiseuille Flow

If a pressure difference exists across the particle or between the ends of the capillaries, then bulk flow will result. The equivalent diffusivity may be estimated by:

$$D_{pf} = \frac{P_t r^2}{8\mu} \quad , \tag{2.32}$$

where P_t is the absolute pressure in dynes/cm^2 and μ is the viscosity in poise. Ruthven (1984) showed in a simple example that for air at 1 atmosphere of pressure and 20°C, Poiseuille flow is a major contributor to the total or overall diffusivity for pores having a radius larger than 10^{-4} to 10^{-5} cm. Kärger and Ruthven (1992) extend this pointing out that the importance of Poiseuille flow also increases with pressure while the molecular diffusion is decreased.

2.4.5 Surface or Intracrystalline Diffusion

Intracrystalline diffusion is described by Ruthven (1984) as an activated process. This implies that the observed diffusion rate, if this mechanism could be isolated, would vary with temperature in accordance with an Arrhenius form equation:

$$D_c = D_\infty e^{-E_d/RT} \quad . \tag{2.33}$$

The diffusional activation energy, E_d, is reported to be generally less than the heat of adsorption. It is further pointed out that the contribution of surface diffusion to the overall effective diffusivity tends to decrease as the temperature increases.

It is also interesting to note that Kärger and Ruthven (1992) indicate that the diffusional activation energy and the activation energy for the chemical reactions may be similar.

Yang (1987) indicates that surface diffusion may have a significant impact to the overall diffusion rate in cases of (1) high surface area and (2) high surface concentrations.

2.4.6 Diffusion in Sodium Mordenites

Satterfield and Frabetti (1967) conducted experiments to determine the diffusion coefficients of C_1 to C_4 paraffin hydrocarbons in "single" crystals of synthetic mordenite. Sorption rates were measured gravimetrically in a sealed glass vessel by use of a calibrated quartz spring. The gas pressure remained essentially constant due to the high gas-to-adsorbent ratio. Gas pressures of 0- to 200-mm Hg were studied. For most of the tests, crystals of a 21- × 21- × 33-μ size were used. Diffusion coefficients were determined to be of the order of 10^{-9} to 10^{-10} cm^2/s by determining the slope of the initial uptake curve plotted as m_t/m_∞ vs $t^{1/2}$. and making use of the expression for the uptake on crystals of arbitrary shape. The expression for the uptake on crystals of arbitrary shape later appeared in the text of Kärger and Ruthven, (1992) as:

$$\frac{m_t}{m_\infty} = \frac{2S_{ex}}{V}\sqrt{\frac{D_c t}{\pi}} \,. \tag{2.34}$$

Late in this study, electron micrographs showed that some of what were thought to be well formed single crystals of the 21- × 21- × 33-μ size were quite rough on the edges and raised the possibility of individual particles of crystallites on the order of 0.1- to 1-μ size. The reported diffusion coefficient for CH_4 at a pressure of 100-mm Hg and 25°C is 3.3×10^{-9} cm^2/s. (Note that this value cannot be confirmed from the data contained in the paper. There was an apparent math error and the value obtained by this author from the published data yields a value of 7.6×10^{-10} cm^2/s.) Recomputing the value assuming an actual crystal diameter of 4-μ and the adsorption rate curve at 27°C, the diffusion coefficient is 1.5×10^{-11} cm^2/s. They also reported very significant effects resulting from light grinding of the crystals with mortar and pestle. Reductions of 20 to 30% were observed in sorption capacity compared to the unground material. It was further speculated that "deleterious effects may result from the pelletizing or extrusion processes commonly used in compacting molecular sieves and other powders into pellets."

This work was expanded by Satterfield and Margetts (1971) to focus on the fast adsorption processes that exceeded the response capabilities of the previous research. It was noted that in the "single crystals" used in their study, 17% of the pore volume was greater than 7 Å. This work utilized a constant volume system and monitored the pressure change. For CH_4 a diffusion coefficient of 1.2×10^{-8} to 3.0×10^{-8} cm^2/s was reported at the point of 50% total adsorption. The CH_4 pressure was 1.7- to 25-mm Hg. It was noted that the diffusion rate varied with total adsorption and had a maximum value near the 50% loading point. Fifty percent of the infinite loading for n-butane is achieved in 25

to 100 s, depending on the pressure of the system. The variation in the diffusion coefficient with loading is partially attributed to temperature effects.

2.5 MODELS FOR ADSORPTION/REACTION ON SOLID OR POROUS MEDIA

2.5.1 General Assumptions and Simplifications

In most cases modeling of the diffusion processes in porous media requires some type of simplifying assumptions. These generally involve the definition of structure of the adsorbent material, the nature or order of the chemical reactions and thermal effects associated with the heat of reaction and adsorption, and finally the behavior of the diffusion coefficient.

In most cases, the first assumption deals with the shape of the adsorbent pellet or subpellets. As will be noted in Sect. 2.5.2, a common assumption is that the pellet is spherical. The second assumption deals with the structure of the pellet itself as this will in large part define the nature of the model. The assumed structure of the adsorbent material to be modeled will be briefly described in Sect. 2.5.3.

Many of the models for adsorption assume that the process is isothermal. The validity of this assumption and the impacts of nonisothermal behavior will be described in Sect. 2.5.6.

The isothermal models described all assume that the diffusivity is constant. This is reported to be a good approximation for small changes in concentration according to

Kärger and Ruthven (1992). The nonisothermal models take into account the temperature dependence of diffusivity and/or equilibrium relationships.

Finally assumptions about the stability of the process system used in the experimental determinations are generally made. One of the common process assumptions is that of constant bulk gas phase composition. This is either based on the use of a very large system, a true constant pressure system, or by careful control of a flowing gas stream. If this assumption is not made, then the changing composition of the gas phase must be addressed in the model.

2.5.2 Particle Shape and Use of Equivalent Spherical Radius

Commercially available extruded adsorbents are not of uniform size. While they appear to be nearly the same diameter, the length varies greatly (see Appendix A.1 for data on the sorbent material used in this study). Kärger and Ruthven (1992) point out that while general solutions have been derived for some situations for the cube, slab, and infinite cylinder, the most convenient form is for the sphere. It is generally accepted to use an equivalent spherical radius, $\bar{r}$, defined as "the radius of a sphere having the same external surface-to-volume ratio." They demonstrate the accuracy of this approximation. The infinite cylinder and the equivalent spherical radius differ by about 25% in terms of dimensionless time to reach 90% conversion. At 50% conversion, the error is <5%. "This is within the margin of error of most uptake measurements so the approximation may be regarded as acceptable."

2.5.3 Structure

As part of various modeling approaches, the structure of the solid pellet has been conceptualized in numerous ways as pointed out in review articles by Ramachandran and Doraiswamy (1982) and Kulkarni and Doraiswamy (1986) on the modeling of noncatalytic gas solid reactions. The simplest approach is that of a spherical, homogenous, nonporous pellet. The next level of complexity assumes the pellet to be porous but still homogenous in composition. It has also been proposed to model certain processes where the solid pellet consists of subparticle or grains which are nonporous. A cracking core model has been proposed in which a nonporous particle becomes porous by cracking. Each of the new subparticles is assumed to remain nonporous. This porous and nonporous nature can be extended to a case where the subparticles are also porous (Kärger and Ruthven, 1992).

In the three latter cases of porous particles, some type of pore structure behavior may also be considered. This includes the assumption of constant pore dimensions or cases where pore closure comes into play. This may include a "single pore model" which assumes that the behavior or changes in a pore is representative of what is happening in a pellet. This may include some changes in pore diameter with time but does not address the pore size distributions which may exist. To account for these pore size distributions, distributed pore models have been developed.

2.5.4 Noncatalytic Reactions of Solid Particles

There are two well accepted basic models in use today which describe noncatalytic reactions of solid particles with a surrounding fluid. These models, which are described in

the text by Levenspiel (1972) and in review articles by Ramachandran and Doraiswamy (1982), and Kulkarni and Doraiswamy (1986), are the shrinking or unreacted core model and the progressive-conversion model. The descriptions and relevant equations that follow are summarized from these references unless noted otherwise.

2.5.4.1 Shrinking or unreacted core model

The shrinking core model, or unreacted core model, as described by Levenspiel (1972, 1979), was developed by Yagi and Kunii in 1955. This is also referred to as the Sharp Interface Model (SIM) by Kulkarni and Doraiswamy (1986). A general graphical representation of this model is presented in Fig. 2.4. The model is described by Levenspiel (1972) as five sequential steps for the gaseous reactant and product components.

For the reactant gases:

1. Diffusion through a boundary layer gas film which surrounds the solid particle.
2. Diffusion though the particle to the surface of the unreacted core.
3. The reaction with the solid reactant at the surface of the solid core.

And for the product gases:

4. Diffusion back though the reacted portion of the particle to the outside surface of the particle.
5. Diffusion through the boundary layer gas film surrounding the solid particle.

It was noted by Levenspiel (1972) that there may be significant variations in relative importance of these five steps, depending on the relative magnitude of the associated resistances to mass transfer. Further, in some situations some of these steps are not relevant. For example, in the case of an irreversible reaction, steps 4 and 5 do not

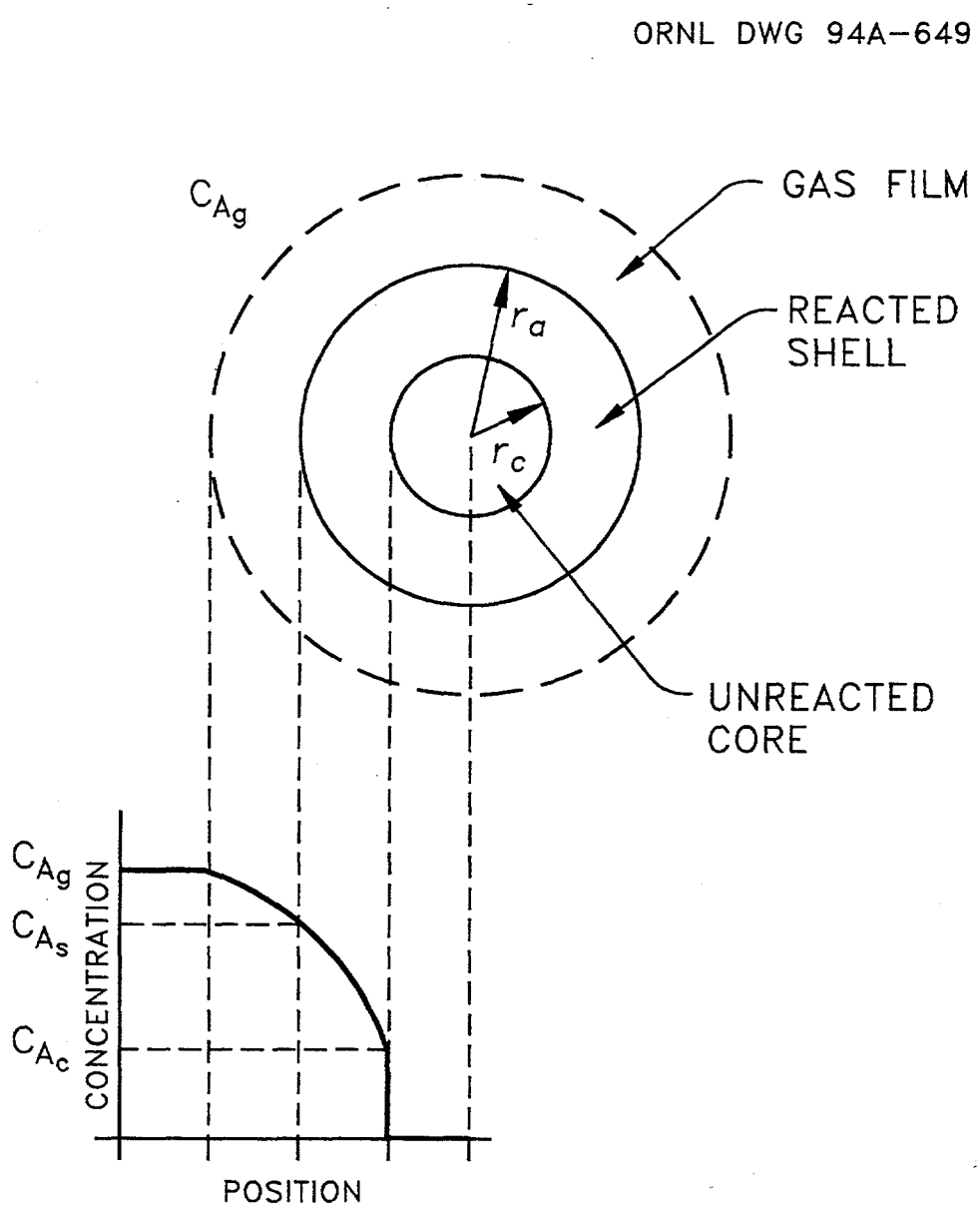

Figure 2.4. Schematic representation of the shrinking core model. Adapted from Figure 4, p. 362, O. Levenspiel, *Chemical Reaction Engineering*, Second Ed. Copyright © 1972 John Wiley & Sons, Inc., New York. Reprinted with permission of John Wiley & Sons, Inc.

contribute directly to the observed resistances to the reactions. The same is true of a reaction producing no gaseous products.

The basic conversion equations for each of the remaining three steps have been developed for various geometries and for both constant size particles and shrinking particles. For a gas-solid reaction of the general form

$$A(g) + bB(s) \rightarrow R(g) + S(s) \tag{2.35}$$

and constant size spherical particles, the following conversion-time expressions are relevant for the first three resistances and can be utilized to compare the observed loading rate data with the theoretical uptake curve:

1. Film Diffusion Controls:

In terms of the flux, the equations describing film diffusion control can be written based on either the moles of the diffusing component, *A*, or the moles of the solid reactant, *B*, that is reacted with *A* according to Eq. (2.35):

$$-\frac{1}{S_{ex}}\frac{dN_B}{dt} = -\frac{1}{4\pi r_a^2}\frac{dN_B}{dt} = -\frac{b}{4\pi r_a^2}\frac{dN_A}{dt} = bk_g\left(C_{Ag} - C_{As}\right) . \tag{2.36}$$

For the limiting case when there is only film diffusion control, C_{As} approaches 0.

By considering the molar density of *B* in the solid and the volume of the solid, the relationship between the rate at which the core shrinks and moles react is given by:

$$-dN_B = -bdN_A = -4\pi\rho_B r_c^2 dr_c . \tag{2.37}$$

Through the use of this relationship, Eq. (2.36) can be integrated to determine how the core shrinks with time. And thus the fractional conversion, X_B, can be expressed in terms of the unreacted core radius by:

$$\frac{t}{\tau_{gasfilm}} = 1 - \left(\frac{r_c}{r_a}\right)^3 = X_B \,, \tag{2.38}$$

where the time for total conversion is given by

$$\tau_{gasfilm} = \frac{\rho_B r_a}{3bk_g C_{Ag}} \,. \tag{2.39}$$

2. Ash Diffusion Controls:

In terms of the flux, the equation for the diffusion of A through the ash or reacted shell can be written:

$$-\frac{1}{S_r}\frac{dNa}{dt} = D_e \frac{dC_A}{dr} \,. \tag{2.40}$$

Integrating this equation over the values of r from the exterior surface of the particle to the outer edge of the unreacted core yields an expression describing the rate of diffusion of component A for any core radius:

$$-\frac{dNa}{dt}\left(\frac{1}{r_c} - \frac{1}{r_a}\right) = 4\pi D_e C_{Ag} \,. \tag{2.41}$$

This assumes that the gas concentration at the surface of the pellet is the same as the bulk gas concentration (i.e., no gas film resistance). By rewriting Eq. (2.41) using the relationship for the radius of the shrinking core vs the moles of B reacted, Eq. (2.37), the relationship of the unreacted core or fractional conversion and time can be obtained

through integration of the resulting equation. The resulting expression in terms of fractional conversion is:

$$\frac{t}{\tau_{ash}} = 1 - 3\left(1 - X_B\right)^{2/3} + 2\left(1 - X_B\right), \tag{2.42}$$

where the time to complete conversion is given by:

$$\tau_{ash} = \frac{\rho_B r_a^2}{6bD_e C_{Ag}}. \tag{2.43}$$

3. Chemical Reaction Controls:

The molar rate of either A or B reacted at the surface of the unreacted core, assuming chemical reaction control only, can be determined based on the general stoichiometry given in Eq. (2.35):

$$-\frac{1}{S_{core}}\frac{dN_B}{dt} = -\frac{b}{S_{core}}\frac{dN_A}{dt} = bk_s C_{Ac}, \tag{2.44}$$

where k_s is the assumed first order reaction constant. Again rewriting this in terms of the shrinking radius and integrating yields the relationship for the conversion vs time:

$$\frac{t}{\tau_{rxn}} = 1 - \frac{r_c}{r_a} = 1 - (1 - X_B)^{1/3}, \tag{2.45}$$

where the time to complete conversion is given by:

$$\tau_{rxn} = \frac{\rho_B r_a}{bk_s C_{Ag}}. \tag{2.46}$$

4. Full Shrinking Core Model

However, in many situations more than one of these resistances is a factor in determining the observed rate of conversion of the particle. The three individual rate

expressions can be combined into a single expression and the intermediate concentrations of component A can also be eliminated as described by Levenspiel (1972, 1979). This yields:

$$-\frac{1}{S_{ex}}\frac{dN_B}{dt}=\left[\frac{b}{\frac{1}{k_g}+\frac{r_a\left(r_a-r_c\right)}{r_c D_e}+\frac{r_a^2}{r_c^2 k_s}}\right]C_{Ag} \quad . \tag{2.47}$$

This expression can easily be converted into a more usable form for the analysis of the gravimetric loading data by using the relationship for conversion in terms of unreacted core radius, r_c, found in Eq. (2.38), and substituting into Eq. (2.47) yielding:

$$-\frac{1}{S_{ex}}\frac{dN_A}{dt}=\left[\frac{b}{\frac{1}{k_g}+\frac{r_a\left(1-\left(1-X_B\right)^{1/3}\right)}{\left(1-X_B\right)^{1/3}D_e}+\frac{1}{\left(1-X_B\right)^{1/3}k_s}}\right]C_{Ag} \quad . \tag{2.48}$$

This expression can be used to determine the values of the three adjustable parameters through a process of curve fitting to minimize the error between experimentally obtained flux or loading data and the calculated values.

Alternately, it has been shown by Levenspiel (1972, 1979) that the total time to reach a given conversion is the sum of the times for the individual mechanisms to reach the same conversion. In other words:

$$t_{total}=t_{gasfilm}+t_{ash}+t_{rxn}. \tag{2.49}$$

Likewise for the complete conversion the time is given by:

$$\tau_{total} = \tau_{gasfilm} + \tau_{ash} + \tau_{rxn}. \qquad (2.50)$$

By replacing the expressions for the individual times to reach a set conversion given by Eqs. (2.38), (2.42), and (2.45) for the individual times into Eq. (2.49), an expression is obtained that allows the determination of the extent of the conversion for any value of time. It should be noted that the conversion is found as the root of the following equation:

$$t_{total} = X_B \tau_{gasfilm} + \left[1 - 3(1 - X_B)^{2/3} + 2(1 - X_B)\right]\tau_{ash} + \left[1 - (1 - X_B)^{1/3}\right]\tau_{rxn} \qquad (2.51)$$

2.5.4.2 Progressive conversion or volume reaction model

Ramachandran and Doraiswamy (1982) indicate that the shrinking core model is applicable to nonporous or relatively nonporous solids. In the case of silver-exchanged mordenite, this may not be the case. The "progressive conversion model" or as referred to by Ramachandran and Doraiswamy, the "volume reaction model," assumes on-going reactions occurring throughout the pellet for all values of time greater than 0 and less than the time for complete conversion (see Fig. 2.5). These reactions may also occur at different rates due to concentration and temperature gradients across the pellet. In one limiting case there is no diffusional resistance, and the reaction occurs uniformly throughout the pellet. At the other limit, the model approaches that of the shrinking core model (Kulkarni and Doraiswamy, 1986).

The model as presented by Ramachandran and Doraiswamy (1982) assumes a general rate of reaction per unit volume as given by:

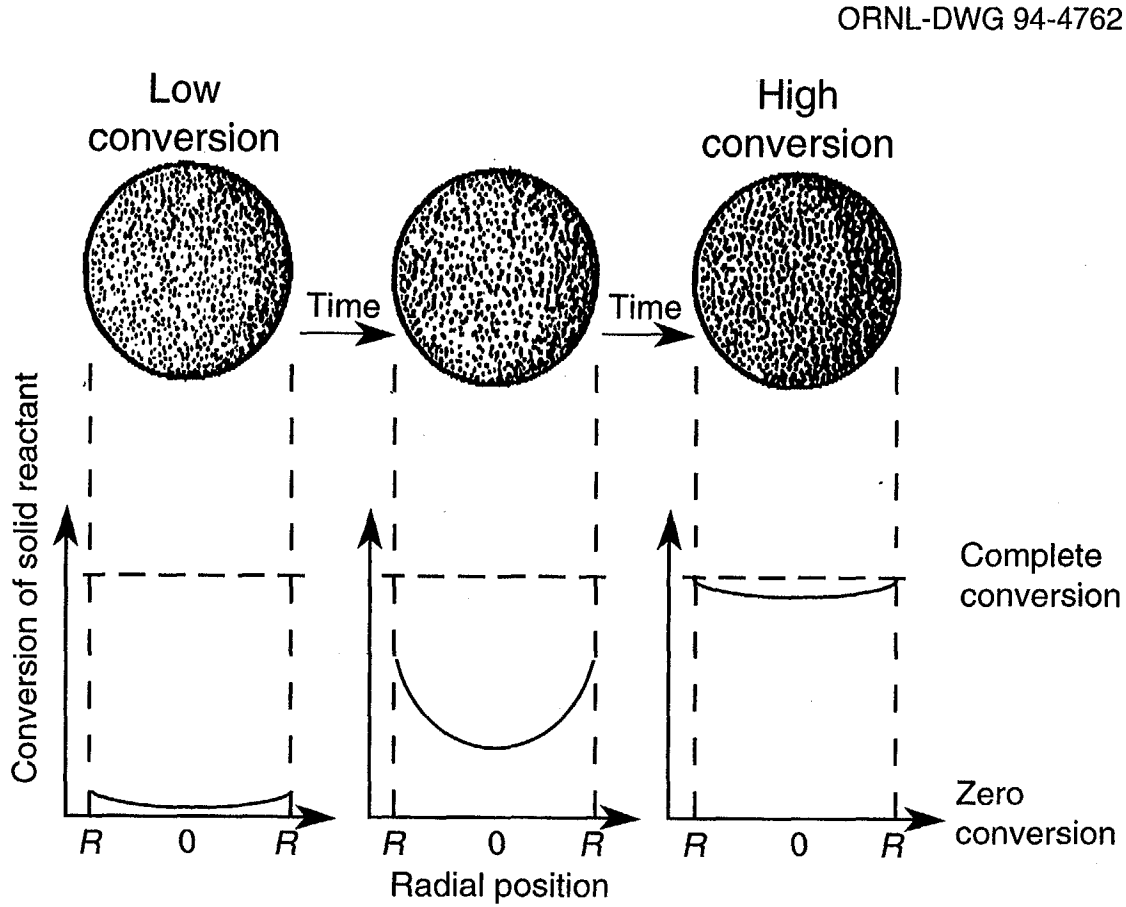

Figure 2.5. Schematic representation of the volume reaction model. Adapted from Figure 2, p. 360, O. Levenspiel, *Chemical Reaction Engineering*, Second Ed. Copyright © 1972 John Wiley & Sons, Inc., New York. Reprinted with permission of John Wiley & Sons, Inc.

$$r_v = k_v A^m B^n \quad , \tag{2.52}$$

where m and n are the order of reaction for A and B respectively.

An approximate analytical solution to this problem was developed by Ramachandran and Kulkarni (1980) for the case in which the reaction is first order with respect to both the solid and gas components. The following assumptions were made in developing the model:

1. constant diffusivity,
2. no structural changes in the solid,
3. isothermal conditions,
4. no external mass transfer gradient, and
5. pseudo-steady-state conditions.

This model was developed using a single-point collocation method with the resulting expression relating fractional conversion and time:

$$\ln\left[\frac{(1-X)}{W_1(1+\zeta)} - \frac{W_2}{W_1}\exp(-\theta)\right] + \theta = \frac{\phi^2}{B_{12}}\left[1 - \frac{(1-X)}{W_1(1+\zeta)} + \frac{W_2}{W_1}\exp(-\theta)\right], \tag{2.53}$$

where the values of the coefficients for spherical geometry are given in Table 2.2.

Table 2.2: Coefficients for the volume reaction model.

	ζ	B_{12}	W_1	W_2
Slab	0	2.5	0.833	0.1667
Cylinder	1	6.0	0.375	0.125
Sphere	2	10.5	0.233	0.1

Source: Ramachandran and Kulkarni (1980).

where θ is the dimensionless time term defined as:

$$\theta = bk_v C_{Ag} t \tag{2.54}$$

and ϕ is Thiele modulus defined as:

$$\phi = r_a \left[\frac{k_v C_{B0}}{D_{s,eff}} \right]^{1/2}. \tag{2.55}$$

The Thiele modulus is the ratio of the maximum kinetic rate to the maximum internal diffusion rate.

At low values of the ($\phi < 0.2$) the concentration profile across the pellet may be considered uniform (Kulkarni and Doraiswamy, 1986). As the values of ϕ increases, this may no longer be assumed to be valid. For values of $0.2 < \phi < 3.0$, a parabolic concentration profile of A extends across the diameter of the pellet and the gas-solid reaction occurs throughout the pellet but at potentially nonuniform rates. As the value of the Thiele modulus increases above 3.0, a reaction zone begins to appear. As the zone thickness approaches zero, the volume reaction model corresponds to the shrinking core model.

The error between the approximate solution and the numerical solutions developed by Dudukovic and Lamba (1978) were analyzed by Ramachandran and Kulkarni (1980). Excellent agreement is obtained for small values of ϕ. Some deviation is noted for $\phi > 5.0$, but at values of $\phi = 10.0$ the difference is within 16%.

2.5.5 Isothermal Models for Porous Media

The two previous models do not consider the nature of the media which in the case of zeolites may be important. Kärger and Ruthven (1992) summarize numerous studies which have focused on the adsorption from the gas phase into a porous zeolite-type structure. In general terms, these studies attempted to incorporate the porous nature of the zeolite pellets by addressing diffusional resistances arising from (1) the micropores, (2) the macropores, or (3) a combination of both macropore and micropore resistance. These models are further summarized below.

2.5.5.1 Micropore diffusion controlling

For the case of micropore diffusion alone, the following transient sorption expression is presented by Kärger and Ruthven (1992):

$$X_B = \frac{m_t}{m_\infty} = 1 - \frac{6}{\pi^2}\sum_{n=1}^{\infty}\frac{1}{n^2}\exp\left(-\frac{n^2\pi^2 D_c t}{r_i^2}\right). \tag{2.56}$$

The development of this equation can also be found in the text by Crank (1975) for the case of nonsteady-state diffusion in a sphere. The two primary assumptions that must be noted are the use of constant diffusivity and that the change in the adsorbed phase concentration is small such that gas phase or surface composition remains constant (Ruthven, 1984).

This model reduces to:

$$X_B = \frac{m_t}{m_\infty} = 1 - \frac{6}{\pi^2}\exp\left(-\frac{\pi^2 D_c t}{r_i^2}\right) \tag{2.57}$$

as time term becomes large. Kärger and Ruthven (1992) point out that a plot of $\ln[1-m_t/m_\infty]$ vs t should approach a straight line. This line will have a slope of $-\pi^2 D_c/r_i^2$ and an intercept of $\ln(6/\pi^2)$. They caution that the long time regions are also affected by thermal effects and that particle size distributions may result in curvature of the semilogarithmic plot.

2.5.5.2 Macropore diffusion controlling

For macropore diffusion the solution is the same with the D_c/r_i^2 term replaced by:

$$\frac{D_p}{r_a^2}\left(\frac{1}{1+K^*\left(1-\varepsilon_p\right)/\varepsilon_p}\right), \tag{2.60}$$

where K^* is an equilibrium constant which has an Arrhenius-type temperature dependence.

2.5.5.3 Combined micropore and macropore diffusion control

Dual-resistance systems in biporous media have been studied by several researchers. Ruckenstein et al. (1971), discussing the dissertation of Vaidyanathan (1971), pointed out that the macropore diffusivity and micropore diffusivity may, in many cases, be quite different by orders of magnitude. In such a case, the observed diffusion process may be significantly affected by the particular structure of the porous solid. While the diffusion behavior of a biporous material had been reported by earlier researchers, the model developed by Vaidyanathan (1971) appears to be the first to address the analysis of transient sorption with the competing effects of macropore diffusion and micropore diffusion combined. The assumptions made in the development of this model are as follows:

1. The system is isothermal.
2. The particle is spherical and composed of small uniform spherical microporous particles.
3. The sorbent is exposed to an infinite source of sorbate such that the surface concentration is constant.
4. The sorbent is exposed to a step change in sorbate concentration at time zero.
5. Adsorption occurs at both the walls of the macropores and micropores.
6. Linear isotherms apply.

The same basic system was also studied by Ma and Lee (1976) and by Lee (1978). These two papers extended the original model to address the case of a finite quantity of sorbate and thus overcame assumption No. 3. All three papers developed a set of similar equations which may be used to evaluate the transient uptake of the sorbate, but the work by Lee appeared to be a bit simpler and faster in terms of computer time to apply as it contained only a single double summation and the others contained the ratio of two double summations. In the case of constant gas phase concentrations, the mathematical solution developed by Lee simplifies to:

$$X_B = \frac{m_t}{m_\infty} = 1 - \frac{18}{\beta + 3\alpha} \sum_{m=1}^{\infty} \sum_{n=1}^{\infty} \left(\frac{n^2 \pi^2}{p_{n,m}^4} \right) \frac{e^{-p_{n,m}^2 D_c t / r_i^2}}{\left\{ \alpha + \frac{\beta}{2} \left[1 + \frac{\cot(p_{n,m})}{p_{n,m}} \left(p_{n,m} \cot(p_{n,m}) - 1 \right) \right] \right\}} \quad , \quad (2.61)$$

where:

$$\alpha = \frac{D_c}{r_i^2} \frac{r_a^2}{D_p} \quad , \quad (2.62)$$

$$\beta = \frac{3\alpha\left(1-\varepsilon_p\right)q_\infty}{\varepsilon_p C_{A,0}}, \text{ and} \tag{2.63}$$

$p_{n,m}$ is given by the roots of the transcendental equation:

$$\alpha p_{n,m}^2 - n^2\pi^2 = \beta\left(p_{n,m}\cot\left(p_{n,m}\right)-1\right). \tag{2.64}$$

Vaidyanathan (1971) discussed the physical significance of the α and β terms. α is the ratio of the time constants for macropore to micropore diffusion. For values of α less than 10^{-3}, macropore diffusion is much faster than micropore diffusion and the process can be considered to be a two-step process for all practical purposes. For values of α greater than 10^{+2} macropore diffusion controls (Ruckenstein et al., 1971). In the range of α between these two limiting cases both mechanisms are important.

The term $\beta/3\alpha$, represents the ratio of sorption in the macropores to micropores at equilibrium. Thus a large value would indicate primarily sorption in the micropores.

2.5.6 Nonisothermal Systems

All of the described models assume that the system being studied is isothermal. When studying an adsorption/reaction process the possibility that the isothermal assumptions could be invalid due to the heat effects from adsorption and/or reaction must be considered. In such a case, the heat effects, which may be significant, must be accounted for in the analysis used to examine the experimental data. Isothermal assumptions are generally only valid when the sorption rates are relatively slow (Kärger and Ruthven, 1992).

Lee and Ruthven (1978) describe the three possible resistances to heat transfer. These are (1) the resistance to heat transfer from the external surface of the pellet to the surrounding fluid; (2) the resistance to heat transfer from the external surface of individual particle within the pellet or, in other words, the internal heat transfer resistances; or (3) the resistance to heat conduction within the individual particle. The relative magnitude of these heat transfer resistances has been analyzed by Lee and Ruthven (1978). Their analysis considered the time constants for the thermal processes in a system where the mass transfer was assumed to be sufficiently rapid to maintain the sorbate concentration at its equilibrium value throughout the pellet. It was shown that for all cases the heat transfer from the external surface will be slower than heat transfer between the crystals of the sample. It was further shown that the ratio of relative time constants for intracrystalline conduction to external heat transfer was approximately 10^{-6} for a bed depth of 1 mm and a crystal diameter of 10 μm. The heat transfer coefficient was estimated to be 5×10^{-4} cal/(cm^2 s °K) and the thermal conductivity to be 4×10^{-4} cal/(cm s °K). Based on this analysis, the temperature throughout the sample was uniform. The relative rates of heat conduction and diffusion were also compared. Even in the case of an intercrystaline diffusion coefficient as large as 10^{-5} cm^2/s, the ratio was on the order of 50 to 100, indicating the heat transfer within the crystal was rapid compared to the rate of diffusion.

In general, the primary resistance to heat transfer is the external film resistance (Kärger and Ruthven, 1992) with the primary mass transfer resistance being intraparticle (micropore), intrapellet (macropore), or within the bed itself.

2.5.6.1 Nonisothermal micropore/macropore diffusion controlling

Lee and Ruthven (1978) examined the nonisothermal case of micropore diffusion. In their work, as presented by Kärger and Ruthven (1992), the uptake on the adsorbent was given by :

$$X_B = \frac{m_t}{m_\infty} = 1 - \sum_{n=1}^{\infty} \frac{9\left[\left(p_n \cot p_n - 1\right)/p_n^2\right]^2 \exp\left(-p_n^2 D_c t / r_i^2\right)}{\frac{1}{\beta'} + \frac{3}{2}\left[p_n \cot p_n \left(p_n \cot p_n - 1\right)/p_n^2 + 1\right]}, \tag{2.65}$$

where p_n was given by the positive roots of the transcendental equation:

$$3\beta'\left(p_n \cot p_n - 1\right) = p_n^2 - \alpha' \tag{2.66}$$

and the parameters α' and β' are defined as:

$$\alpha' = \frac{h_m S}{C_p}\frac{r_i^2}{D_c} \tag{2.67}$$

and

$$\beta' = \frac{\Delta H}{C_p}\left(\frac{\partial q^*}{\partial T}\right)_P. \tag{2.68}$$

Only the positive roots of the transcendental equation were used since the equation is symmetrical about zero.

If macropore diffusion is controlling, the same basic equations apply except that the D_c/r_i^2 term is replaced with a comparable term, D_{eff}/r_a^2, which contains the effective diffusivity, D_{eff}, and the pellet radius, r_a (Kärger and Ruthven, 1992). The effective diffusivity is defined by:

$$D_{eff} = \frac{\varepsilon_p D_p}{\varepsilon_p + \left(1 - \varepsilon_p\right)K^*}. \tag{2.69}$$

This is essentially the same substitution that was made in the case of isothermal micropore to macropore cases.

The two limiting cases for this model are the isothermal case and the heat transfer limiting case. The isothermal case is obtained when either α' approaches ∞ (infinitely rapid heat transfer) or β' approaches 0 (infinite heat capacity). Under the isothermal conditions it was shown by Lee and Ruthven (1978) and Ruthven et al. (1980) that the roots of the transcendental equation become $p_n = n\pi$ and that the equation for conversion becomes simply:

$$X_B = 1 - \frac{6}{\pi^2}\sum_{n=1}^{\infty}\frac{1}{n^2}\exp\left(-\frac{n^2\pi^2 D_c t}{r_i^2}\right) \tag{2.70}$$

which is the same as the transient conversion equation for micropore diffusion controlling, Eq. (2.57).

Lee and Ruthven (1978) discussed the significance of the α' and β' terms in the determination of the acceptability of using an isothermal assumption. Of the two criteria presented, the first is the more rigorous in that $\alpha'/(1+\beta') >> \pi^2$ for the system to be considered isothermal. But it was also indicated that for small values of β', the thermal effects become only significant in the long time periods and it was proposed that if $\alpha'/\beta' >$ 60 then the variation in the calculated time constants assuming isothermal conditions would not vary from the nonisothermal values by more than 15% for loadings below 85%.

For small values of α', the kinetics are controlled solely by heat transfer and the uptake can be determined by the following equation:

$$X_B = 1 - \frac{\beta'}{1+\beta'} \exp\left(-\frac{h_m S t}{C_p (1+\beta')} \right). \tag{2.71}$$

2.5.6.2 Nonisothermal bed diffusion controlling

In 1981, Ruthven and Lee published a third paper in a continuing series on nonisothermal sorption. This paper made the claim that earlier kinetic studies were incorrect in assuming that the primary diffusional resistance is within the pores of the zeolite crystals. The claim was made that, in fact, the primary diffusional resistance was within the bed itself. In such a case, the governing equation for uptake on the sorbent is:

$$X_B = \frac{m_t}{m_\infty} = 1 - \sum_{n=0}^{\infty} \frac{2 \exp\left(-p_n^2 D_{eff} t / l^2 \right)}{\left[p_n^2 \cot^2 p_n \left(1 + 2/\beta' \right) + p_n^2 + \cot p_n \right]}, \tag{2.72}$$

where p_n is given by the positive roots of the equation

$$\cot p_n = \frac{\beta' p_n}{\alpha' - p_n^2} \tag{2.73}$$

and the parameters α' and β' are defined as:

$$\alpha' = \frac{h_m S}{C_p} \frac{l^2}{D_{eff}} \tag{2.74}$$

and

$$\beta' = \frac{\Delta H}{C_p} \left(\frac{\partial q^*}{\partial T} \right)_P. \tag{2.75}$$

2.6 THEORETICAL RESPONSES TO PROCESS VARIATIONS

2.6.1 Temperature Effects

Levenspiel (1972) in discussing the shrinking core model indicated that the chemical reaction step is generally far more sensitive to temperature variation than the diffusion steps. Based on this, variations in temperature should allow separation between the diffusion mechanisms controlling and the reaction step controlling.

Kärger and Ruthven (1992) have summarized the following about the temperature response of microporous zeolite catalysts. First, the reaction rate constant generally follows the Arrhenius law, $k_s = k_\infty e^{-E/RT}$. Second, in a conventional catalyst material, the macropore diffusion occurs mainly by the Knudsen or molecular mechanisms. Knudsen diffusion increases relative to the square root of temperature [see Eq. (2.27)], and molecular diffusion is only weakly dependent on temperature. Then if at relatively low temperatures the adsorption process was initially in the reaction controlled regime, it is expected that as the temperature rises, k_s will increase more rapidly than the effective diffusivity. This more rapid increase in reaction rate will result in the transition in the observed adsorption rate from one of reaction control to one of macropore diffusion control.

However, in the case of a zeolite catalyst subject to intracrystalline diffusion limitation, the expected behavior of temperature dependence may be significantly different. First, the intracrystalline diffusion is an activated process and, as such, the diffusivity varies with temperature in accordance with an Arrhenius law equation, $D_c = D_\infty e^{-E_d/RT}$,

and Kärger and Ruthven (1992) indicated that the diffusional activation energy may be comparable with the activation energy of the chemical reaction. Yang (1987) stated for zeolites with small diameter pores the apparent activation energy for diffusion of nonpolar molecules is on the order of 3 to 11 kcal/mol. It is further stated that the apparent activation energy for diffusion is a function of the size and shape of the diffusion molecule and the effective pore diameter.

2.6.2 Concentration Effects

The relationship of concentration to diffusivity is also discussed in the text by Yang (1987). He describes four different trends that have been observed with increasing sorbate concentration:

1. The diffusivity decreases.
2. The diffusivity increases.
3. The diffusivity decreases and then increases.
4. The diffusivity increases to a maximum and then decreases.

One explanation for the decrease in diffusivity with increased concentration is a decrease in mean jump distance. This is the result of increased molecular collisions. Darken's relation is suggested to account for the increase in diffusivity. Yang indicates that there is little doubt that there is some concentration dependence but concludes that as a whole this relationship is not well understood.

2.6.3 Velocity Effects

The fluid velocity has its impact on the boundary layer surrounding the pellet. By increasing the fluid velocity, the boundary layer resistance is lowered for both mass transfer and heat transfer in the nonisothermal case. In the isothermal case, by varying the gas velocity it may be possible to distinguish between film diffusion control and ash layer control since both may have similar responses to variations in particle size, but the ash diffusion will be unaffected by changes in the fluid velocity (Levenspiel, 1972).

2.6.4 Particle Diameter

The response to variations in this parameter is in many cases a key step in the determination of the controlling mechanism. For example, in the case of the shrinking core model, the time needed to reach a given conversion is a function of particle radius (Levenspiel, 1972). For reaction control, $t \propto r_a$, for film diffusion controlling, $t \propto r_a^{1.5 \text{ to } 2.0}$, and for ash diffusion, $t \propto r_a^2$.

2.7 SUPPORTING HEAT AND MASS TRANSFER COEFFICIENT CORRELATIONS

2.7.1 Mass Transfer Coefficients

The mass transfer coefficient can be estimated by the use of the Sherwood number provided that the particle diameter and the molecular diffusivity are known. Wakao and Funazkri (1978) evaluated the effects of fluid dispersion coefficients on particle-to-fluid mass transfer coefficients in packed beds. They propose the use of the following

correlation for the estimation of the Sherwood number over the range of Reynolds numbers from about 3 to 10,000:

$$N_{Sh} = \frac{k_g 2r_a}{D_{AB}} = 2 + 1.1 N_{Sc}^{1/3} N_{\mathrm{Re}}^{0.6}. \tag{2.76}$$

They state that this correlation is preferred over the popular Ranz and Marshall equation:

$$N_{Sh} = 2 + 0.6 N_{Sc}^{1/3} N_{\mathrm{Re}}^{1/2}. \tag{2.77}$$

While the Ranz and Marshall correlation for single sphere is commonly used for both heat and mass transfer, it was shown by Wakao and Funazkri (1978) to have significantly under estimated the mass transfer coefficient.

The lower bound of reliability of the proposed correlation appears to be conservatively based. In Wakao and Funazkri's (1978) analysis of reported data on liquid systems, the data sets obtained below a Reynolds number of about 3 were discounted due to possible effects of natural convection. In addition, the bulk of gas phase data obtained below a Reynolds number of 3 was also omitted in their analysis for a variety of reasons. Figure 4 of their paper shows relatively good agreement with the limited gas phase data accepted down to Reynolds numbers of about 2.

2.7.2 Heat Transfer Coefficients

The following correlation for the heat transfer coefficient, h_m, for the total surface of a sphere submerged in an infinite flowing stream is presented by Bird et al.(1960). The correlation presents the N_{Nu} as a function of N_{Re} and N_{Pr}.

$$N_{Nu} = 2.0 + 0.6\left(N_{\mathrm{Re}}\right)^{1/2}\left(N_{\mathrm{Pr}}\right)^{1/3}, \tag{2.78}$$

where:

$$N_{Nu} = \frac{h_m 2r_a}{k_f}, \tag{2.79}$$

$$N_{Re} = \frac{2r_a v_\infty \rho_f}{\mu_f}, \text{ and} \tag{2.80}$$

$$N_{Pr} = \left(\frac{C_p \mu}{k_f}\right)_f . \tag{2.81}$$

It can easily be seen from Eq. (2.78) that in a motionless stream, the N_{Nu} would equal 2.0.

2.8 OPERATING AND PREVIOUS TEST CONDITIONS

Thomas et al. (1978) indicated that 237 mg I_2/g AgZ is the maximum theoretical loading and that they were able to regularly achieve loadings of ~160 mg I_2/g AgZ or higher in the saturation zone of the filter beds. This resulted in a silver utilization of >67%. Across the entire bed, the average loading was 100 to 130 mg I_2/g AgZ.

Information by Nichols et al. (as reported by Slansky, 1977) indicated that operation at a higher temperature of 150°C alleviated the deleterious effects noted from dry air purge when no hydrogen pretreatment was employed.

Jubin (1980) showed significant improvement in the loading capacity of the silver mordenite at operating temperatures above 150°C. In this series of tests, 73 mg CH_3I/g Ag°Z was the maximum observed loading on the 4- to 6-in.-thick test beds, which were divided into 1-in. segments. No attempt was made to reach saturation in these tests, and

the loading phase was terminated when the DF across the test bed fell below 10^3. Variations in NO, NO_2, and CH_3I concentrations result in minimal effects on the observed loadings.

There are no major installations of AgZ reported in the literature surveyed, but the Tokai reprocessing plant in Japan began installing AgX iodine adsorbers in 1979 (Kikuchi et al., 1985). The installation consisted of four units. One adsorber unit was installed in the main plant to process a combined off-gas from the shear, dissolver, high-level liquid waste system, and the VOG system. The three other units were installed in the waste disposal facility. An alkaline scrubber was used to treat all of the off-gas streams individually in the main plant before they were routed to the AgX trap. The caustic scrubber was very effective in removing the major portion of the iodine from the dissolution off-gas, but lower efficiencies were observed for the scrubber on the VOG stream which were attributed to the higher level of organic iodides in this stream. The waste from the caustic scrubbers was sent to the high-level liquid waste system where it was treated. A portion of this iodine was subsequently revolatilized during from the waste treatment processes.

The reported operating temperature of the AgX filter beds in the Tokai plant were <50°C. There was also a notable loss in iodine DF for filters installed in the waste facility when exposed to high levels of NO_x. The overall DFs across the AgX filters ranged from 10 to 70. The authors indicated that this was probably due to the low operating temperature and, in the case of the main plant filters, to the presence of organic iodides. The filter bed in use when these data were obtained provided for a 5-cm-deep bed and

operated with a 5- to 20-cm/s face velocity. It was noted that a new off-gas AgX filter system planned for the VOG system specified an operational temperature of 150°C and a face velocity of 20 cm/s and 7.5-cm-deep beds.

Murphy et al. (1977), using typical loading conditions as shown in Table 2.3, achieved DFs of 10^4 to 10^5. Loadings in the saturation zone of the bed reached 187 mg I_2/g AgZ. The saturation zone was defined by these researchers as the first two to three beds of the test adsorber column in which the iodine loading is virtually constant.

Table 2.3: Conditions for loading tests of AgZ by Murphy et al.[a]

Experimental variable	Iodine loading
Bed diameter (cm)	5
Bed depth (cm)	15
Particle size (mesh)	10–20
Superficial face celocity (m/min)	15
Bed temperature (°C)	150
Inlet pressure (mm Hg)	700
Carrier gas	Air
Iodine concentration at 21°C and 1 atm (mg/m^3)	1500[b]
NO_2 concentration (%)	2
NO concentration (%)	2
Dew point (°C)	35
Iodine flux to and from bed ($mg/min*cm^2$)	1.5[c]

[a]Source: Murphy , 1977.

[b]Actual DOG concentration is anticipated to be about 380 mg of I_2/m^3.

[c]Actual DOG iodine flux would be about 0.4 $mg/(min*cm^2)$.

Scheele et al. (1984) summarized the expected iodine concentration in the DOG from a fuel reprocessing plant. The off-gas iodine concentrations were estimated to be as high as 4×10^{-5} mol/L, or 5700 mg/m^3, or as little as 10% or possibly even 1% of this value. The chemical form of the iodine was expected to be primarily elemental iodine, but some organic iodides, primarily CH_3I, were also predicted to be present.

One of the most recent potential large-scale applications of silver-exchanged mordenite was the proposed new head-end facility for the PUREX plant located in Hanford, Washington. The normal, off-normal, and stand-by conditions are shown in Table 2.4. Scheele and Burger (1987) and Scheele et al. (1988) conducted a series of deep-bed tests directed at establishing the design of an off-gas system to remove radioiodine from the DOG for this facility. The standard test conditions used in their studies are shown in Table 2.5.

Jubin (1980), in a series of tests using an 8-run fractional 2^n factorial-designed experiment, showed the need for the pretreatment of the silver-exchanged zeolite and for loading improvements arising from water vapor in the carrier gas and higher loading temperatures. The results were discussed in Sect. 2.1. The test conditions used in this study are presented in Table 2.6. Similar test conditions were used in follow-on tests conducted by Jubin (1982).

Table 2.4: Normal, off-normal, and stand-by operating conditions for the iodine control systems at the proposed process facility modification to the PUREX plant.

	Level		
Operating parameters	Normal	Off-normal	Stand-by
Gas composition (dry basis)			
NO_x, vol%	2	18	0
NO, vol%	~1	9	0
NO_2, vol%	~1	9	0
O_2, vol%	12	14	21
N_2, vol%	86	68	78
CH_3I, μmol/L	0.1	0.1	0
(mg/m^3)	14	14	0
H_2O, vol%	3	3	3
Face velocity, m/min	5	5	5
Bed temperature (°C)	150	230	50–150
Packing size, mesh	–10+16	–10+16	–10+16

Source: Scheele and Burger (1987).

Table 2.5: Standard test conditions used by Scheele and Burger in their evaluation of AgZ for use in the iodine control systems at the proposed process facility modification to the Purex plant.

Operating parameters	Level
CH_3I μmol/L	10.5–21.0
mg/m^3	1490–2980
NO, vol%	1–9
NO_2, vol%	1–9
H_20, mmol/L	2.5
Face velocity, m/min	5.6
Bed temperature (°C)	150–230
Packing size, mesh	–10+16
Carrier gas	Air

Source: Scheele and Burger (1987).

Table 2.6: Conditions used by Jubin for loading tests of AgZ.[a]

Experimental variable	Iodine loading
Bed diameter (cm)	5.08
Bed depth (cm)	15.24
Number of layers in total bed	6
Particle size (in. diam)	1/16
Superficial face velocity (m/min)	10
Bed temperature (°C)	100 or 150
Carrier gas	Air
Iodine concentration at 21°C and 1 atm (mg/m^3)	500 or 1000
NO_2 concentration (%)	0 or 1.4
NO concentration (%)	0 or 3.1
Dew point (°C)	–54 or 30
Pretreatment (200°C for 24 h)	Air or 4.5% H_2 in Ar

[a]Source: Jubin (1980).

2.9 TEST METHODS AND TECHNIQUES

2.9.1 Silver-Exchanged Mordenite Preparation

The sodium in the zeolite structure can be exchanged for other metal cations. A batch method for silver exchange is presented by Pence et al. (1970), and both batch and plug flow techniques are described by Thomas et al. (1977). Jubin (1980) also described the batch method used to carry out the exchange of several cations on mordenite and faujasite. The method used by Jubin (1980) involved multiple contacts of 3 L of 1-*M* silver nitrate or lead nitrate solution with 1500-g batches of zeolite at 40°C. The solution was circulated by a small pump. At regular intervals the solution was drained and replaced with fresh solution. This was continued until no change in silver or lead solution concentration was detected. Following the metal nitrate contacts the exchanged zeolite

was washed with deionized water to remove the solution adhering to the material. This was followed by a heated air drying at 60°C for 24 h to remove excess water from the zeolite matrix.

2.9.2 Constant Pressure Techniques

When possible, direct measurements of the adsorption process provide the simplest of the experimental methods for determining the adsorption and/or desorption curves (Kärger and Ruthven, 1992). Volumetric and gravimetric methods can be used to monitor the process following the exposure of the sorbent to a step change in sorbate pressure.

For a volumetric method, a constant system pressure is maintained through the use of a gas burette to vary the system volume during the sorption period. The quantity of sorbate adsorbed or desorbed is directly monitored by observing the system volume. Obviously the uptake can also be monitored by observing the weight change of the sorbent. The use of a sufficiently large reaction vessel and relatively small quantity of sorbent can ensure that the pressure change in the test system is relatively small. A sensitive microbalance is also required to carry out the gravimetric measurements due to the small sample size (Kärger and Ruthven, 1992).

2.9.3 Constant Volume Systems

While a constant pressure system is desirable, a constant volume system is relatively easy to construct, and this type of system overcomes some of the equipment requirements described previously. Vaidyanathan (1971) used two different microbalance

systems to obtain loading data from a static gas system. One system employed a Cahn Electrobalance and the other, a McBain-Baker-type calibrated quartz spring. In this study, both systems were operated in virtually the same manner. The sorbent sample was placed on the balance tray which was suspended from the balance which, in turn, was enclosed in a glass vessel. The sorbate gas was introduced to the glass vessel following system calibration. Both the gas pressure and sorbent weight were monitored.

Lee (1976) utilized a well stirred constant volume sorption chamber in which the test pellets were contained in a spinning basket. The concentration change in the gas phase was periodically monitored by gas chromatography. Kärger and Ruthven (1992) point out, however, that this system does not guarantee that the gas film resistance can be ignored due to the problems overcoming the tendency of the fluid to spin with the basket.

2.9.4 Deep-Bed Studies on AgZ and Ag°Z

Previous studies by Jubin (1980, 1982) utilized deep-bed reactors with a flowing inlet gas stream. The system was operated at constant inlet pressure. However the sorbate concentration was reduced by at least a factor of 1000 across the beds during most of the test. In fact, most tests were terminated when 0.1% of the inlet CH_3I concentration was observed in the effluent. In addition, no intermediate loading data were obtained by the test methods employed. Iodine loading was determined either by gamma counting techniques through the use of an I^{131} tracer or by neutron activation. This method has the advantage of testing the AgZ in a flowing gas system similar to that in which the material would be used.

2.9.5 Resulting Test and Measurement Requirements

To understand the behavior of the system studied, it was necessary to select a measurement system and establish process parameters which could be used to differentiate between the various potential mechanisms which could control the mass transfer rate. Once the parameters were identified, a systematic determination of their significance on the mass transfer was conducted. In the case of the "single pellet" tests, the measurement system needed to be capable of detecting the weight gain of 0.5 to 1.0% of the maximum weight gain. This maximum weight gain was controlled by the maximum amount of iodine adsorbed and on the mass of adsorbent used. It was also important to establish operation conditions such that the gas phase concentration remained essentially constant not only throughout the run but also across the bed. The amount of adsorbent used was limited by the requirement that all pellets needed to be exposed to the same gas concentration. This implied that the bed depth must be limited to 1 to 2 pellets.

3. EXPERIMENTAL

3.1 EXPERIMENTAL OBJECTIVES

The objective of this study was to develop an understanding of the microscale mechanisms involved in the removal and retention of gaseous methyl iodide on a silver-exchanged mordenite media. This was to be accomplished through utilization of well established fundamental mass transfer and chemical reaction mechanisms to interpret the experimentally obtained adsorption data.

This study required three primary steps. First was the selection of appropriate adsorption equipment and conditions for investigating the mass transfer behavior. Such a system needed to provide realistic conditions for the testing of this material in terms of CH_3I concentrations and hydrodynamic conditions of the flowing gas stream. Second was the fabrication and installation of the test equipment in the laboratory followed by the completion of a series of tests in which the silver-exchanged mordenite adsorbent was subjected to a flowing gas stream containing methyl iodide to obtain adsorption loading or conversion data as a function of time and various operational parameters. And finally the third phase was the evaluation and/or development of mass transfer models for the determination of the controlling resistances in this specific adsorption process by comparison of the predictions of these models with experimental data.

3.2 SELECTION OF TEST CONDITIONS AND METHODS

3.2.1 Conditions

A critical component for this work, as in any scientific study, was the establishment of a clear definition and boundaries for the test conditions. The conditions selected for this study were similar to those used in the previous bulk loading studies. This was to permit comparison of the data obtained in these studies with those reported in the literature. However, there was the need to limit the number of process variables and/or gaseous components involved to facilitate the analysis of the data. The boundaries placed by these limiting conditions are important since they may define or restrict the applicability of the results.

As in numerous other studies [Jubin (1980, 1982), Burger and Scheele (1981), Scheele et al. (1983), and Scheele and Burger (1987)], methyl iodide was chosen as the chemical form for the iodine in this study because it is a more difficult form to retain in an adsorption process than elemental iodine. If CH_3I can be successfully retained on the silver mordenite, then the elemental iodine will also be retained (Scheele and Burger, 1987).

Experimental data were collected over a range of conditions selected to differentiate between the anticipated primary controlling mechanisms, and further data were collected to evaluate specific process behavior observed in the initial series of tests.

The variables considered were pellet diameter, methyl iodide concentration, gas velocity, temperature, and, later in the study, water vapor content of the carrier gas. The

first four conditions were selected to examine the effects of these primary variables by varying each one while holding the others at a standard condition. For example, to determine if there was any effect due to the gas film surrounding the pellet, it was important to vary the velocity of the flowing gas stream while holding all other variables at the reference condition. To evaluate all the factors required four tests in addition to a baseline test at the standard conditions. In addition to these five tests, two duplicate tests were planned to allow a determination of the level of experimental error. An experiment at a third concentration level was also planned. Table 3.1 provides a listing of the ranges considered for each of the independent variables.

Table 3.1: General test conditions.

Variable	Range or values considered
Pellet diameter (in.)	**1/16** and 1/8
Gas velocity (m/min)	1, 2, 5, and **10**
Methyl iodide concentration (mg/m^3)	250, 500, **1000**, and 1500
Temperature (°C)	125, **150**, and 200
Water content [dew point (°C)]	–40, **–15 to –18**, –11

Note: Bold values were considered reference conditions.

Following the completion of the initial series of tests, 13 additional tests were conducted to explore specific aspects of this process and to gain further clarification on the behavior observed during the initial tests. There were four specific avenues examined: (1) the effects of either increasing or decreasing the water vapor content of the air,

(2) further lowering of the gas velocity, (3) lower CH_3I concentration, and (4) lower operating temperatures. Two unique runs were conducted first to determine the amount of water adsorbed from the instrument air and second to determine the CH_3I loading on the zeolite media without chemical reaction occurring. Table 3.2 presents a complete listing of the conditions studied in each test.

3.2.2 Selection of Test Methods

These adsorption studies were conducted on a "single pellet" system (i.e., a system in which a very thin layer of adsorbent media was exposed to the sorbate stream such that all pellets were exposed to a uniform gas composition). Thus the effects of a changing gas composition through the test bed were considered to be negligible.

One of the significant changes in this study from those conducted in the past on AgZ or Ag°Z was the decision to not use an I^{131} tracer. This decision was not the initial choice but was driven in large part to the difficulty in obtaining methyl iodide containing tracer levels of I^{131}.

The specific method for monitoring the adsorption process was selected to provide a constant pressure system and to allow for the direct measurement of the quantity of iodine adsorbed on the bed rather than monitor small changes in gas composition. This method was selected based upon several issues: (1) the inability to obtain sufficient quantities of methyl iodide containing I^{131} tracer to allow tracer studies as conducted by Jubin (1980, 1982) in the past; (2) the accuracy and cost of either wet chemical or neutron

Table 3.2: Summary of single pellet test conditions.

Test No.	Size (in.)	Velocity (m/min)	CH_3I conc. (mg/m^3)	H_2O added	Temperature (°C)	Notes
Initial series:						
3	1/16	10	1000		150	
4						Test aborted
5	1/8	10	1000		150	
6	1/16	10	1000		150	
7	1/8	10	1000		150	
8	1/16	5	1000		150	
9						
10	1/16	10	1000		200	
11	1/16	10	1500		150	
12	1/16	10	500		150	
Supplemental tests:						
13	1/16	10	1000	yes	150	
14	1/16	10	250		150	
15	1/16	2	1000		150	
16	1/16	1	1000		150	
17	1/16	10	0		150	Air only
18	1/16	1	1000	dry	150	
19	1/16	10	1500		150	Short run
20	1/16	10	1500		150	Short run
21	1/16	10	1000		200	
22	1/8	10	1500		150	
23	1/16	10	1000		150	
24	1/8	15	1000		150	
25	1/16	10	1000		150	NaZ loading
26	1/16	10	1000		125	

activation analysis of the stable iodine loaded on the bed; and (3) the desire for continuous weight change data during the entire loading process.

The test method selected to obtain methyl iodide loading/silver conversion data was an adaptation of the classic microbalance gravimetric technique. The primary difference from the methods utilized by researchers such as Lee or Vaidyanathan, who used constant volume systems which either allowed periodic gas concentration measurement by sampling and fluid movement around the adsorbent particles or continuous weight measurements in a static gas, was the suspension of the sample bed from the balance into flowing gas stream. This provided a system in which the uptake on the sorbent could be continually monitored by direct measurement of the bed weight under constant pressure/concentration conditions. It further allowed the direct variation of the gas velocity such that investigation into the potential role of the gas film resistance on heat or mass transfer was possible.

3.3 EXPERIMENTAL SETUP AND PROCEDURE

3.3.1 Test Equipment

Figure 3.1 is a schematic diagram of the process system showing the principal equipment components. The entire system was located inside a walk-in laboratory hood, with the exception of the dry air, hydrogen/argon and nitrogen cylinders, and the process control and data collection instrumentation.

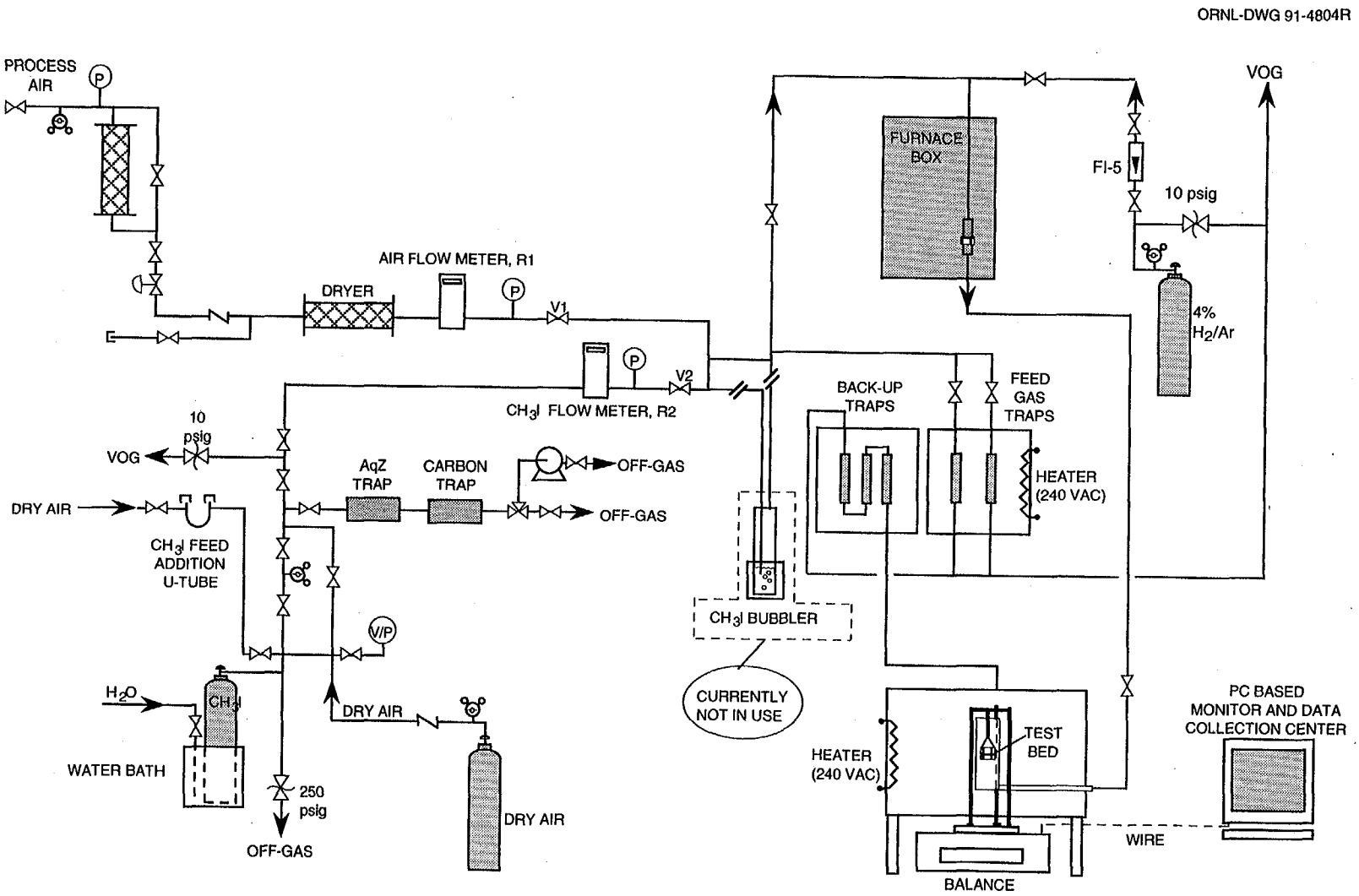

Figure 3.1. Schematic of experimental setup.

To briefly describe the test system, a stream of dilute methyl iodide was fed into the test reaction chamber in which the bed containing the selected sorbent material was located. The test bed composed of a thin layer of Ag°Z pellets, 1 to 2 pellets deep, was supported by a stainless steel wire basket which was lowered into a glass gas reaction chamber. The limited quantity of sorbent placed in the bed provided an assurance that all pellets were subjected to the same gas concentration and that the gas concentration was virtually unchanged as it passed through the test bed due to any adsorption. The glass chamber was connected to the feed gas header. The basket itself was suspended from a tripod device which rested on the pan of an electronic balance (Sartorius Instruments Model LC620P) used to measure the weight changes of the sorbent material. This configuration allowed the basket to be free floating within the reaction chamber. Thus it was possible to directly determine the weight change on the test material in a flowing system. Weight data were collected from electronic balance via a serial connection to an adjacent personal computer.

The glass reaction chamber was mounted in an electrically heated enclosure used to control process temperature. The heated enclosure was fabricated from a rigid insulating construction material. This was then enclosed in a secondary Plexiglas box to prevent disturbances to the balance due to air currents in the hood.

The Model LC620P, poly-range electronic balance used throughout the test was manufactured by Sartorius Instruments, (Goettingen, Germany). This balance has a capacity of 120/240/620 g. Readability of the balance is 0.001/0.002/0.005 g and

standard deviation or reproducibility is ≤±0.001/0.001/0.003 g. Data from the Sartorius balance was recorded on an IBM PC/XT connected via an RS232 interface.

Gas flows were controlled by needle valves and standard gas regulators. Gas flows were monitored either by calibrated rotometers or electronic mass flow meters. The main air line during the single pellet runs was monitored by an Omega Engineering, Inc., (Stamford, Connecticut) model FMA-56-12-I, 0 to 30 standard L/min mass flow meter, serial number 7889. The CH_3I-air mixture during the single pellet runs was monitored by an Omega Engineering, Inc., Model FMA-56-07-ST, 0 to 1 standard L/min mass flow meter, serial number 13139. The Omega flow meters have an accuracy of ±2% of full scale. The flow rate of the FMA-5000 series flow meters was referenced to "standard" conditions of 21°C (70°F) and 760 mm of mercury.

Temperature control was accomplished by placing the entire bed in an electrically heated insulated enclosure. Temperature was controlled by a Barber-Coleman controller model 522B-40185-010-1-00-8732 coupled with a type K thermocouple junction inserted directly into the flowing gas stream directly above the bed of adsorbent material.

The gas which passed through the sorbent test material was passed through a series of 1-in. I.D. back-up filters loaded with either activated charcoal and silver-exchanged faujasite. The gas leaving the back-up filters was discharged through the building/VOG. As far as possible, the entire system was designed to limit personnel entry into the hood. The valves and rotometers were located behind small access doors in the main hood doors.

3.3.2 Reagents

Methyl iodide was laboratory-grade material purchased from J. T. Baker Chemical Company (Phillipsburg, NJ, Product No. 2692-00) or E. M. Science Chemical Company (Cherry Hill, NJ, Product No. IX0185-1). Silver nitrate was purchased from Alfa Products (Danvers, MA, Product No. 87344-1).

The bulk sodium form mordenite was purchased from Norton Chemical Company (Akron, Ohio) under the trade name of Zeolon™ 900. All 1/16-in.-diam AgZ material was produced from lot No. 78637. This product line has subsequently been discontinued. Similar material is now available from the PQ Corporation located in Valley Forge, Pennsylvania [Porrey (1993) and Vaughan (1988)]. The 1/8-in. silver-exchanged mordenite used in this study was purchased from Ionex Corporation (Boulder, Colorado) under the trade name of Ionex 900. The material from Ionex Corporation was supplied with a certified silver assay. In addition, samples of both the 1/16- and 1/8-in. AgZ material were analyzed for silver content by the Analytical Chemistry Division at ORNL.

The hydrogen/argon gas mixtures were obtained from Linde Gases of the Southeast (Wilmington, North Carolina) and the chemical stores at Martin Marietta Energy Systems, Inc. (MMES). The hydrogen content was analyzed prior to use to verify that the mixture was below the flammability limit of 4.6%.

The air used in the work was obtained from two sources. The low-pressure air (<50 psia) used as the carrier gas was plant/instrument air which was routinely checked by the facility engineer to verify that the dew point did not exceed 15°C. The high-pressure

dry air which was used to pressurize the CH_3I cylinder was obtained from MMES stores. The nitrogen used during the temperature equilibration steps was also obtained from MMES stores.

During several specific tests the carrier gas was further dried by passing it through a drying bed filled with Drierite (calcium sulfate). The bed itself was 3 in. diam and 2 ft long. The dew point of the gas leaving the bed at the start of test T18 was –40°C. By the end of the test the dew point had risen to –30°C. During one other test, T13, the carrier gas was humidified by passing a portion of it through a bubbler column containing deionized water. The humidifier tank was constructed out of a 2-ft section of 3-in. glass pipe. Standard glass pipe of this size has a 3-in. I.D. The metered flow of instrument air was injected at the bottom of the tank through a glass frit disperser.

3.3.3 Procedure Outline for "Single Pellet" CH_3I Loading Tests

Each test began by placing a known quantity of AgZ into a stainless steel basket suspended in the flowing gas stream. The basket which was permanently suspended from the tripod stand was lowered carefully into the reaction chamber, taking great care that neither the legs nor the basket was in contact with the insulating box or glass reaction chamber.

Table 3.3 presents, in outline form, the sequence of steps used to pretreat the AgZ prior to loading with methyl iodide and the flush or post treatment steps to flush CH_3I from the bed and thus determine the amount chemisorbed vs physisorbed. Each of these

Table 3.3: Outline procedure for "single pellet" CH_3I loading tests.

Bed pretreatment (standard for all tests)

- Drying
  - 24-h air
  - 11.4 L/min of dry instrument air
  - Temperature: 150°C
- Nitrogen temperature equilibration
  - 4+ h N_2
  - 0.4 L/min
  - Temperature: 200°C
- Silver reduction
  - 8 to 20 h 4% H_2/Ar
  - 0.4 L/min
  - Temperature: 200°C
- Second nitrogen temperature equilibration
  - 4+ h N_2
  - Same flow rate as to be used in CH_3I loading
  - Same temperature as to be used in CH_3I loading

Loading conditions: (Specific test conditions listed in Table 3.2)

- H_2O vapor content
  - >–15°C (7.3×10^{-5} mol/L) or –40°C (5.6×10^{-6} mol/L)
- Pellet diameters
  - 1/16 in. or 1/8 in.
- Gas velocities
  - 1, 2, 5, or 10 m/min
- CH_3I gas concentrations
  - 250, 500, 1000, or 1500 mg/m^3
- Bed temperature
  - 125, 150, or 200°C

Air flush (standard for all tests)

- 24+ h air
- 11.4 L/min or dried instrument air
- Temperature: 150°C

pretreatment, loading, and post loading steps were monitored for weight changes with the data being stored in a computer file. Summary data are presented in Appendix A.2. The full data files for the methyl iodide loading portions of each test are recorded in data files on the PC used in the laboratory, and printed copies have been placed in the laboratory logbook.

3.4 ANALYTICAL TECHNIQUES

3.4.1 Direct Weight Determinations

Loadings during the single pellet experiments were determined by gravimetric analysis. This was accomplished by recording the weight of the Ag°Z contained into the stainless steel basket suspended in the flowing gas stream by an electronic balance (Sartorius Instruments Model LC620P.) The RS232 port of the balance was connected to an IBM PC which recorded the weights as requested by the monitoring software. The software used to communicate with the Sartorius balance and to log the data was written in Microsoft Quick BASIC version 4.5. A complete listing of the program may be found in Appendix A.3. This software recorded the sample weight, time of weighing, and rate of weight change to a data file for later detailed analysis.

This electronic balance proved to be sensitive to temperature fluctuations occurring during the data collection periods. These fluctuations were observed to be the result of two factors. First were changes in the temperature of the laboratory occurring each time the air conditioning/heating system was turned off by the facility temperature

setback system. Once this was identified, the problem was partially corrected by disabling the timer for this particular laboratory (not in the best interest of energy conservation, but this was sacrificed in the name of science!) and by placing a secondary enclosure around the heated box and the scale to stabilize the temperature by utilizing the thermal energy lost through the insulation of the heated enclosure surrounding the reaction chamber. The second fluctuation occurred with changes in the heating requirement due to increased gas flow rates or increased operational temperature. The scale was located approximately 6 cm below the bottom of the heated box. If the box temperature was increased, the temperature of the scale would slowly increase to a new steady-state temperature. This process typically required approximately 4 h. During this time, temperature-induced shifts in the indicated weights were observed. At each change in bed temperature or gas flow rate a stream of nitrogen was introduced at the desired flow rate and the system was allowed to equilibrate. This equilibration was monitored by both weight measurements as well as two thermocouples attached directly to the electronic balance.

3.4.2 Scanning Electron Microscope

Scanning electron microscope images were obtained through the services of MMES's ORNL and Y-12 Plant. Three types of images were obtained for the samples submitted for this method of analysis. The topography of the material was shown in secondary electron images (SEI). Back-scattered electron images (BEI) showed variations in the image intensity across a portion of the pellet which is related to variations

in the average atomic number in the region under examination. The specific distribution of silver, iodine, silicon, and aluminum across the specimen were shown by elemental maps.

3.4.3 Photographic

High magnification or macro photographs were also obtained through the services of ORNL to examine the pellet cross section and to observe on a macro scale any general color variations which might be related to the adsorption of methyl iodide on the sorbent.

3.4.4 Density

The density of the mordenite material was determined by the analytical services at MMES's Y-12 plant by two methods. The first was by pycnometer and the second was part of the mercury porosimetry measurements.

3.4.5 Pore Size Distributions

Mercury porosimetry was used to determine the pore size distributions over the range of 100 to 0.01 μ.

3.4.6 Adsorption-Desorption Isotherms/Surface Area

A Micromeritics Instrument Corporation Digisorb 2000 was used by analytical services at MMES's Y-12 plant to collect adsorption-desorption data. These data were used to provide an analysis of the Brunauer, Emmett, and Teller (BET) surface area.

3.4.7 Void Fraction Determinations

Due to the different physical limitations of mercury porosimetry and pycnometry techniques, it is possible to determine the void volume for different pore size ranges (Walker, 1994). By using the differences between the real density and the bulk density data from the mercury porosimetry, the void volume may be calculated which excludes pores below 0.01 μ. By using the difference between the bulk density and the dried pycnometer density, the total pore volume may be determined.

3.4.8 Dew Point Determinations

The dew point of the instrument air used as the carrier gas was determined using a Lectrodryer dew point apparatus. This very simple device provides a direct indication of the moisture content of the flowing gas stream. The gas stream was introduced into the apparatus at a rate of approximately 2.35 L/min. After a 5-min purge of the apparatus, acetone was added to the inside of the polished cup. Crushed dry ice was slowly added to the acetone while constantly stirring with a thermometer. At the first sign of moisture on the polished outer surface of the cup, the temperature was read. This method was accurate within ±3°C (Lectrodryer Bulletin DP-A2).

3.5 ANALYSIS OF DATA AND MODEL SELECTION

As noted, the measured or dependent variable for this study was the mass gained by the mordenite material over time, and the independent variables are pellet size, temperature, bulk gas phase concentration, and gas velocity. The weight gained by the

adsorbent vs time in terms of either the mass flux (equated to iodine reacted) into the adsorbent or as conversion of the silver into AgI was compared to well established reaction/diffusion models. The least square method of curve fitting was used to optimize the adjustable parameters in each model.

The two primary criteria applied to the selection of the appropriate model for this system was (1) the ability of the model to account for the systematic variation in operating parameters without arbitrary changes in the adjustable parameters and (2) the determination of consistent diffusion coefficients for the experimental conditions evaluated.

4. EXPERIMENTAL RESULTS

4.1 OPTICAL AND SUPPORTING CHARACTERIZATION STUDIES

Five samples of the mordenite materials used in this study were submitted to the Product Quality Department at the MMES Y-12 Plant for determination of pore size distribution, density, and characterization of the uniformity of silver and iodine distribution where applicable. The samples analyzed were the 1/16-in. sodium mordenite, the 1/16- and 1/8-in. AgZ, and the 1/16- and 1/8-in. pellets from tests T19 and T20 respectively. The last two samples were analyzed only for silver and iodine distribution.

4.1.1 Electron Microscope and Optical Observations

In general, the BEI taken across the entire cross sectional of several fractured AgZ pellets showed no significant variation in the average atomic number. [The analytical report by Walker (1994) is the basis for much of the following discussion concerning the results obtained by electron microscope examination.] On one or two pellets, some localized accumulation of the silver was noted in a few small areas. Aside from these few areas, no silver gradient was noted within the pellets (see Figs. 4.1 and 4.2).

The distribution of silver within the individual particles or crystals that make up the pellets was examined using higher magnification BEI. For the pellets prior to hydrogen pretreatment it was observed that the silver was uniformly distributed. However, following pretreatment with 4.5% hydrogen and subsequent loading with

PHOTO 6083-94

Figure 4.1. Back-scattered electron image of Test 19 1/16-in. AgZ showing uniform silver distribution.

PHOTO 6081-94

Figure 4.2. Back-scattered electron image of Test 19 1/16-in. AgZ showing slightly nonuniform silver distribution.

methyl iodide (samples from tests T19 and T20), very small particles (<1 or 2 μ) were seen on the surfaces of the larger crystalline structure (Fig. 4.3). An elemental map (Fig. 4.4) obtained through energy dispersive x-ray analysis of one pellet showed that these fine particles contain a higher concentration of silver than in the surrounding material. In addition to the presence of these fine silver-containing particles, there remained a relatively uniform distribution of silver across the mordenite pellet cross section. No specific area of silver depletion was detected when compared to the silver distribution prior to hydrogen pretreatment and iodine loading.

A low concentration of iodine was also observed to be uniformly distributed in the mordenite pellets analyzed from Test No. 19 (24% final conversion) and Test No. 20 (35% final conversion). Measurements to determine the extent of the remaining unreacted silver in the mordenite particles after the exposure to methyl iodide were not attempted. Examination of the fine silver-containing particles showed that while these are rich in silver, they contained virtually no iodine. Using the same technique on the larger mordenite particles or crystals showed that they, on the other hand, contained a low concentration iodine that appeared to be uniformly distributed.

The SEI of the pellets examined showed the voids and macropores present in this material. The SEI of several pellets taken from each of the five samples submitted for analysis, showed that there was the possibility for significant variation from pellet to pellet. These variations fell into two categories. First there was some variation in the general structure of the pellets. Some were observed to have substantial voids in the pellet interior (Fig. 4.5), while others pellets appeared to contain separate cores (Fig. 4.6). The

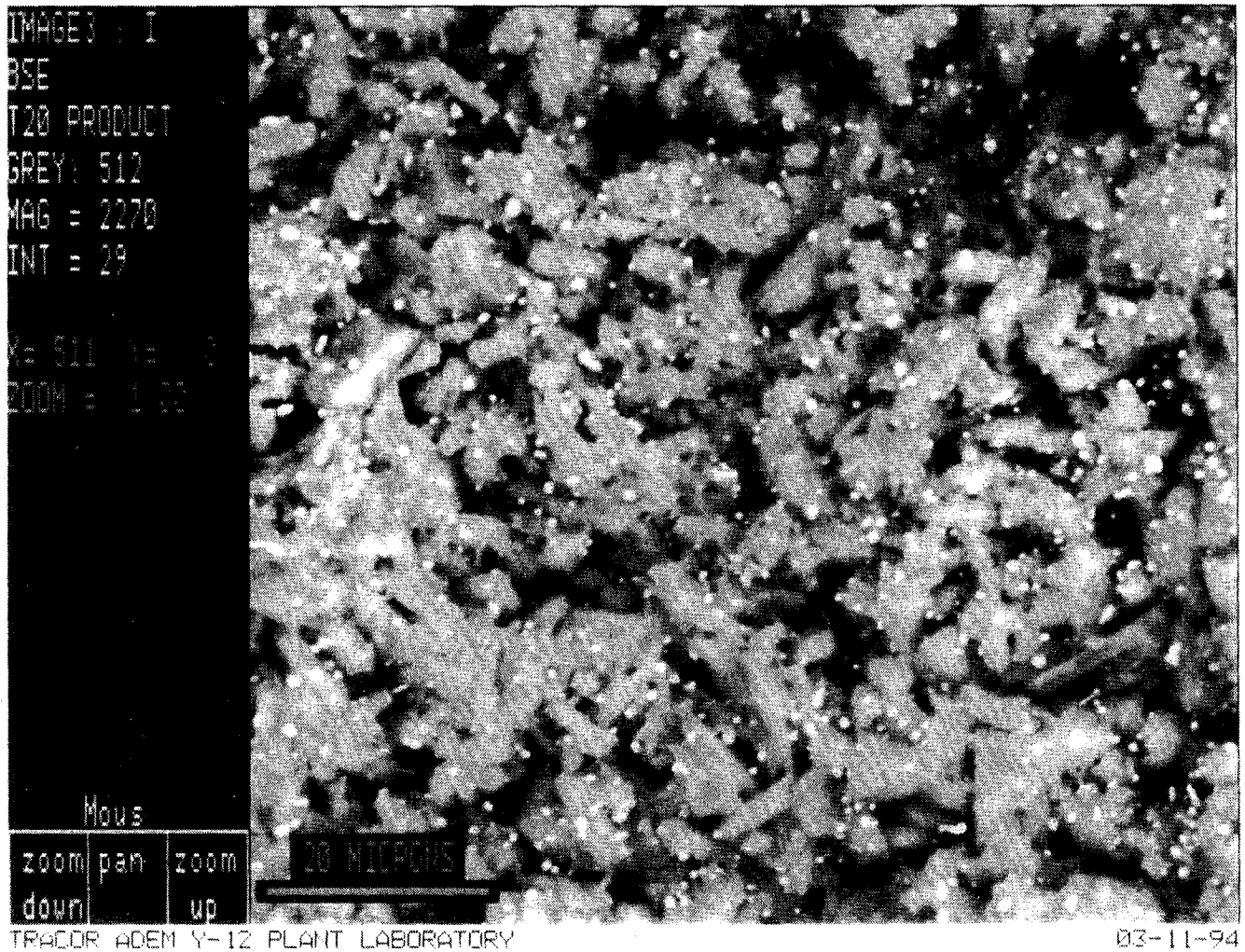

Figure 4.3. Back-scattered electron image of 1/8-in. Test 20 AgZ showing silver particles in pellet structure.

PHOTO 6086-94

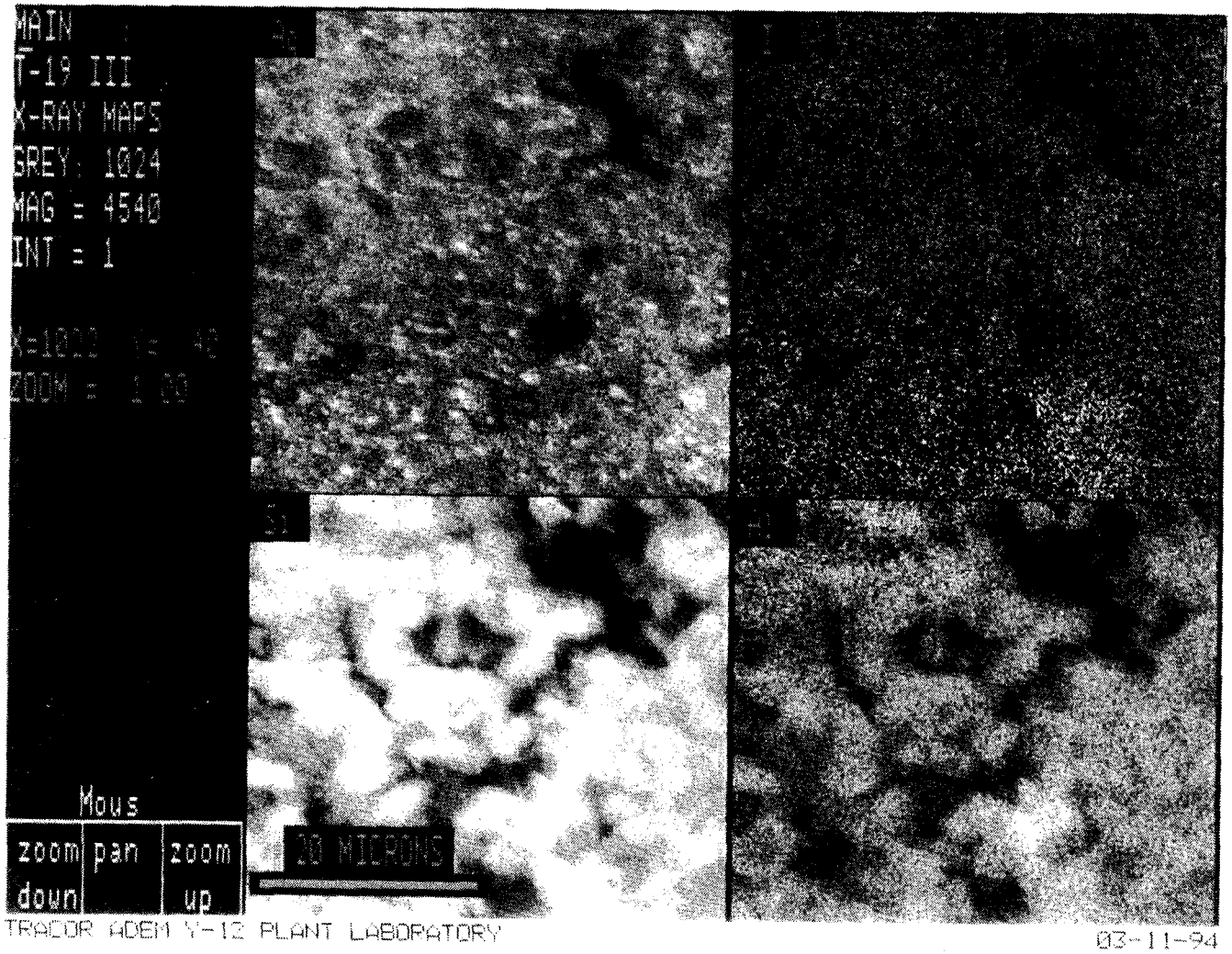

Figure 4.4. X-ray map of Test 19 1/16-in. AgZ showing uniform iodine distribution and distribution of other elements.

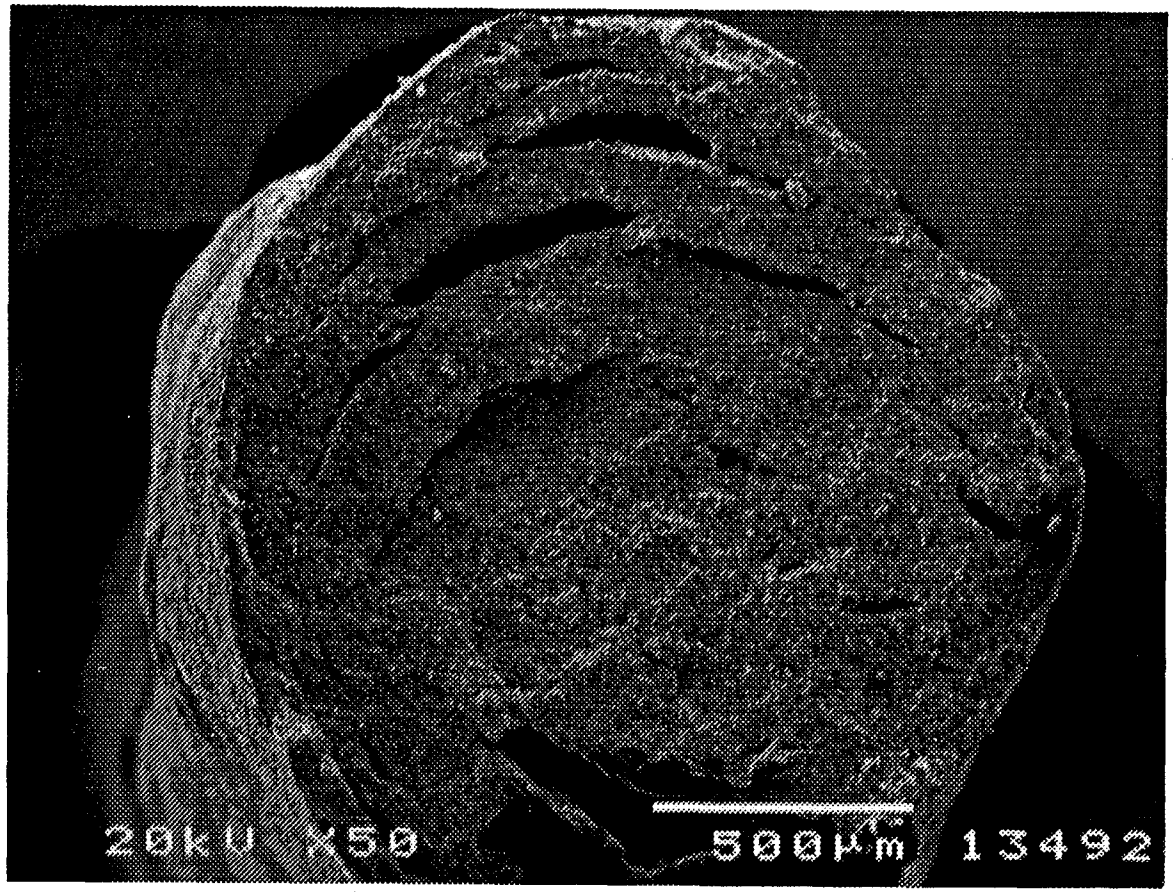

Figure 4.5. Secondary electron image of 1/16-in. AgZ showing large voids in pellet structure (ORNL Electron Micrograph Photo 13492-50X).

PHOTO 6079-94

Figure 4.6. Secondary electron image of 1/8-in. AgZ showing a separate core in pellet structure.

second type of variation involved the crystalline particles that comprised the overall structure. Some were well formed, and others had very rough and irregular surfaces. In addition, they appeared to vary in size and overall shape (Figs. 4.7–4.9). In addition to the qualitative observations concerning the topography of the material, these photographs were used to estimate the size of the mordenite particles or crystals. Both the 1/16- and 1/8-in. pellets were composed of individual crystals estimated to be 4.0 μ in equivalent spherical diameter. This compared favorably with the Zeolon™ 100 synthetic mordenite material produced by Norton and reported to be a powder of crystals with an average size of 6 to 12 μ (Norton, 1976).

What appears to be a shrinking core behavior, as shown by color changes in the pellets, was observed through optical photographs taken but never published during the deep-bed studies previously completed and reported by this author [Jubin (1980, 1982)]. The test from which these pellets were taken was conducted under the following conditions: a bed temperature of 200°C, a CH_3I concentration of 1000 mg/m^3, and a gas velocity of 10 m/min at standard temperature and pressure. The loadings for the individual pellets were not determined, and only the average loading on each of the 2.54-cm-thick bed segments was measured by tracer analysis. At very low CH_3I loadings on the AgZ (~3% average conversion) the pellet from the fourth or last bed segments shows no sign of any visible ring (Fig. 4.10). As the average bed segment loading increases, a clearly developed ring around the core is apparent. This is shown in Fig. 4.11 at an average bed segment conversion of ~19%. However, at higher average loadings (~40%

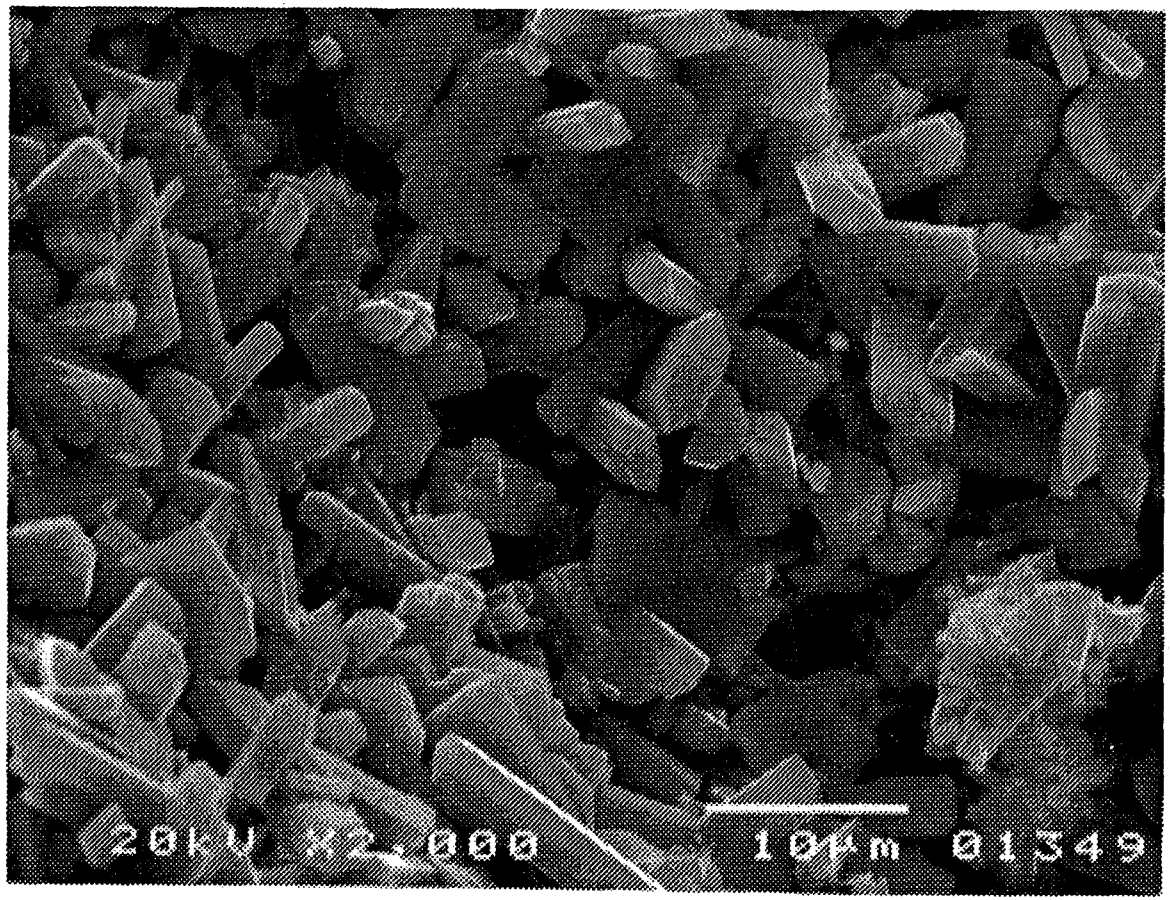

Figure 4.7. Secondary electron image of 1/16-in. AgZ showing well defined crystal structure ORNL Electron Micrograph Photo 01349-2000X).

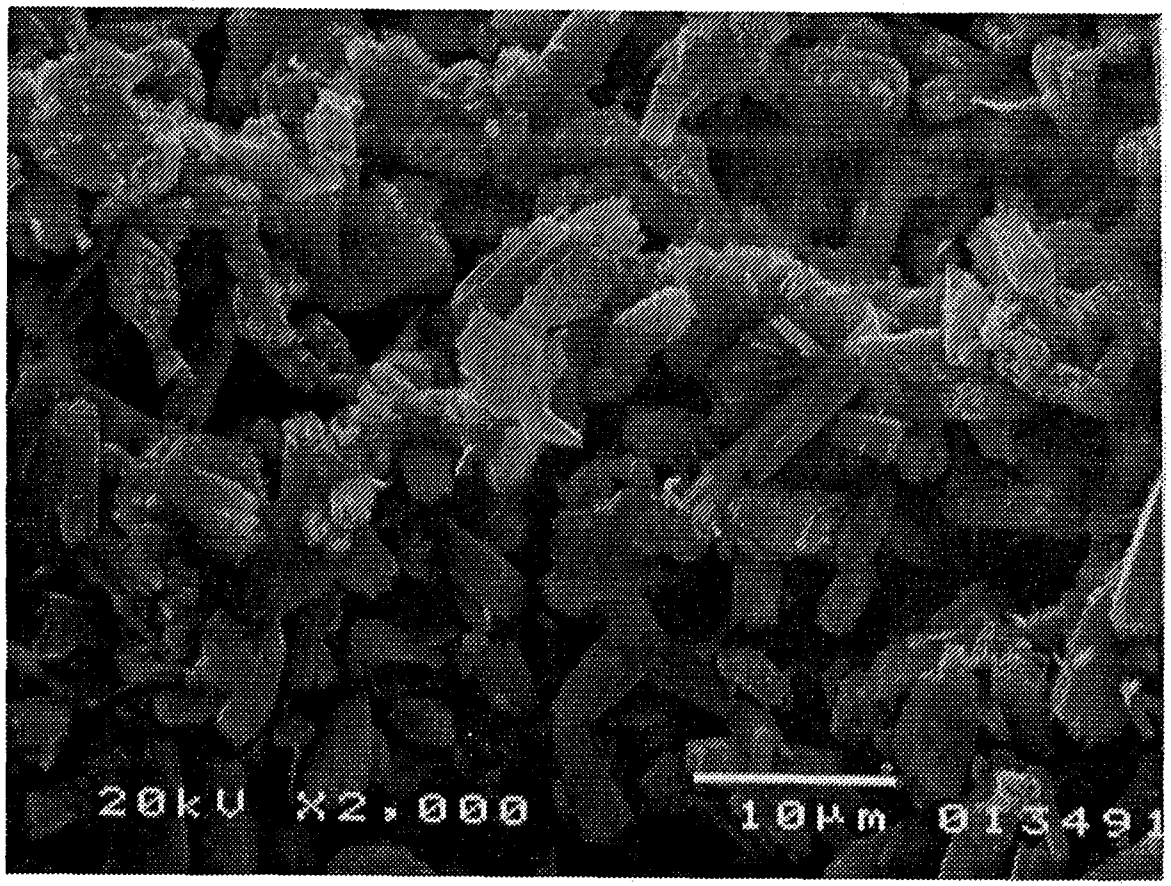

Figure 4.8. Secondary electron image of 1/8-in. AgZ showing poorly defined crystal structure (ORNL Electron Micrograph Photo 013491-2000X).

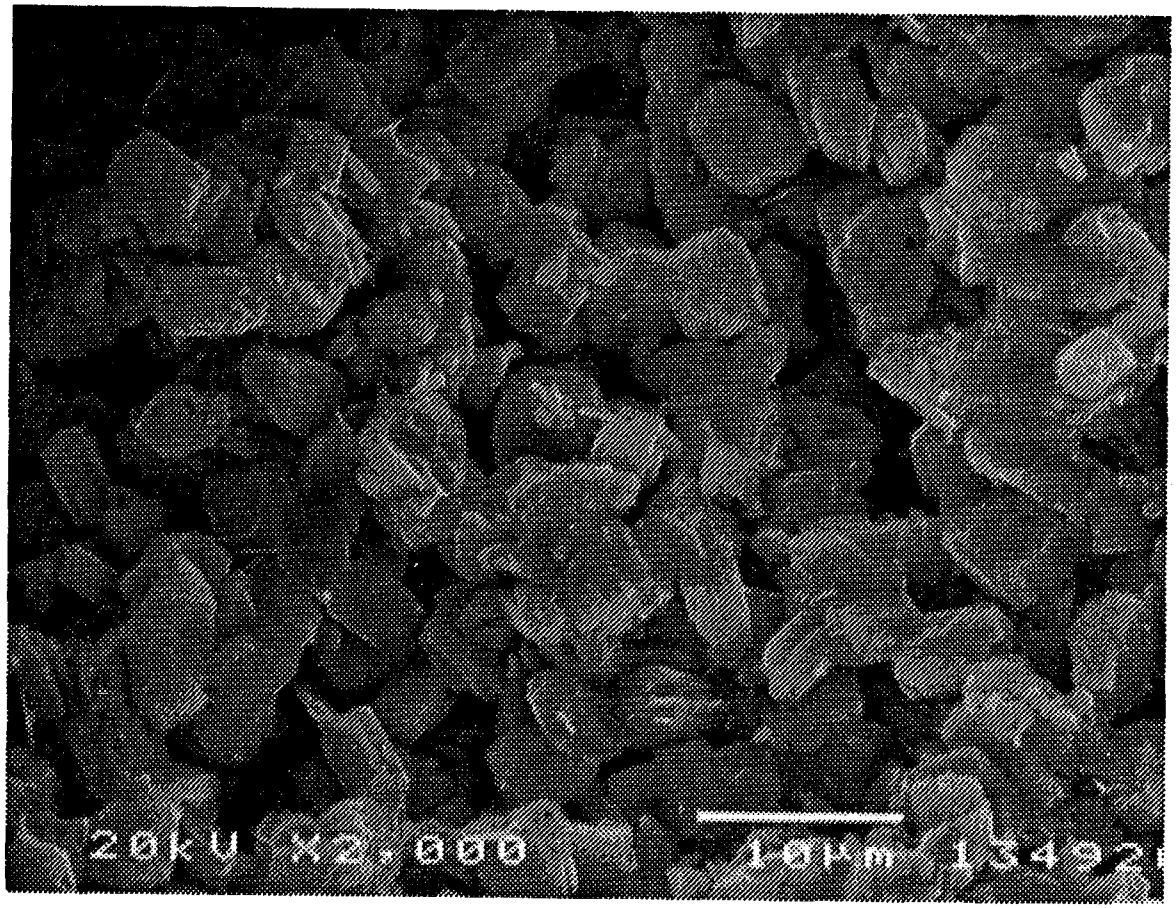

Figure 4.9. Secondary electron image of 1/16-in. AgZ showing poorly defined crystal structure (ORNL Electron Micrograph Photo 13492-2000X).

Figure 4.10. Optical image of 1/16-in. AgZ from bed with an average conversion of ~3% (ORNL PHOTO 5081-94).

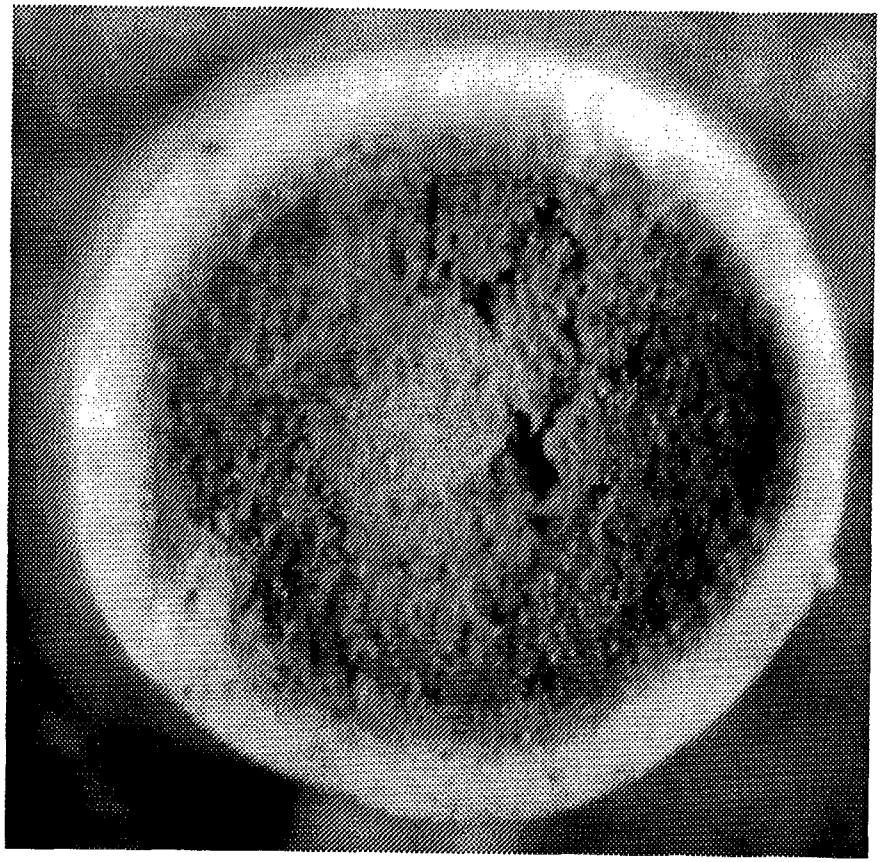

Figure 4.11. Optical image of 1/16-in. AgZ from bed with an average conversion of ~19% (ORNL PHOTO 5085-94).

conversion) the color variation across the diameter of the pellet virtually disappears (Fig. 4.12). In this latter photograph, which is of several pellets from the first bed segment, it appears that only a very small core remains in one pellet while in the other pellet no core is visible.

4.1.2 Density

Two techniques were utilized by the analytical services at MMES's Y-12 plant to determine the density of the mordenite material (Walker, 1994). The first method utilized a pycnometer to obtain density data before drying and then again after drying of the material at 125°C over a weekend. Data obtained in conjunction with the mercury porosimetry analysis provided the second set of density measurements. This technique provided data before and after filling voids in the pellets with mercury. The results from both techniques are shown in Table 4.1.

4.1.3 Pore Size Distributions

Mercury porosimetry was used to obtain the pore size distribution from 100 μ down to 0.01 μ (Walker, 1994). The results are shown in Fig. 4.13 for 1/8-in. AgZ, 1/16-in. AgZ, and 1/16-in. NaZ. These pores fall into the macropore region as defined by IUPAC. The standard deviation in the pore size was estimated to be approximately ± 0.5 μ.

The mesopore size distributions were determined by nitrogen adsorption-desorption data obtained utilizing a Micromeritics Instrument Corporation Digisorb 2000 at the same time the BET surface areas were determined, see Sect. 4.1.6. Pore size

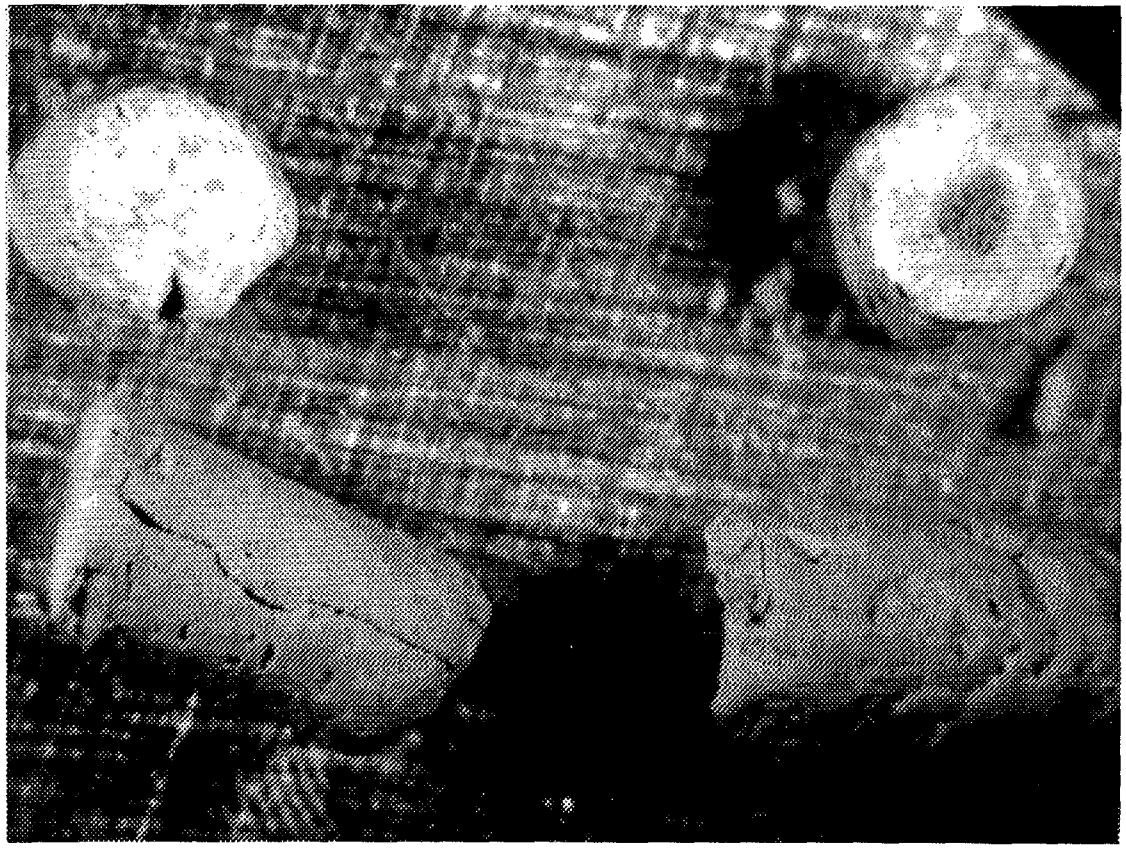

Figure 4.12. Optical image of 1/16-in. AgZ from bed with an average conversion of ~40% (ORNL PHOTO 5084-94).

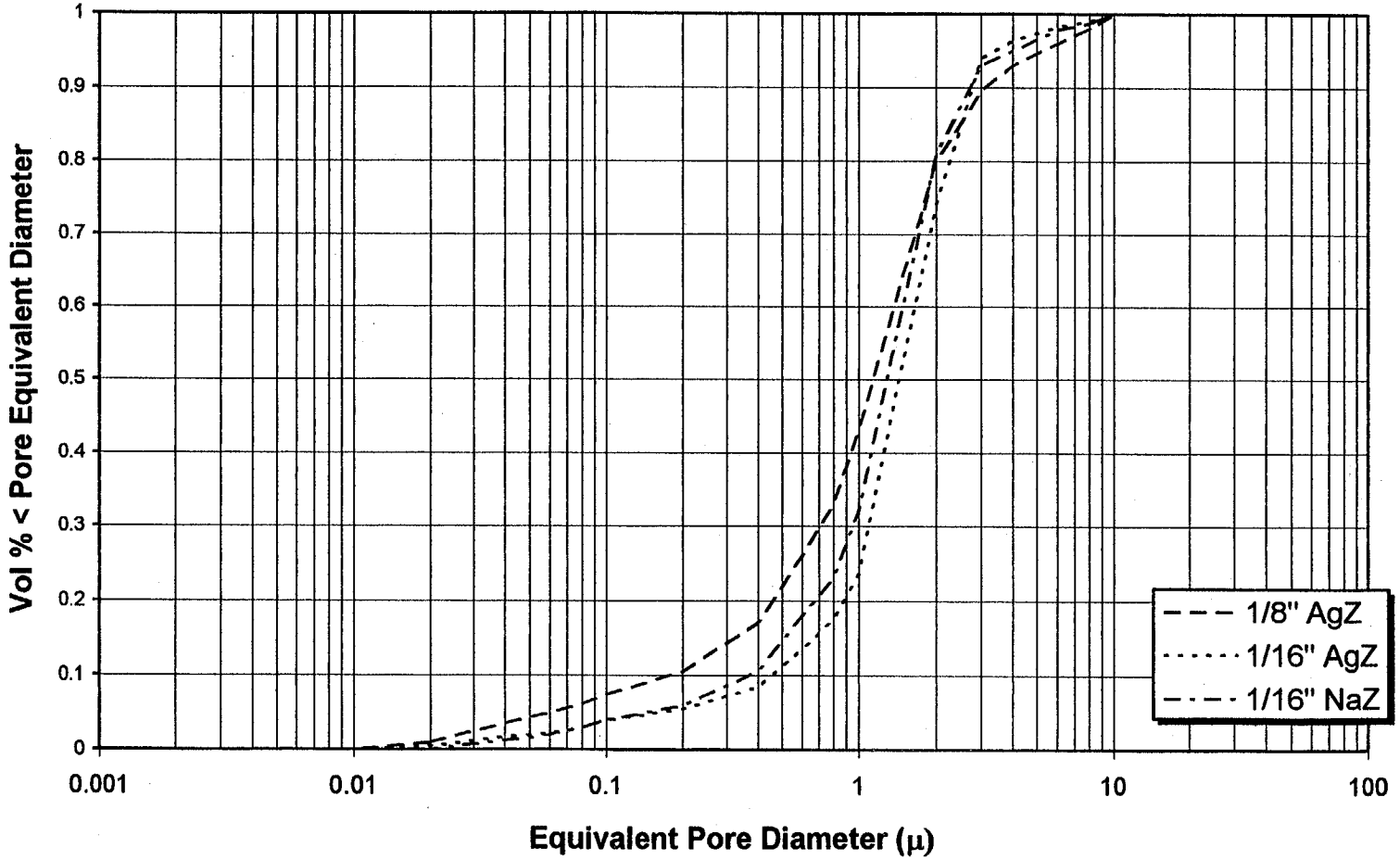

Figure 4.13. Pore volume distribution in macropore-mesopore region for 1/8-in. AgZ, 1/16-in. AgZ, and 1/16-in. NaZ.

Table 4.1: Density analysis of typical silver-exchanged mordenite.

	Pycnometer density		Porosimetry density	
Material	As received	Dried	Bulk	Real
1/8-in. AgZ	2.53	2.63	1.66	2.38
1/16-in. AgZ	2.56	2.58	1.73	2.48
1/16-in. NaZ	2.18	2.19	1.44	2.06

Source: Walker (1994).

distribution for the mesopores are shown in Fig. 4.14 for 1/8-in. AgZ, 1/16-in. AgZ, and 1/16-in. NaZ.

The micropore size was taken directly from literature values. The micropore structure of mordenite was reported by IONEX (1986), Meier and Olson (1992), and Breck (1974) to consist of elliptical 6.5 to 6.7 by 7.0 Å channels with perpendicular 2.6 to 2.9 by 5.7 Å channels separated by 2.8 Å restrictions.

4.1.4 Void Fraction Determinations

The void volumes in the mordenite structure were calculated using the differences in the density data shown in Table 4.1. Using the difference between the real density and the bulk density, as determined by mercury porosimetry, the void fraction of the pores greater than 0.01 μ was calculated. The microporosity and mesoporosity (i.e., pores below 0.01 μ) were then included by using the difference between the bulk density and the pycnometer density (Walker, 1994). Independently, the pore volumes and surface areas, which include pore diameters between 20 and 600 Å, were determined from

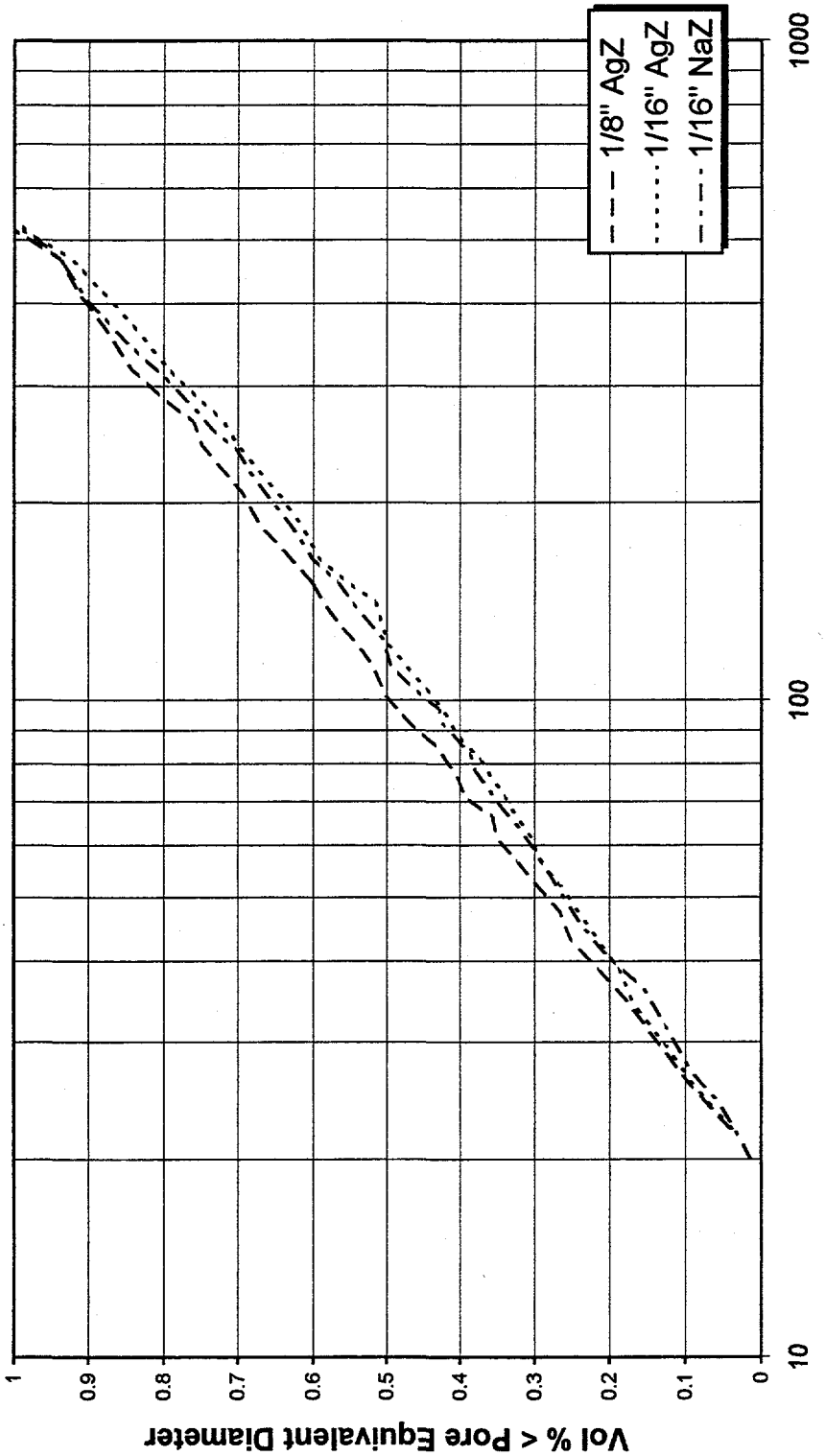

Figure 4.14. Pore volume distribution - mesopore region.

adsorption-desorption data obtained using a Micromeritics Instrument Corporation Digisorb 2000. The results of these determinations are presented in Table 4.2.

Table 4.2: Void volume analysis of typical silver-exchanged mordenite.

	Mercury porosimetry (>0.01 μ)		Pycnometer		Nitrogen adsorption (20 to 600 Å)
Material	Volume (cc/g)	(%)	Volume (cc/g)	(%)	Volume (cc/g)
1/8-in. AgZ	0.1822	30.25	0.2222	36.88	0.0109
1/16-in. AgZ	0.1748	30.24	.0.1904	32.94	0.0080
1/16-in. NaZ	0.2090	30.10	0.2378	36.88	0.0110

Source: Walker (1994).

The micropore volume was estimated to be 0.07 cc/g assuming a cylindrical pore of the 7 Å average diameter and a total surface area of 400 m^2/g. This value would appear to be a factor of 2 to 3 times larger than the volume calculated by the difference between the volume determined from the pore volume based on the mercury porosimetry and the pycnometer data. If the smaller 2.8-Å pore is considered to be separate but of an equal length, then the calculated pore volume is 0.058 cc/g with 71.4% of the total surface area in the large pores.

4.1.5 Surface Area

The surface area associated with the mesopores was determined from data obtained by the Micromeritics Digisorb 2000 (Walker, 1994). The results are shown in

Table 4.3. The major fraction, >50%, of the surface area associated with pores having a diameter in the range between 20 and 600 Å was between a diameter of 20 to 50 Å.

Table 4.3: Surface area as determined by Micromeritics Digisorb 2000.

Material	BET surface area (m^2/g)	Peak area pore size (Å)
1/8-in. AgZ	7.242	22–30
1/16-in. AgZ	4.826	22–30
1/16-in. NaZ	6.598	24–32

Source: Walker (1994).

The macropore area was estimated by assuming a cylindrical pore of the average diameter and the macropore volume determined by mercury porosimetry. This yielded areas of 0.140, 0.116, and 0.149 m^2/g for the 1/8-in. AgZ, 1/16-in. AgZ, and 1/16-in. NaZ respectively.

The Norton Company (1976) reported the total surface area for Zeolon™ 900 to be 400 to 450 m^2/g. This would indicate that 98 to 99% of the surface area is associated with the micropores.

4.2 FUNDAMENTAL DIFFUSION AND MASS AND HEAT TRANSFER COEFFICIENTS

Three fundamental diffusion coefficients can be calculated from readily available data. These are the molecular or mutual diffusion coefficient, the Knudsen diffusivity, and

the Poiseuille Flow diffusion coefficient. The later two were calculated for both the macropores and the micropores at the appropriate temperature for each run. The mass transfer coefficients as estimated from the Sherwood number are also presented. These results are summarized in Table 4.4. The heat transfer coefficients estimated by use of the Nusselt number are also shown in Table 4.4.

4.2.1 Molecular Diffusivity

The molecular diffusivity of CH_3I in air was estimated using the Chapman-Enskog equation presented in Chapter 2 as Eq. (2.20). The required Lennard-Jones parameters were obtained where possible from standard textbook values. When values were not available, the values were estimated from T_c and V_c values according to the rules recommended by Sherwood et al. (1975). The literature and calculated values may be found in Appendix A.1. When needed the following equations were used for estimating Lennard Jones parameters:

$$\frac{\varepsilon_{AB}}{K} = 0.75(T_c) \tag{4.1}$$

$$\sigma_{AB} = \frac{5}{6} V_c^{1/3}. \tag{4.2}$$

Values for the collision integral, Ω_{AB} were obtained from Table 2.2 in the text by Sherwood et al. (1975). The effective molecular diffusivity was calculated for the macropores using Eq. (2.22) to estimate the tortuosity factor. The resulting molecular diffusivity values are:

Table 4.4: Calculated mass and heat transfer coefficients based on physical measurements and fundamental analysis.

	Test case data						Key dimensionless groups			
Run No.	Pellet diam (cm)	Gas feed rate (L/min)	Mass flow rate (g/s cm^2)	CH_3I flow (g/min)	Average CH_3I gas conc. (g/L)	Temperature (°C)	N_{Re}	N_{Sh}	N_{Pr}	N_{Nu}
T3	0.159	11.40	2.16E-02	1.78E-02	9.97E-04	150	18.61	9.38	0.68	4.27
T5	0.318	11.40	2.16E-02	1.45E-02	8.07E-04	150	36.08	12.97	0.68	5.16
T6	0.159	11.40	2.16E-02	1.72E-02	9.64E-04	150	18.61	9.38	0.68	4.27
T7	0.318	11.40	2.16E-02	1.74E-02	9.78E-04	150	36.08	12.97	0.68	5.16
T8	0.159	5.74	1.09E-02	9.55E-03	1.06E-03	150	9.37	6.89	0.68	3.61
T10	0.159	11.40	2.16E-02	1.36E-02	6.81E-04	200	17.12	9.08	0.68	4.18
T11	0.159	11.40	2.16E-02	1.86E-02	1.04E-03	150	18.61	9.38	0.68	4.27
T12	0.159	11.40	2.16E-02	9.55E-03	5.35E-04	150	18.61	9.38	0.68	4.27
T13	0.159	11.40	2.16E-02	1.56E-02	8.77E-04	150	18.61	9.38	0.68	4.27
T14	0.159	11.40	2.16E-02	4.05E-03	2.24E-04	150	18.61	9.38	0.68	4.27
T15	0.159	2.28	4.31E-03	3.22E-03	8.85E-04	150	3.72	4.81	0.68	3.02
T16	0.159	1.14	2.16E-03	1.89E-03	1.04E-03	150	1.86	3.85	0.68	2.72
T18	0.159	1.14	2.16E-03	1.39E-03	7.38E-04	150	1.86	3.85	0.68	2.72
T19	0.159	11.40	2.16E-02	2.45E-02	1.38E-03	150	18.61	9.38	0.68	4.27
T20	0.318	11.40	2.16E-02	1.88E-02	1.06E-03	150	36.08	12.97	0.68	5.16
T22	0.318	11.40	2.16E-02	2.45E-02	1.38E-03	150	36.08	12.97	0.68	5.16
T26	0.159	11.40	2.16E-02	1.21E-02	7.20E-04	125	19.46	9.54	0.68	4.32

Table 4.4 (continued).

Run No.	Gas film: Diffusivity D_{ab} (cm^2/s)	Gas film: Mass transfer coeff. k_g [a] (cm/s)	Gas film: Mass transfer coeff. k_g [b] (cm/s)	Calculated tortuosity factor	Macropore diffusivity $D_{ab,eff}$ (cm^2/s)	Knudsen diffusivity, D_k: Theoretical Micropore (cm^2/s)	Theoretical Mesopore (cm^2/s)	Theoretical Macropore (cm^2/s)	Knudsen diffusivity, D_k: Effective Micropore (cm^2/s)	Effective Mesopore (cm^2/s)	Effective Macropore (cm^2/s)
T3	1.76E-01	8.33E+00	1.67E-01	3.72E+00	1.42E-02	5.61E-04	4.19E-03	1.30E+00	6.44E-05	4.81E-04	1.74E-01
T5	1.76E-01	5.94E+00	0.00E+00	3.66E+00	1.46E-02	5.61E-04	4.19E-03	1.40E+00	5.54E-05	4.14E-04	1.91E-01
T6	1.76E-01	8.33E+00	1.73E-01	3.72E+00	1.42E-02	5.61E-04	4.19E-03	1.30E+00	6.44E-05	4.81E-04	1.74E-01
T7	1.76E-01	5.94E+00	1.81E-01	3.66E+00	1.46E-02	5.61E-04	4.19E-03	1.40E+00	5.54E-05	4.14E-04	1.91E-01
T8	1.76E-01	6.12E+00	6.85E-02	3.72E+00	1.42E-02	5.61E-04	4.19E-03	1.30E+00	6.44E-05	4.81E-04	1.74E-01
T10	2.09E-01	9.54E+00	2.04E-01	3.72E+00	1.68E-02	5.93E-04	4.27E-03	1.37E+00	6.81E-05	5.08E-04	1.84E-01
T11	1.76E-01	8.33E+00	1.31E-01	3.72E+00	1.42E-02	5.61E-04	4.19E-03	1.30E+00	6.44E-05	4.81E-04	1.74E-01
T12	1.76E-01	8.33E+00	6.33E-02	3.72E+00	1.42E-02	5.61E-04	4.19E-03	1.30E+00	6.44E-05	4.81E-04	1.74E-01
T13	1.76E-01	8.33E+00	7.14E-02	3.72E+00	1.42E-02	5.61E-04	4.19E-03	1.30E+00	6.44E-05	4.81E-04	1.74E-01
T14	1.76E-01	8.33E+00	3.07E-01	3.72E+00	1.42E-02	5.61E-04	4.19E-03	1.30E+00	6.44E-05	4.81E-04	1.74E-01
T15	1.76E-01	4.27E+00	3.40E-02	3.72E+00	1.42E-02	5.61E-04	4.19E-03	1.30E+00	6.44E-05	4.81E-04	1.74E-01
T16	1.76E-01	3.42E+00	8.72E-02	3.72E+00	1.42E-02	5.61E-04	4.19E-03	1.30E+00	6.44E-05	4.81E-04	1.74E-01
T18	1.76E-01	3.42E+00	5.66E-02	3.72E+00	1.42E-02	5.61E-04	4.19E-03	1.30E+00	6.44E-05	4.81E-04	1.74E-01
T19	1.76E-01	8.33E+00	1.13E-01	3.72E+00	1.42E-02	5.61E-04	4.19E-03	1.30E+00	6.44E-05	4.81E-04	1.74E-01
T20	1.76E-01	5.94E+00	3.43E-01	3.66E+00	1.46E-02	5.61E-04	4.19E-03	1.40E+00	5.54E-05	4.14E-04	1.91E-01
T22	1.76E-01	5.94E+00	1.83E-01	3.66E+00	1.46E-02	5.61E-04	4.19E-03	1.40E+00	5.54E-05	4.14E-04	1.91E-01
T26	1.61E-01	7.73E+00	1.70E-01	3.72E+00	1.30E-02	5.44E-04	4.07E-03	1.26E+00	6.25E-05	4.66E-04	1.68E-01

Table 4.4 (continued).

Run No.	Combined bulk and Knudsen diffusivity: Micropore (cm^2/s)	Combined bulk and Knudsen diffusivity: Macropore (cm^2/s)	Heat transfer coefficient, H_m (cal/s cm^2 °K)	Run No.
T3	6.41E-05	1.32E-02	1.78E-03	T3
T5	5.52E-05	1.36E-02	1.11E-03	T5
T6	6.41E-05	1.32E-02	1.78E-03	T6
T7	5.52E-05	1.36E-02	1.11E-03	T7
T8	6.41E-05	1.32E-02	1.50E-03	T8
T10	6.78E-05	1.54E-02	1.78E-03	T10
T11	6.41E-05	1.32E-02	1.78E-03	T11
T12	6.41E-05	1.32E-02	1.78E-03	T12
T13	6.41E-05	1.32E-02	1.78E-03	T13
T14	6.41E-05	1.32E-02	1.78E-03	T14
T15	6.41E-05	1.32E-02	1.25E-03	T15
T16	6.41E-05	1.32E-02	1.13E-03	T16
T18	6.41E-05	1.32E-02	1.13E-03	T18
T19	6.41E-05	1.32E-02	1.78E-03	T19
T20	5.52E-05	1.36E-02	1.11E-03	T20
T22	5.52E-05	1.36E-02	1.11E-03	T22
T26	6.22E-05	1.21E-02	1.71E-03	T26

[a] Gas film mass transfer coefficient calculated from theory.

[b] Gas film mass transfer coefficient determined by least squares curve fitting of shrinking core model to full set of experimental data

		$D_{AB,eff}$ (cm^2/s)	
	D_{AB} (cm^2/s)	1/16 in.	1/8-in.
150°C	0.1764	0.01423	0.01461
200°C	0.2086	0.01627	——

Calculated values for the tortuosity factor are 3.66 to 3.72, which are within the range of 1.7 to 4.5 reported by Yang (1987) as typical values for zeolite material.

4.2.2 Mean Free Path of CH_3I

Based on Eq. (2.23), which was described by Treybal (1980), the mean free path for CH_3I was estimated at both 150 and 200°C. These values are 4.6×10^{-8} m and 5.2×10^{-8} m respectively. These values would indicate that Knudsen diffusion would be predominant in pores with a radius smaller than about 50 Å. This was clearly in the mesopore range as defined by IUPAC. It is also worth noting that the peak pore area determined as part of the surface area analysis was in the 20- to 50-Å range.

4.2.3 Knudsen Diffusivity

The Knudsen diffusivity values were computed for the macropores, mesopores, and the micropores based on Eq. (2.24) and the effective Knudsen diffusivity by Eqs. (2.28) and (2.30). But it should be noted that in the case of the macropores, the Knudsen diffusivity was calculated to be greater than the molecular diffusivity which was incorrect from a physical standpoint. The computed values for the micropores and mesopores are:

	Micropore		
		$D_{k,eff}$ (cm^2/s)	
	D_k (cm^2/s)	1/16-in.	1/8-in.
150°C	5.61×10^{-4}	6.44×10^{-5}	5.54×10^{-5}
200°C	5.93×10^{-4}	6.81×10^{-5}	

	Mesopore		
		$D_{k,eff}$ (cm^2/s)	
	D_k (cm^2/s)	1/16-in.	1/8-in.
150°C	4.19×10^{-3}	4.81×10^{-4}	4.81×10^{-4}
200°C	4.27×10^{-3}	5.08×10^{-4}	

4.2.4 Poiseuille Flow Diffusion Coefficient

Poiseuille flow diffusion coefficients can be estimated assuming a pressure drop across the pellet. However, based on the system in use, virtually no pressure drop would exist across the pellet or pore. Thus Poiseuille flow will not be considered further in this analysis.

4.2.5 Combined Diffusivities

The combined diffusivities were calculated by Eq. (2.31) and, as can be seen in Table 4.4, the combined term for the micropore region was dominated by the Knudsen diffusivity while the macropore region was dominated by the effective molecular diffusivity as would be expected.

4.2.6 Gas Film Mass Transfer Coefficient

The gas film mass transfer coefficients were estimated using Eq. (2.76) and the calculated values of the molecular diffusivities determined in Sect. 4.2.1. The calculated values of the mass transfer coefficient for each run is also shown in Table 4.4. These calculated values of the mass transfer coefficient were then compared with the values obtained by fitting the experimentally obtained loading data with the shrinking core model assuming resistance through the gas film was controlling. The calculated values based on the loading data, assuming that only gas film resistance was controlling, were a factor of 10 to 100 times smaller than those based on fundamental analysis. This was one indication that it was safe to assume that the gas film resistance was not the controlling resistance to mass transfer.

4.2.7 Heat Transfer Coefficient

The heat transfer coefficient was calculated from Eq. (2.78). The values ranged from 1.11×10^{-3} to 1.78×10^{-3} cal/(s cm^2°K). The calculated values for each set of run conditions are also shown in Table 4.4.

4.3 BASELINE ADSORPTION DATA

4.3.1 Water Uptake by AgZ

One obvious concern in analyzing the CH_3I uptake data was the possible impact of concurrent weight gain by the adsorption of water from the flowing gas stream. Test T17 was performed to measure the quantity of water adsorbed as a function of time. The

weight gain is shown in Fig. 4.15. After approximately the first 16 h that the bed was subjected to the flowing instrument air at 150°C, an observed gain of approximately 0.05 g had occurred on the 2.5416-g bed and the loading appeared to have leveled off. After 40 h the total had risen to about 0.07 g. Over the next 50 h the loading appeared to stabilize at a total weight gain of about 0.075 ± 0.005 g. The weight gain that occurred between the 20- and 40-h time marks may have been the result of a possible variation/increase in the water content of the instrument air as a function of the relative humidity of a Tennessee summer day. There was, however, no direct proof of this possibility other than the periods of stable weight occurred roughly 24 h apart.

To determine the significance of these gains due to water uptake these data must be compared to the total weight gains observed when CH_3I was present in the flowing gas stream to determine the possible impact on the CH_3I loading data. The typical weight gain was on the order of 0.45 g in 60 h, as in the case of T10 (data file T10LOAD). In cases such as T18 (data file T18LOAD), in which lower gas velocities were used, 0.504 g was loaded onto the bed in 161 h of which 0.4 g was loaded in about 82 h. The water contribution could be as high as 15 to 20%.

4.3.2 CH_3I Loading on NaZ

It was assumed at the start of this study that any weight gain on the mordenite pellet was primarily associated with chemical bonding with the silver contained in the pellet. It appeared necessary to verify this assumption and to possibly obtain some information to differentiate between the transient loading curve that would be observed

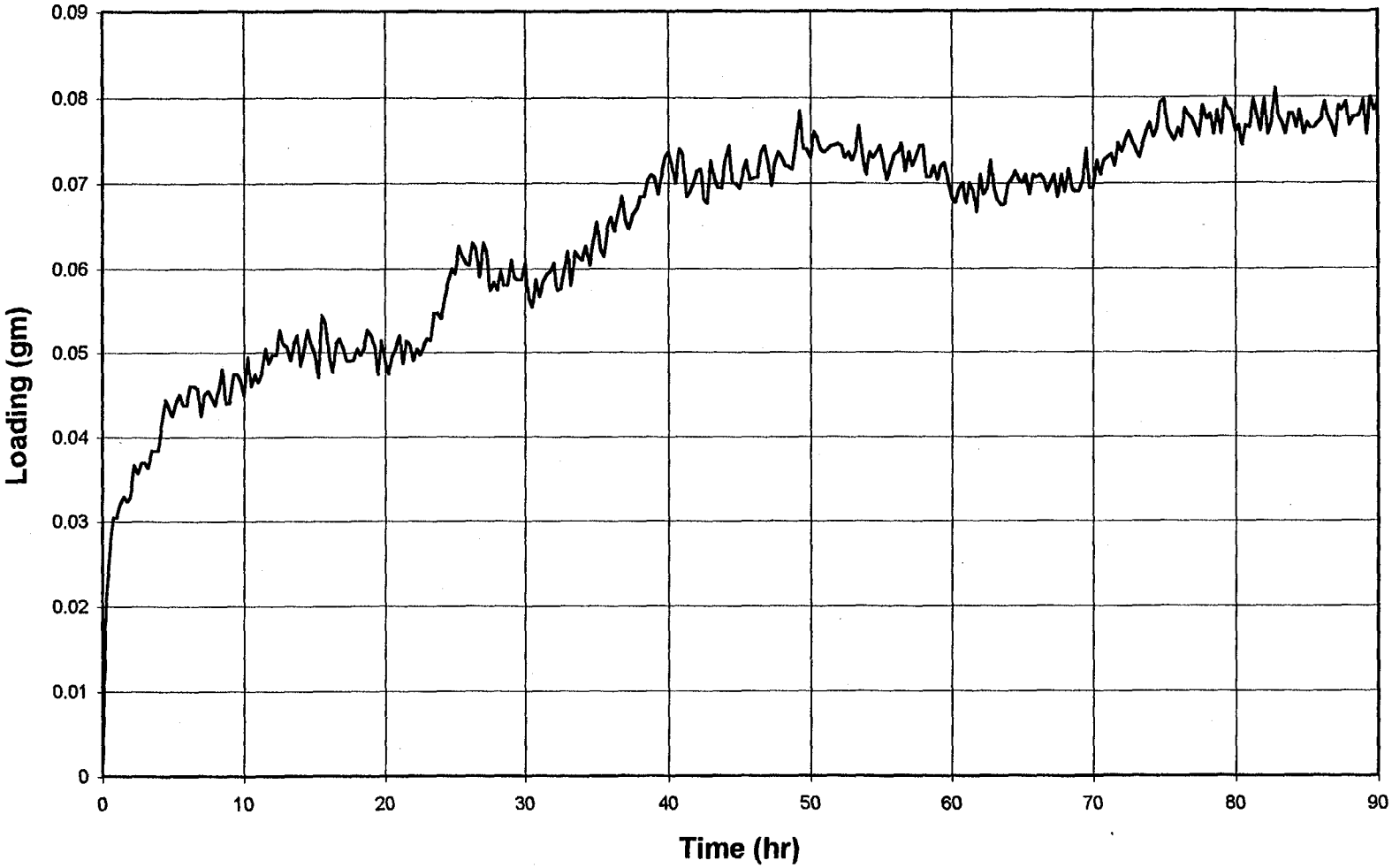

Figure 4.15. Water uptake during Test T17 onto 1/16-in.-diam AgZ.

resulting from chemical adsorption by the silver contained in the mordenite structure and the physical adsorption on the zeolite structure. Test T25 (data file T25LOAD) was conducted to determine the loading rate and quantity of CH_3I adsorbed on the unexchanged sodium form of the mordenite. The adsorption and desorption curve is presented in Fig. 4.16. As can be seen from this figure, 0.0807 g was loaded over the 22-h test period. Following the loading cycle, an air purge of 70 h was conducted. During this period a net gain of 0.0353 g was observed that must be attributed to a water vapor.

The total CH_3I loading should be compared with loading curves from tests such as T3, in which 0.335 g were gained over the same time period to examine the significance. It is also interesting to note that between the 4th and 22nd h of exposure the loading on T25 increased by only 0.018 g, while T3 increased 0.192 g.

Two conclusions are readily apparent from this test: (1) very little CH_3I was loaded on the mordenite without the presence of silver and (2) the loading that was observed cannot be clearly distinguished from the observed uptake with instrument air alone. As shown in Fig. 4.17, the difference of uptake in the 22 h in which CH_3I was present is approximately 0.03 g as compared with instrument air alone as observed in test T17. Based on these data it would appear relatively safe to assume that the observed weight gains on the beds that were measured during the CH_3I loading tests required a chemical reaction between the CH_3I and the silver.

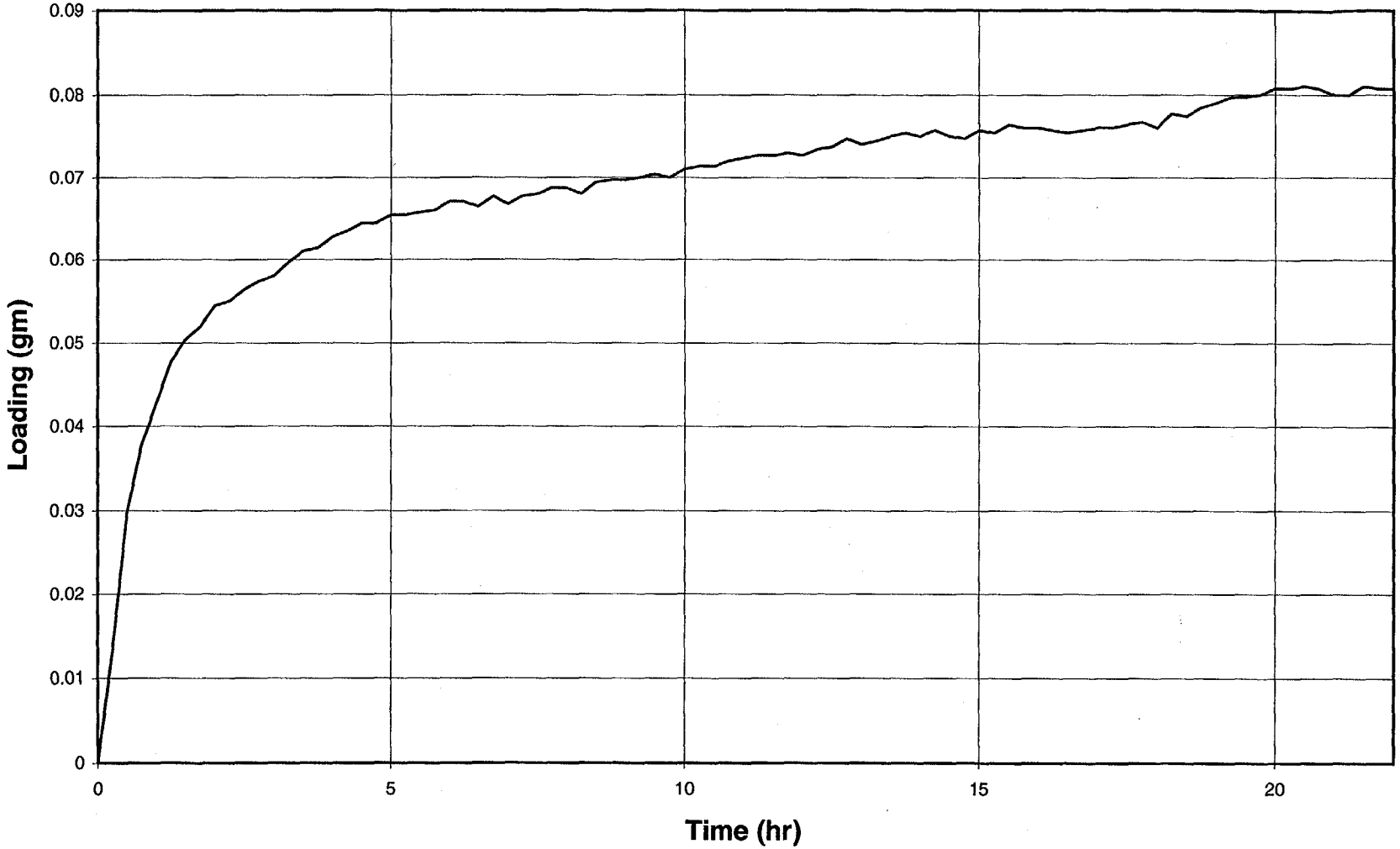

Figure 4.16. Methyl iodide uptake during Test T25 onto 1/16-in.-diam NaZ.

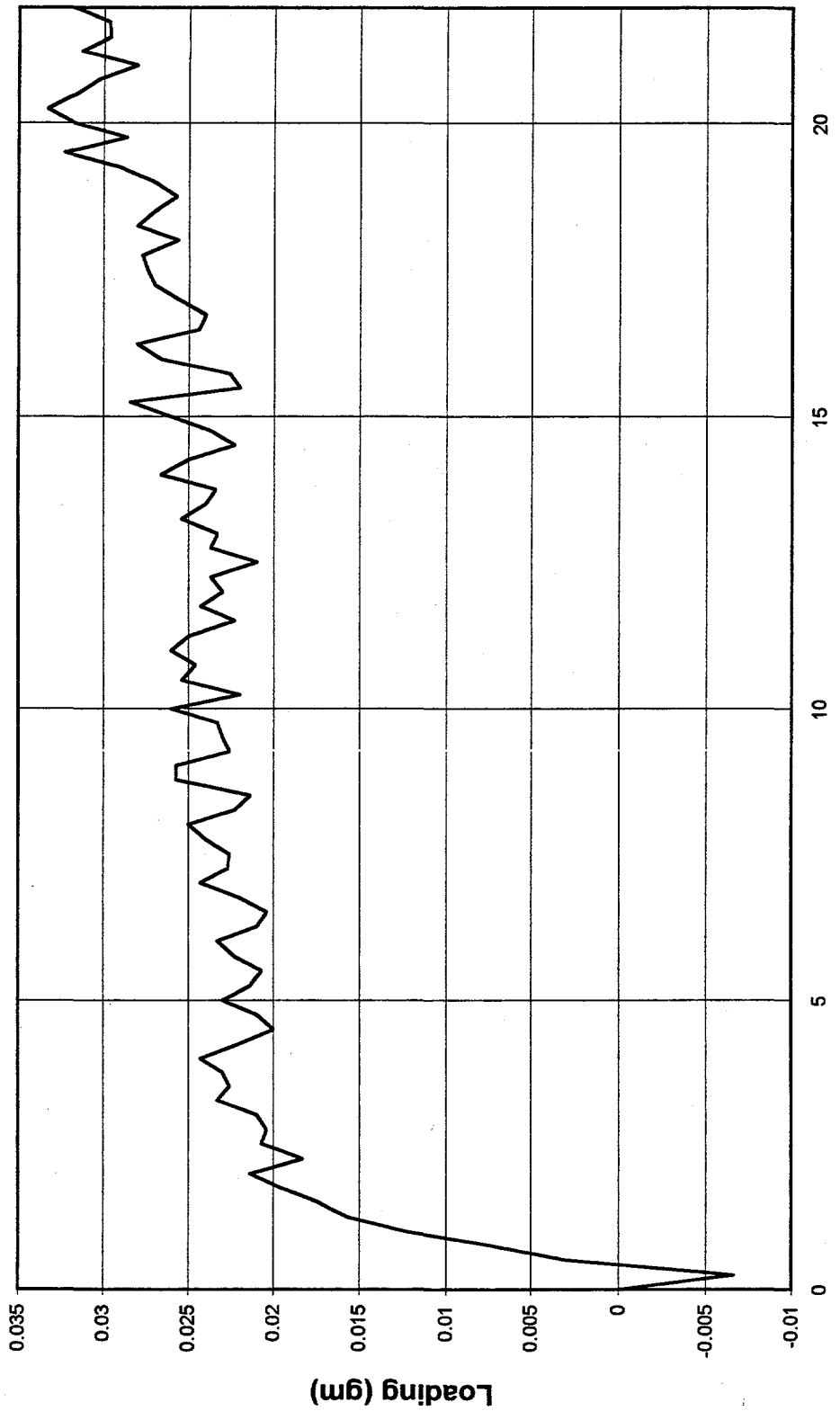

Figure 4.17. Methyl iodide uptake on NaZ corrected for water uptake.

4.4 CH_3I ADSORPTION STUDIES

4.4.1 CH_3I Loading Data

The CH_3I loading curves for all of the experimental runs are shown in Figs. 4.18–4.36. The raw loading data as collected from the balance in the PC data files are archived on magnetic disk at ORNL in the Building 7601 permanent data storage area. In some cases the loading was recorded in multiple files and brief gaps in the data collection occurred. The air flush portions of the tests may also be included in the loading files as this phase of the tests was conducted as a continuation of the test conditions with only the CH_3I flow stopped. A summary of the actual test conditions is presented in Table 4.5. Special notes concerning the data files can be found in the summary data located in Appendix A.2.

Notes which relate to any variation in the treatment of the sample prior to or during the loading cycle are presented in Table 4.6. While it was not believed that the duration of such steps as nitrogen temperature adjustment or low temperature hydrogen pretreatment would affect the loading this data was recorded and may have benefit in understanding any unexpected behavior between otherwise similar tests.

Tests T3–T12 were designed to evaluate the effects of the four basic parameters of pellet size, temperature, flow rate and CH_3I concentration as each parameter was varied individually from a reference condition. The initial series of tests also provided two sets of duplicates tests to allow an estimation of error.

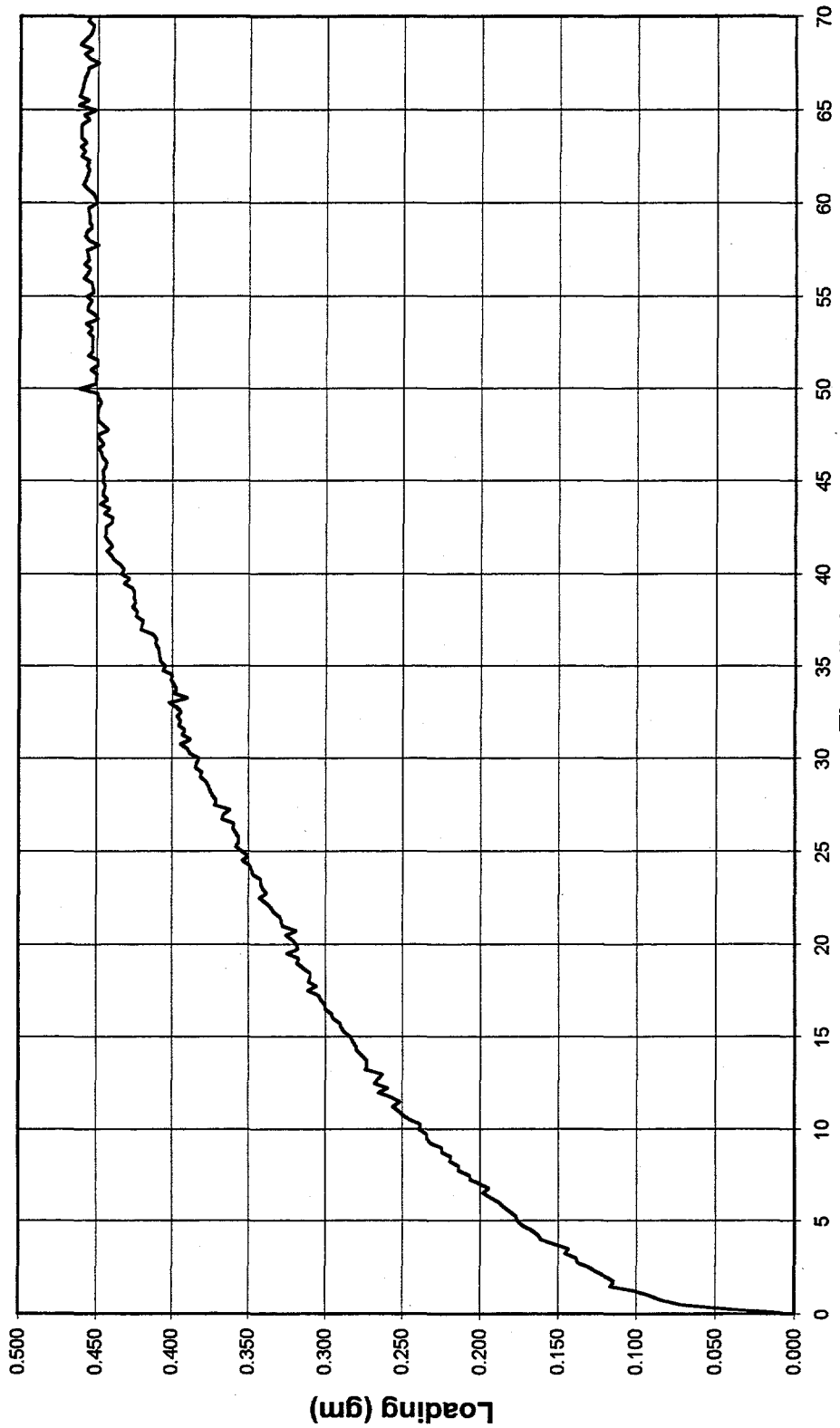

Figure 4.18. CH_3I loading curve from Test T3.

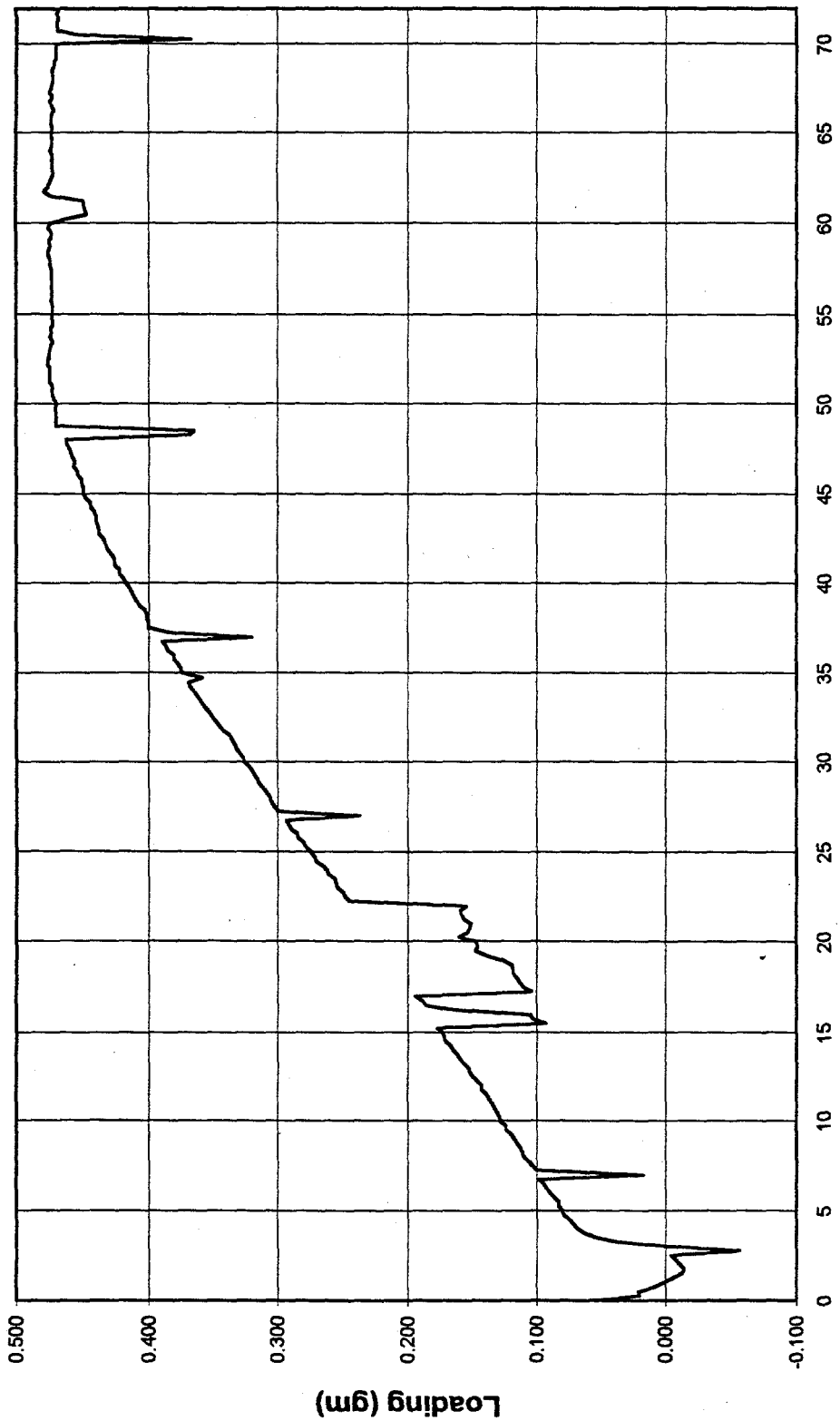

Figure 4.19. CH_3I loading curve from Test T5.

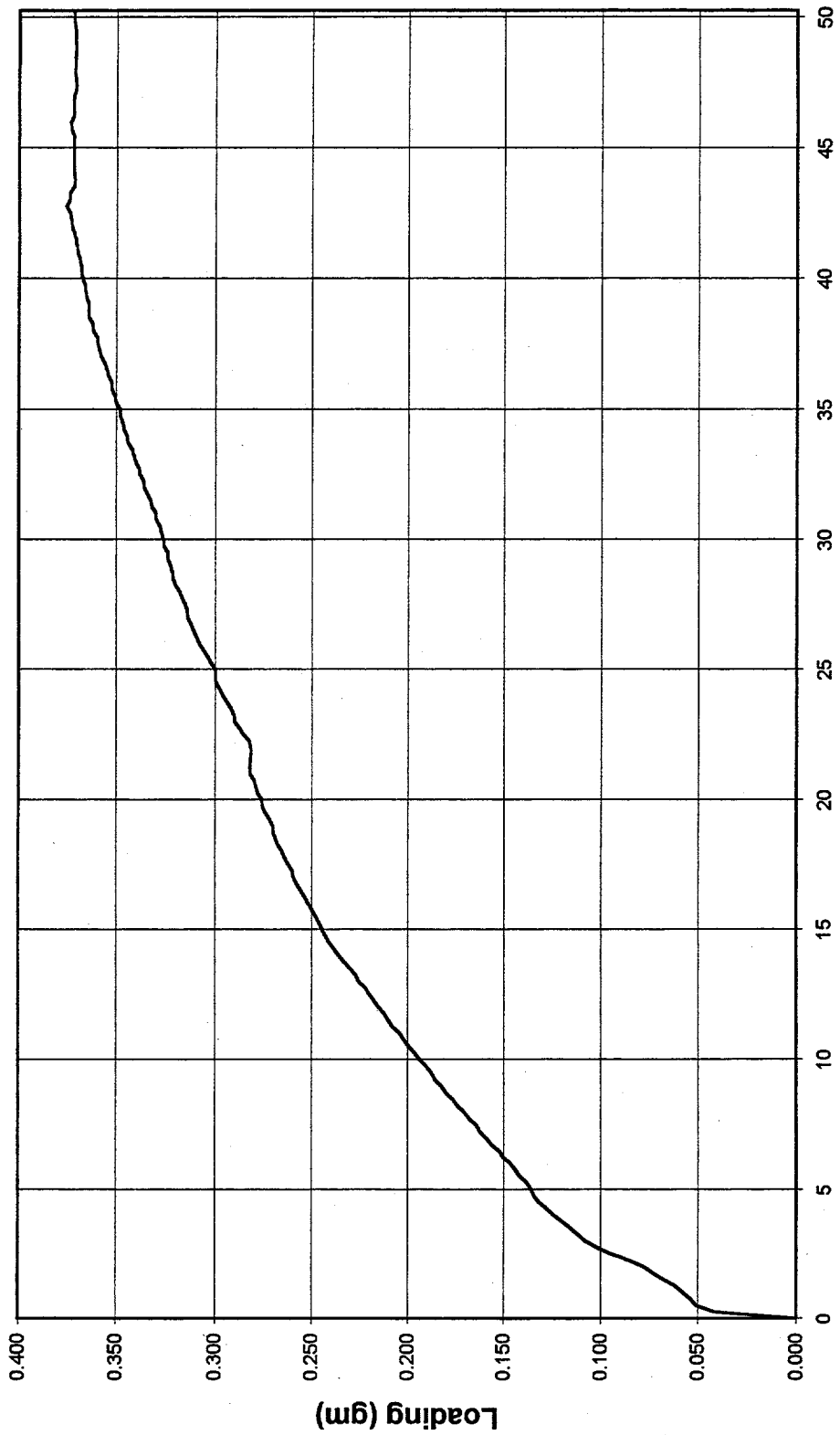

Figure 4.20. CH_3I loading curve from Test T6.

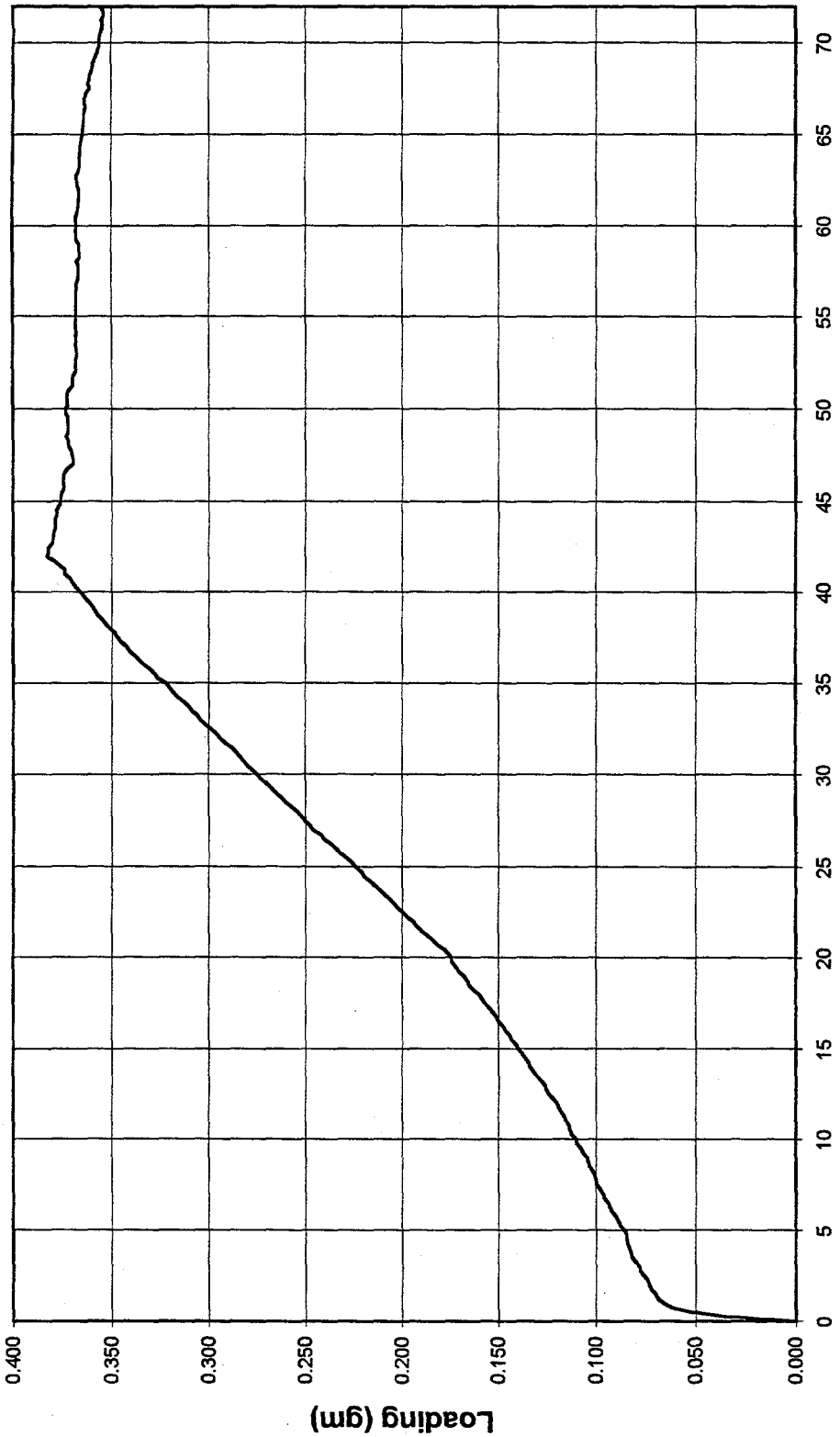

Figure 4.21. CH_3I loading curve from Test T7.

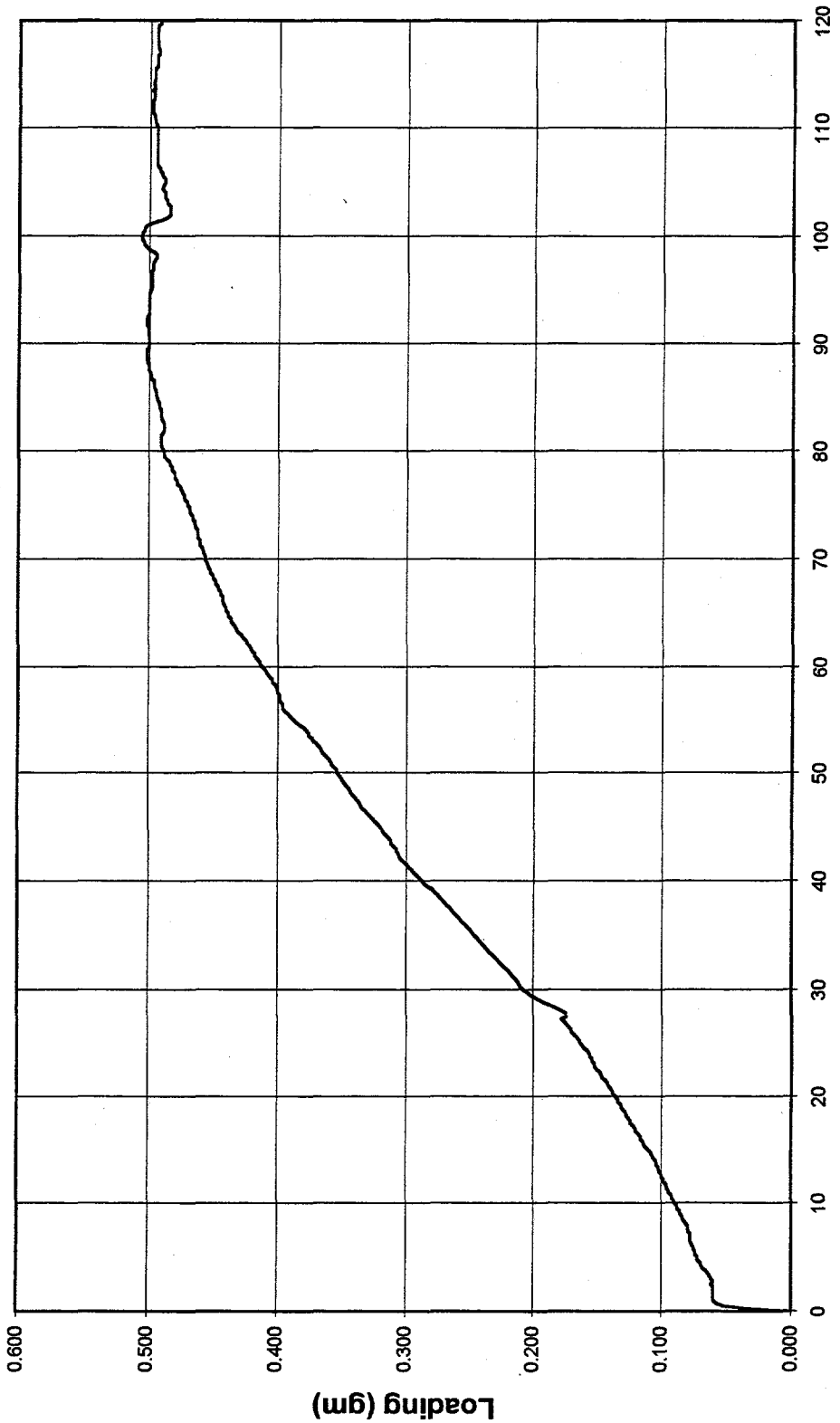

Figure 4.22. CH_3I loading curve from Test T8.

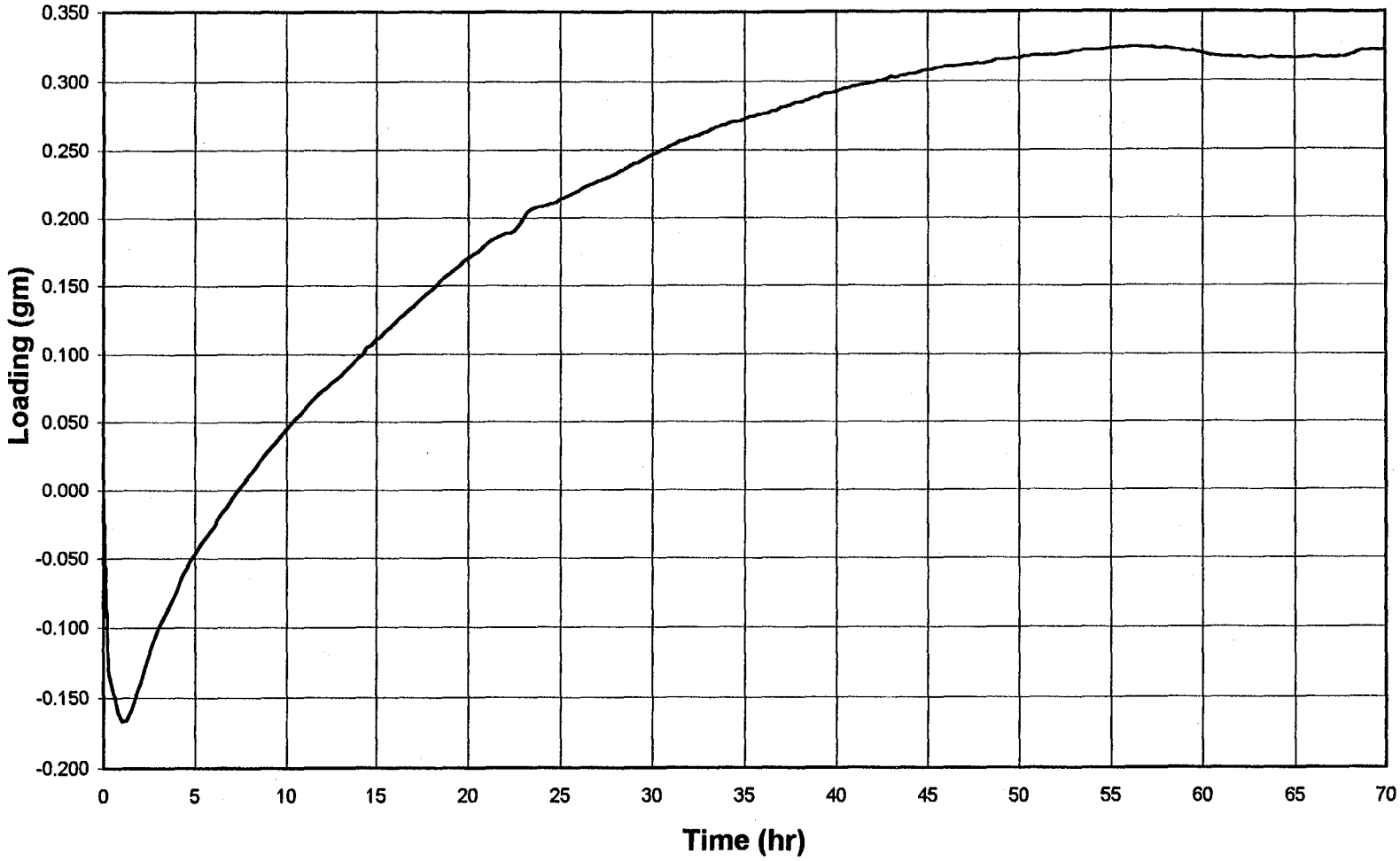

Figure 4.23. CH_3I loading curve from Test T10.

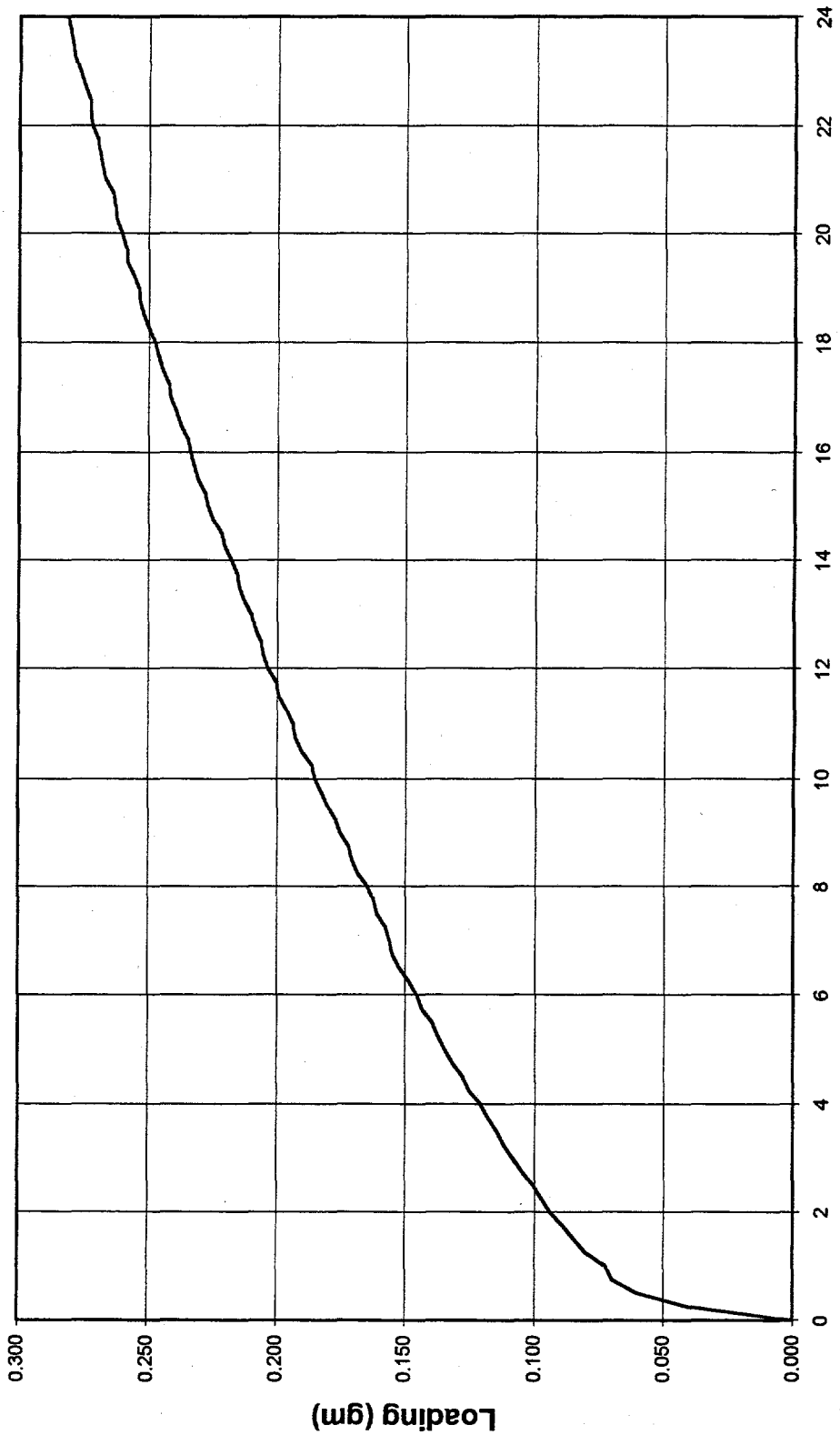

Figure 4.24. CH_3I loading curve from Test T11.

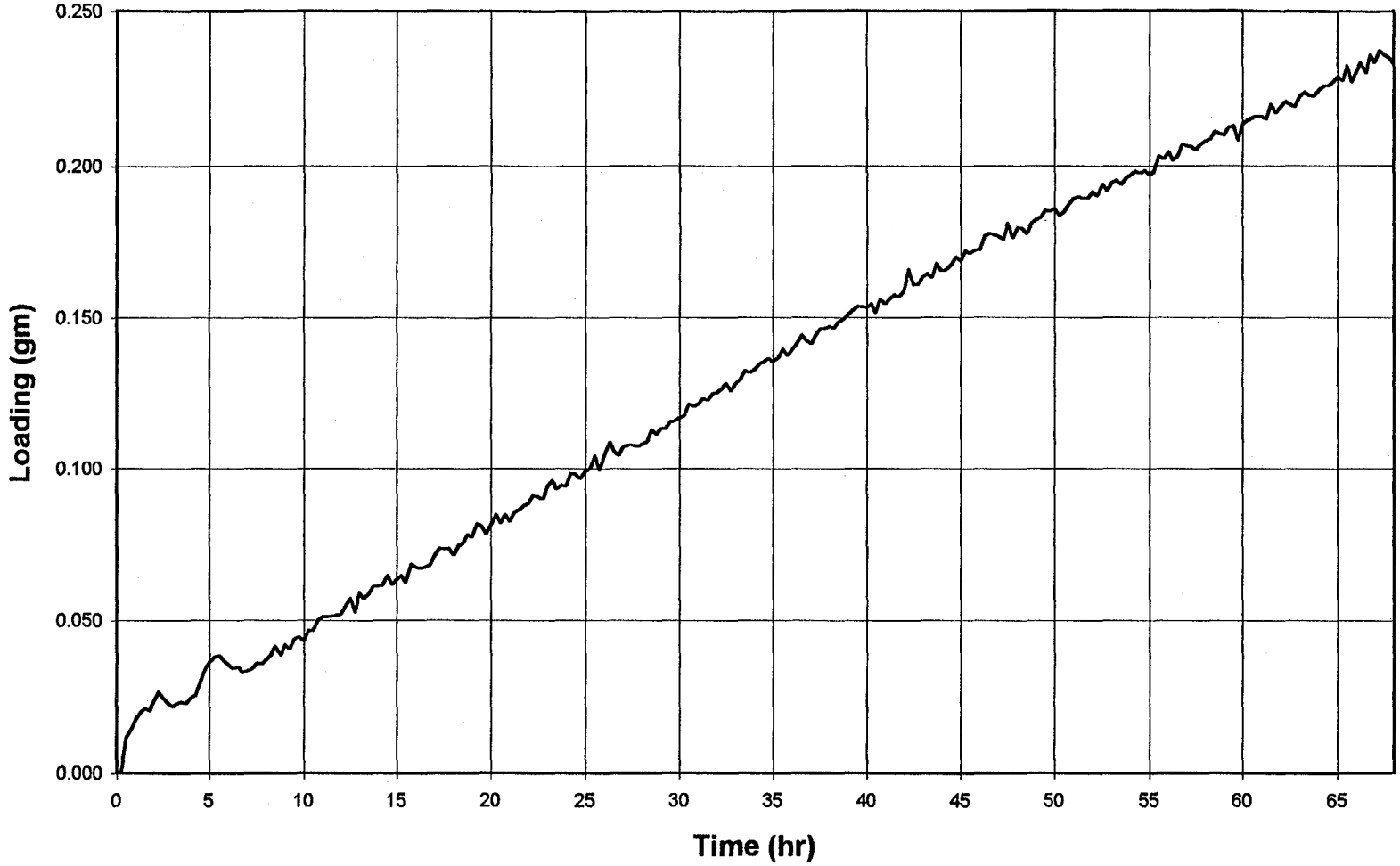

Figure 4.25. CH_3I loading curve from Test T12.

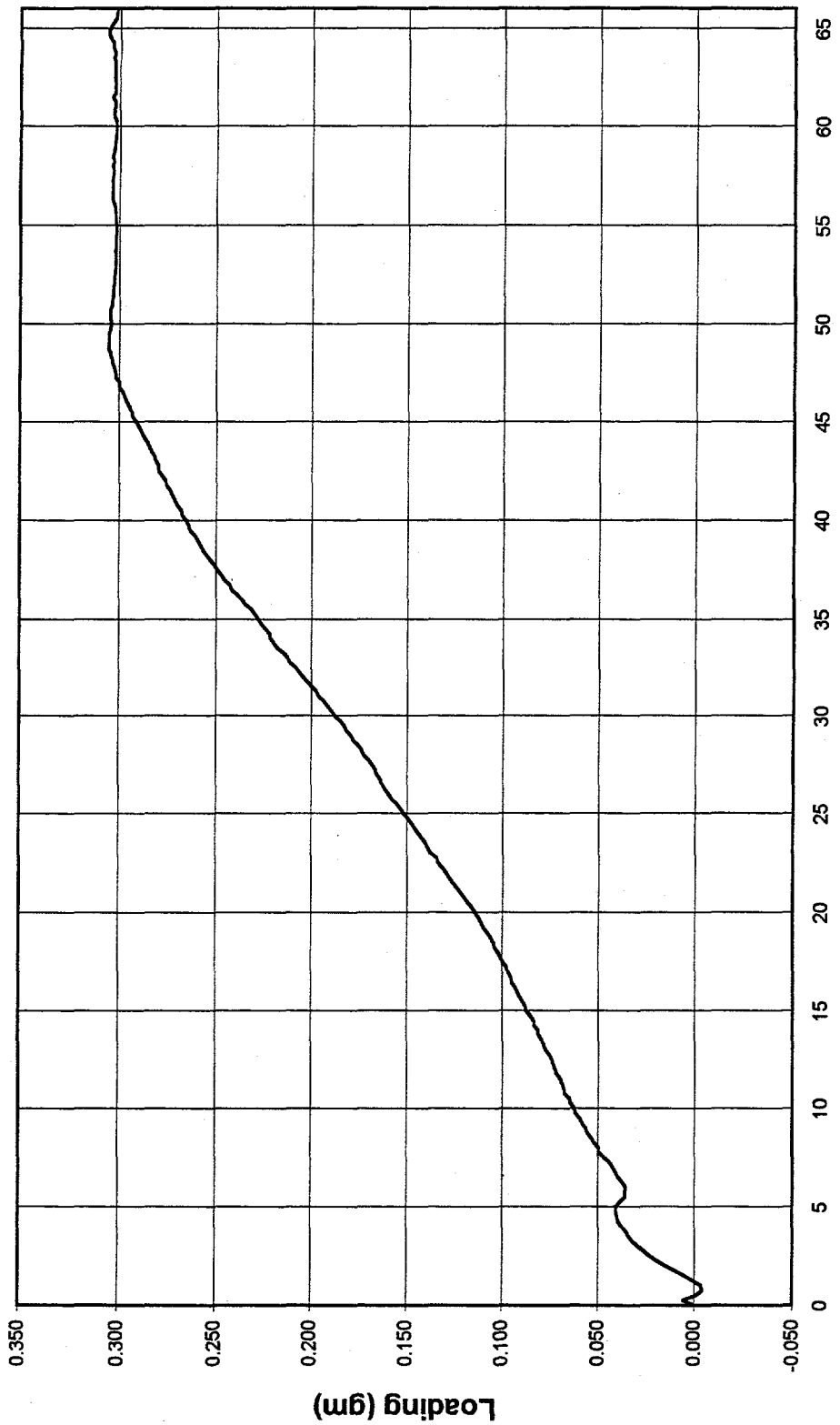

Figure 4.26. CH_3I loading curve from Test T13.

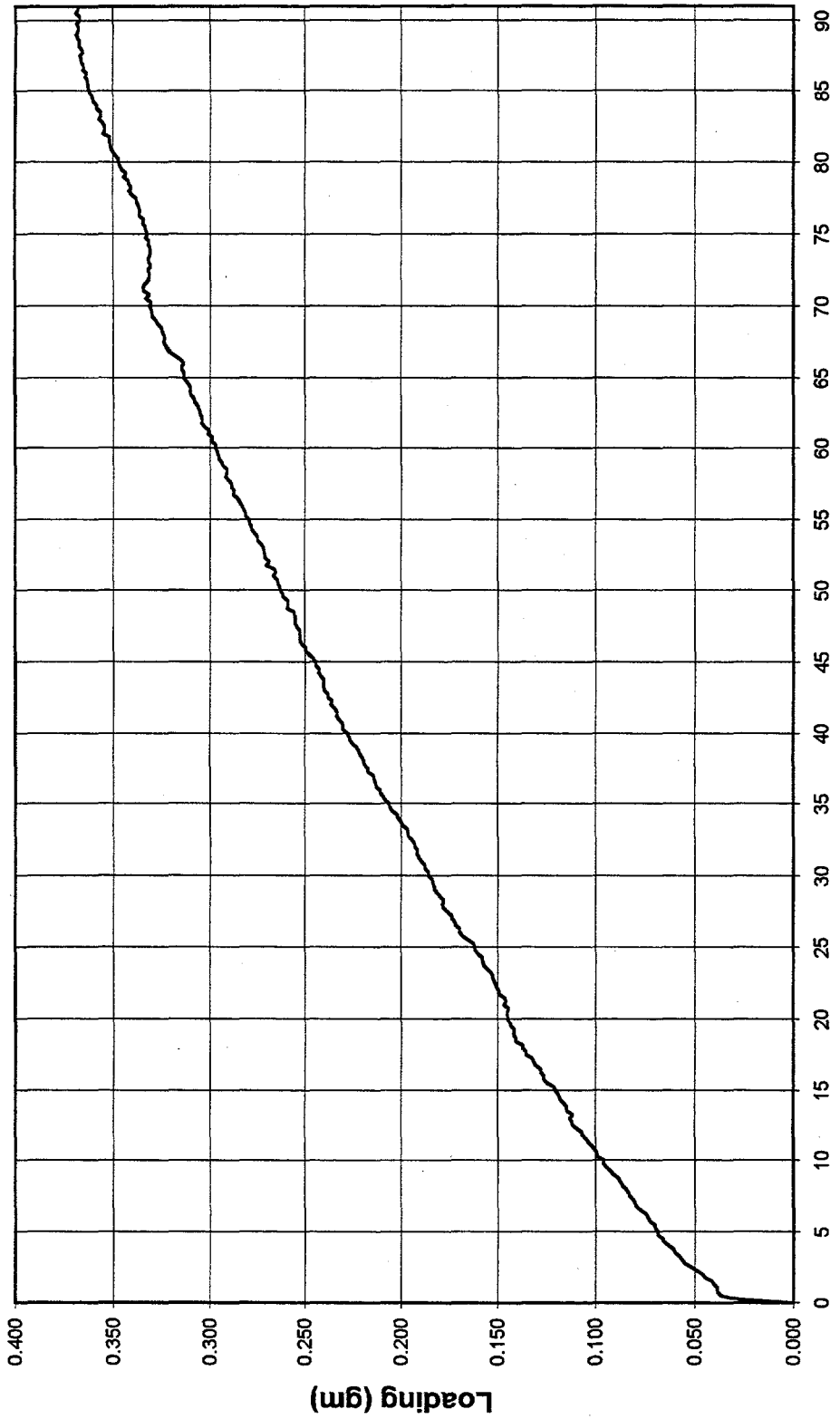

Figure 4.27. CH_3I loading curve from Test T14.

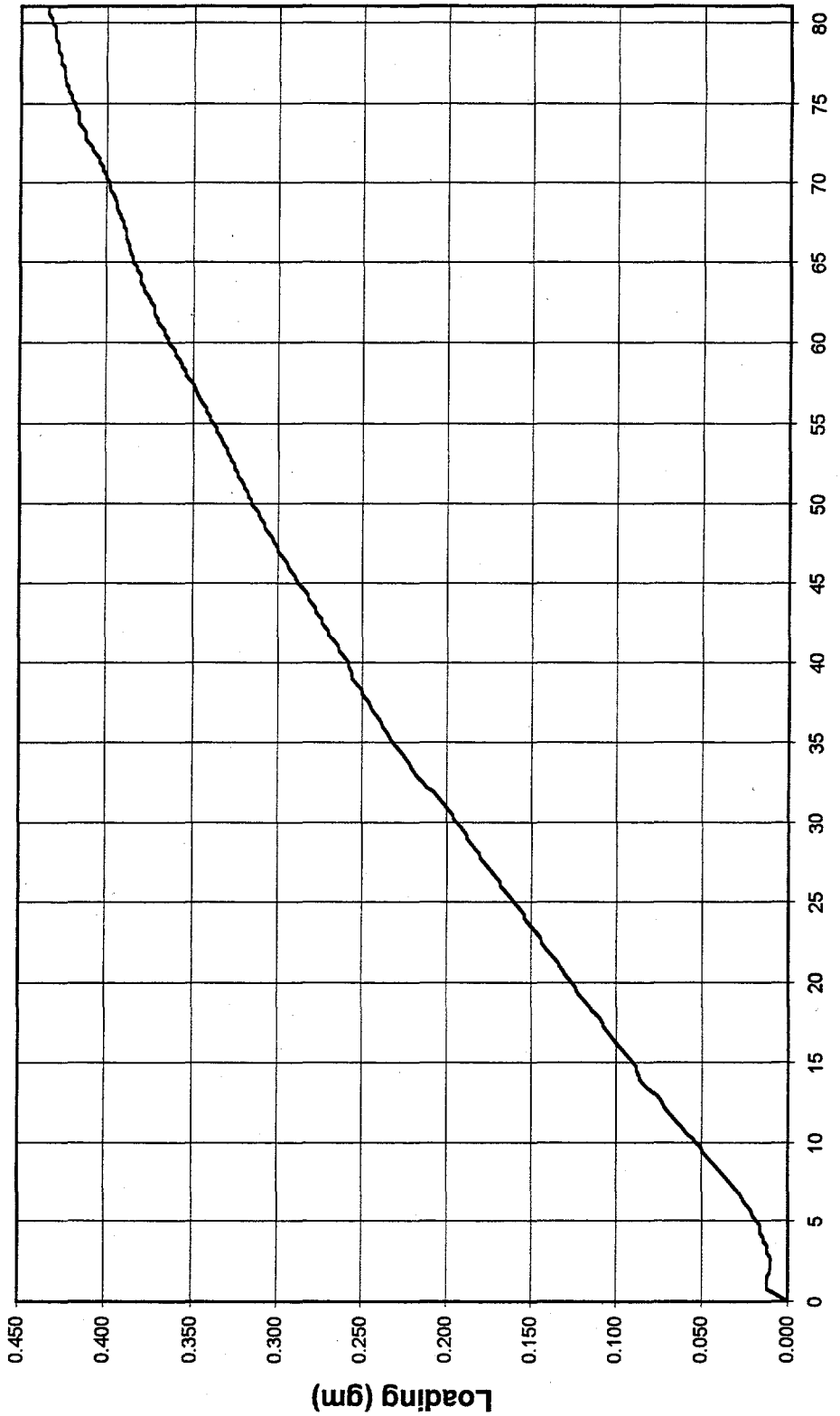

Figure 4.28. CH_3I loading curve from Test T15.

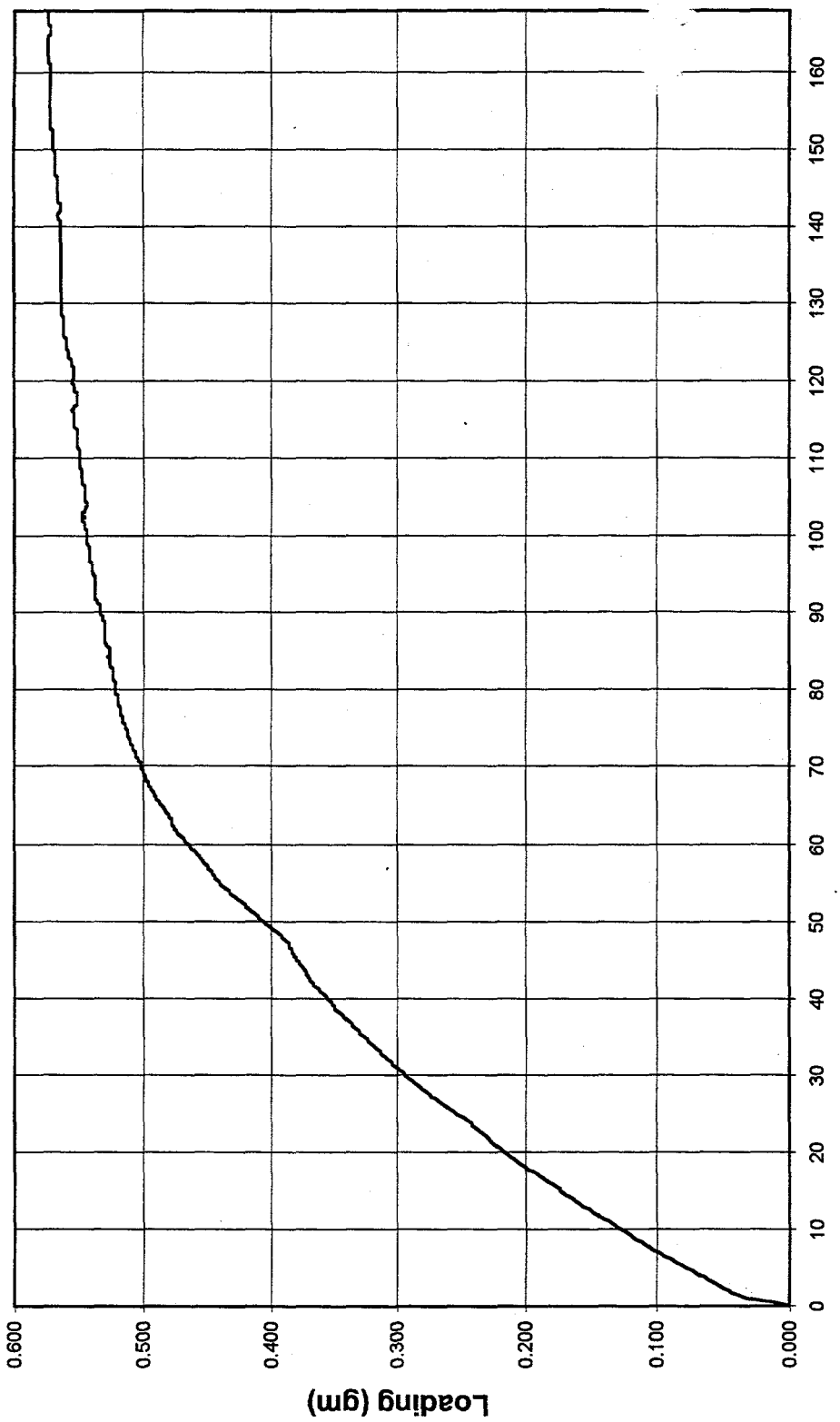

Figure 4.29. CH_3I loading curve from Test T16.

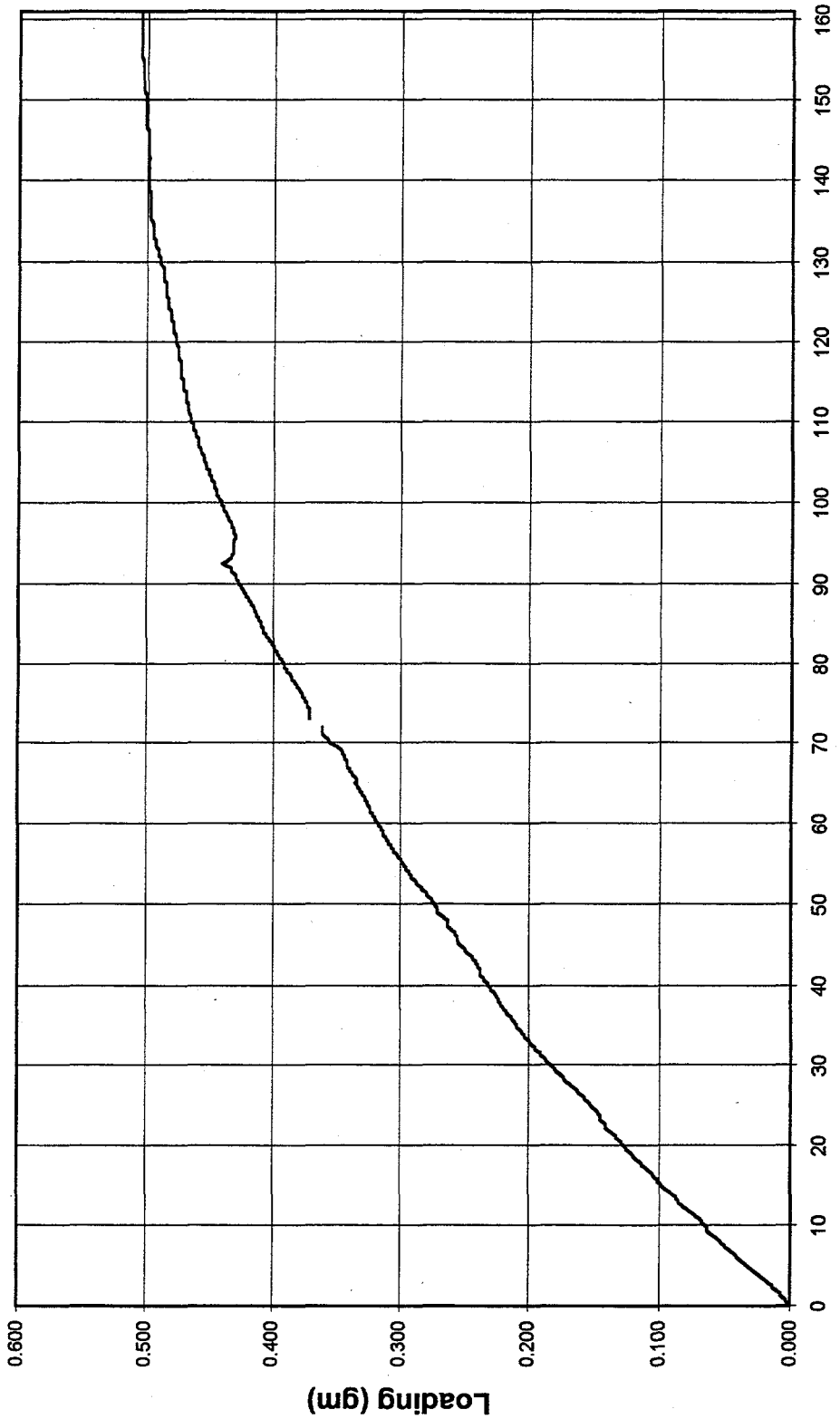

Figure 4.30. CH_3I loading curve from Test T18.

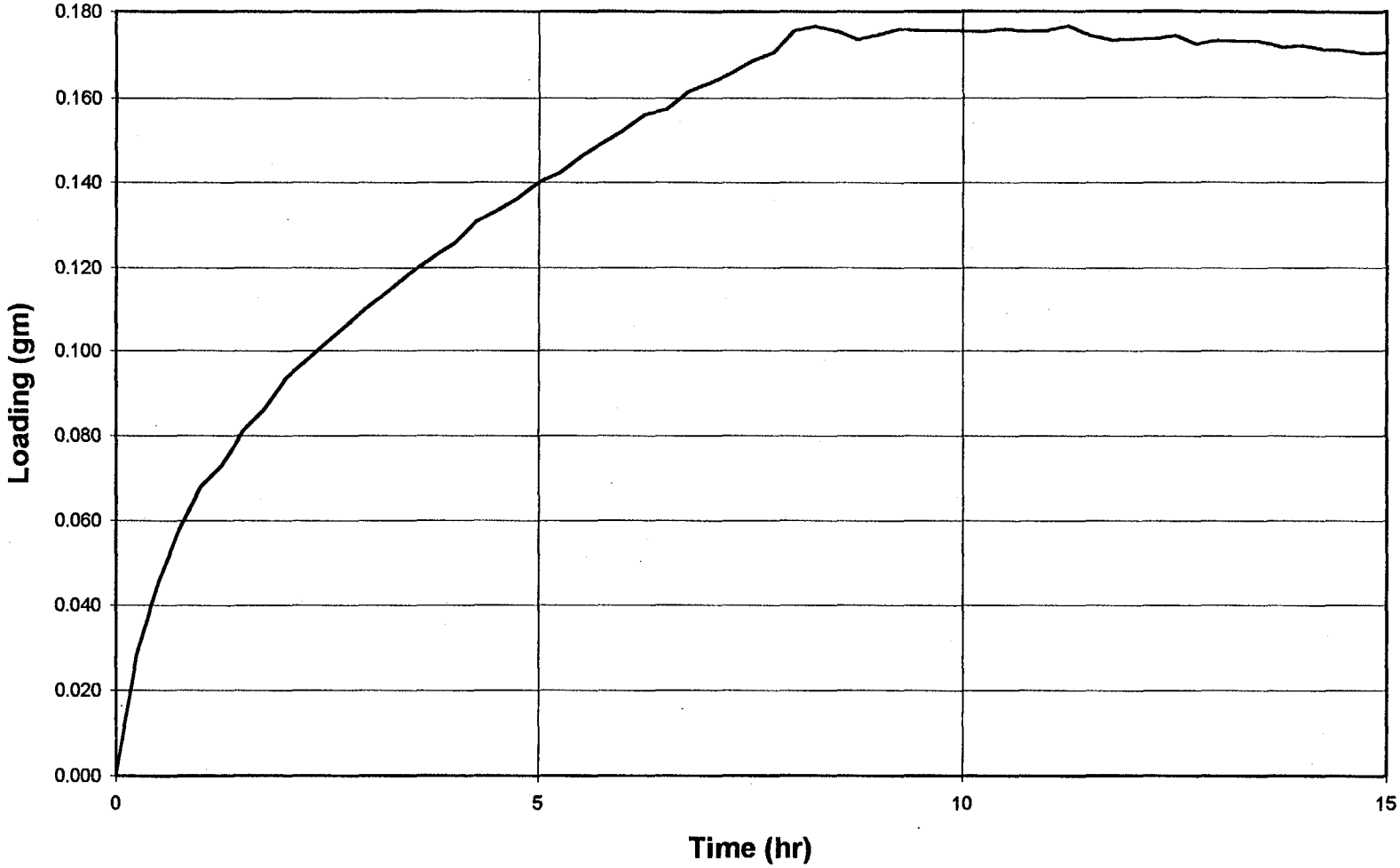

Figure 4.31. CH_3I loading curve from Test T19.

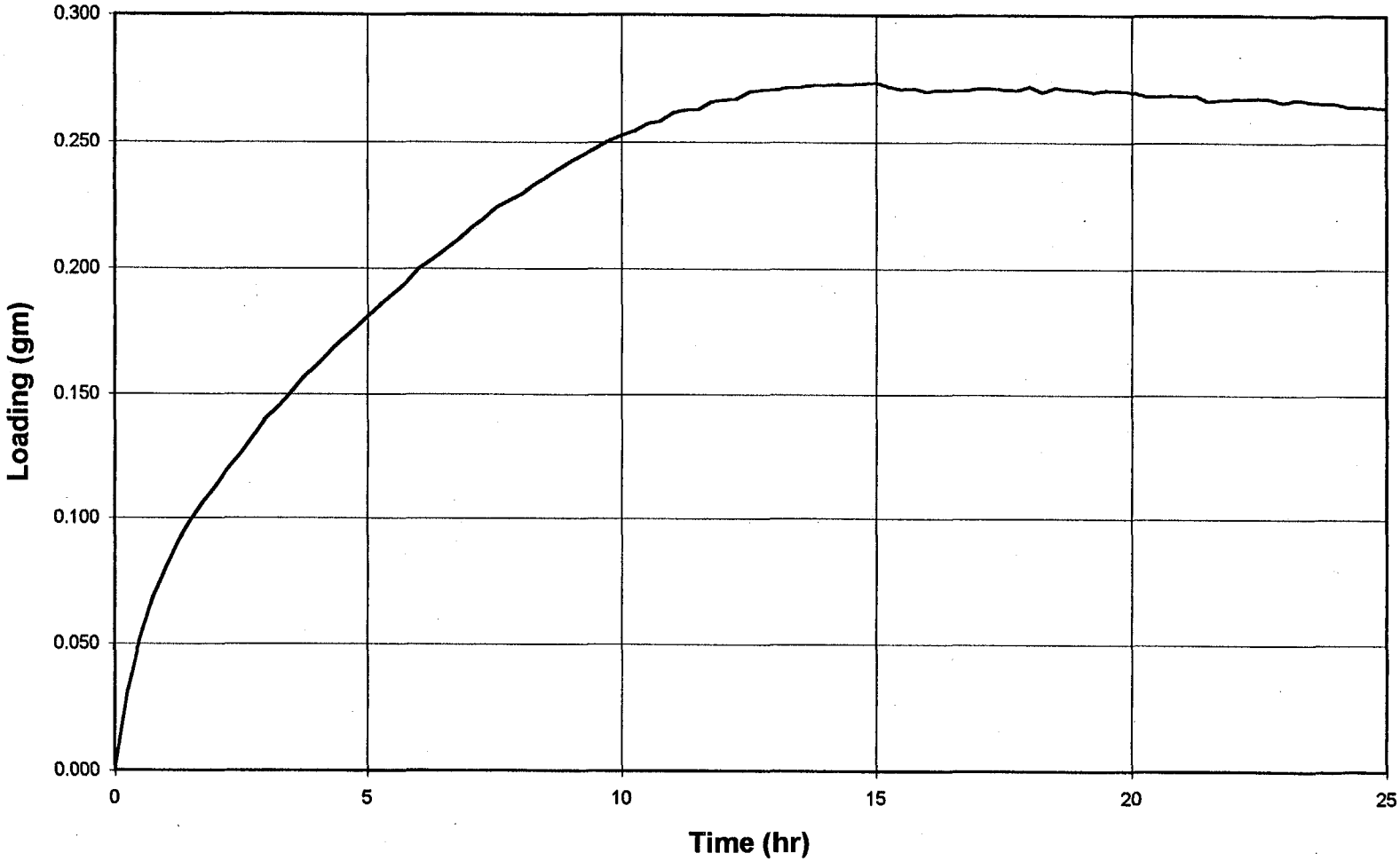

Figure 4.32. CH_3I loading curve from Test T20.

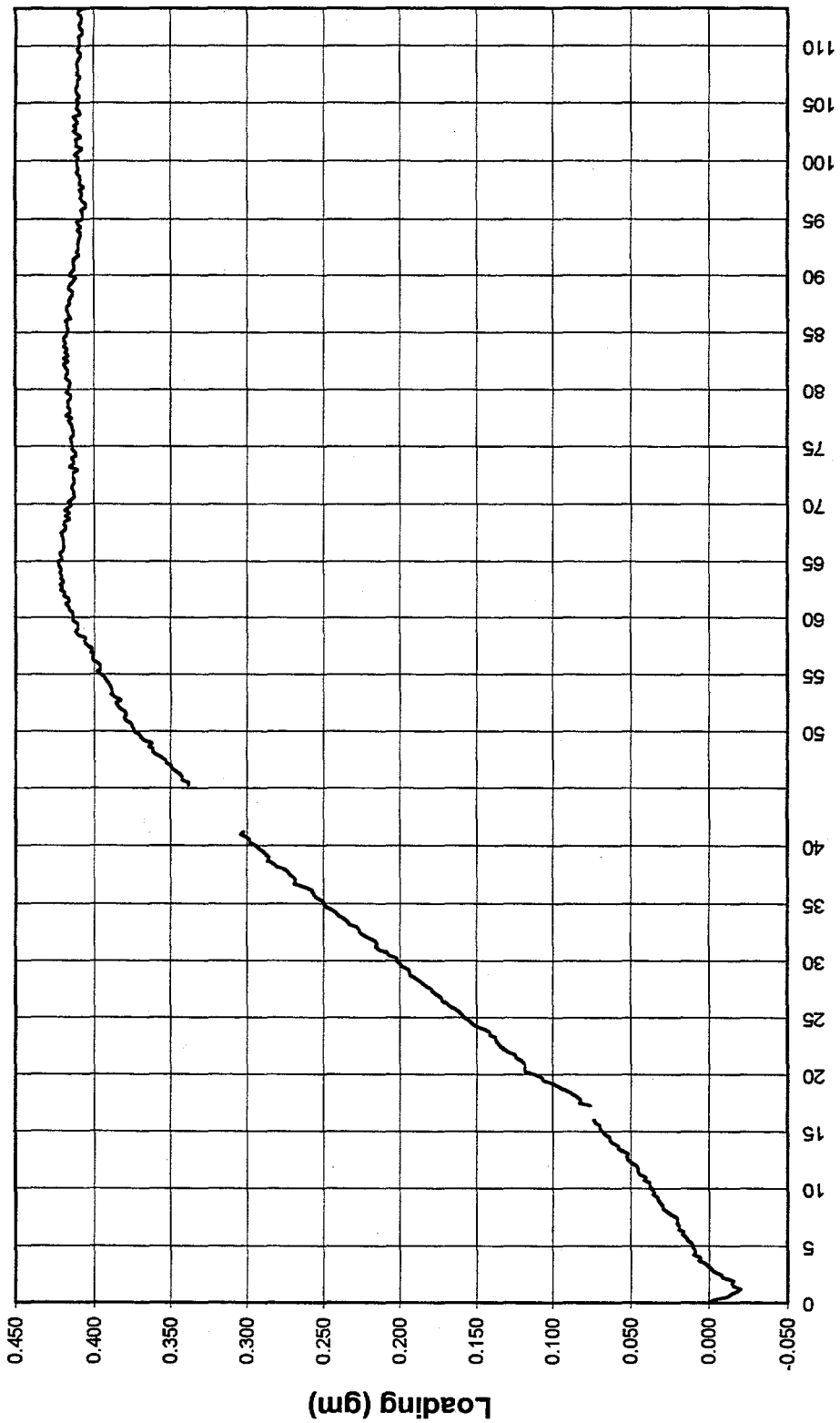

Figure 4.33. CH_3I loading curve from Test T21.

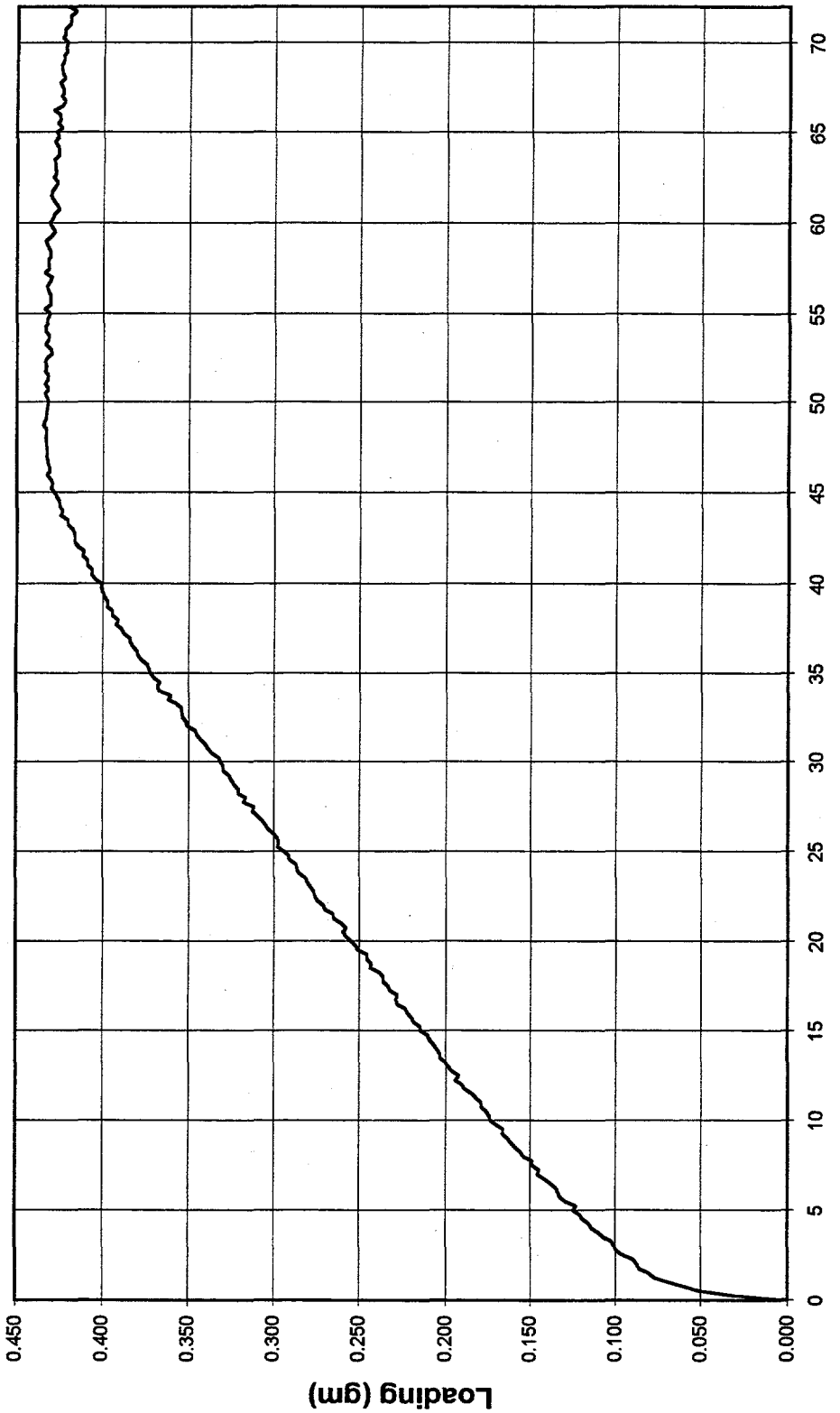

Figure 4.34. CH_3I loading curve from Test T22.

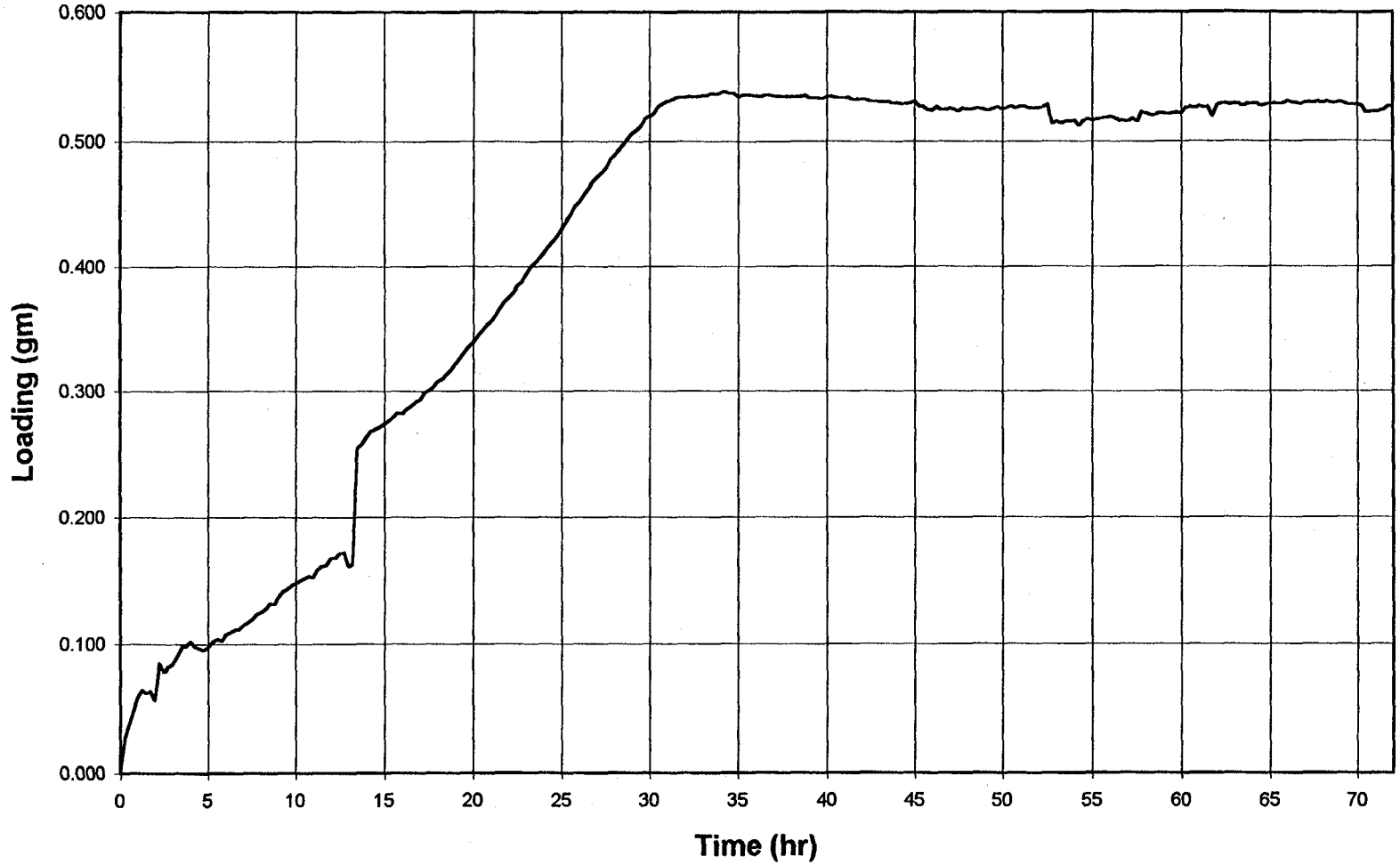

Figure 4.35. CH_3I loading curve from Test T24.

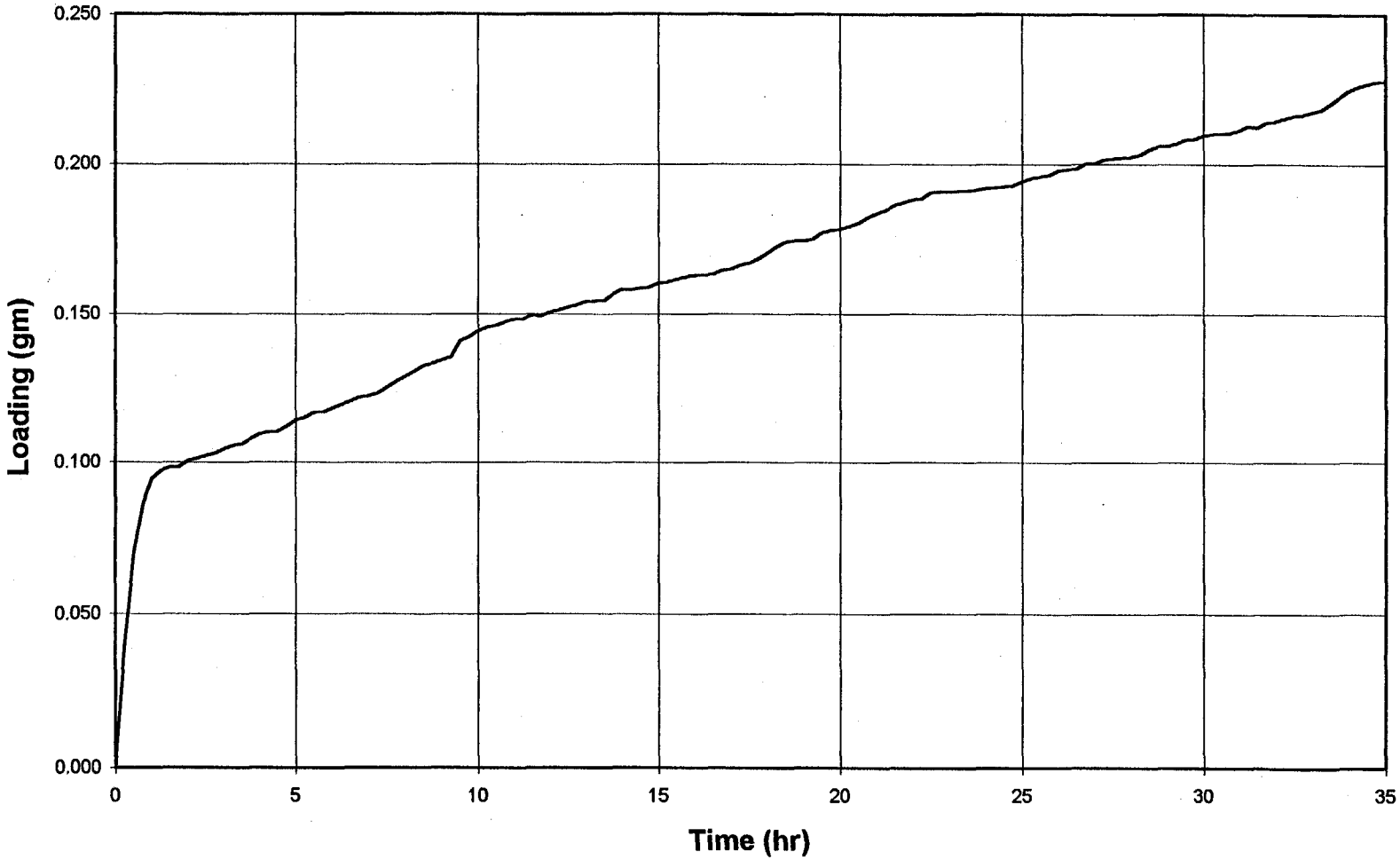

Figure 4.36. CH_3I loading curve from Test T26.

Table 4.5: Summary of single pellet tests.

Test No.	Size (in.)	Velocity (m/min)	CH_3I concentration (mg/m^3)		H_2O added	Temperature (°C)	Notes
Initial series:			Planned	Actual[a]			
3	1/16	10	1000	1559		150	
4							Test aborted
5[b]	1/8	10	1000	1275		150	
6	1/16	10	1000	1505		150	
7	1/8	10	1000	1523		150	
8	1/16	5	1000	1675		150	
9							Test aborted
10[c]	1/16	10	1000	1190		200	
11	1/16	10	1500	1634		150	
12[c]	1/16	10	500	837		150	
Supplemental tests:							
13[c]	1/16	10	1000	1367	yes	150	
14[c]	1/16	10	250	355		150	
15[c]	1/16	2	1000	1410		150	
16	1/16	1	1000	1124		150	
17	1/16	10	0	0		150	Air only
18	1/16	1	1000	1217	dry	150	
19	1/16	10	1500	2150		150	Short run
20	1/16	10	1500	1636		150	Short run
21[b]	1/16	10	1000			200	
22	1/8	10	1500	1367		150	
23[b]	1/16	10	1000		yes	150	Water data missing
24[b]	1/8	15	1000			150	Data questionable
25	1/16	10	1000			150	NaZ loading
26	1/16	10	1000	1059		125	

[a]Actual CH_3I concentrations determined by pressure drop in the gas supply cylinder vs time measurements.

[b]Data from runs T5, T21, T23, and T24 not used in analysis due to equipment difficulties or questions of validity or conditions.

[c]Data quality may be impacted by possible temperature shift at balance. This is discussed in detail in Sect. 5.2.1.

Table 4.6: Summary of pretreatment conditions and times.

Run No.	Air drying (h)	N_2 (h)	H_2 (h)	N_2 (h)	Notes
T3	24.0	5.2	18.9	5.0	
T5	22.3	3.4	20.6	3.0	
T6	22.4	3.9	40.8	11.4	Some portion of H_2 time with no H_2 flow?
T7	64.9	4.0	20.0	6.2	
T8	24.3	2.3	44.5	4.0	
T10	27.0	19.4	23.8	4.3	
T11	24.0	17.0	22.5	4.0	
T12	24.0	4.0	23.5	18.5	
T13	22.7	4.9	20.0	5.1	
T14	17.9	5.8	18.8	27.8	At two rate–low rate used overnight
T15	16.0	6.0	21.0	4.0	22-h period of no flow following 20 h of H_2 then an additional 1 h of H_2
T16	21.1	4.3	18.8	4.0	
T18	21.4	4.0	20.5	10.0	After 5 h of run there was 115.7 h of air flow followed by another 5 h of N_2
T19	24.3	4.4	20.5	6.5	
T20	21.0	4.3	20.8	5.0	
T22	20.0	4.1	39.5	4.0	
T26	20.3	4.5	24.0	3.0	

Following the completion of the initial series of tests and preliminary comparison with simple models, several additional follow-on or supplemental experiments were defined to explore specific behavior that could not be explained by the simple model. These tests specifically provided data on the impact of lower gas velocities (T15, T16, and T18) in efforts to resolve any effects of the gas film and lower CH_3I concentrations (T14) on possible reaction rate controlling conditions.

The impacts of variations in the water vapor content of the gas stream were examined by adding a small additional amount of water vapor (T13) and by further drying the instrument air carrier gas (T18). Under the "standard test conditions," the CH_3I concentration calculated at standard temperature and pressure was 7.045×10^{-6} mol/L. The H_2O concentration at a measured dew point of –15°C is 7.259×10^{-5} mol/L. However, when the instrument air was further dried to –40°C the water concentration was reduced to 5.639×10^{-6} mol/L, which was below the stoichiometric ratio for either reaction Eqs. (2.5) or (2.7). The water addition through the use of the bubbler introduced an additional 2.792×10^{-5} mol/L. This raised the dew point to at least –11°C. The water rate was based on the water lost from the humidifier over a period of 64 h. It was noted, however, that the air rate to the bubbler had decreased over the weekend. Higher rates and thus a higher dew point could have been expected during the initial portions of the loading process.

Tests T19 and T20 were special short tests made to provide samples for electron microscope analysis. The loading times were selected to keep the conversion below 50%.

The samples were then to be analyzed for variations in iodine loading across the pellet radius.

Finally, due to the observation that there seemed to be some disturbances in the recorded loadings at the elevated temperatures which were attributed to the thermal response of the balance at higher temperatures, a run, T26, was made at lower temperatures to attempt to determine the activation energy associated with the intracrystalline or micropore diffusion.

4.4.2 Weight Loss Following Termination of CH_3I Flow

Following each loading period, the loaded AgZ was exposed to a flowing gas stream at the same temperature and rate as was used in the CH_3I adsorption phase of the test. This desorption phase was to determine the approximate amount of iodine that was not chemically bound in the mordenite structure. Table 4.7 shows the total iodine lost from the bed and the rate in grams per hour that the iodine was lost.

The total weight loss from the pellets was generally about 1 to 2% of the total iodine loaded.

Table 4.7: Weight loss during the air flush following loading with CH_3I.

Run No.	Initial weight (g)	Final weight (g)	Desorption data: Total weight of iodine loaded (g)	Desorption data: Duration (h)	Weight loss (g)	Loss rate (g/h)	% lost	% Lost per hour
3	150.046	150.050	0.455	28.00	–0.0037	–1.32E-04	–0.813	–2.90E-02
5	150.050	150.041	0.477	19.75	0.0090	4.56E-04	1.888	9.56E-02
6	149.418	149.416	0.374	7.75	0.0020	2.58E-04	0.535	6.90E-02
7	149.901	149.874	0.383	30.00	0.0273	9.10E-04	7.128	2.38E-01
8	149.480	149.481	0.237	31.25	–0.0010	–3.20E-05	–0.421	–1.35E-02
10	149.582	149.580	0.470	14.00	0.0017	1.21E-04	0.362	2.58E-02
11	149.680	149.667	0.367	53.00	0.0130	2.45E-04	3.542	6.68E-02
12	149.480	149.481	0.237	24.00	–0.0010	–4.17E-05	–0.421	–1.76E-02
13	149.262	149.258	0.306	17.50	0.0040	2.29E-04	1.308	7.48E-02
14	No flush data recorded							
15	149.604	149.598	0.506	2.00	0.0060	3.00E-03	1.186	5.93E-01
16	149.716	149.712	0.560	4.00	0.0040	1.00E-03	0.714	1.79E-01
18	149.760	149.740	0.505	22.00	0.0200	9.09E-04	3.958	1.80E-01
19	149.476	149.476	0.171	7.25	0.0000	0.00E+00	0.000	0.00E+00
20	149.874	149.866	0.270	11.75	0.0077	6.55E-04	2.855	2.43E-01
22	149.942	149.928	0.435	23.25	0.0143	6.15E-04	3.290	1.41E-01
26	Initial period not recorded.							

5. DISCUSSION

5.1 ANALYSIS OF OPTIMIZATION TECHNIQUES AND FORTRAN IMPLEMENTATION OF POTENTIAL MODELS

To determine the mechanism(s) controlling the mass transfer of CH_3I onto the silver-exchanged mordenite, the experimentally obtained data were compared against widely accepted models of adsorption behavior. The nine models chosen from the literature for use in this study were selected because the underlying assumptions which form the basis of their development were believed to be compatible with the structure and likely behavior of the mordenite material being studied. The potential models that were evaluated against the observed adsorption uptake curves were:

1. Shrinking core – gas film control
2. Shrinking core – ash layer diffusion control
3. Shrinking core – reaction control
4. Shrinking core – combined resistances
5. Volume reaction model
6. Micropore diffusion control
7. Macropore diffusion control
8. Combined micropore and macropore diffusion control
9. Nonisothermal micropore diffusion control

Each of the nine models from the literature, which are described in Chapter 2, were translated into appropriate FORTRAN code using Microsoft Corporation's Powerstation FORTRAN compiler, Version 1.0. In each case, the formulation of the model equations is such that given the appropriate rate-controlling parameters, the degree of conversion or a mass flux at a specific time can be directly or indirectly computed. The term "indirectly computed" means that the conversion cannot be directly computed but must be found by iteration or by some root-finding method. The best values for the rate-controlling parameters were determined by linear or multidimensional regression curve fitting techniques utilizing the experimentally obtained loading data as the reference. The following discussions will address the implementation of the models and the curve fitting techniques utilized to obtain the model parameters.

5.1.1 Selection of the Optimization Function

The fitting of the proposed models to the experimentally obtained data to determine the diffusion coefficients and other adjustable parameters obviously necessitated the use of some type of minimization function. The most obvious method available was to minimize the sum of the squares of the errors between the model and the data. This can be expressed as shown by Press et al. (1992a) as:

$$\text{minimize over } a_1 \ldots a_M\text{: } \sum_{i=1}^{N}\left[y_i - y\left(x_i; a_1 \ldots a_M\right)\right]^2, \tag{5.1}$$

where $y(x)$ is the proposed model with M adjustable parameters for the data set consisting of the N data points, (x_i, y_i).

There were several decisions to be made at the onset of the data analysis concerning the optimization process. The first issue was the choice between the use of the flux term or the conversion term in the optimization. The use of the conversion term was selected primarily because of the noise in the experimental data, especially at very low loading rates. In cases such as T18, the flux over a number of sample periods was recorded as zero as the weight gain over the time period was less than the sensitivity of the balance. During the next sample period the balance would indicate a weight gain of 0.001 g over a single 15-min period. This resulted in a "square wave" flux curve that was clearly an artifact of the low loading rates and the accuracy of the balance used for the weight determinations.

The approach chosen was to use the conversion or bed loading term which integrated the flux terms into a relatively smooth curve. Based on a few simple trials with simple models, this approach appeared to provide a steady and practical basis for the data analysis. An alternate approach to deal with this behavior was through the use of a moving data average in which the last "*n*" data points were averaged together and thus "smoothed" the data to a certain degree.

Once the conversion was selected as the basis of the minimization function, the second issue that needed to be resolved was whether to use the simple error or to in some way normalize or weight the error. One example of normalizing the error term would be to divide the error by the actual conversion observed as is described in Eq. (5.2).

$$\text{minimize over } a_1 \ldots a_M\text{: } \sum_{i=1}^{N}\left[\frac{y_i - y(x_i;a_1 \ldots a_M)}{y_i}\right]^2 \tag{5.2}$$

Normalizing the error in such a manner placed more emphasis on the early portion of the loading curve. For example, an absolute difference of 2% in the maximum equilibrium weight gain at the 10% conversion level is 20% normalized error but at the 50% conversion level it is only a 4% normalized error. A comparison of the coefficients determined by both methods for the four models associated with the shrinking core-type model is shown in Table 5.1 for data points 1 through 40 and in Table 5.2 for the full range of the data collected.

In many cases there was little difference between the computed values of the diffusion coefficients of either function being optimized (compare Figs. 5.1 and 5.2). However, in the case where the data and the model differ significantly, the normalizing function resulted in a significant different "optimum" value for the adjustable parameters and thus in the estimation of the conversion at longer time frames. This is very apparent in Figs. 5.3 and 5.4 for the case of predicted conversion curves for test T16 in which there is a significant difference in the "optimum" value for the determined diffusion coefficient.

Since the standard or simple form of the minimization function appeared to provide a better fit over the long time periods, the non-normalized least squares method based on conversion was selected as the method to be used throughout the balance of this study.

Table 5.1: Comparison of the simple sum of the square of the error in the conversion term vs the normalized sum of the square of the error optimization methods for the first 40 data points in each data set.

	Gas film				Ash diff				Rxn control			
	Simple		Normalized		Simple		Normalized		Simple		Normalized	
Run No.	k_g (cm/s)	Error[a]	k_g (cm/s)	Error	D_e (cm^2/s)	Error	D_e (cm^2/s)	Error	k_s (cm/s)	Error	k_s (cm/s)	Error
T3	1.69E-01	1.65E-01	1.86E-01	4.84E+00	1.06E-03	2.88E-03	1.09E-03	1.04E-01	1.96E-01	1.26E-01	2.19E-01	3.92E+00
T6	1.76E-01	1.17E-01	1.95E-01	3.98E+00	1.09E-03	3.04E-03	1.06E-03	1.54E-01	2.04E-01	8.33E-02	2.28E-01	3.11E+00
T7	1.76E-01	8.12E-02	1.89E-01	6.75E+00	9.91E-04	1.45E-02	1.08E-03	1.29E+00	1.89E-01	7.56E-02	2.03E-01	6.35E+00
T8	6.94E-02	7.75E-02	7.40E-02	7.01E+00	1.84E-04	1.75E-02	1.99E-04	1.70E+00	7.39E-02	7.31E-02	7.90E-02	6.64E+00
T10	2.07E-01	1.57E-04	2.07E-01	1.40E-03	1.37E-03	1.28E-03	1.36E-03	1.15E-02	2.36E-01	2.76E-06	2.36E-01	2.45E-05
T11	1.33E-01	1.17E-01	1.46E-01	4.99E+00	6.66E-04	3.22E-03	7.02E-04	2.16E-01	1.50E-01	9.56E-02	1.66E-01	4.27E+00
T12	6.41E-02	7.52E-03	6.55E-02	5.27E+00	7.19E-05	1.27E-03	8.50E-06	2.26E+01	6.58E-02	7.23E-03	6.69E-02	5.21E+00
T13	7.23E-02	4.64E-04	7.29E-02	2.54E-02	1.81E-04	4.22E-04	1.78E-04	2.31E-02	7.62E-02	3.14E-04	7.67E-02	1.71E-02
T14	3.11E-01	3.06E-02	3.41E-01	5.04E+00	7.36E-04	1.81E-03	7.79E-04	4.79E-01	3.29E-01	2.80E-02	3.63E-01	4.71E+00
T15	3.45E-02	2.22E-03	3.21E-02	3.28E+00	3.07E-05	7.07E-03	1.74E-05	3.12E+00	3.52E-02	2.31E-03	3.26E-02	3.28E+00
T16	8.83E-02	1.50E-02	9.73E-02	2.02E+00	2.66E-04	5.65E-03	1.20E-04	8.05E+00	9.49E-02	1.18E-02	1.04E-01	1.68E+00
T18	5.73E-02	2.45E-04	5.26E-02	5.27E-01	7.13E-05	9.53E-03	1.19E-05	1.32E+01	5.90E-02	3.18E-04	5.33E-02	6.08E-01
T19	1.14E-01	6.12E-02	1.27E-01	3.36E+00	5.08E-04	1.60E-04	5.07E-04	2.71E-02	1.27E-01	4.93E-02	1.42E-01	2.83E+00
T20	3.35E-01	1.08E-01	3.72E-01	3.78E+00	3.91E-03	1.45E-03	3.67E-03	1.75E-01	3.87E-01	7.60E-02	4.35E-01	2.89E+00
T22	1.83E-01	8.57E-02	2.02E-01	4.96E+00	1.50E-03	2.56E-03	1.58E-03	1.71E-01	2.03E-01	7.24E-02	2.25E-01	4.35E+00
T26	1.70E-01	1.94E-01	1.81E-01	7.12E+00	7.41E-04	4.07E-02	8.07E-04	1.50E+00	1.89E-01	1.76E-01	2.02E-01	6.52E+00
Total errors		1.06E+00		6.30E+01		1.13E-01		5.28E+01		8.77E-01		5.64E+01

Table 5.1. (continued).

Full shrinking core								
	Simple				Normalized			
Run No.	k_g (cm/s)	D_e (cm^2/s)	k_s (cm/s)	Error	k_g (cm/s)	D_e (cm^2/s)	k_s (cm/s)	Error
T3	9.90E+99	1.06E-03	1.83E+13	2.88E-03	9.90E+99	1.09E-03	7.60E+14	1.04E-01
T6	9.90E+99	1.19E-03	2.73E+00	2.59E-03	9.90E+99	1.06E-03	5.01E+13	1.54E-01
T7	9.90E+99	9.91E-04	9.64E+99	1.45E-02	9.90E+99	1.08E-03	2.00E+15	1.29E+00
T8	9.90E+99	1.84E-04	5.03E+13	1.75E-02	2.25E+21	1.99E-04	5.28E+05	1.70E+00
T10	9.90E+99	1.28E-01	2.38E-01	2.22E-06	9.90E+99	1.36E-01	2.38E-01	2.03E-05
T11	9.90E+99	6.66E-04	9.26E+13	3.22E-03	9.90E+99	7.02E-04	6.40E+13	2.16E-01
T12	9.90E+99	7.19E-05	1.63E+11	1.27E-03	4.86E+10	6.98E-04	7.33E-02	5.11E+00
T13	9.90E+99	5.83E-04	1.11E-01	1.18E-05	9.90E+99	5.83E-04	1.11E-01	6.40E-04
T14	9.90E+99	7.36E-04	3.97E+13	1.81E-03	9.90E+99	7.79E-04	1.31E+15	4.79E-01
T15	2.04E+14	7.84E+10	3.52E-02	2.31E-03	4.35E+12	1.58E-01	3.26E-02	3.28E+00
T16	9.90E+99	4.80E-04	2.27E-01	9.30E-04	9.90E+99	7.32E-04	1.60E-01	7.00E-01
T18	9.95E+13	2.58E+11	5.90E-02	3.18E-04	5.26E-02	7.11E+01	2.44E+04	5.27E-01
T19	9.90E+99	5.08E-04	6.11E+06	1.60E-04	9.90E+99	5.36E-04	3.48E+00	1.98E-02
T20	9.90E+99	4.52E-03	3.15E+00	1.50E-04	9.90E+99	4.62E-03	2.81E+00	1.26E-02
T22	9.90E+99	1.50E-03	6.98E+13	2.56E-03	9.90E+99	1.58E-03	1.69E+15	1.71E-01
T26	9.90E+99	7.41E-04	1.53E+13	4.07E-02	9.90E+99	8.07E-04	2.02E+13	1.50E+00
Total errors				9.09E-02				1.53E+01

[a]Error terms are the resultant sum of the square of the error between the experimental data and the proposed model.

Table 5.2: Comparison of the simple sum of the square of the error in the conversion term vs the normalized sum of the square of the error optimization methods for the full data sets.

	Gas film				Ash diff				Rxn control			
	Simple		Normalized		Simple		Normalized		Simple		Normalized	
Run No.	k_g (cm/s)	Error[a]	k_g (cm/s)	Error	D_e (cm^2/s)	Error	D_e (cm^2/s)	Error	k_s (cm/s)	Error	k_s (cm/s)	Error
T3	7.44E-02	2.46E+00	8.21E-02	2.18E+01	1.05E-03	6.89E-03	1.06E-03	1.28E-01	1.05E-01	1.16E+00	1.22E-01	1.28E+01
T6	7.76E-02	3.44E+00	8.59E-02	2.33E+01	1.33E-03	4.52E-02	1.25E-03	5.47E-01	1.20E-01	1.16E+00	1.41E-01	1.05E+01
T7	1.14E-01	1.74E-01	1.20E-01	1.17E+01	1.70E-03	6.41E-01	1.24E-03	6.05E+00	1.36E-01	1.76E-01	1.39E-01	1.02E+01
T8	4.20E-02	1.93E-01	4.38E-02	1.33E+01	3.17E-04	8.44E-01	2.24E-04	7.98E+00	5.00E-02	2.27E-01	5.06E-02	1.17E+01
T10	1.13E-01	4.56E+00	1.22E-01	1.14E+01	2.75E-03	4.73E-01	2.39E-03	2.04E+00	2.08E-01	1.85E-01	2.17E-01	3.66E-01
T11	8.33E-02	5.30E-01	9.21E-02	1.14E+01	6.85E-04	4.50E-03	6.93E-04	2.24E-01	1.01E-01	3.49E-01	1.14E-01	8.55E+00
T12	4.74E-02	2.30E-02	5.02E-02	7.70E+00	1.87E-04	1.91E-01	3.61E-05	8.19E+01	5.20E-02	1.43E-02	5.43E-02	6.70E+00
T13	5.52E-02	3.94E-02	5.68E-02	1.19E+00	4.85E-04	9.70E-01	3.16E-04	8.67E+00	6.76E-02	6.93E-02	6.62E-02	7.90E-01
T14	1.61E-01	3.17E-01	1.78E-01	1.65E+01	9.94E-04	8.08E-02	8.93E-04	1.53E+00	1.86E-01	2.03E-01	2.07E-01	1.30E+01
T15	4.82E-02	2.55E-02	4.22E-02	8.90E+00	3.32E-04	1.19E+00	4.44E-05	6.65E+01	5.67E-02	9.42E-02	4.44E-02	1.22E+01
T16	5.80E-02	4.39E-01	6.41E-02	8.68E+00	6.59E-04	6.81E-01	2.96E-04	3.02E+01	7.63E-02	6.20E-02	8.23E-02	3.69E+00
T18	5.08E-02	3.32E-02	5.23E-02	9.29E-01	3.10E-04	4.93E-01	3.69E-05	8.53E+01	5.87E-02	2.43E-03	5.74E-02	9.23E-01
T19	1.14E-01	6.12E-02	1.27E-01	3.36E+00	5.08E-04	1.60E-04	5.07E-04	2.71E-02	1.27E-01	4.93E-02	1.42E-01	2.83E+00
T20	2.87E-01	2.11E-01	3.19E-01	5.46E+00	3.88E-03	1.87E-03	3.70E-03	1.80E-01	3.40E-01	1.44E-01	3.84E-01	4.05E+00
T22	9.21E-02	1.05E+00	1.02E-01	1.74E+01	2.16E-03	2.98E-01	1.87E-03	1.73E+00	1.23E-01	3.89E-01	1.37E-01	1.05E+01
T26	7.36E-02	9.91E-01	8.01E-02	2.18E+01	5.08E-04	9.40E-02	5.51E-04	2.91E+00	8.67E-02	7.95E-01	9.59E-02	1.83E+01
Total errors		1.46E+01		1.85E+02		6.01E+00		2.96E+02		5.08E+00		1.27E+02

Table 5.2. (continued).

Full shrinking core								
	Simple				Normalized			
Run No.	k_g (cm/s)	D_e (cm^2/s)	k_s (cm/s)	Error	k_g (cm/s)	D_e (cm^2/s)	k_s (cm/s)	Error
T3	9.90E+99	1.05E-03	1.02E+06	6.89E-03	9.90E+99	1.06E-03	2.33E+12	1.28E-01
T6	9.90E+99	1.56E-03	8.42E-01	1.73E-02	9.90E+99	1.41E-03	1.55E+00	3.66E-01
T7	9.18E+99	4.72E+11	1.36E-01	1.76E-01	9.90E+99	1.24E-03	2.82E+04	6.05E+00
T8	9.20E+99	4.74E+11	5.00E-02	2.27E-01	9.90E+99	2.26E-04	6.47E+00	7.98E+00
T10	9.90E+99	8.86E-03	2.99E-01	3.13E-02	9.90E+99	1.09E-02	2.77E-01	5.57E-02
T11	9.90E+99	6.85E-04	1.36E+06	4.50E-03	9.90E+99	6.93E-04	6.97E+99	2.24E-01
T12	9.90E+99	3.01E-03	5.59E-02	1.27E-02	2.17E+11	8.23E-04	6.72E-02	5.65E+00
T13	9.64E+99	4.22E+12	6.76E-02	6.93E-02	9.67E+99	1.80E+11	6.62E-02	7.90E-01
T14	9.90E+99	1.66E-03	4.95E-01	3.26E-02	9.90E+99	9.23E-04	8.29E+00	1.52E+00
T15	9.89E+99	9.13E+12	5.67E-02	9.42E-02	9.25E+99	2.11E+10	4.44E-02	1.22E+01
T16	9.90E+99	4.12E-03	9.24E-02	1.97E-02	9.90E+99	1.65E-03	1.24E-01	1.39E+00
T18	9.90E+99	1.35E-02	6.03E-02	1.87E-03	1.00E-01	4.42E+01	1.21E-01	7.52E-01
T19	9.90E+99	5.08E-04	6.11E+06	1.60E-04	9.90E+99	5.36E-04	3.48E+00	1.98E-02
T20	9.90E+99	4.19E-03	5.05E+00	1.21E-03	9.90E+99	4.47E-03	3.05E+00	2.38E-02
T22	9.90E+99	4.38E-03	2.54E-01	9.79E-02	9.90E+99	2.09E-03	1.72E+00	1.57E+00
T26	9.90E+99	5.08E-04	2.07E+13	9.40E-02	9.90E+99	5.51E-04	1.43E+15	2.91E+00
Total errors				8.87E-01				4.16E+01

[a]Error terms are the resultant sum of the square of the error between the experimental data and the proposed model.

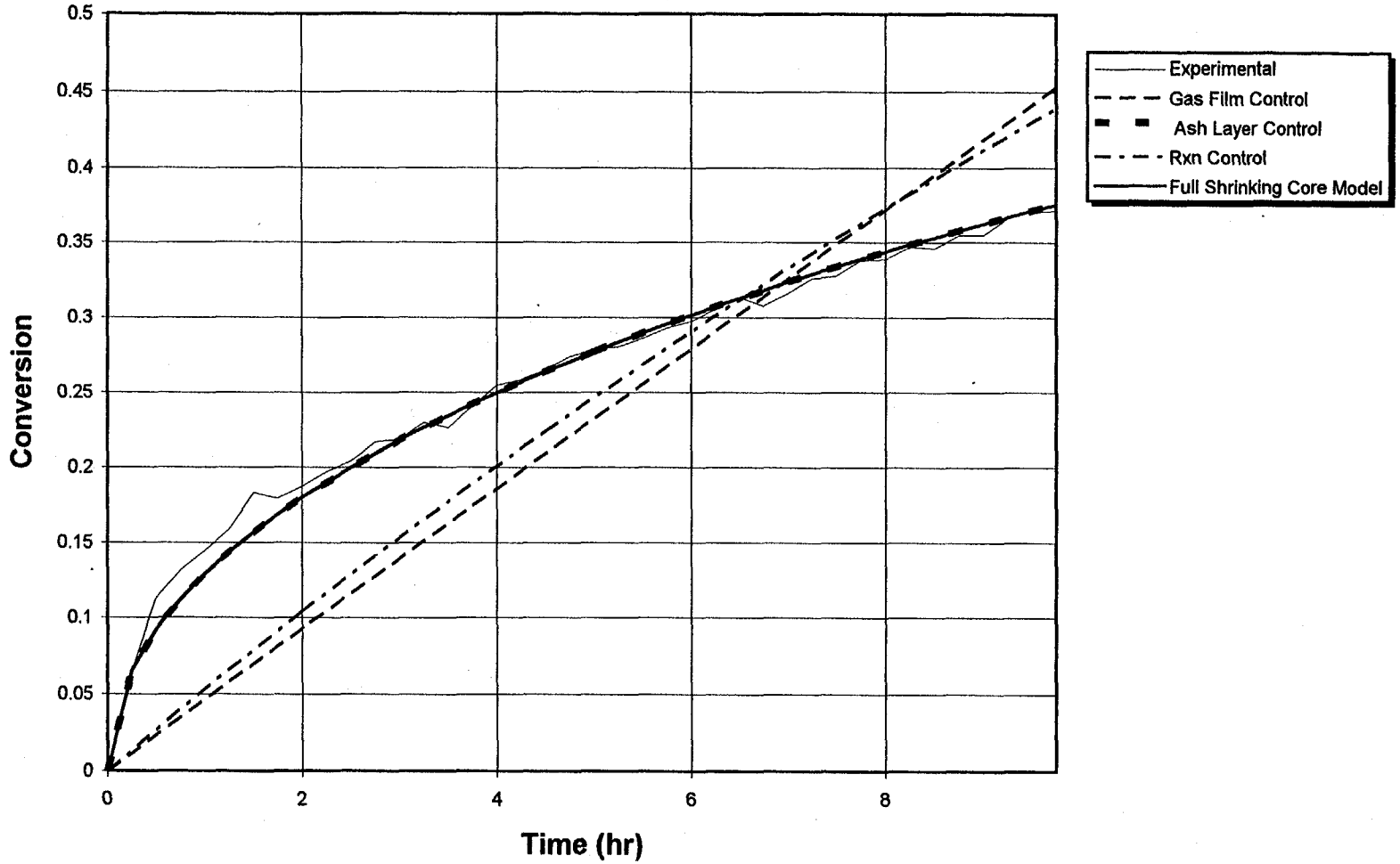

Figure 5.1. Shrinking core model for Test T3 optimized based on simple sum of the squares of the error for data points 1–40.

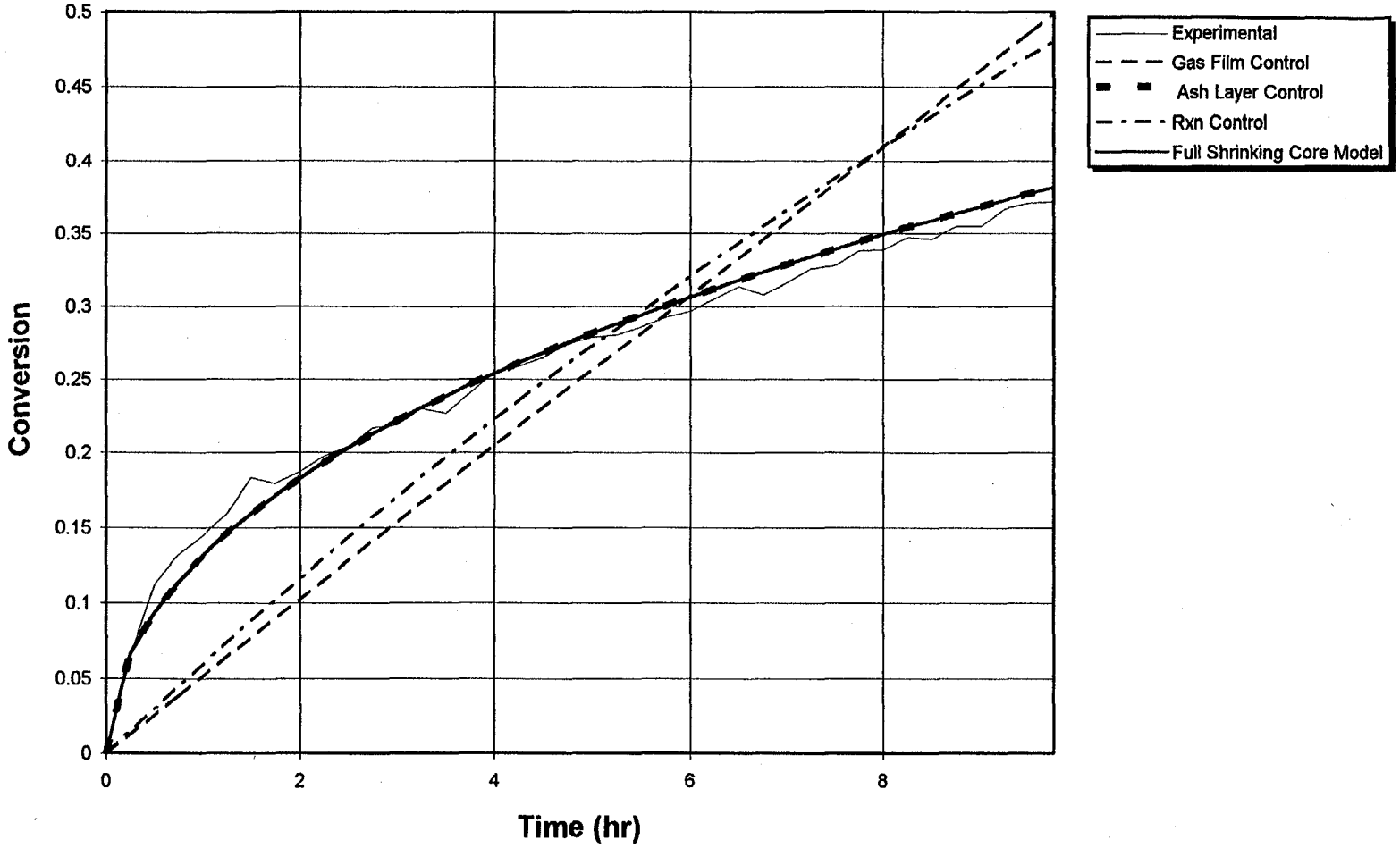

Figure 5.2. Shrinking core model for Test T3 optimized based on normalized sum of the squares of the error for data points 1–40.

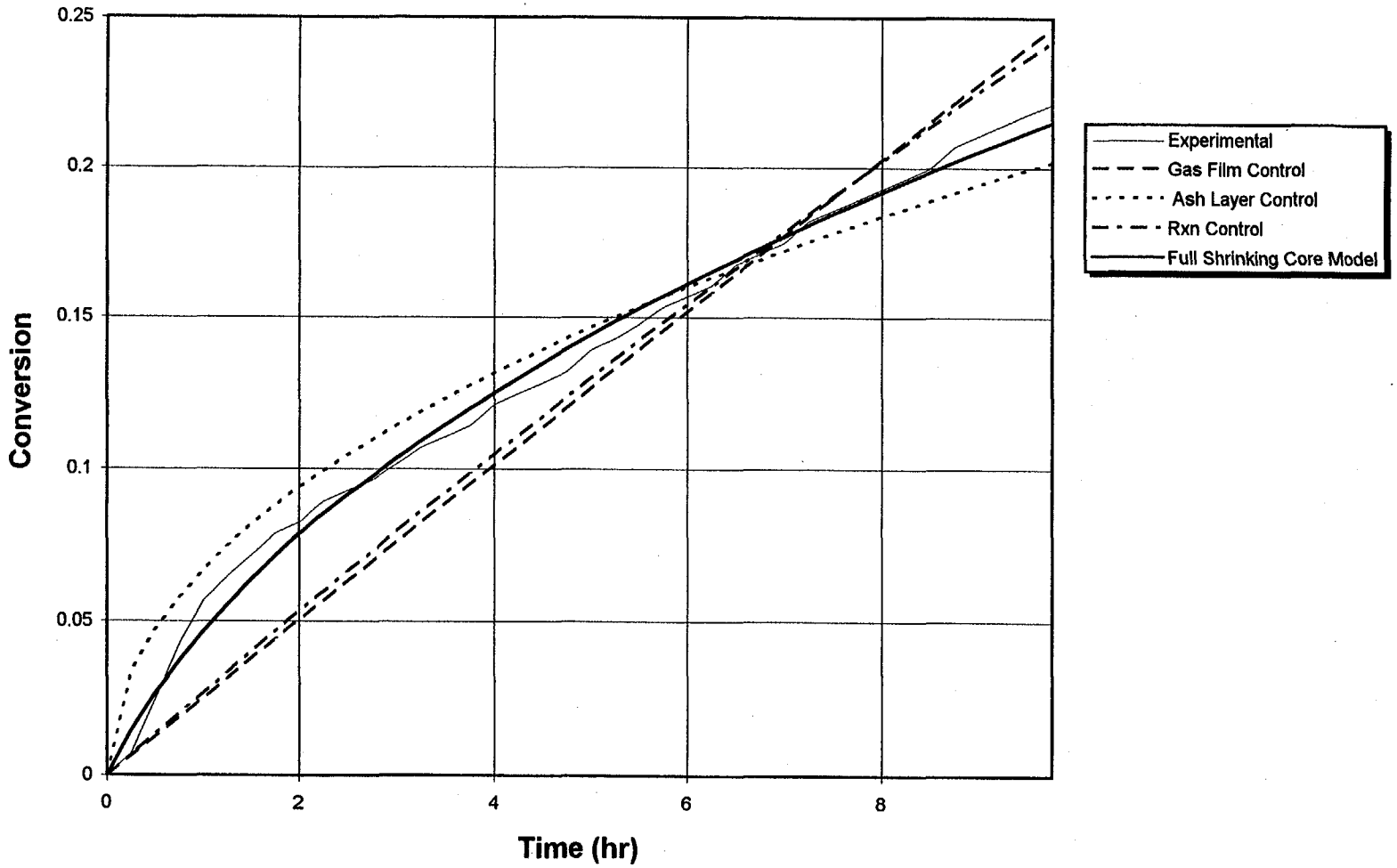

Figure 5.3. Shrinking core model for Test T16 optimized based on simple sum of the squares of the error for data points 1–40.

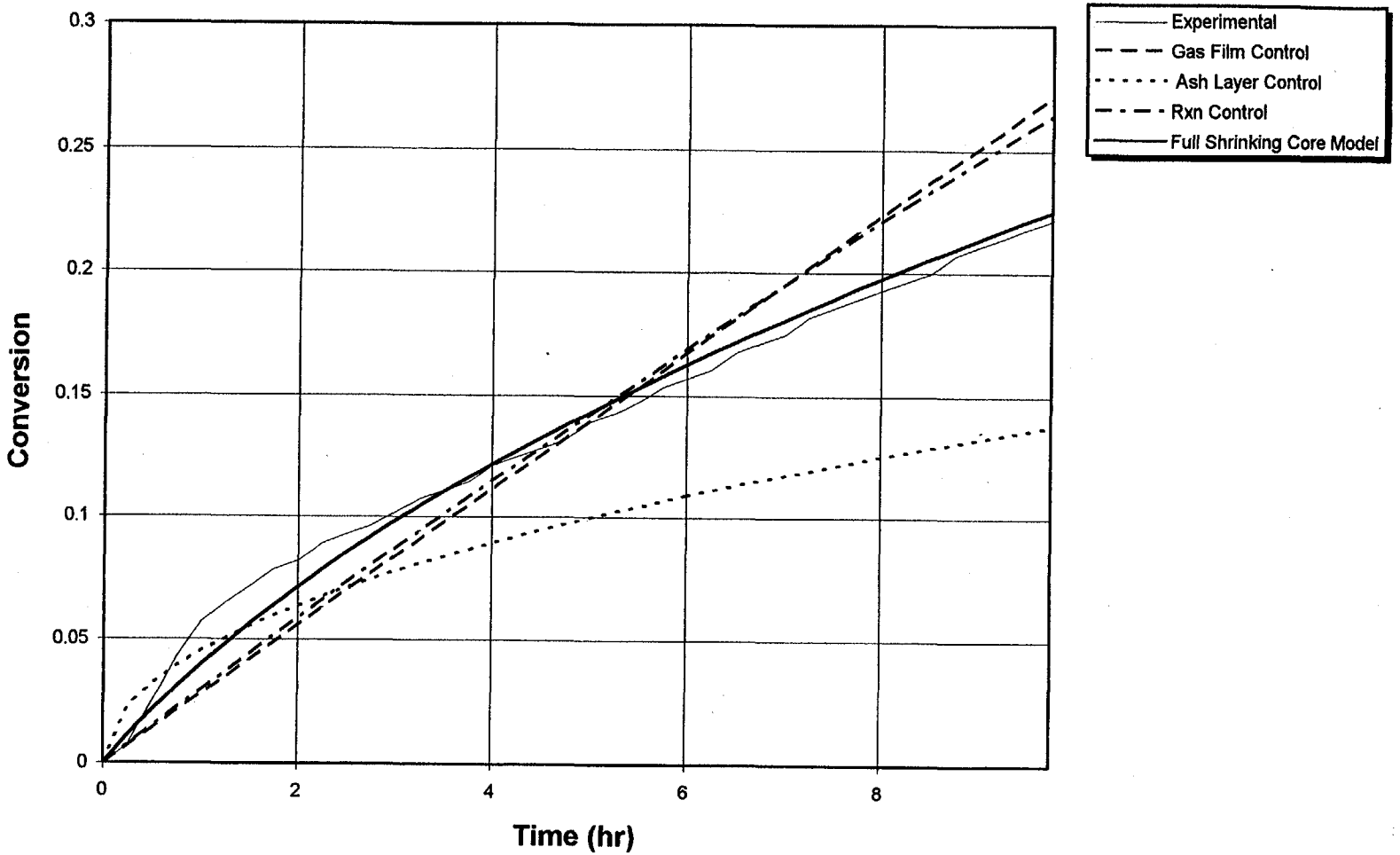

Figure 5.4. Shrinking core model for Test T16 optimized based on normalized sum of the squares of the error for data points 1–40.

5.1.2 Minimization Routines

Two classes of data fitting models were employed in this study. The first, and by far the simplest, was the single parameter model. In this case, it was a relatively simple matter to find the minimum using any of a variety of minimization techniques. The FORTRAN function FMIN described by Forsythe et al. (1977) was used for all single parameter models. This function used a combination of a golden section search technique and successive parabolic interpolation. This provided a very robust function not requiring the determination of derivatives. This was virtually the same as the "Brent" method described by Press et al. (1992a).

As was apparent from the discussion of the proposed models, several of these models required multidimensional minimization to extract the relevant parameters. These models included the full shrinking core, the bimodal, the nonisothermal, the micropore, and the volume reaction model. The determination of "best fit" to the experimental data in the case of a multiparameter model was significantly more complex. Press et al. (1992a), in discussing multidimensional minimization, indicated that this generally required some combination of the following: (1) evaluation of the derivative of the function being minimized, (2) large amounts of computing time, and (3) potentially large storage arrays. Vaidyanathan (1971) utilized the so-called flexible "simplex" method to fit the bimodal model to his data. He pointed out that the technique used in his work suffered from slow convergence and that the determined minimum was subject to the starting point of the search. This "simplex" approach was also discussed by Press et al. (1992a), and they indicated that this "method just crawls downhill ...without making any assumptions about

your function. This can be extremely slow, but it can also, in some cases, be extremely robust." They go on, however, to recommend the POWELL method as being faster in most cases and state that it can be used when derivatives are not easy to calculate. This method was also recommended for consideration even when derivatives can be calculated. Based on this recommendation, the POWELL method was selected and the implementing FORTRAN function and the other functions it relies on were all obtained from the software library available from Press et al. (1992b). The only functional modification to the library functions was the conversion to double precision.

Figure 5.5 provides a logic flow chart for the BIMODAL Plus FORTRAN code used in this analysis.

5.1.3 Limitations on FORTRAN Implementation of Models

The bimodal model and the nonisothermal models required the determination of a large number of roots to specific transcendental equations. The bisection technique was used to determine the root of such an equation once a specific root has been bounded. This method assumed, however, that the root was, in fact, bracketed. In the case of bimodal model, the roots to the transcendental Eq. (2.64) were required. The roots to this equation were bracketed by $(n-1)\pi$ and $n\pi$. The FORTRAN function RTBIS described by Press et al. (1992a) was used to find the roots. However, due to computational limitations, roots could not be found closer than $\pm 5 \times 10^{-9}\pi$ to $n\pi$. Once this limit was reached, all further roots were considered to be $n\pi$.

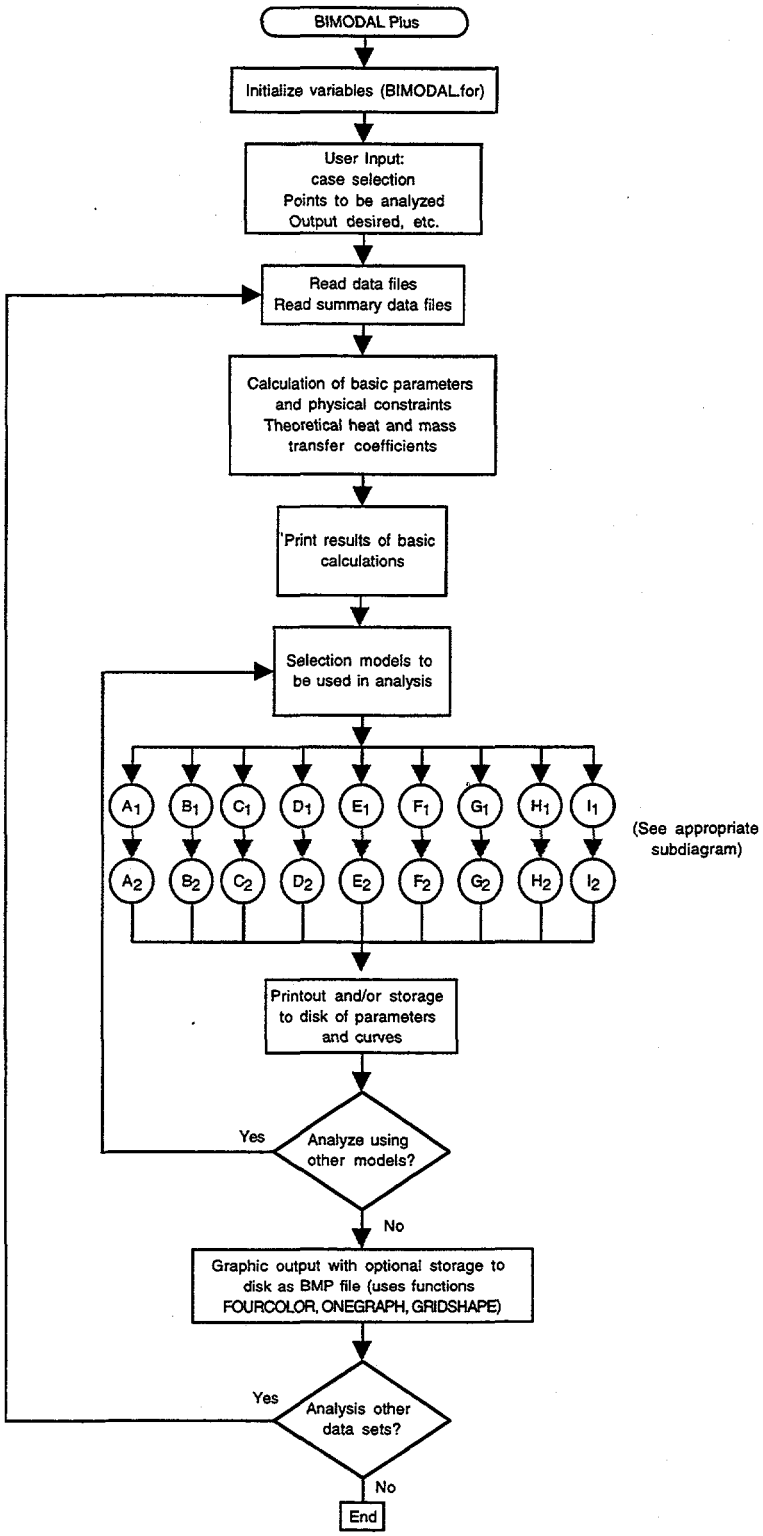

Figure 5.5. Flow chart to BIMODAL Plus FORTRAN code for fitting model parameters to experimentally obtained loading curves.

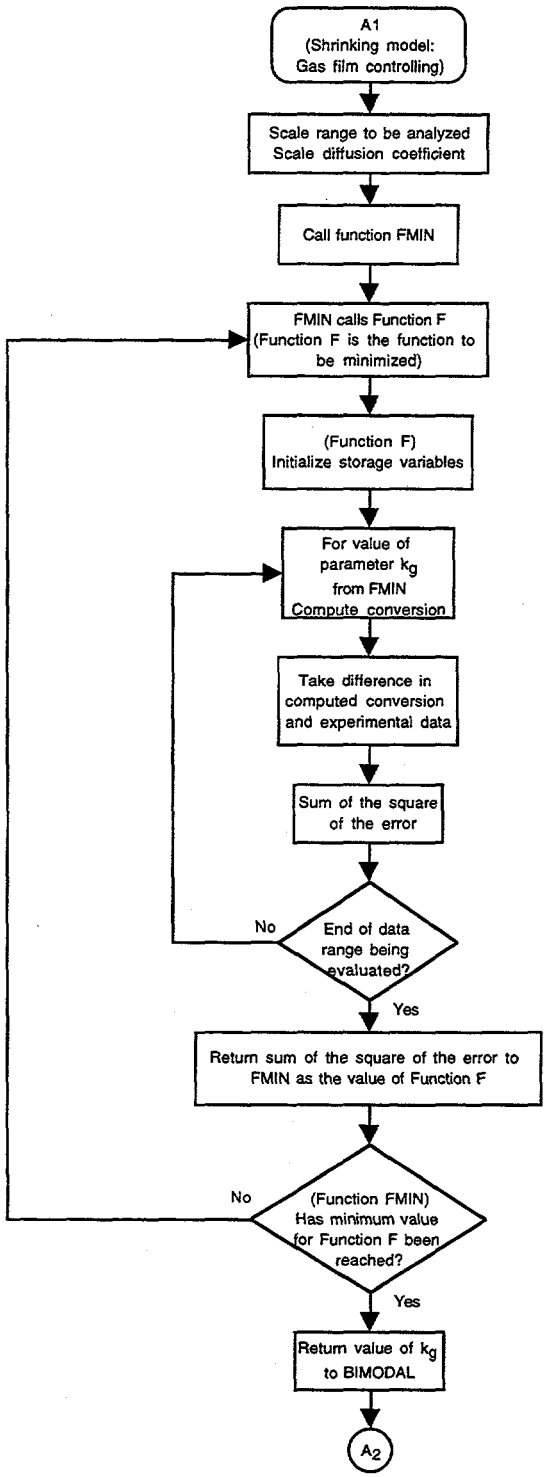

Figure 5.5. (continued).

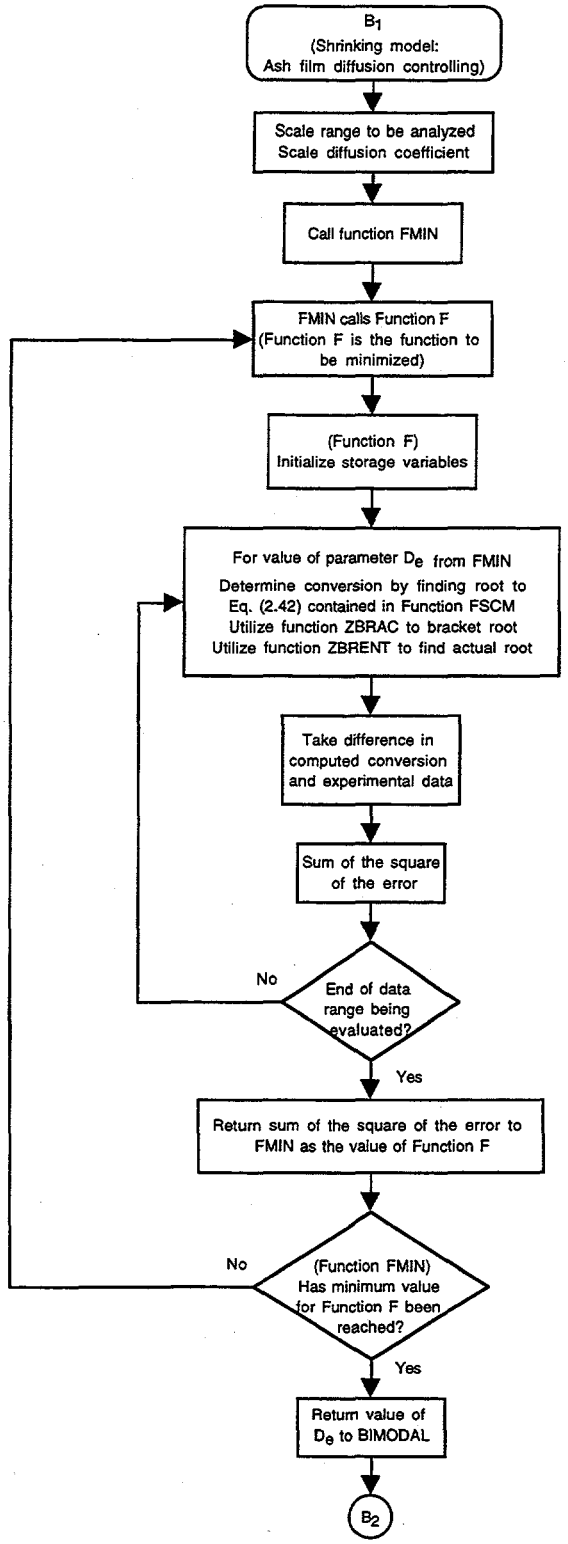

Figure 5.5. (continued).

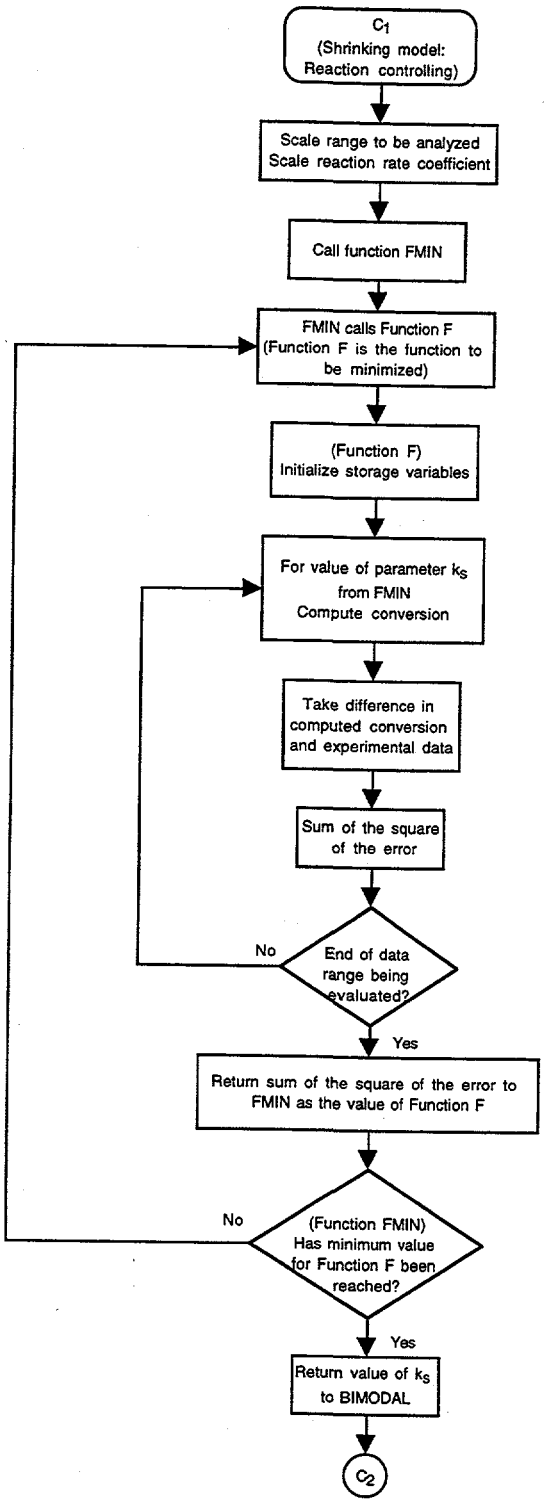

Figure 5.5. (continued).

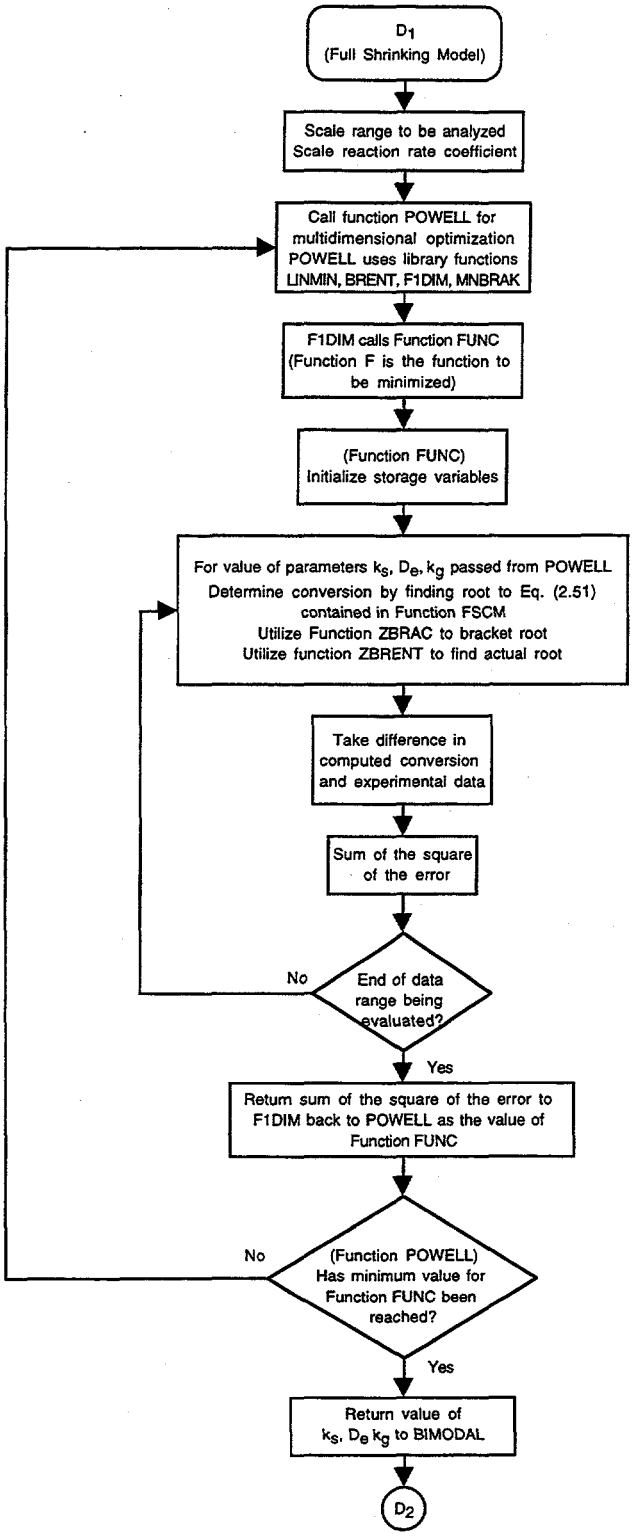

Figure 5.5. (continued).

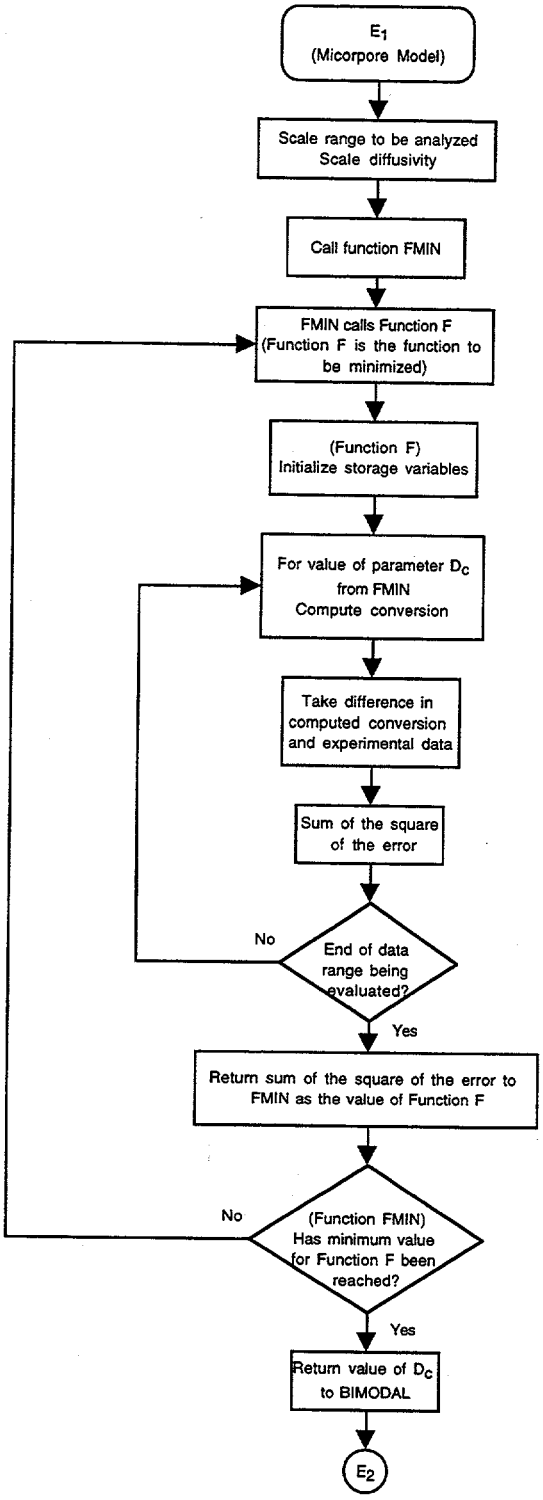

Figure 5.5. (continued).

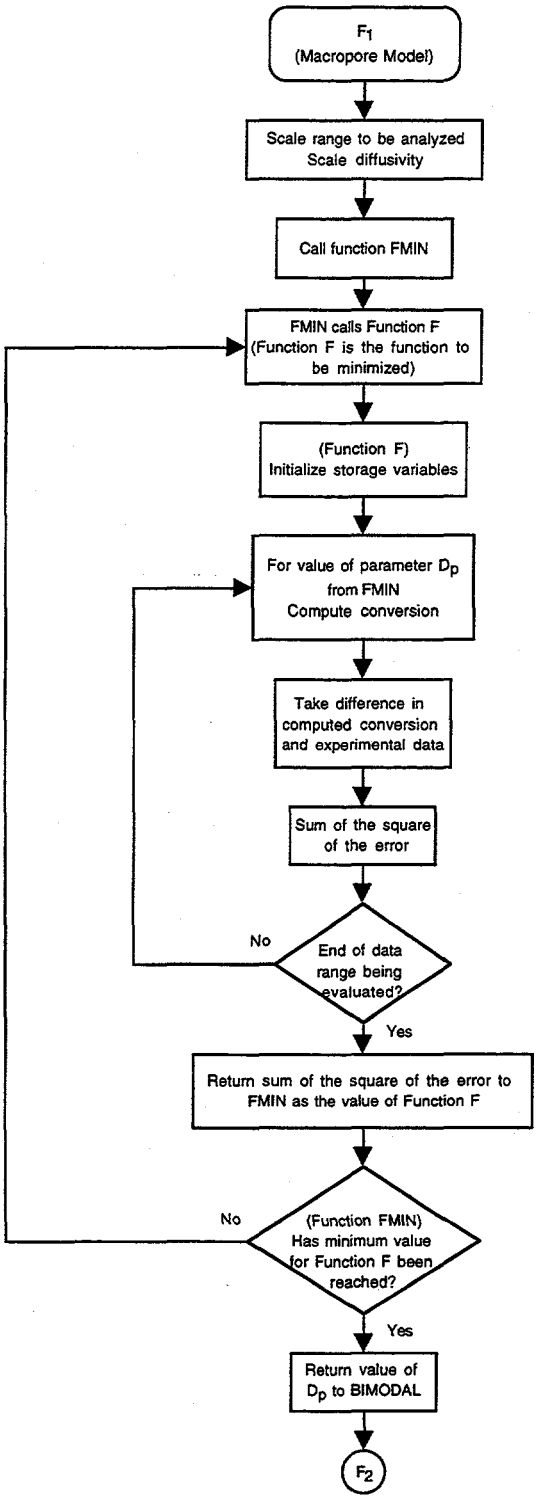

Figure 5.5. (continued).

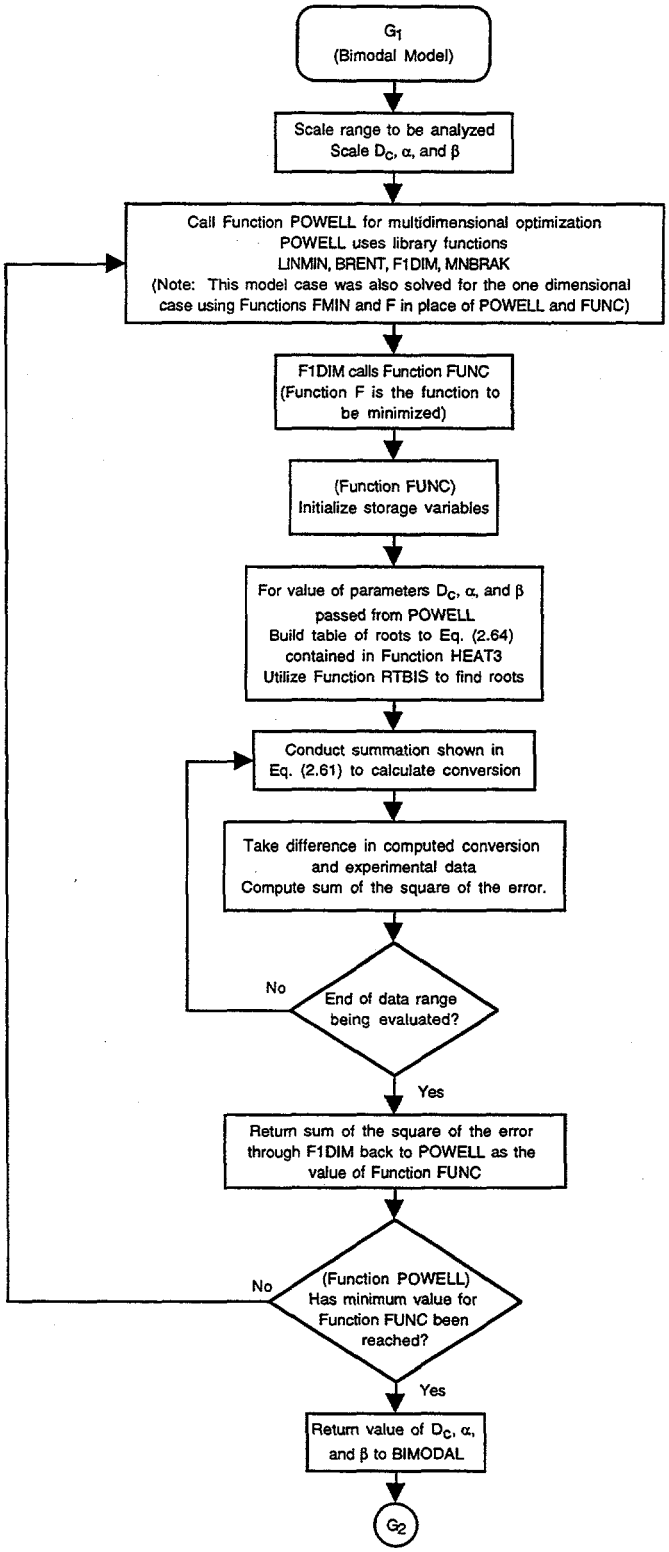

Figure 5.5. (continued).

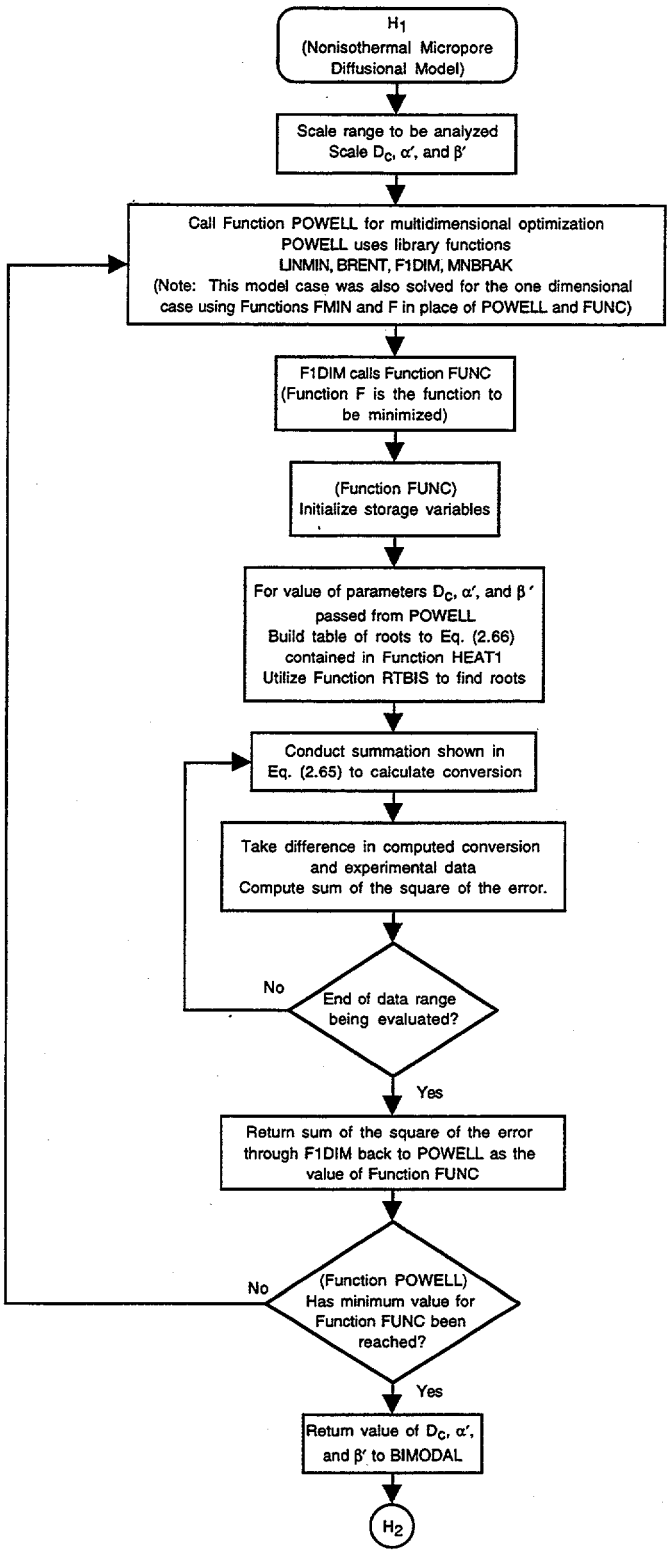

Figure 5.5. (continued).

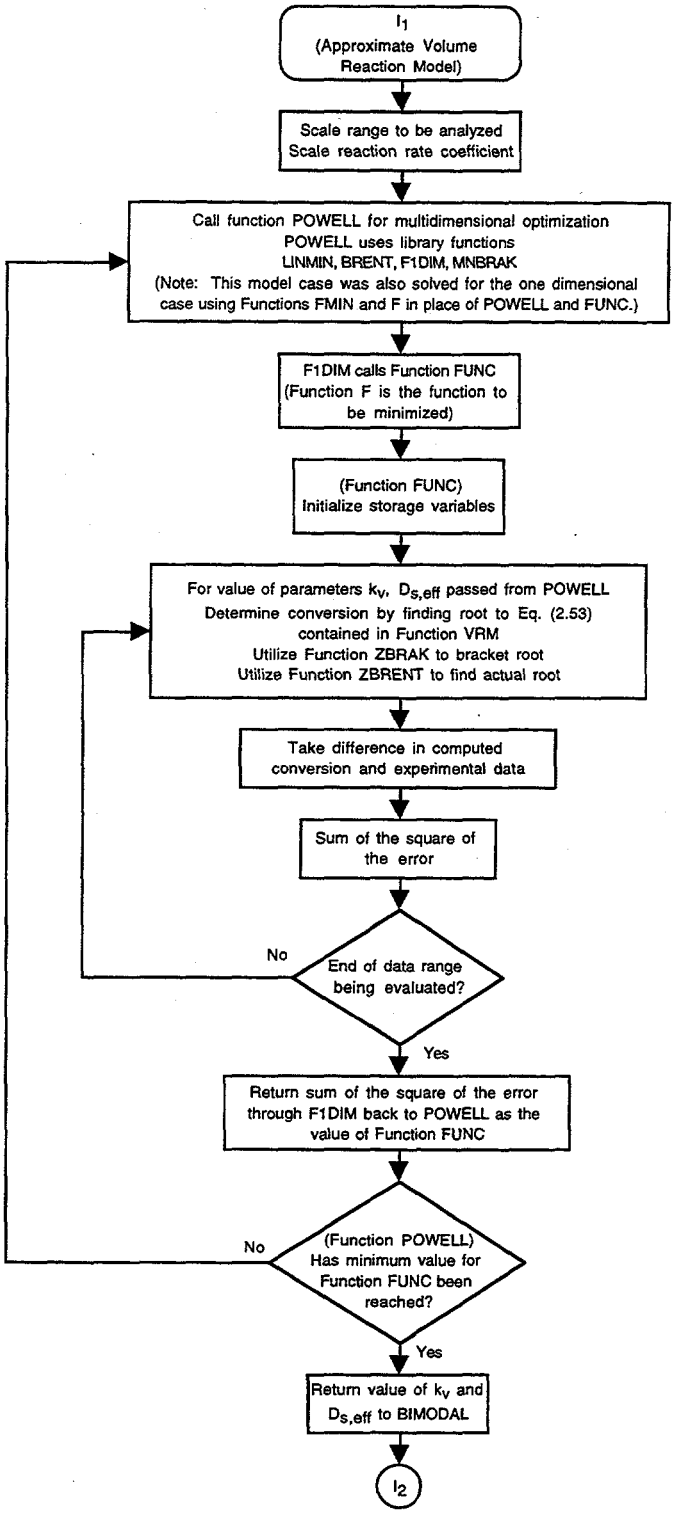

Figure 5.5. (continued).

A value of 1×10^{-7} was selected for the convergence tolerances for use with the single-dimensional least square minimization routine, FMIN, and the multidimensional routine, POWELL, which internally used a routine similar to FMIN. This value is related to the uncertainty interval of the result returned by the minimization function, which is to say that results returned by the function had significance down to about the 7^{th} decimal place. However, it was also necessary to scale the adjustable parameters such that the manipulated value was in the range of approximately 10^{+6} down to 10^{-3}. By proper selection of scaling factors, the result returned from the optimization routine had at least 3 to 4 significant figures and in most cases, 7 or more, which considering the uncertainties associated with the data implied far more certainty or significance than actually exists. Only three figures are shown in any derived parameter. Table 5.3 summarizes the scaling factors used in the optimization routines.

Where required, the initial search ranges for the various parameters were selected from literature values or from preliminary hand calculations done to determine the magnitude of the specific term. In all cases, a broad range was identified around the probable value to avoid an artificial constraint on the "optimized" values.

5.1.4 Adaptive Strategies

There were two primary challenges in performing the multidimensional optimizations. The first was the selection of initial search conditions such that the problem was mathematically bounded, and the second was reaching the convergence point in a reasonable amount of computer time.

Table 5.3: Scaling factors and initial search values used in minimization routines within the BIMODAL Plus FORTRAN code for optimization of diffusion parameters for the selected diffusion models.

Model	Scaling factor	Range[a]	Expected value	Value of internal adjustable working parameter at tolerance
Shrinking core				
Gas film (k_g)	10^5	10^{-10} to 10^6	10^{-2}	10^{+3}
Diffusion (D_e)	10^5	10^{-10} to calc[b]	10^{-4}	10^{+1}
Reaction (k_s)	10^5	10^{-10} to 10^6	10^{-2}	10^{+3}
Volume reaction				
Diffusion ($D_{s,eff}$)	10^7		10^{-4}	10^{+1}
Reaction (k_v)	10^3		10^{-2}	10^{+3}
Micropore (D_c)	10^{20}	10^{-1} to 10^8	10^{-14}	10^{+6}
Macropore (D_p)	10^{10}	10^{-4} to 10^4	10^{-9}	10^{+1}
Bimodal				
D_c	10^{10}		10^{-14}	10^{-4}
α	1		10^{-3} to 10^{+3}	10^{-3} to 10^{+3}
β	1		10^{-3} to 10^{+3}	10^{-3} to 10^{+3}
Nonisothermal				
D_c	10^{10}		10^{-14}	10^{-4}
α'	1		10^{-3} to 10^{+3}	10^{-3} to 10^{+3}
β'	C_p			

[a]Range is required only for single-dimensional optimization; starting guess is required for multidimensional optimization.

[b]Calculated from maximum conversion in data set.

Several of the models contain single or double summation expressions. Since these summation operations must be repeated for every time step and for every iteration in the optimization process, it was highly beneficial to terminate this process once the contribution of additional terms was less than a set value. The criteria for termination of the summation loops was typically set to terminate if the last term added to the summation was less than 1×10^{-6} of the sum to that point. In all cases where double summations were required at least ten terms were summed in the 'x' direction (interior summation) and five terms in the 'y' direction (outside summation).

In the case of the bimodal model, which utilized a double summation, a very large array containing roots to the transcendental equation was required to provide reasonable assurance that the summation would not be terminated prematurely. To provide this assurance, an array of approximately 50,000 elements was required or an array 800×60. The general trend that was observed while working with this model was that if the required "x" dimension was large, then the "y" dimension was small, and vise versa. In a specific case, the exact number of required rows or columns was determined by the model parameters being used for the given iteration. Once a near optimum value was obtained for the parameters (i.e., the parameters were changing less than 5% per iteration), it was noted that the array element used in the summation became fixed. Based on this observation it was possible to tailor or adapt the number of roots that were to be calculated for the next iteration based on the previous iteration's requirements. The root-finding portion of the next iteration needed only to calculate the number of roots required to fill that portion of the "root" array that would be used in the subsequent summation process. A small number of additional roots were calculated in each direction to provide assurance that in all cases sufficient roots existed for the summation process even with small variations in the parameters with each successive iteration. In other words, if the maximum "x," (X_{max}), and maximum "y," (Y_{max}), array position used in the n–1 iteration were 50 and 10 respectively, then for the n^{th} iteration, only roots for "x" values up to X_{max} + 50 or 100 terms and "y" up to Y_{max} + 5 or 15 terms were calculated. This allowed the array of roots to grow up to the maximum array size of 800 by 200 or shrink to the

smallest size possible and minimize the computational time requirements. This significantly reduced the computational time once the search routines had narrowed the search and allowed the use of smaller arrays in the initial bounding searches for the adjustable parameters.

5.2 CH_3I ADSORPTION–MODEL COMPARISONS

5.2.1 General Model Requirements and Analysis Methodology

In the identification of a model to describe the adsorption of CH_3I onto silver-exchanged mordenite it was required that certain general observations be accounted for by the selected model. These were:

1. The possible formation of a rapidly shrinking shell of reacted material as observed in Figs. 4.10 to 4.12. Noting, of course, that the unreacted core was no longer visible once 30 to 50 % conversion was achieved.

2. Fairly uniform iodine loading across the pellet diameter at 30 to 40% conversion of silver or greater, as noted in Sect. 4.1.1.

3. Observation from past studies that higher loading was achieved prior to breakthrough with increased operation temperature.

4. Observation from past studies that lower loading was achieved prior to breakthrough with very low water vapor content in the feed gas stream.

Based on preliminary analysis using simple adsorption models and visual observations of the uptake curves, it became clear that the system was more complex than those described by the simple models. It was also observed in comparing Tables 5.1 and 5.2, where there was some variation in the computed values of the adjustable parameters depending on the period of time considered in the evaluation. One possibility that was

considered during the preliminary analysis of the data was the impact of the reported decrease in loading capacity of silver mordenite following extended exposure to air at elevated temperature. Long-term exposure, as reported by Thomas et al. (1977), was times of more than 16 to 64 h. If this was the case, it was hypothesized that there might be some type of oxidation of the silver taking place and thus affecting either the number of silver sites available or a change in the reaction mechanisms involved. As a result of this possibility the preliminary analysis process focused primarily on the first 40 data points or 10 h of loading. It should, however, be noted that the behavior observed by Thomas et al. was for AgZ and not for Ag°Z.

Following this initial scoping analysis with simple models, two directions were taken. The first was to obtain additional data focused on providing information on specific CH_3I uptake responses to an expanded range of process condition variations. These were discussed in Sect. 3.2.1 as the supplemental tests. The second direction was to expand the range of models used to analyze the data and to explore alternate explanations of the observed CH_3I uptake behavior.

Two alternate explanations for the observed behavior were recognized. The first of these was that a two-step process could, in some cases, account for the apparent shift in the values of the simple model parameters in the long time periods. One such two-step model is described as one of the limiting cases for the bimodal model put forth by Vaidyanathan (1971) and expanded by others. Such a model provides for the rapid

attainment of an initial "equilibrium" loading that is followed by a slower approach to the final equilibrium loading.

The second of the alternate explanations was that some perturbations in the recorded loading data occurred in the first few time steps of several of the tests. These perturbations were thought to be most likely the result of the temperature sensitivity of the electronic balance used to monitor the bed weight. As discussed in Sect. 3.4.1, it had been observed that the temperature changes in the insulated box containing the reaction chamber resulted in changes in the observed weight as recorded from the electronic balance. Thermocouples were installed at two locations on balance to monitor the balance temperature throughout the tests, and the spacing between the balance and the heated box was increased to help reduce the radiated heat to the balance. As expected, higher box temperatures were required at higher gas rates to achieve the same outlet gas temperature. This is due to higher delta temperature required for heat transfer at the increased mass flow rate. In spite of the efforts to thermally stabilize the balance prior to the loading phase by flowing a nitrogen stream across the bed at the same rate as the planned air-CH_3I stream to establish the thermal demand on the heaters, and thus reach the proper temperature in the enclosure, small variations in the heat load could have been translated into the observed unusual shape to the first 2 to 4 h of the loading curve.

Figures 4.18–4.36 and the temperature data recorded during each run indicate that such behavior was observed for runs T5, T10, T12, T13, T14 and T15. Figures 5.6 and 5.7 are examples of the temperature fluctuations observed that result in the observed shifts in recorded weights. T10 underwent the most significant deviation in which the

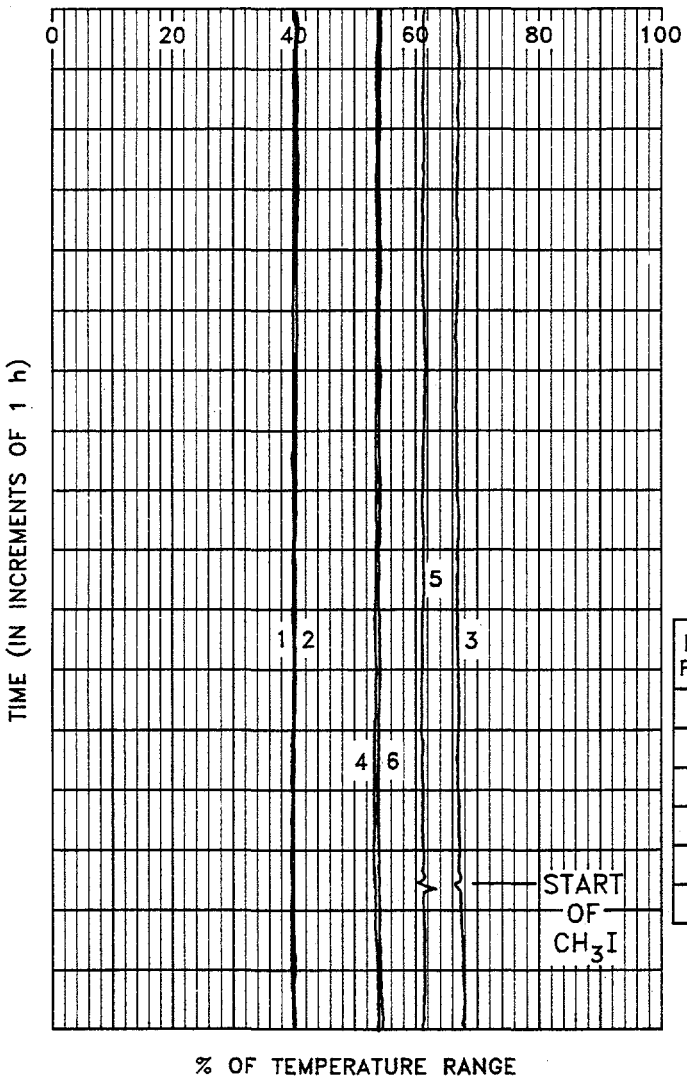

DATA POINT	LOCATION	TEMPERATURE RANGE (°F)
1	HOOD	0–200
2	ROOM	0–200
3	BOX	0–500
4	BALANCE, FRONT	0–200
5	GAS STREAM	0–500
6	BALANCE, REAR	0–200

Figure 5.6. Typical temperature control performance as observed in Run T8.

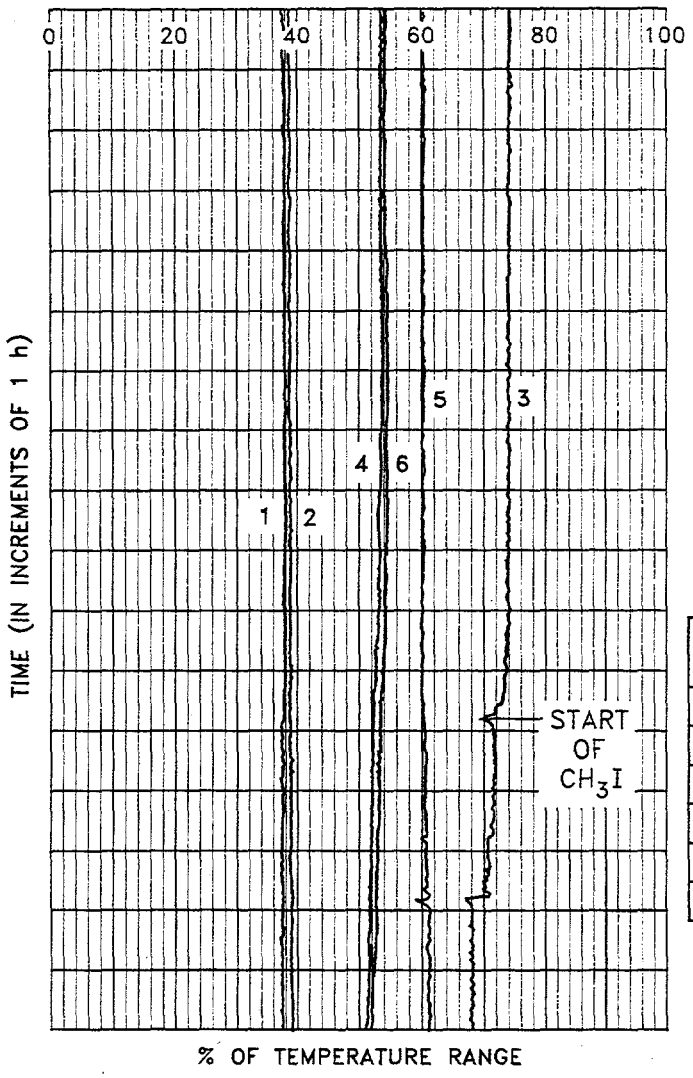

DATA POINT	LOCATION	TEMPERATURE RANGE (°F)
1	HOOD	0–200
2	ROOM	0–200
3	BOX	0–500
4	BALANCE, FRONT	0–200
5	GAS STREAM	0–500
6	BALANCE, REAR	0–200

Figure 5.7. Temperature fluctuation observed for run T14 at time of CH_3I addition to gas stream.

temperature at the top of the balance shifted just over 2°C in 4 h. The other runs noted above showed temperature fluctuations on the order of 1 to 1.5°C over 4 to 10 h. All of the other runs show no abnormalities in the first few hours of loading. In addition, the runs that were considered to be stable appeared to maintain the balance temperatures within 0.25 to 0.50°C during the entire run. In all cases there is a small upset in the box and gas temperature that occurs as the CH_3I is started.

As a result of the observed shifts in the recorded weights attributed to thermal upsets in the electronic balance for several of the runs, it appeared that analysis over long time periods was preferred for this study. Therefore, only the full data sets were examined for each model in the following analysis of the data. The parameters obtained from the short time period must be viewed in light of the possible associated uncertainty. The resulting parameter fits were evaluated for consistency with and without the questionable data sets.

Some attempt was made to compensate for the temperature-induced error in the initial weight recorded for T10 by adding 0.15 g to each data point and thus raising the curve to extrapolate to a conversion of 0 at time 0. The first 30 data points were not considered in any analysis due to the shape of the uptake curve. Run T13 exhibited a similar problem, a weight compensation of 0.025 g was used and data points 1–24 were ignored. In general, curve fitting results from runs T10 and T13 were not considered reliable as a result of this correction factor.

No attempt was made to correct the observed data for weight gains due to water uptake. As was shown in Sect. 4.3.1, the weight gain due to water in the absence of CH_3I was on the order of 10 to 20% of the total observed weight gain during periods of CH_3I loading. It is not known at this time if there is any displacement of water by the diffusion of CH_3I or the degree of water consumption in any reaction occurring within the AgZ matrix. It was shown in the long duration runs, T16 and T18, that a very high degree of theoretical silver utilization was achieved during these runs. Data from Thomas et al. (1977) indicated that it was possible to achieve ~80% conversion of the silver in the saturation region of a deep bed. Tests T15, T16, and T18, which attempted to achieve full utilization of the silver, reached 92%, 99%, and 85% respectively. All had exposure times in excess of 135 h. It was implied from this limited and somewhat indirect data that the amount of weight gain due to water adsorption may have been less than that observed for water alone if the limit of conversion is about 80%, as reported by Thomas. The remainder of the weight gain over 80% might be attributed to water uptake. However, without more specific data, no compensation was practical.

The recorded CH_3I adsorption data appeared to be basically sound in spite of these possible interfering factors. The weight gain attributable to water was shown to be small relative to the total weight gain in Sect. 4.3.1. The temperature fluctuations in the first few hours in several of the tests were easily detected on the strip charts, they did not affect most of the experimental runs, and when they did, they did not generally extend beyond the first 4 h of the loading period.

5.2.2 Nonisothermal Models

One of the first determinations that must be made in the selection of a model is whether the process can be considered isothermal. The answer to this question will then determine the class of models that must be utilized. To make this determination, two approaches were taken. The first was to utilize the nonisothermal model described by Lee and Ruthven (1978) in an attempt to extract consistent heats of adsorption and diffusion coefficients by assuming that the experimental system was nonisothermal and that it would behave according to the model. If the assumption is correct, then for all of the data sets, relatively consistent parameters should be obtained.

As described in Sect. 2.5.6.1, the conversion is given by Kärger and Ruthven (1992) as:

$$X_B = \frac{m_t}{m_\infty} = 1 - \sum_{n=1}^{\infty} \frac{9\left[\left(p_n \cot p_n - 1\right)/p_n^2\right]^2 \exp\left(-p_n^2 D_c t / r_i^2\right)}{\frac{1}{\beta'} + \frac{3}{2}\left[p_n \cot p_n \left(p_n \cot p_n - 1\right)/p_n^2 + 1\right]}. \tag{2.65}$$

The value of p_n was given by the positive roots of the transcendental equation:

$$3\beta'\left(p_n \cot p_n - 1\right) = p_n^2 - \alpha', \tag{2.66}$$

and the parameters α' and β' are defined as:

$$\alpha' = \frac{h_m S}{C_p} \frac{r_i^2}{D_c} \tag{2.67}$$

and

$$\beta' = \frac{\Delta H}{C_p}\left(\frac{\partial q^*}{\partial T}\right)_P. \tag{2.68}$$

It was first attempted to utilize the nonisothermal model to obtain values for α', β', and the diffusion coefficient, D_c, using multidimensional minimization techniques. As can be noted from Eq. (2.67), the α' term in this model can also be calculated from the available data if the diffusion coefficient is known. It was hoped that the optimum value for α' would correspond to the directly calculated values. However, the values obtained for α' when allowing the minimization routine to use all three parameters were widely scattered, ranging 10^{-12} to 10^{+4}. Based on these poor results, the value of α' was constrained to the calculated value and the optimization routine was rerun to obtain values of the diffusion coefficient and β'. The values obtained are shown in Table 5.4, along with the sum of the squares of the error for each run and the total for all runs.

It was suggested by Lee and Ruthven (1978) that a determination as to the magnitude of the deviation from isothermal behavior by thermal effects can be made by evaluating the ratio of α'/β'. When this ratio exceeds 60, the difference in the value of D_c/r_i^2 calculated by assuming that the system was isothermal and by considering the nonisothermal case does not exceed 15% over the range of 0 to 85% conversion or equilibrium adsorption. Over the first 10 h of loading, the values of α' and β' determined by curve fitting resulted in values of α'/β' over 100 for all runs except T10, T13, T15, and T18. Questions concerning runs T10, T13, and T15 have previously been discussed in regard to the possible introduction of temperature effects on the balance and hence the recorded data. However, as the time frame considered in the analysis is lengthened, more

Table 5.4: Summary of nonisothermal model parameters obtained through optimization of curve fits for full data sets.

Run No.	D_c (cm^2/s)	α'^a	β'	Error[a]	$\alpha'/(1+\beta')^c$	α'/β'^d
T3	1.87E-14	2.57E+05	2.62E+02	1.07E-02	9.77E+02	9.80E+02
T6	2.80E-14	1.72E+05	1.83E+03	1.63E-02	9.40E+01	9.40E+01
T7	1.75E-13	8.49E+03	6.59E+03	2.00E-01	1.29E+00	1.29E+00
T8	2.22E-13	1.83E+04	2.17E+04	2.67E-01	8.45E-01	8.45E-01
T10	4.46E-08	1.37E+00	3.04E+00	5.06E-03	3.38E-01	4.49E-01
T11	1.20E-14	4.00E+05	7.71E-07	5.32E-03	4.00E+05	5.19E+11
T12	4.27E-14	1.13E+05	4.77E+04	1.19E-02	2.37E+00	2.37E+00
T13	3.08E-11	1.57E+02	2.40E+04	1.33E-01	6.52E-03	6.52E-03
T14	6.58E-15	7.33E+05	1.09E+04	3.09E-02	6.70E+01	6.70E+01
T15	6.16E-11	5.53E+01	2.04E+04	1.53E-01	2.71E-03	2.71E-03
T16	1.04E-13	2.95E+04	9.25E+03	1.98E-02	3.19E+00	3.19E+00
T18	5.91E-11	5.19E+01	2.15E+04	3.86E-03	2.42E-03	2.42E-03
T19	1.16E-14	4.17E+05	4.89E-06	1.31E-04	4.17E+05	8.52E+10
T20	1.82E-14	8.18E+04	1.57E+02	1.07E-03	5.19E+02	5.22E+02
T22	2.73E-14	5.46E+04	2.40E+03	9.48E-02	2.27E+01	2.27E+01
T26	5.80E-15	8.52E+05	5.95E-07	8.86E-02	8.52E+05	1.43E+12
			Error sum:	1.04E+00		

[a]Error terms are the resultant sum of the square of the error between the experimental data and the proposed model.

[b]Calculated from Eq. (2.67).

[c]Ratio should be $>>\pi^2$ to meet isothermal conditions.

[d]Ratio should be >60 to meet isothermal conditions.

runs had ratios that were less than 60. When considering all of the loading data for each run, only T3, T6, T11, T14, and the two short runs T19 and T20 still theoretically met the numerical criteria for using isothermal assumptions.

It is worthwhile to note that the values of α' and β' determined by curve fitting varied significantly. Based on the definition of β', that term should vary in proportion to the value of the $\left(\frac{\delta q}{\delta T}\right)$. The values of β' presented in the literature (Lee and Ruthven, 1978, Ruthven et al., 1980, and Ruthven and Lee, 1981) were fairly constant and fell in the range of 0.17 to about 2.33. Calculated values from this study ranged from 7.7×10^{-7} to $4.8 \times 10^{+4}$. As a result these values were highly suspect and although the model, as a whole, provided relatively good curve fits to each individual data set, there was no consistency in any of the derived parameter values. The determination as to the validity of an isothermal assumption was not clearly shown to be true or false.

A second verification of the significance of the potential nonisothermal behavior was achieved though analysis of maximum temperature variation due to the heat of adsorption and chemical reaction. It was shown theoretically by Lee and Ruthven (1978) that while the primary resistance to mass transfer was in the diffusion through the solid while the primary resistance to heat transfer was in the gas film surrounding the solid particle. For a constant rate of reaction, the heat transfer resistance tended to increase with decreasing gas velocity and the temperature of the solid increased accordingly. The maximum loading rate for any run appeared to occur in the early time periods and the run

with the highest initial loading was T3 with 0.0913 g being loaded in the first hour. The lowest calculated value for the heat transfer coefficient, shown in Table 4.4, was 1.11×10^{-3} cal/(cm^2 s °K). Values for the heat of adsorption were obtained from Table 2.6 in the text by Ruthven (1984). The highest value shown was 26 kcal/mol, but most values were less than 20 kcal/mol. Finally the heat associated with the chemical reaction between CH_3I and silver was estimated from heat of formation data and specific heat data from the *Handbook of Chemistry and Physics* (1993), Perry et al. (1992), and Reid et al. (1977). Since the actual reaction has not been clearly identified, the heat of reaction for Eq. (2.4) was utilized. This equation had calculated heats of reaction of –27.8 and –27.6 kcal/mol (–116.5 and –115.6 kJ/mol) of silver reacted at 150 and 200°C respectively. This heat of reaction was the highest of the assumed possible reactions involving CH_3I, excluding the reactions involving silver ions in an aqueous solution. Then to be even more conservative, a value of –200 kJ/mol of silver reacted was assumed for the purposes of these calculations. This was clearly significantly larger than the heat of reaction for any of the proposed reactions. This analysis, using conservative assumptions for all variables, indicated a maximum delta temperature between the pellet and the bulk fluid as a result of both the heat of adsorption and chemical reaction of 0.37°C. Based on this result it clearly appeared that the assumption of isothermal adsorption was substantiated.

5.2.3 Shrinking Core Model

The ability of this model to fit the experimental data was briefly touched on in Sect. 5.1.1, in which the convergence method was discussed. However, here we shall look at the subject in a bit more detail.

First, by examining Table 5.1 or 5.2 it was clear that the diffusion through the gas film was not the controlling mechanism. In virtually every case in which the parameters for three terms of the full shrinking core model were used as adjustable parameters in the minimization of the error between the model and experimental data, the computed value for k_g was on the order of 10^{100} cm/s. This value was the upper limit set for in the search routines. In the few cases where it did not reach the upper bounds, the value is still above 10^{10} cm/s. The application of this value into the Eq. (2.39) for $\tau_{gasfilm}$ and the subsequent application into summation of the resistances showed that the resistance was mathematically negligible. Further, the values of k_g determined for the gas film alone were compared to the values of k_g as estimated by use of the Sherwood number and the molecular diffusivity D_{AB}. The values of k_g estimated by the Sherwood number were on the order of 3 to 9 cm/s. However, if the assumption was made that the controlling resistance was the gas film, then the values for k_g determined by the least squares curve fitting method ranged from 0.04 to just over 0.3 cm/s. This difference of up to several orders of magnitude was a second clear indication that some other resistance aside from the gas film diffusion was the controlling resistance in the mass transfer. In addition, the shape of the uptake curve was not indicative of gas film resistance control.

Second, there appeared to be two distinct classes of behavior or types of loading curves. The first class may be described by diffusion control through the ash layer which appeared to describe several of the cases (e.g., T3); however in most of the runs, the loading curve appeared to have a "knee" which the shrinking core model cannot fit. One such example is run T11. These uptake curves tended to show a rapid weight gain followed by a slower rate of weight gain. This "knee" may also be an indicator that possibly two or more mechanisms were controlling the adsorption process and that there was a transition from one to the other.

If the ring observed on the pellets, as shown in the Fig. 4.12, was related to the loading of iodine on the pellet then it was easily shown that at 40% utilization the radius of the unreacted core should be ~78% of the overall pellet radius. The observed radius in Fig. 4.12 was only ~27% of the pellet radius for the pellet that still shows a core. This 27% equates ~93% conversion if a strict shrinking core model was correct. It should also be recalled that the BEI of the pellets from T19 and T20 showed no significant iodine gradient, which appeared to be relatively consistent with the photographic evidence at higher iodine loadings. These data tended to lead to the conclusion that while there may initially be the appearance of the shrinking core-type behavior, there was also a second slower process that accounted for the loading above some nominal level of loading associated with the shrinking core.

The effective diffusivity calculated from the data collected over the time periods of the first 40 (10 h) data points ranges from 1.84×10^{-4} to 3.91×10^{-3} cm^2/s for the runs

that did not exhibit any thermal upset in the balance. This effective diffusivity was also compared to that predicted by fundamental analysis of the zeolite pore structure and physical constants for the diffusing component. By comparison of the above effective diffusivities with the combined effective diffusivities shown in Table 4.4 for either the Knudsen diffusivity in the micropore/mesopore range of 5×10^{-5} to 5×10^{-4} cm^2/s or the effective molecular diffusivity of $\sim 1.4 \times 10^{-2}$ cm^2/s in the macropore range, it was observed that the value obtained by curve fitting falls between the two bounding cases.

The second class of behavior that was observed was one in which reaction control alone appeared to adequately model conversion or loading of the bed. Of particular note was test T18, in which the water content of the feed gas stream was reduced to below the stoichiometic ratio for the CH_3I in the gas stream. In examining Table 5.1 for the case of the first 10 h of the loading, only the reaction term was utilized. The regressed reaction rate was 5.90×10^{-2} cm/s. This run should be compared with T16, which was conducted under the same conditions but without the drying of the air. This run exhibited the characteristics of diffusional control from the outset. As pointed out by Levenspiel (1979), it is possible for a shift to occur in the controlling mechanism from reaction to diffusion through the reacted shell but the opposite is not observed. It would appear from this one data set that water does play a key role in the reaction process. Provided that sufficient water was available, the process was controlled by the diffusion processes, but under low water vapor conditions, the adsorption rate was limited by the reaction rate.

The addition of water vapor in run T13 over the same time period was inconclusive due to the noise in the data induced by the thermal effects on the balance.

To briefly summarize this point, first, as was discussed in Sect. 4.3.2, very little CH_3I was loaded onto the mordenite without silver present. Second, as observed in test T18, the loading rate appeared to be affected by the presence of water vapor. This combined behavior involving CH_3I, H_2O, and Ag was consistent with the chemical reaction described by Eqs. (2.5) and/or (2.6). This behavior was also consistent with the observed deep-bed behavior in which higher loadings occurred in a segment prior to bed breakthrough in the presence of water vapor than in the cases with very dry gas streams (Jubin, 1980, 1982 and Burger and Scheele, 1981). The data reported in these past studies were for the loading of a fixed length bed up to the time that the effluent gas exceeded a set value. These observations were consistent with the shift to the slow reaction controlling mechanism at low water concentrations and with increased water concentration, the reaction rate increased and the diffusional resistance became controlling. In relationship with the observations made in the deep-bed studies, the faster the controlling rate, the more iodine would be loaded in a fixed-length bed prior to breakthrough.

It was pointed out by Carberry (1976) that for the shrinking core model to be valid in the case of porous media, the reaction constant, k_s, must be large enough such that the reaction zone is very thin. To assure that this was true, the following condition involving the Damköhler number, N_{Da}, which is defined as $k_s r_d / D_p$, must be met:

$$N_{Da} \geq \frac{40{,}000}{LS}, \tag{5.3}$$

where L is the pellet volume to external surface ratio and S is the total surface area per unit volume. Based on physical dimensions of the 1/16-in. AgZ material, N_{Da} must be greater than 0.178, assuming a total surface area of 400 m^2/g. Using a diffusion coefficient of 1×10^{-3} cm^2/s (from test T3) it was determined that as long as the reaction rate constant was greater than 2×10^{-3} cm/s, the shell in which the reaction was occurring was thin enough to make the shrinking model valid. In all cases evaluated in this study the calculated reaction rate constant was significantly greater than this value. Even considering the case of T18, in which reaction control was believed to be the controlling mechanism, this regressed reaction rate was 5.90×10^{-2} cm/s. Therefore based on this criteria, the shrinking core model remained a valid option.

Using the shrinking core model it was possible to find a set of parameters that seems to successfully model each individual loading curve. However, it was less obvious why some sets of data were diffusion controlled and other similar sets appeared to be reaction controlled. This model by itself was unable to explain the apparent change in controlling mechanism. However, it provides strong evidence that:

1. the mass transfer process was not controlled by the gas film resistance;
2. there was a diffusional component, and the effective diffusivities in the first few hours of loading were in the range of 1.84×10^{-4} to 3.91×10^{-3} cm^2/s for the runs in which the data showed no thermal upset in the balance during the initial period; and
3. the reaction rate became controlling at low water vapor concentrations.

To summarize the observations for the shrinking core model, it was seen by comparing all of the models analyzed in this study that the shrinking core model provided either the best or the second best overall fit to the data. If both the diffusivity and the reaction rate constant are allowed to vary for each set of data and the consistency in the determined parameters was not a strong criteria, then the shrinking core model provided the best fit by far. However, if either the reaction rate or the diffusivity were fixed (see Table 5.5), then the bimodal model with a fixed micropore diffusivity value, which will be discussed in Sect. 5.2.5, produced a smaller total sum of the squares of the error term.

5.2.4 Volume Reaction Model

As stated before, the data obtained from the electron microscopic examination of the loaded AgZ material indicated that there was no significant iodine concentration gradient across the pellet diameter. This of course must be balanced with the photographic observations shown in Figs. 4.10–4.12, in which at least at low loadings there was the appearance of the formation of a shrinking core as described in Sect. 5.2.3. Taking these two observations together indicated that a process other than a simple shrinking core was occurring. In theory, the volume reaction model provided a model that could possibly explain these observations. This model is bounded at one extreme by the shrinking core and at the other extreme by a uniform sorbate concentration across the pellet diameter. Since both of these limiting cases were analyzed with separate models, it is the region between these two limits that was of interest with this model. Thus the

Table 5.5: Evaluation of shrinking core model ... the constraint that only one parameter is adjustab...

	Best fit from least square ... sis			
	Constraining factor		C... ...ing factor	
	$D_e = 5.0^{-3}$ cm^2/s[b]		...0 cm/s[c]	
Run No.	k_s (cm/s)	Error[a]	D_e (cm...	Error
T3	1.05E-01	1.16E+00	1.19E-...3	2.25E-02
T5	1.67E-01	1.24E+00	2.80E-03	3.23E+00
T6	1.20E-01	1.16E+00	1.52E-03	1.80E-02
T7	1.36E-01	1.76E-01	2.00E-03	5.55E-01
T8	5.00E-02	2.27E-01	3.37E-04	8.04E-01
T10	2.08E-01	1.85E-01	3.48E-03	2.77E-01
T11	1.01E-01	3.49E-01	7.68E-04	9.22E-03
T12	5.20E-02	1.43E-02	1.99E-04	1.74E-01
T13	6.76E-02	6.93E-02	5.25E-04	9.00E-01
T14	1.86E-01	2.03E-01	1.25E-03	4.52E-02
T15	5.67E-02	9.42E-02	3.56E-04	1.11E+00
T16	7.63E-02	6.20E-02	7.22E-04	5.75E-01
T18	5.87E-02	2.43E-03	3.33E-04	4.44E-01
T19	1.27E-01	4.93E-02	5.89E-04	1.07E-03
T20	3.40E-01	1.44E-01	6.03E-03	1.24E-02
T22	1.23E-01	3.89E-01	2.50E-03	2.10E-01
T26	8.67E-02	7.95E-01	5.58E-04	1.29E-01
	Total errors:	6.32E+00		8.52E+00

[a]Error terms are the resultant sum of the square of the error between the experimental data and the proposed model.

[b]Assumes that the primary resistance to mass transfer is the reaction rate.

[c]Assumes that the primary resistance to mass transfer is diffusion through the ash layer.

model parameters must be chosen such that the model represents the region between these two bounding cases.

As indicated by Levenspiel (1972) and others, the volume reaction model can, in many cases, be effectively used to describe the conversion process in porous media. The implementation of this model however was not a trivial matter. The model itself is a two-parameter model and as such requires a multidimensional minimization routine to optimize these parameters. The two parameters to be determined were either the micropore diffusivity and the reaction rate constant or these could be combined into two other dimensionless, adjustable parameters, the Thiele modulus, ϕ, and a time term, θ. The Thiele modulus, ϕ, is a ratio of the maximum kinetic rate to the maximum internal diffusion rate (Dudukovic and Lamba, 1978) and thus contained both the micropore diffusivity and the reaction rate constant. The value of ϕ is related to the thickness of the reaction zone (Kulkarni and Doraismamy, 1986). As ϕ approaches ∞, the model reduces to a sharp interface. Conversely, as ϕ becomes small, the concentration of component A becomes uniform across the pellet diameter. The characteristic reaction time, θ, is a function of only the bulk phase concentration and the reaction rate constant. Obviously these parameters are interrelated. To work around this interaction, the reaction rate and diffusivity were used as the adjustable parameters. The appropriate values for ϕ and θ were calculated from the adjustable parameters in each step of the multidimensional least square optimization process.

However, it was noted by examination of Eq. (2.53) that the desired term, the conversion X_B, cannot be explicitly determined but must be found as a root to that equation given the set of adjustable parameters. This is virtually the same method of solution required for the shrinking core model. However, as the number of time steps increased and with them the corresponding time term, θ, it became difficult to find roots to the equation using the root-finding function used elsewhere in this analysis. [The initial function utilized, ZBRAC, from the *Numerical Recipes FORTRAN Diskette, Second Edition*, Press et al. (1992b), had successfully been used in a number of the other models including the shrinking core model.] The FORTRAN function initially tried started with a small search range and expanded the search range until a root was bracketed. However, the logarithmic term in Eq. (2.53) became undefined as the conversion term became larger for certain values of θ or ϕ tried by the minimization routine. This was overcome through the use of an alternate root-bracketing function that utilized a bounded range in which to locate the root. [This function named ZBRAK was also from the *Numerical Recipes FORTRAN Diskette, Second Edition*, Press et al. (1992b).] This type search was practical because the only physically possible roots lie between values of X_B of 0 and 1. The utilization of this method did not completely overcome the possibility of an unbounded situation if values of θ or ϕ were unrealistically large or small. This was handled by forcing the function being minimized to return large values for cases where the trial produced nonviable solutions. (This same method was also used elsewhere to force the minimization routine to remain within the bounds of physically significant values for the

adjustable parameter.) One other approach that was attempted was to fix the value of ϕ, then conduct the optimization only by adjusting the reaction rate constant and the associated value of θ. Once a minimum sum of the squares of the error was found, the diffusivity was back calculated from the Thiele modulus.

The results of this model where both adjustable parameters were optimized simultaneously are shown in Table 5.6 for the case where the full data sets were considered in the optimization process. It can be noted by comparison with Table 5.2 and Table 5.7 that the total sum of the squares of the errors for all of the tests was only a factor of ~2 lower than for the cases of ash diffusion, reaction control, micropore diffusion, or macropore diffusion control taken individually. And for the case of the full shrinking core model, the volume reaction model yields a sum of the total errors ~3 times higher, which was a bit surprising considering that both models considered reaction and diffusional resistances. It should be pointed out that the approximated model which was used in this study was reported to show significant deviations from the more rigorous numerical solutions at values of $\phi > 10$ (Ramachandran and Kulkarni, 1980). However, for the sake of understanding the behavior process under conditions in which the volume reaction model would apply, values <10 were of primary interest since the shrinking core model was valid at high values of ϕ.

Table 5.6: Volume reaction model parameters for full data sets.

Run No.	$D_{s,eff}$ (cm^2/s)	k_v ($cm^3/mol^{n-1}s$)	ϕ	θ	Error[a]
T3	9.48E-03	1.35E-03	1.98E-03	1.50E+00	7.62E-01
T6	3.35E-02	1.58E-03	1.14E-03	1.71E+00	5.98E-01
T7	1.27E-08	1.10E-03	3.13E+00	1.11E+00	1.86E-01
T8	2.53E-09	8.52E-04	3.04E+00	1.13E+00	2.45E-01
T10	4.46E-08	3.04E-03	1.37E+00	3.04E+00	5.06E-03
T11	1.01E-09	7.75E-03	1.45E+01	8.32E-01	4.10E-02
T12	1.46E-09	1.12E-03	4.58E+00	5.01E-01	1.19E-02
T13	3.50E-09	1.15E-03	3.00E+00	1.22E+00	1.02E-01
T14	4.29E-03	2.18E-03	3.72E-03	7.02E-01	1.57E-01
T15	3.26E-09	9.17E-04	2.77E+00	1.02E+00	1.29E-01
T16	3.40E-02	9.45E-04	8.71E-04	1.45E+00	2.34E-02
T18	3.64E-09	9.21E-04	2.63E+00	8.02E-01	2.37E-03
T19	1.19E-26	8.46E-03	4.41E+09	4.30E-01	6.24E-03
T20	4.91E-09	1.17E-02	1.64E+01	6.67E-01	6.17E-03
T22	3.38E-03	7.23E-04	4.92E-03	1.42E+00	2.34E-01
T26	3.68E-10	9.61E-03	2.74E+01	6.53E-01	1.36E-01
				Error sum:	2.64E+00

[a]Error terms are the resultant sum of the square of the error between the experimental data and the proposed model.

Table 5.7: Micropore and macropore model parameters for the full data sets.

	Micropore		Macropore	
Run No.	D_c (cm^2/s)	Error[a]	D_p (cm^2/s)	Error
T3	1.82E-14	1.16E-02	4.50E-09	1.16E-02
T6	2.26E-14	7.44E-02	5.57E-09	7.44E-02
T7	6.73E-15	6.68E-01	6.23E-09	6.68E-01
T8	5.66E-15	8.75E-01	1.40E-09	8.75E-01
T10	3.43E-14	6.74E-01	8.45E-09	6.74E-01
T11	1.20E-14	5.32E-03	2.97E-09	5.32E-03
T12	1.65E-15	1.95E-01	4.07E-10	1.95E-01
T13	7.18E-15	1.02E+00	1.77E-09	1.02E+00
T14	3.72E-15	8.75E-02	9.17E-10	8.75E-02
T15	4.90E-15	1.22E+00	1.21E-09	1.22E+00
T16	1.17E-14	7.49E-01	2.88E-09	7.49E-01
T18	3.81E-15	5.10E-01	9.39E-10	5.10E-01
T19	1.16E-14	1.31E-04	2.85E-09	1.31E-04
T20	1.66E-14	2.13E-03	1.54E-08	2.13E-03
T22	1.24E-14	3.47E-01	1.15E-08	3.47E-01
T26	5.80E-15	8.86E-02	1.43E-09	8.86E-02
	Error sum:	6.53E+00		6.53E+00

[a]Error terms are the resultant sum of the square of the error between the experimental data and the proposed model.

The best fits obtained for four different data sets which exhibit a range of loading behavior are presented in Figs. 5.8–5.11. The four sets were selected from those that appeared to have no notable thermal instability in the balance. As is readily apparent, the approximate volume reaction model does not seem to fit the experimental data well in any of the situations. At best it seems to be uniformly average in its ability to model the adsorption of CH_3I on Ag°Z.

As can be observed in Table 5.6, the values of the Thiele modulus, ϕ, and the time term, θ, were widely scattered, indicating that while the model could be arbitrarily made to give a "best fit" to a given set of data, no consistent values for either the effective diffusivity or the reaction rate constant were determined by the curve fitting method utilizing this model. Since no consistent values were produced from this analysis and from the resulting shape of the predicted "best fit" uptake curves for values of ϕ for which the model was considered relatively accurate (i.e., less than ~5), the ability of this type of model to explain the observed behavior was in doubt. Therefore this form of a model and its assumptions about the adsorption process were not seriously considered beyond this point.

5.2.5 Macropore/Micropore Model

Mathematically, these two models are essentially the same. In the micropore diffusion case, the radius of the crystal is the dimensional term used and in the macropore

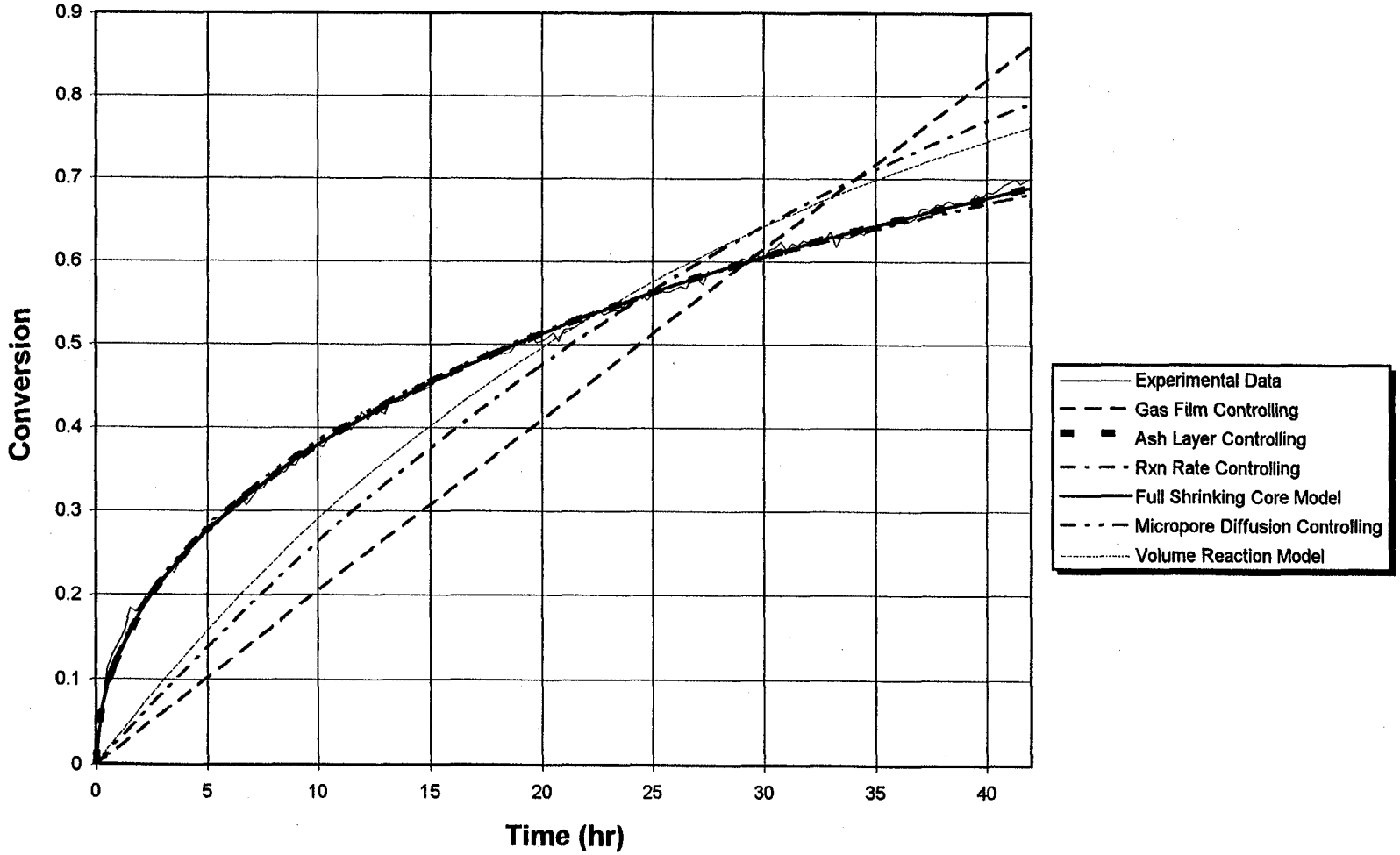

Figure 5.8. Comparision of the "best" fit for the shrinking core, micropore, and volume reaction models with data from Test T3.

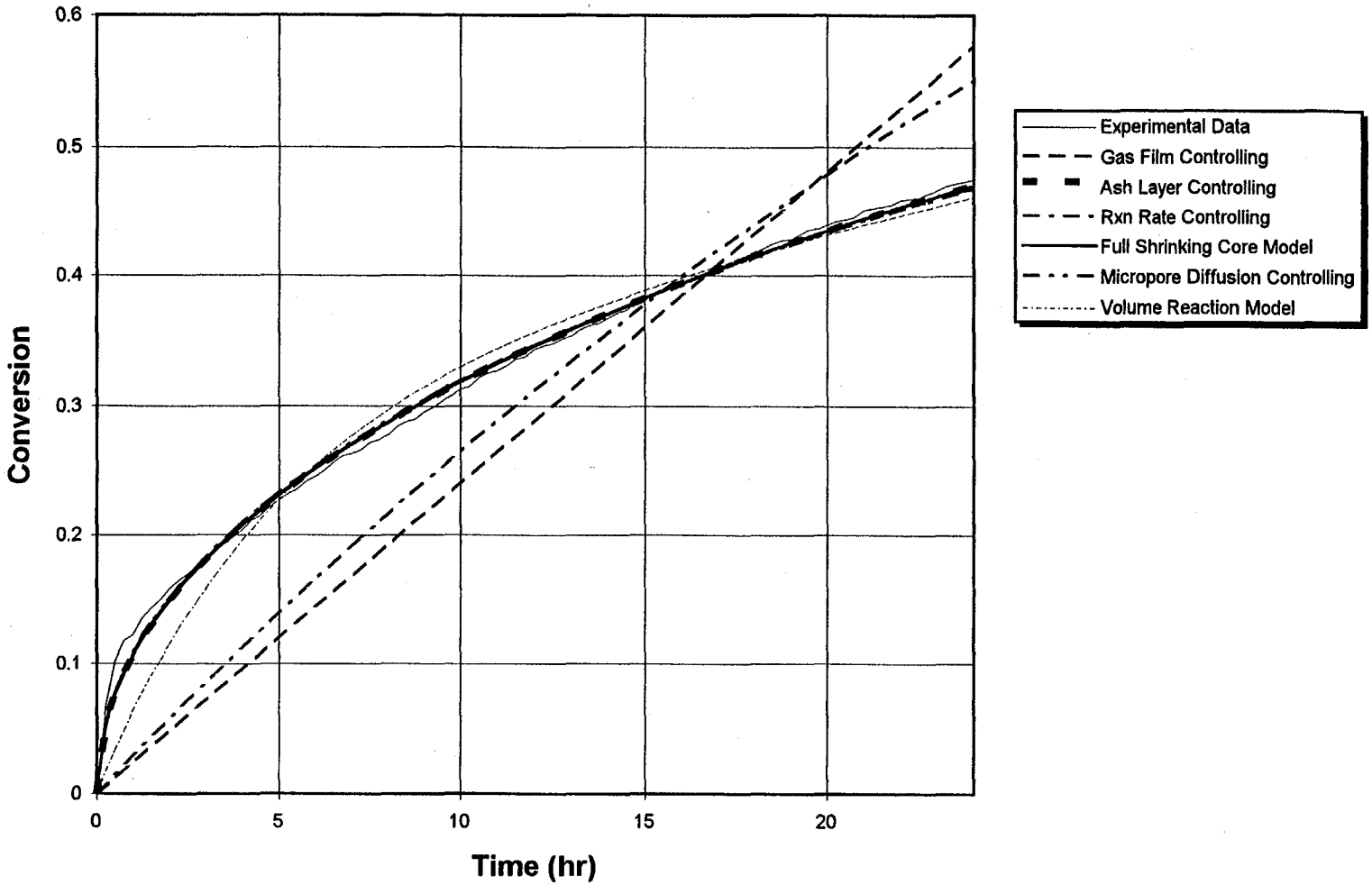

Figure 5.9. Comparision of the "best" fit for the shrinking core, micropore, and volume reaction models with data from Test T11.

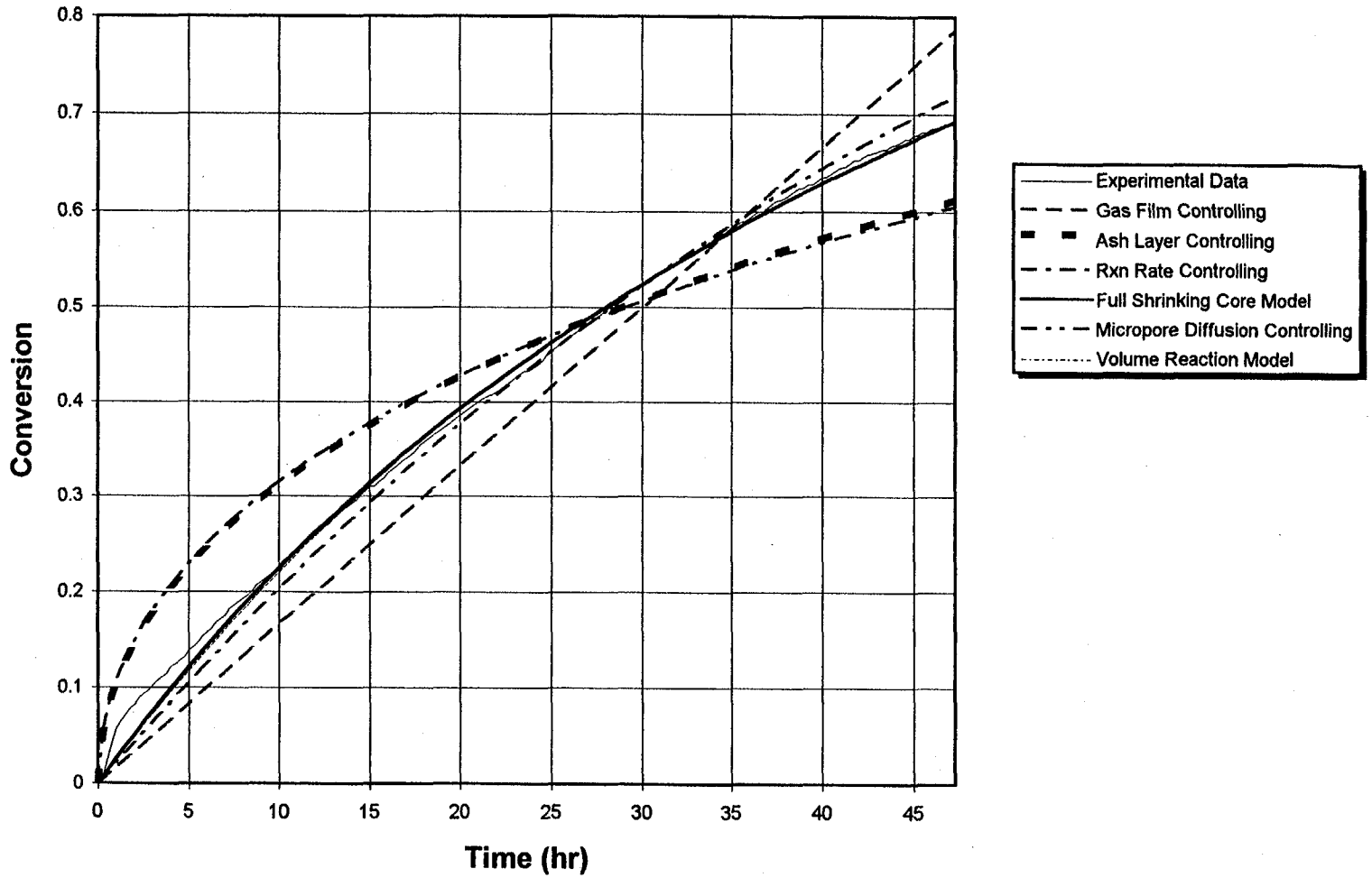

Figure 5.10. Comparision of the "best" fit for the shrinking core, micropore, and volume reaction models with data from Test T16.

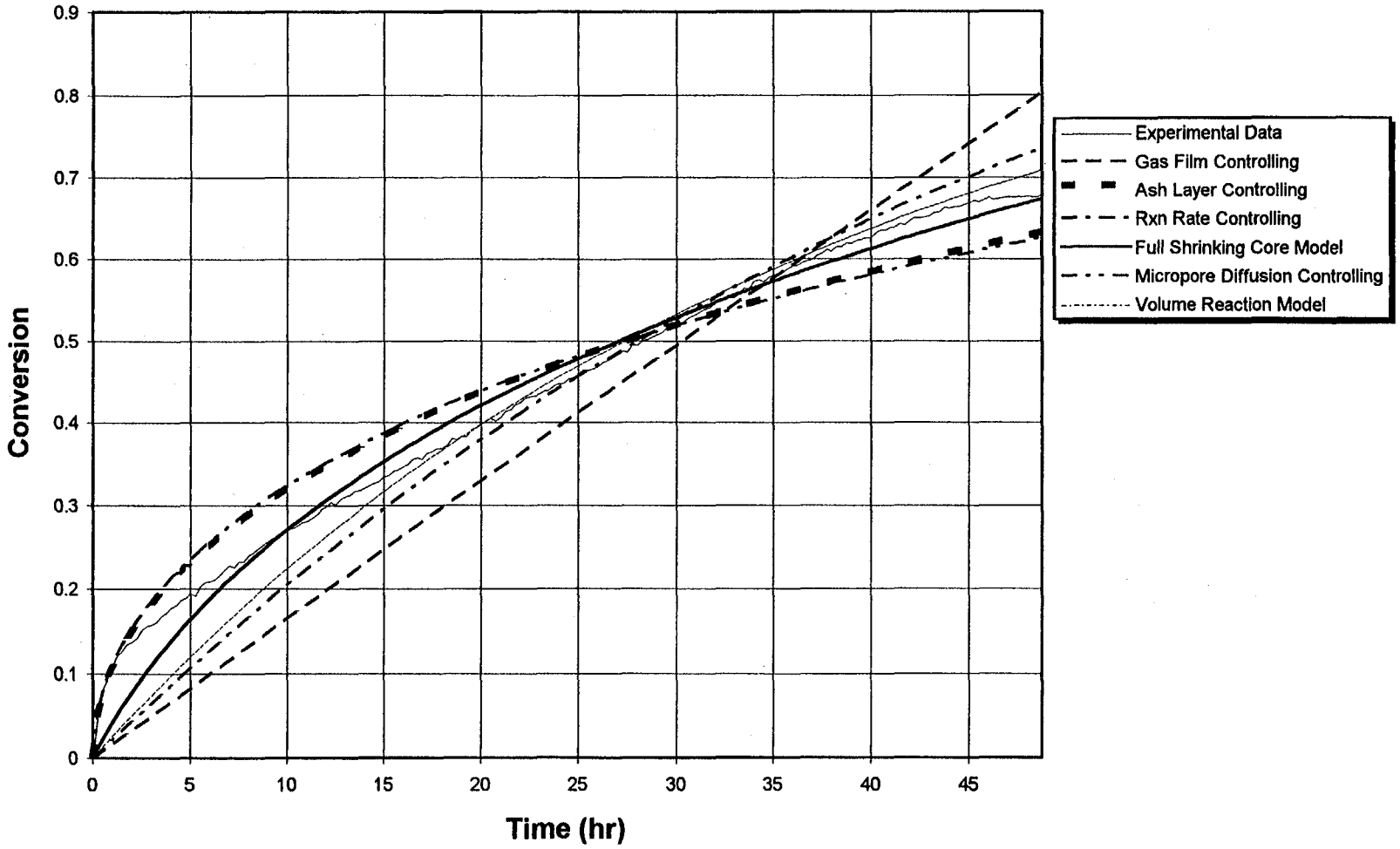

Figure 5.11. Comparision of the "best" fit for the shrinking core, micropore, and volume reaction models with data from Test T22.

case, the pellet radius is the relevant term. In the case of the macropore model, the diffusivity term that is obtained from the curve fitting analysis is an effective diffusivity which contains an equilibrium constant. This equilibrium constant, under cases of a linear equilibrium, relates the adsorbed phase concentration 'q' to the gas phase concentration 'C' by:

$$q = K^* C \ . \tag{5.4}$$

The results of both micropore and macropore models obviously yield the same error terms (Table 5.7) and were virtually the same as those obtained for the ash diffusion term of the shrinking core model by itself. Again consider Figs. 5.8–5.11, and it can be noted that neither model provided a particularly good prediction of the overall experimental behavior. However, as noted in Sect. 2.5.5.1, for large values of time, a plot of the term $\ln(1-X_B)$ vs time should yield a straight line with a slope of $-\pi^2 D_c/r_i^2$ and an intercept of $\ln(6/\pi^2)$ at a value of time equal to zero if micropore diffusion is the controlling mechanism.

Examples of such plots are shown in Figs. 5.12–5.15. Table 5.8 is a tabulation of the resulting micropore diffusion coefficients obtained from the slopes of this type analysis of all data sets. The correlation coefficient values, R^2, showed very high correlation for the linear regression of this data. This indicated that in the later time frame during the loading process, the effective micropore diffusivity was constant and, based on the data from this study, fairly consistent over a significant range of operating conditions. All of the slopes of the uptake curve plotted as the $\ln(1-X_B)$ vs time were obtained for values of

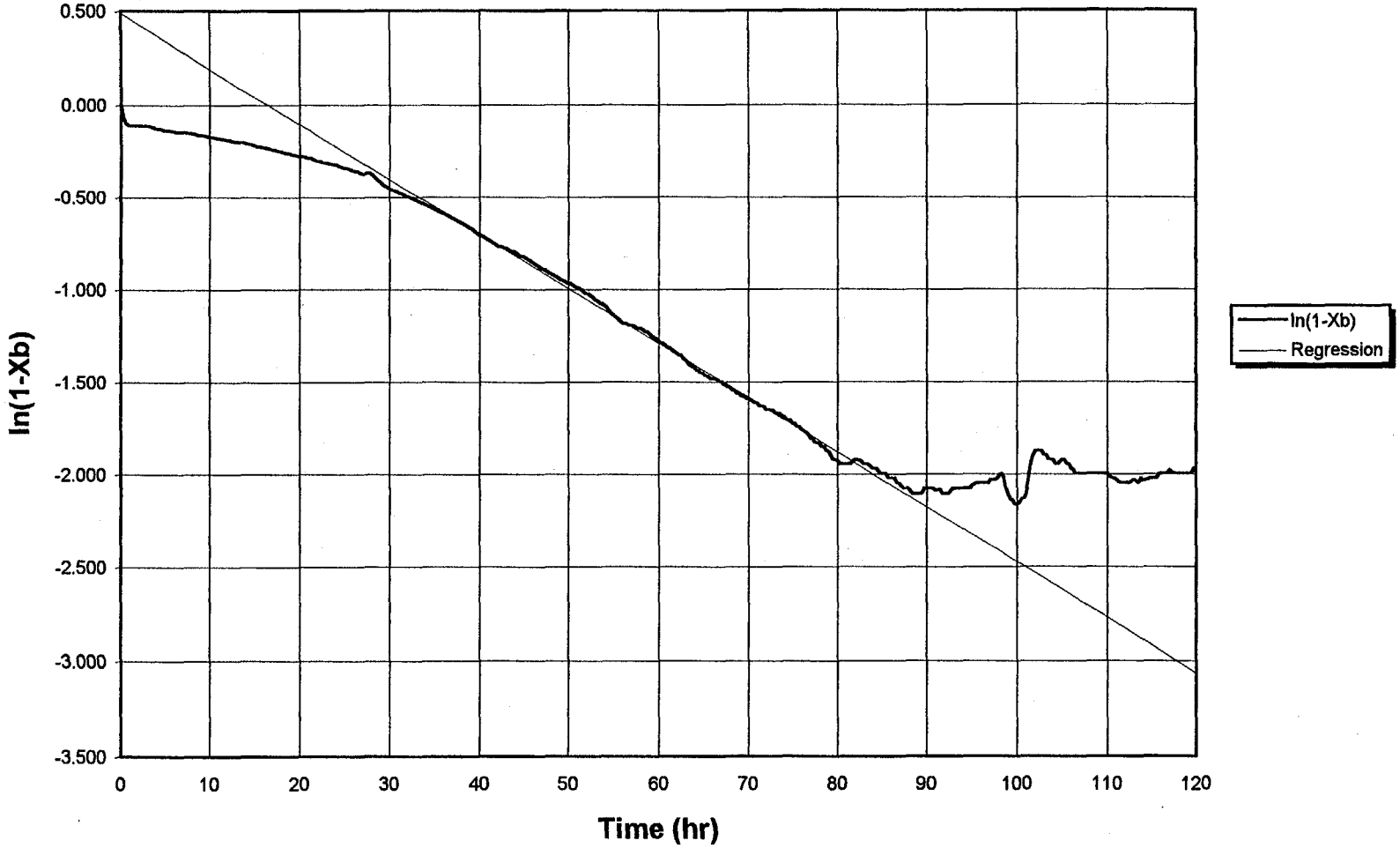

Figure 5.12. Determination of D_c from slope of the uptake curve plotted as $\ln(1-X_B)$ vs time for Run T8.

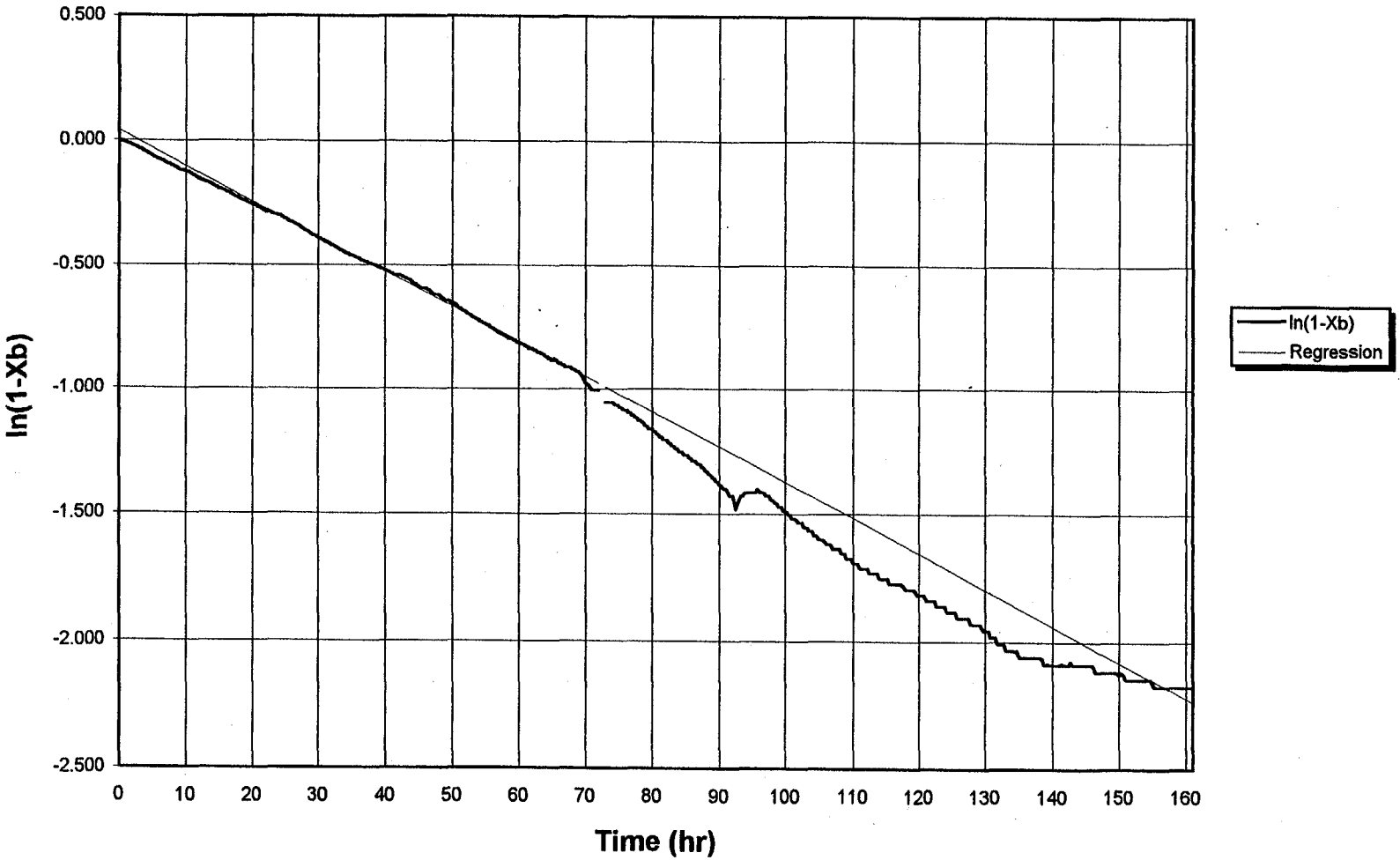

Figure 5.13. Determination of D_c from slope of the uptake curve plotted as l ln(1–X_B) vs time for Run T18.

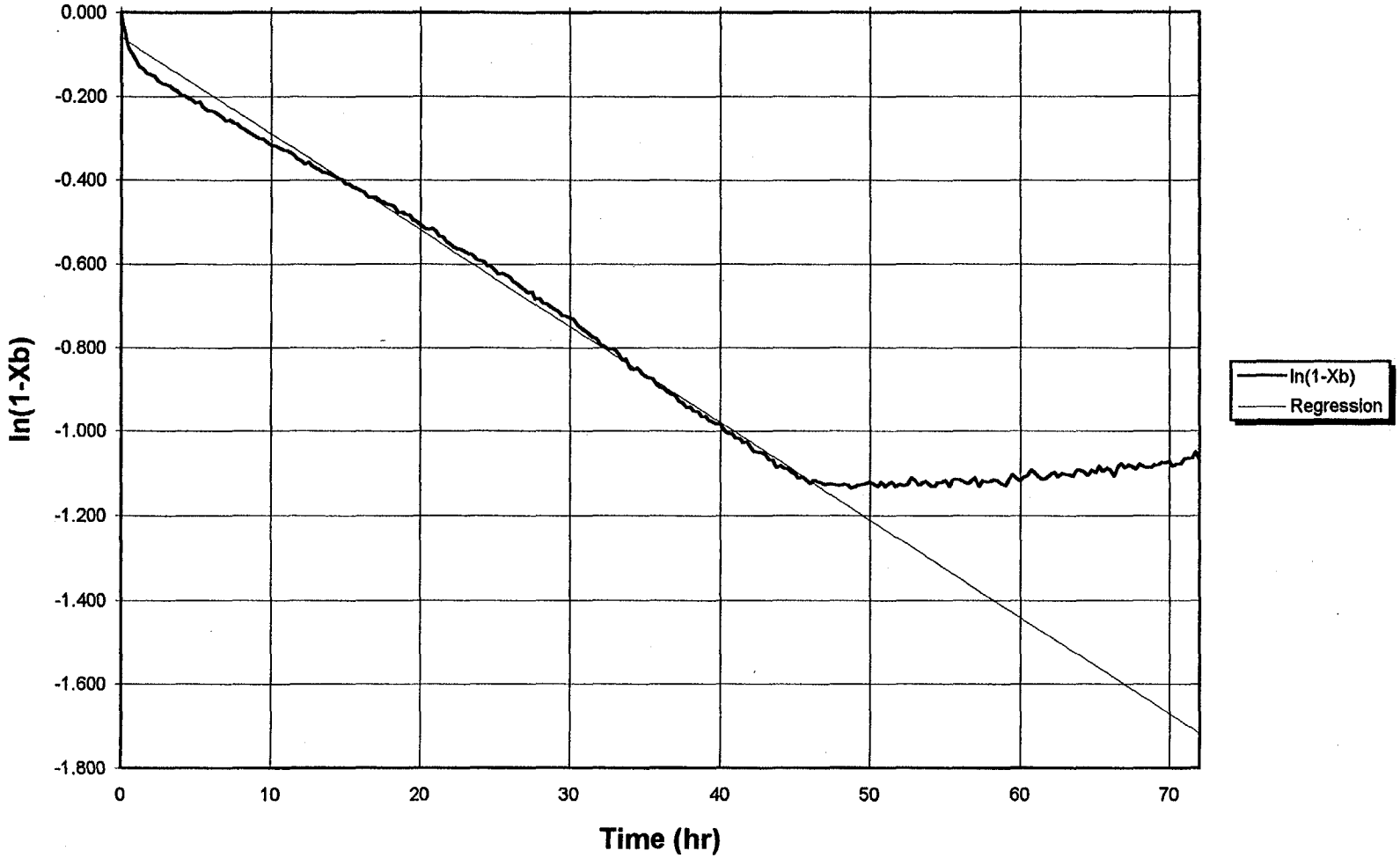

Figure 5.14. Determination of D_c from slope of the uptake curve plotted as $\ln(1-X_B)$ vs time for Run T22.

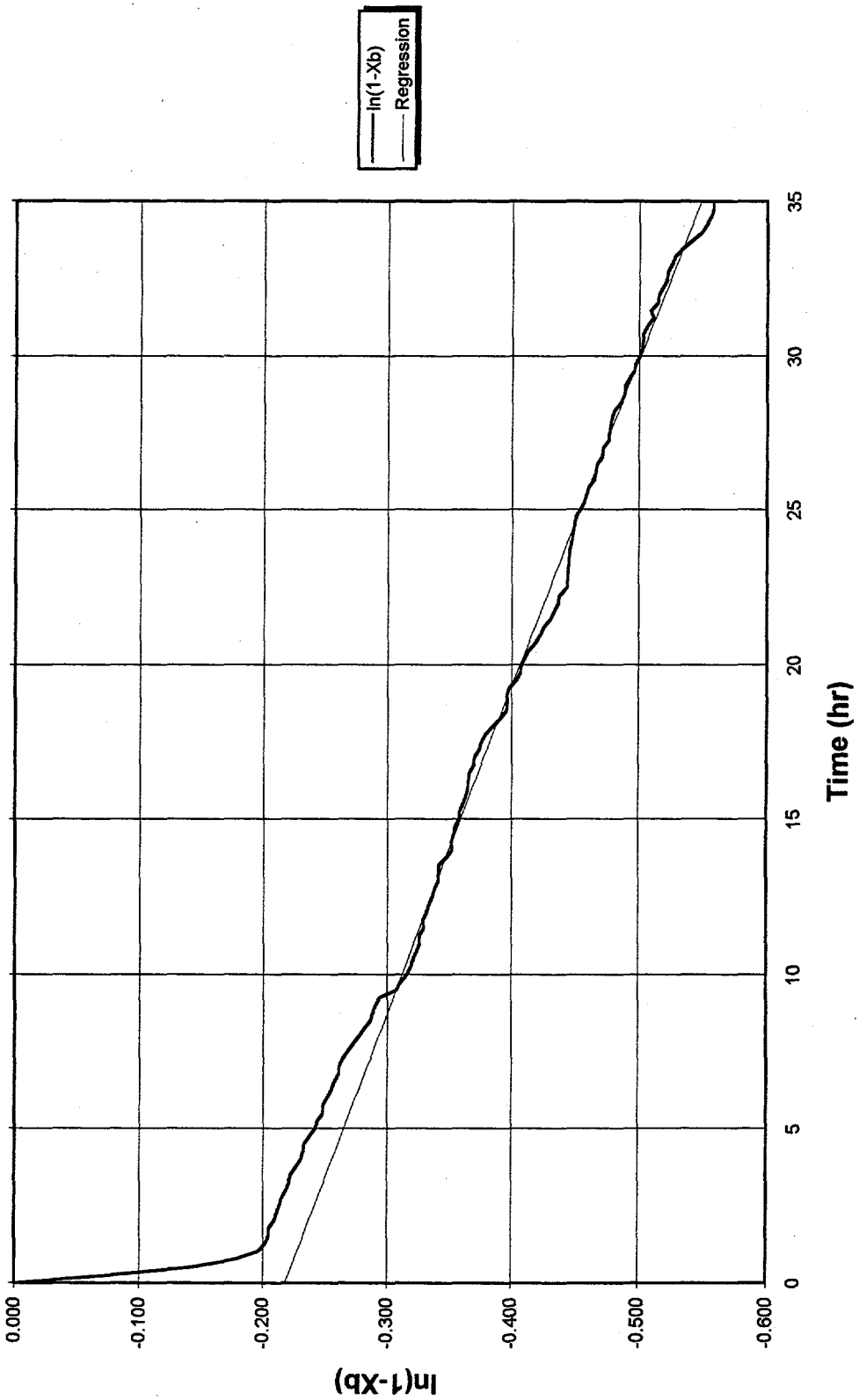

Figure 5.15. Determination of D_c from slope of the uptake curve plotted as $\ln(1-X_B)$ vs time for Run T26.

Table 5.8: Micropore diffusivities calculated from slope of the uptake curve plotted as $\ln(1-X_B)$ vs time.

	Range considered				Weight adjustment to observed	Linear regression of $\ln(1-X_B)$			
Run No.	Beginning time (h)	End time (h)	Beginning conv. (fraction)	End conv. (fraction)	Loading (g)	Slope	Intercept	Correlation coefficient (R^2)	Regressed D_c (cm^2/s)
T3	20	40	0.505	0.685		–5.98E-06	–0.275	0.99	2.42E-14
T6	10	40	0.393	0.744		–7.76E-06	–0.25	0.997	3.15E-14
T7	30	40	0.429	0.571		–8.21E-06	0.331	0.999	3.33E-14
T8	30	80	0.363	0.854		–8.23E-06	0.488	0.998	3.34E-14
T10	10	40	0.082	0.572		–7.10E-06	0.126	0.989	2.88E-14
T10	10	40	0.136	0.621	0.025	–7.73E-06	0.0953	0.991	3.13E-14
T10	10	40	0.185	0.67	0.050	–8.49E-06	0.0669	0.993	3.44E-14
T10	10	40	0.381	0.865	0.150	–1.40E-05	0.0478	0.999	5.67E-14
T11	10	24	0.313	0.475		–5.40E-06	–0.187	0.998	2.19E-14
T12	20	60	0.146	0.384		–2.30E-06	0.00906	0.998	9.32E-15
T13	20	47.25	0.214	0.566		–6.36E-06	0.226	0.997	2.58E-14
T14	10	60	0.159	0.491		–2.78E-06	–0.0698	0.999	1.13E-14
T15	30	80	0.356	0.794		–6.33E-06	0.264	0.998	2.57E-14
T16	30	70	0.525	0.896		–1.07E-05	0.53	0.976	4.34E-14
T16	30	45	0.525	0.678		–7.36E-06	0.0543	0.999	2.98E-14
T16	45	70	0.678	0.896		–1.33E-05	1.1	0.997	5.39E-14
T18	20	70	0.223	0.624		–3.93E-06	0.0409	0.999	1.59E-14
T19[a]									
T20[a]									
T21	45.45	60	0.635	0.772		–9.10E-06	0.454	0.99	3.69E-14
T22	10	40	0.271	0.626		–6.4E-06	–0.0585	0.995	2.57E-14
T26	10	35	0.273	0.428		–2.62E-06	–0.218	0.995	1.06E-14

[a]Not determined due to short run length.

time greater than 10 h. For all runs except for T12, T14, T16, T18, and T26, the value of D_c was between 2.19×10^{-14} and 3.34×10^{-14} cm^2/s.

T12 and T14, which utilized low CH_3I gas concentrations, exhibited lower values of D_c, 9.32×10^{-15} and 1.13×10^{-14} cm^2/s respectively. It has also been noted earlier that both of these runs were subject to some thermal instability in the early readings.

The value of D_c for T26 is also somewhat lower than the rest of the data sets. The calculated value is 1.06×10^{-14} cm^2/s, which in this case could be attributed to the lower bed temperature used in this run since D_c in theory follows an Arrhenius-type temperature response.

T18, which was conducted with a dry air stream, exhibited the same type behavior as the other runs and had a comparable value for D_c of 1.59×10^{-14} cm^2/s, which seemed to indicate that in the long time period the adsorption rate may also be controlled by micropore diffusion.

The data from run T10 were clearly subjected to a thermal upset of the balance. If it were assumed for a moment that the initial weight was in error, (this cannot be proven at this point), the data seemed to indicate that possibly a lower starting weight should have been recorded. Then assuming that the starting weight was in fact lower, then the resulting conversion was higher at any point in time and the resulting value of D_c must also be higher. To illustrate this point, the slope calculations were rerun on T10 with the observed CH_3I loading weight increased by 0.025, 0.05, and 0.15 g. These values were selected based on the magnitude of the drop in weight observed in Fig. 4.23. The

resulting values of D_c were 3.13×10^{-14}, 3.44×10^{-14}, and 5.67×10^{-14} cm^2/s. The higher values of D_c would be expected in light of the higher bed temperature, but this information drawn from the data in this manner was obviously open to question. What can be seen from this exercise was the sensitivity of the value of D_c to errors in the recorded weights and the derived conversion. This also indicated that the value of D_c for run T10 is most likely higher than the narrow range observed for the majority of the other tests.

T16 yielded values for D_c of 2.98×10^{-14} or 5.39×10^{-14} cm^2/s, depending on which portion of the loading curve is being analyzed. It was noted from the run log that there was some shift in the CH_3I feed rate that may have occurred and was not detected until after the weekend. This may have occurred about the time that the shift in the slope occurred.

There was no notable distinction in the values of the determined micropore diffusivity between pellet size or by the addition of supplemental water vapor or any of the variations in the pretreatment steps.

The value for the y-intercept, however, was somewhat scattered. This was attributed to other mechanisms controlling the initial portions of the uptake curve, as will be discussed in the section on the bimodal model. One point worth stating here is that in all cases the y-intercept was numerically greater than the expected value of $\ln(6/\pi^2)$ at time zero. One explanation for this observation was that the observed uptake on the pellets was slower in the initial time periods than would have been observed if all microspheres in the pellet were exposed to a uniform value of CH_3I at time zero. This could occur if there

were a second diffusional process which controlled the CH_3I concentration profile across the pellet in the early time periods.

As noted previously, the Y-12 analytical data reported a fairly uniform distribution of iodine across the cross section of the pellet. A uniform distribution would not be observed in the case of a strictly shrinking core or in a macropore diffusion-controlled situation. This was one of the observations which seemed to support a micropore diffusion playing a role in the overall controlling mechanism.

Some of the scatter may also be attributed to the thermal variations in the balance used and in the resulting weight gain data during the first few hours after the start of the loading phase.

5.2.6 Bimodal Model

5.2.6.1 Curve fitting

By examination of Eqs. (2.61) through (2.63) it can be observed that the bimodal model is defined by three specific parameters in addition to the physical measurement of the particle sizes and porosities. These parameters are the macropore diffusivity, D_p, the micropore diffusivity, D_c, and an equilibrium constant, q_∞/C_o. These can be combined along with the physical measurements into the terms α and β. Clearly, however, a difficulty in this system is that α is a function of both D_p and D_c and β is a function of α. Ideally the solution to this model would be greatly simplified if D_c, D_p, and the equlibrium constant could be determined seperately.

Initially it was attempted to determine the three parameters of the bimodal model, D_c, α, and β, by a multidimensional minimization operation. It was noted during the early attempts to conduct the minimization operations that as the initial search point was varied, the same values of the "optimum" parameters were not always obtained. This was a clear indication of problems in locating a global minimum. Similar behavior was noted by Vaidyanathan (1971). As a result of these concerns, each of the data sets were evaluated over the range of anticipated values for α and β for which the full bimodal model must be utilized.

The ranges were selected to examine the behavior of the model between the bounding conditions and thus under conditions where both mechanisms are important. For values of α less than 10^{-3}, macropore diffusion is much faster than micropore diffusion. In this case, the process can be considered to be a two-step process for all practical purposes, meaning that the macropore diffusion process is virtually complete before the diffusion in micropores begins. For values of α greater than 10^{+2}, macropore diffusion controls. In the range of α between these two limiting cases, both mechanisms are important. Therefore values of α and β from 10^{-3} to 10^{+2} in six even steps on a logarithmic scale were used to create a "surface map" of the errors resulting from a single dimensional minimization of the least square error with the experimental data by adjusting the micropore diffusion coefficient at each node on the map grid. Examples of these plots are shown in Figs. 5.16–5.19. Appendix A.4 contains the summary results from this

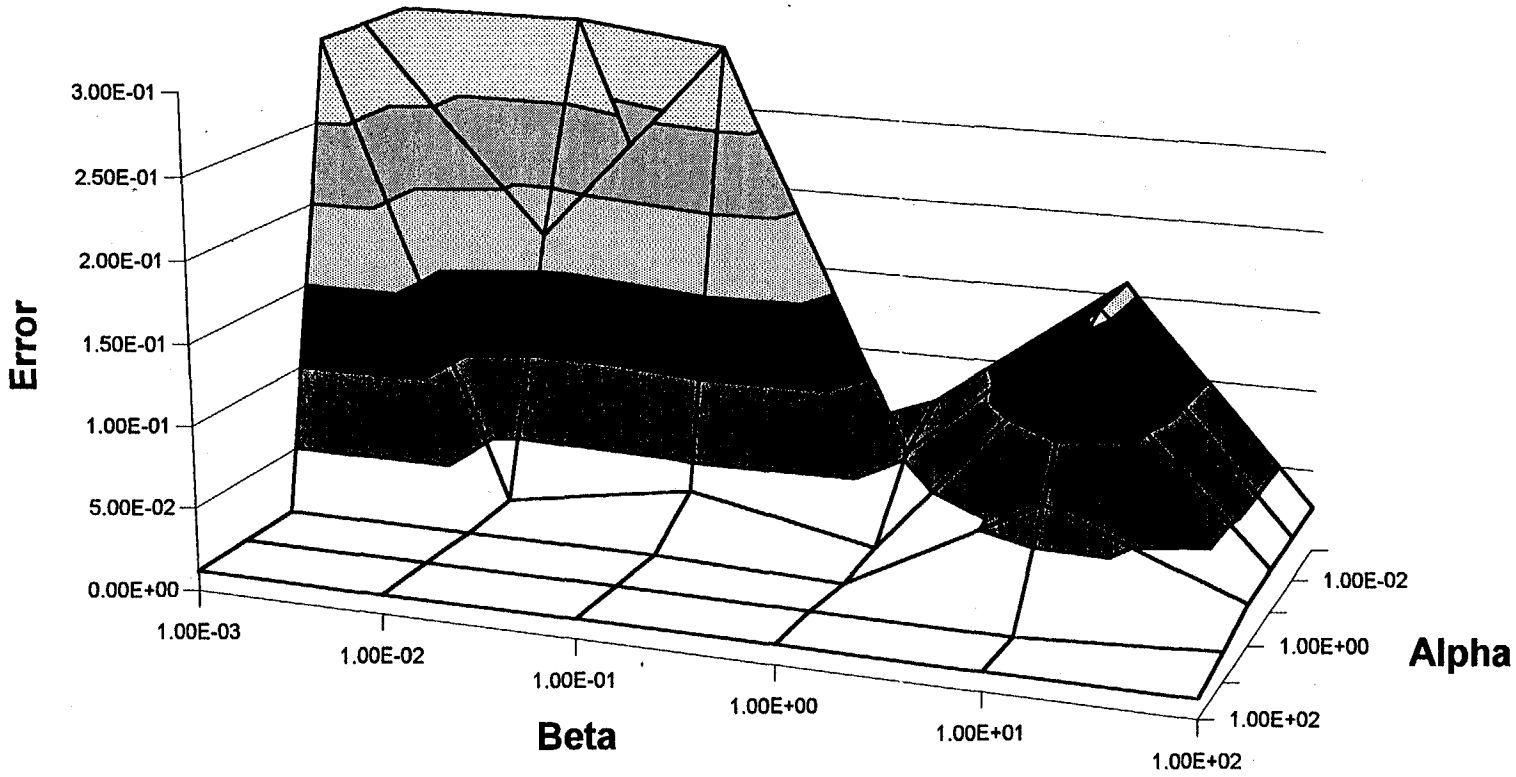

Figure 5.16. Surface map of error term from bimodal model as a function of the parameters α and β for Run T3.

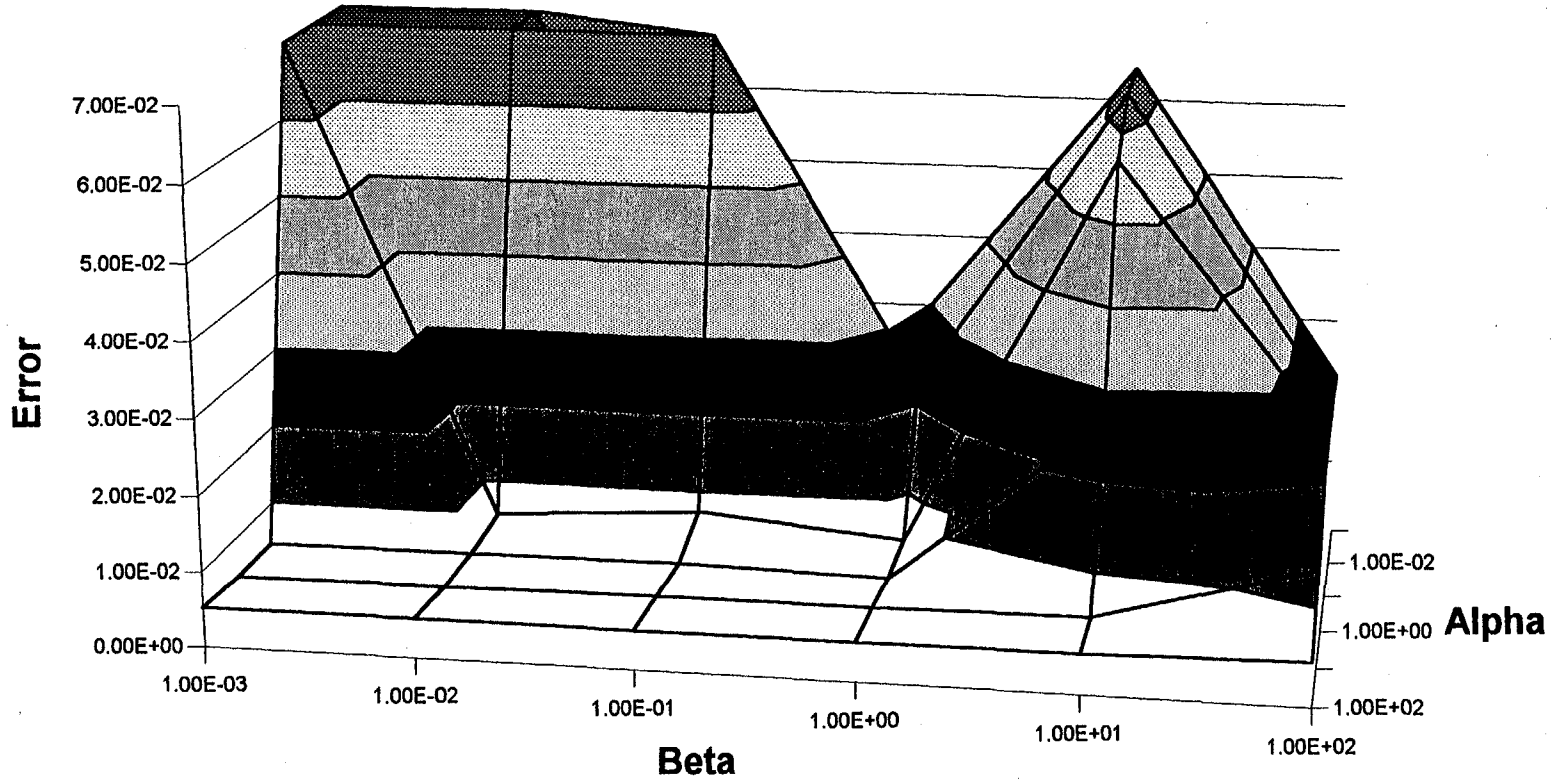

Figure 5.17. Surface map of error term from bimodal model as a function of the parameters α and β for Run T11.

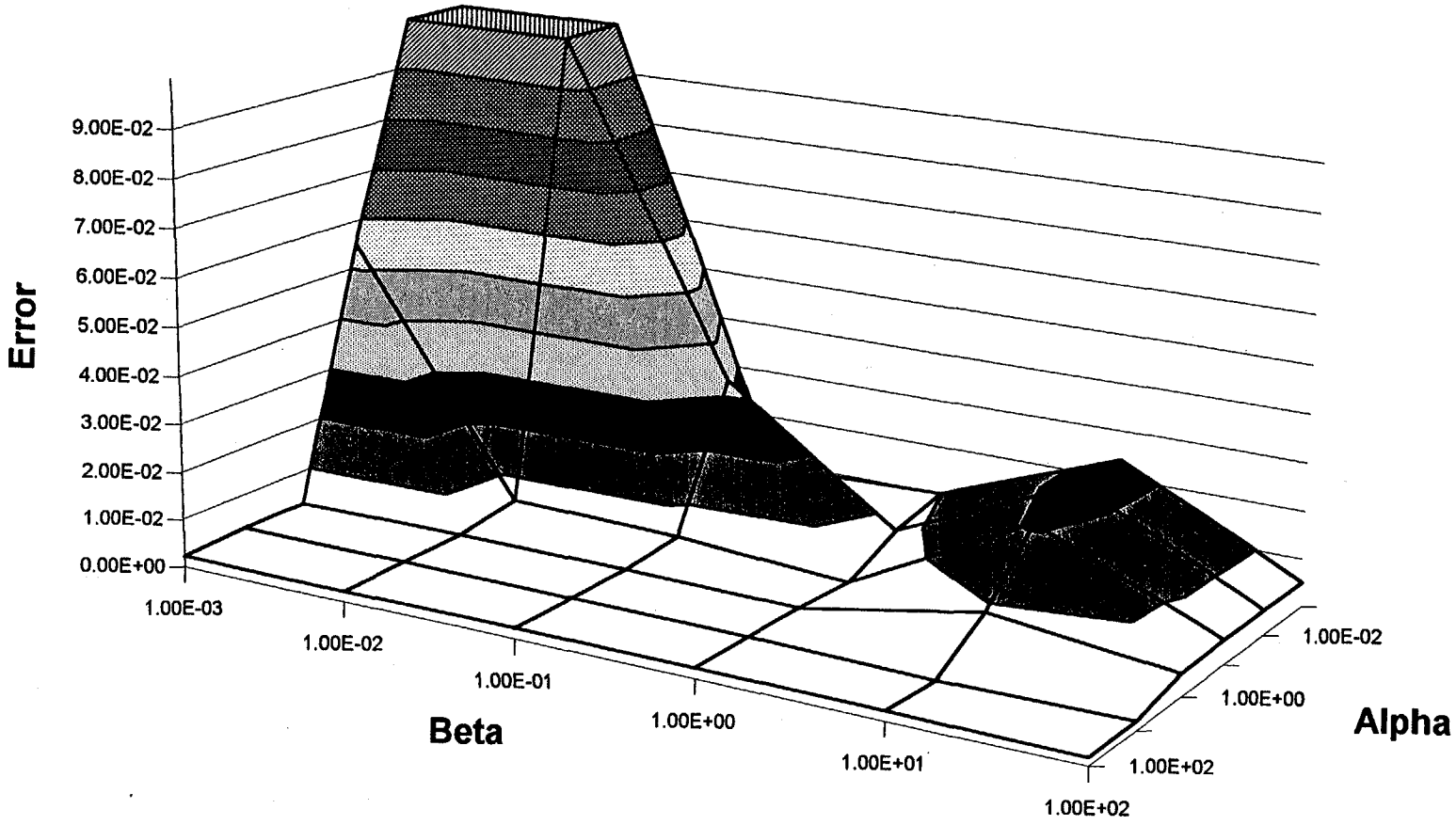

Figure 5.18. Surface map of error term from bimodal model as a function of the parameters α and β for Run T20.

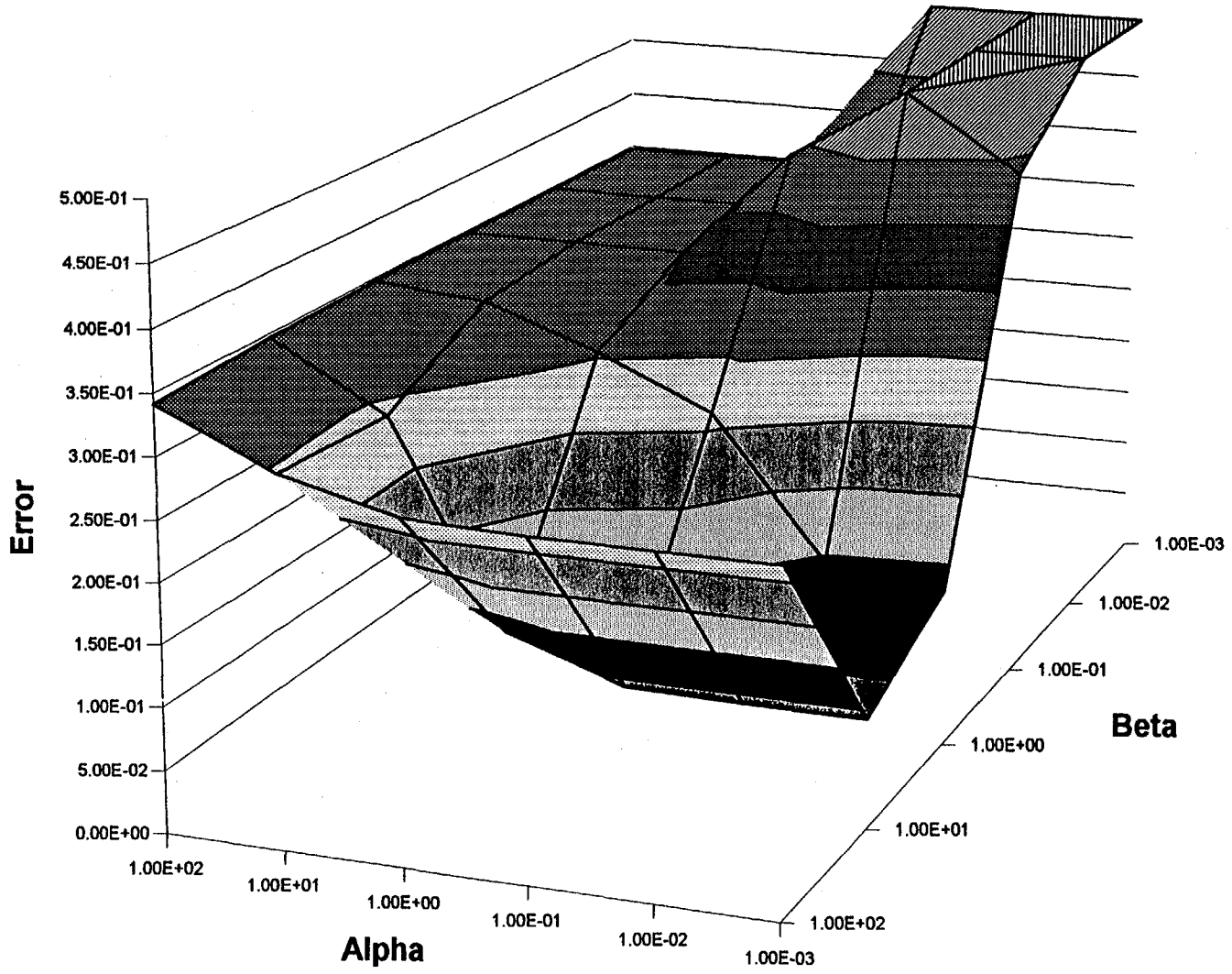

Figure 5.19. Surface map of error term from bimodal model as a function of the parameters α and β for Run T22.

analysis in terms of the parameters D_c, α, β, and the resulting least square error for the analysis of complete data sets.

As can be observed from the plots of the surface formed as a function of α and β, the determination of a "best fit" to the data was not always obvious over the range of values where both mechanisms may be controlling. It was observed that there could be numerous combinations of α and β that by adjusting D_c, provided nearly the same sum of the squares of the error.

In tests T11, T19, and T20 all of which were short-duration runs and had limited conversion, a "plane" of minimum or near minimum values for the sum of the square of the errors was observed. This plane was characterized by high values of α, on the order of 10 to 100 and no clear distinction with respect to the value of β. As the loading increased among these three sets the plane remained, but a shallow minimum point appeared in the region of smaller values of α and with a β value of about 10. This plane at values of $\alpha \geq$ 10 is important in that it has the physical significance of the macropore diffusion resistance controlling case. Runs T3, T11, and T14 (the latter test is subject to some doubts noted earlier) showed an actual minimum point in the range of α's and βs examined. This point was at an α value of about 1.0 and a β value of 1.0 for both T3 and T11. For T14 the α and β values were 0.1 and 10 respectively. The plane remained in all of these cases. Under conditions of high loading or a low loading rate, a valley was formed which began at an α value of about 1.0 and moved in the direction of smaller values of α. The value of β in all of these cases was about 10. The term "about" is used because the actual bottom

of the valley could be on either side of this value and was not explicitly determined in the mapping analysis. The minimum values for the adjustable parameters of D_c, α, and β obtained from the surface mapping approach are summarized in Table 5.9.

Based on the theoretical development of the bimodal model, the ratio of $\beta/(3\alpha)$ should provide some insight concerning the ratio of the microsphere and macrosphere uptake at equilibrium, but since there appeared to be a range of α values that resulted in virtually the same fit, no precise values could be drawn based on this information. The trend in the runs that had high loadings indicated that the ratio of $\beta/(3\alpha)$ was generally greater than 30, and in some cases over 3000, which indicated limited uptake in the macrosphere relative to the microsphere. This would appear to be a realistic value considering the difference in the amount of surface area determined for the macropore and mesopores combined as compared to that of the micropores.

As just noted, it appeared that there could be several values of the adjustable parameters that provided good fits to the experimental data. Shown in Figs. 5.20–5.25 are the calculated loading curves for T6 and T22 as a function of α and β utilizing the value of the diffusion coefficient that resulted in a minimum least squares error for each case. As a result of what appeared to be multiple solutions, it was concluded that this method provided inadequate resolution to clearly identify any "correct" or "more correct" set of parameters to describe the adsorption process of CH_3I on Ag°Z.

The tables of D_c values (Tables A.4.1–A.4.16) determined from the surface mapping approach to locating the best fit to the experimental data were then examined for

Table 5.9. Bimodal model minimums based on error surface mapping.

	Best fit by mapping surface					Best fit by using closest/best match to D_c calculated by slope							
Run No.	D_c (cm^2/s)	α	β	Error[a]	$\beta/3\alpha$	D_c (cm^2/s)	α	β	Error[a]	$\beta/3\alpha$	r_a(cm)	r_l(cm)	D_g[b] (cm^2/s)
T3	2.95E-14	1.000	1.000	7.81E-03	0.333333	2.95E-14	1.000	1.000	7.81E-03	0.333333	0.09808	0.0002	7.09E-09
T6	3.22E-14	0.010	1.000	1.40E-02	33.33333	3.22E-14	0.010	1.000	1.40E-02	33.33333	0.09808	0.0002	7.74E-07
T7	4.23E-14	0.001	10.000	3.40E-01	3333.333	4.23E-14	0.001	10.000	3.40E-01	3333.333	0.19715	0.0002	4.11E-05
T8	3.59E-14	0.001	10.000	4.67E-01	3333.333	3.59E-14	0.001	10.000	4.67E-01	3333.333	0.09808	0.0002	8.63E-06
T10	1.49E-13	0.001	10.000	2.96E-01	3333.333	4.64E-14	0.001	1.000	3.54E-01	333.3333	0.09808	0.0002	1.12E-05
T11	2.00E-14	1.000	1.000	4.11E-03	0.333333	2.00E-14	1.000	1.000	4.11E-03	0.333333	0.09808	0.0002	4.81E-09
T12	1.45E-14	0.001	10.000	5.51E-02	3333.333	1.45E-14	0.001	10.000	5.51E-02	3333.333	0.09808	0.0002	3.49E-06
T13	4.23E-14	0.001	10.000	4.81E-01	3333.333	1.23E-14	0.001	1.000	4.81E-01	333.3333	0.09808	0.0002	2.96E-06
T14	2.60E-14	0.100	10.000	1.98E-02	33.33333	2.60E-14	0.001	10.000	2.21E-02	3333.333	0.09808	0.0002	6.25E-06
T15	3.26E-14	0.001	10.000	5.84E-01	3333.333	3.26E-14	0.001	10.000	5.84E-01	3333.333	0.09808	0.0002	7.84E-06
T16	6.27E-14	0.001	10.000	2.02E-01	3333.333	6.27E-14	0.001	10.000	2.02E-01	3333.333	0.09808	0.0002	1.51E-05
T18	2.70E-14	0.001	10.000	1.58E-01	3333.333	2.70E-14	0.001	10.000	1.58E-01	3333.333	0.09808	0.0002	6.49E-06
T19	1.95E-14	1.000	1.000	2.32E-04	0.333333	1.95E-14	1.000	1.000	2.32E-04	0.333333	0.09808	0.0002	4.69E-09
T20	2.18E-14	0.100	1.000	1.71E-03	3.333333	2.18E-14	0.100	1.000	1.71E-03	3.333333	0.19715	0.0002	2.12E-07
T22	6.50E-14	0.001	10.000	8.72E-02	3333.333	1.95E-14	0.001	1.000	1.31E-01	333.3333	0.19715	0.0002	1.89E-05
T26	6.50E-14	0.001	10.000	8.72E-02	3333.333	1.95E-14	0.001	1.000	1.31E-01	333.3333	0.09808	0.0002	4.69E-06
			Error sum:	2.81E+00					2.95E+00				

[a]Error terms are the resultant sum of the square of the error between the experimental data and the proposed model.
[b]Calculated from a by Eq. (2.62).

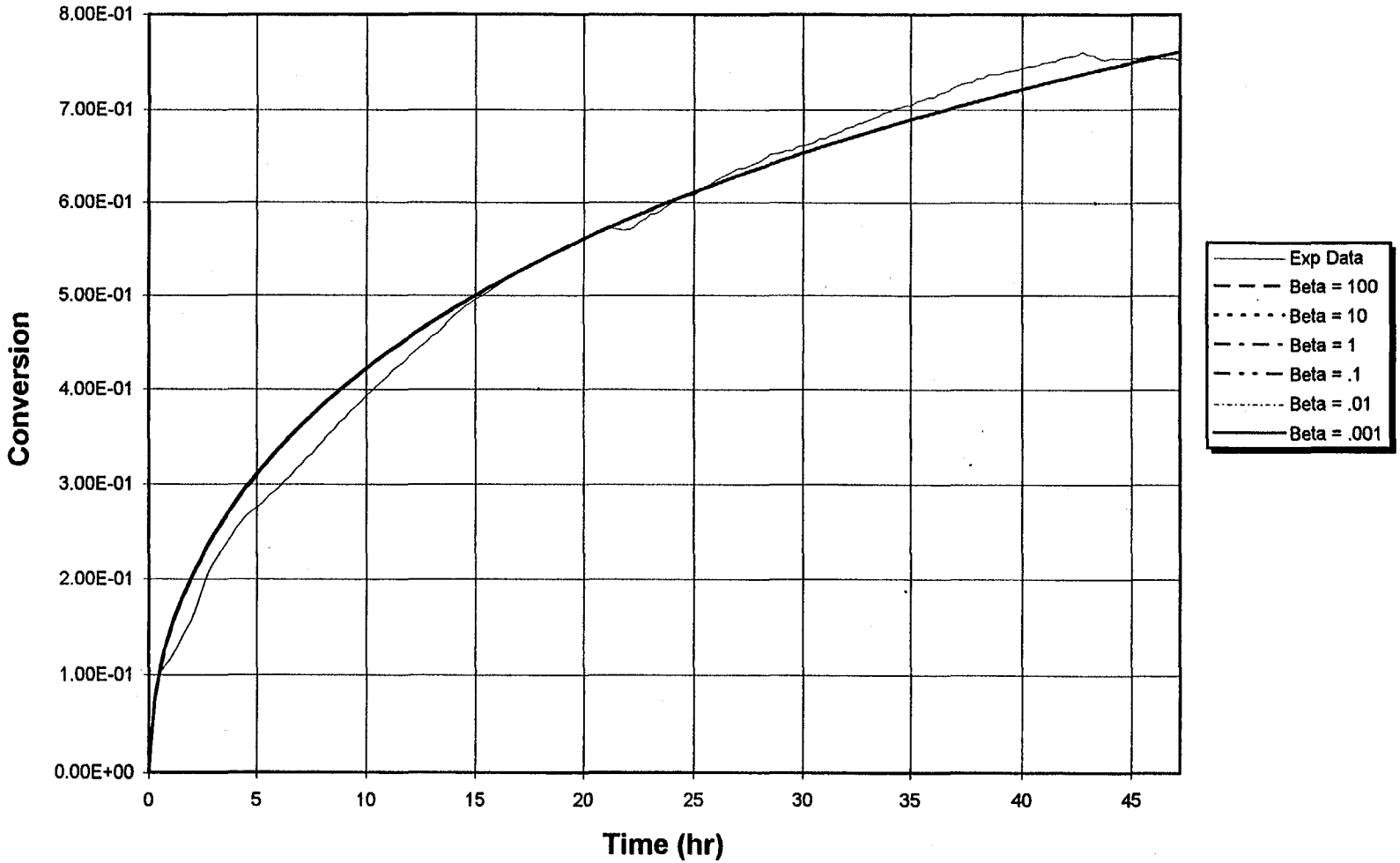

Figure 5.20. Optimized loading curve for run T6 as a function of β holding α at 100.

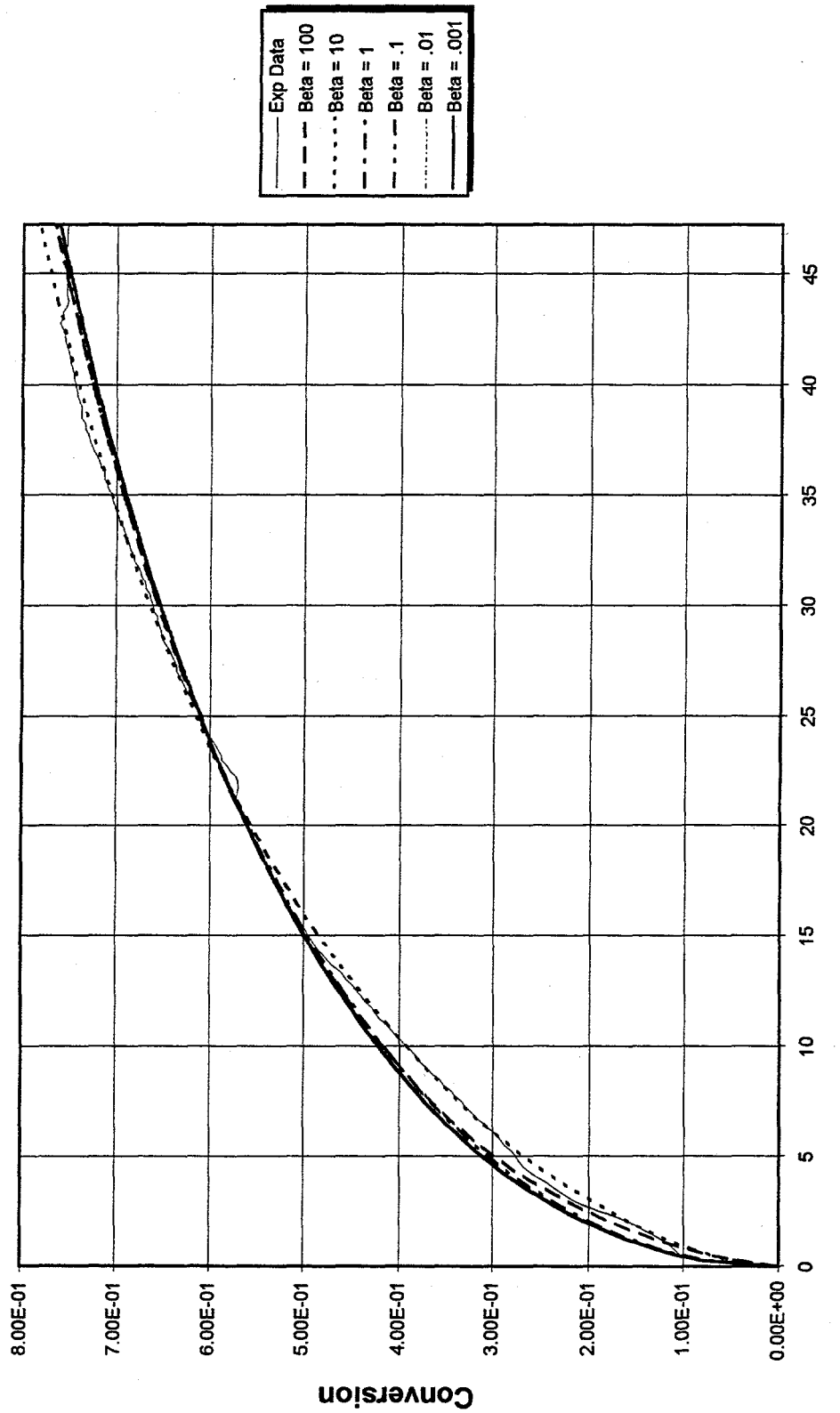

Figure 5.21. Optimized loading curve for run T6 as a function of β holding α at 1.0.

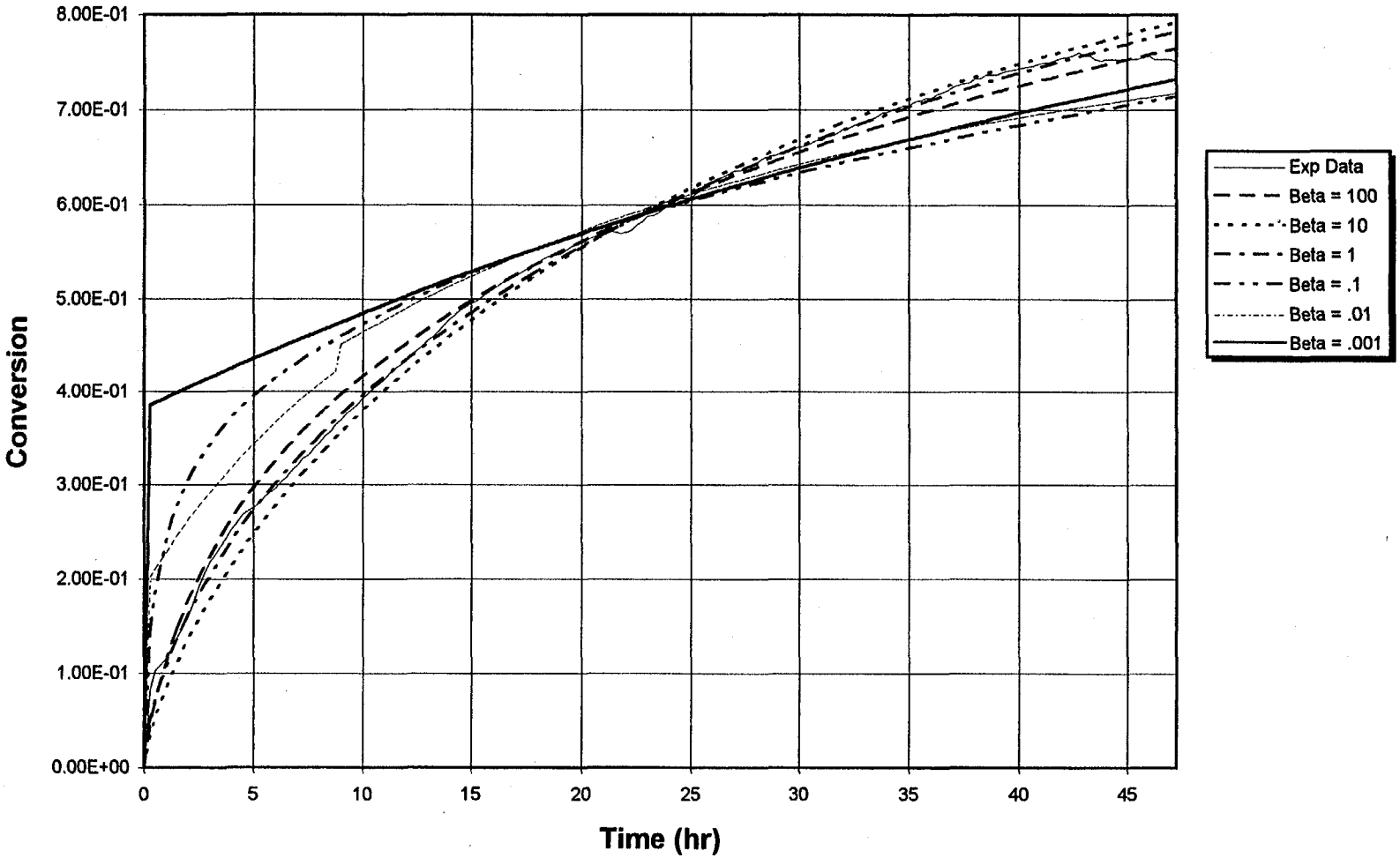

Figure 5.22. Optimized loading curve for run T6 as a function of β holding α at 0.01.

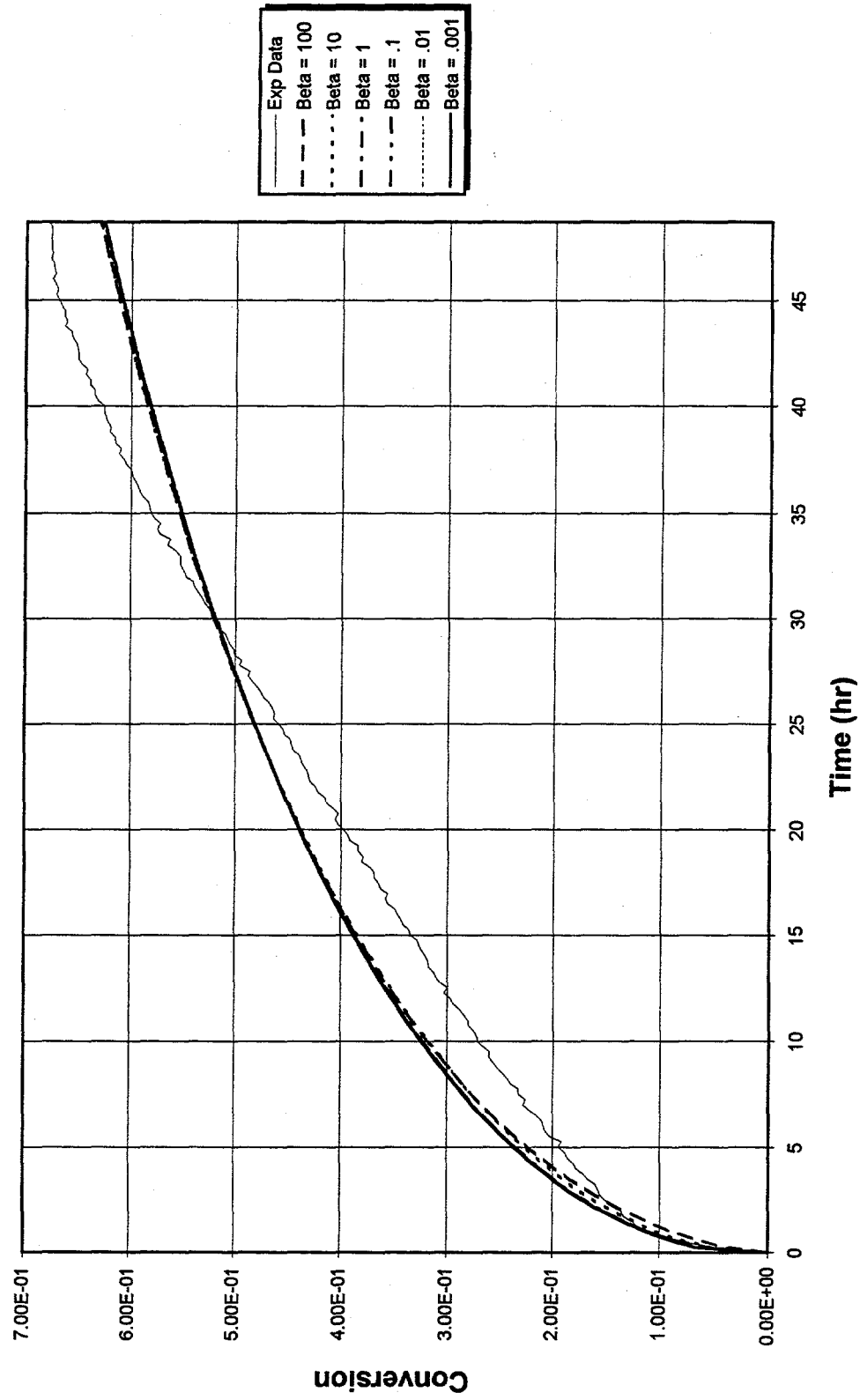

Figure 5.23. Optimized loading curve for run T22 as a function of β holding α at 10.

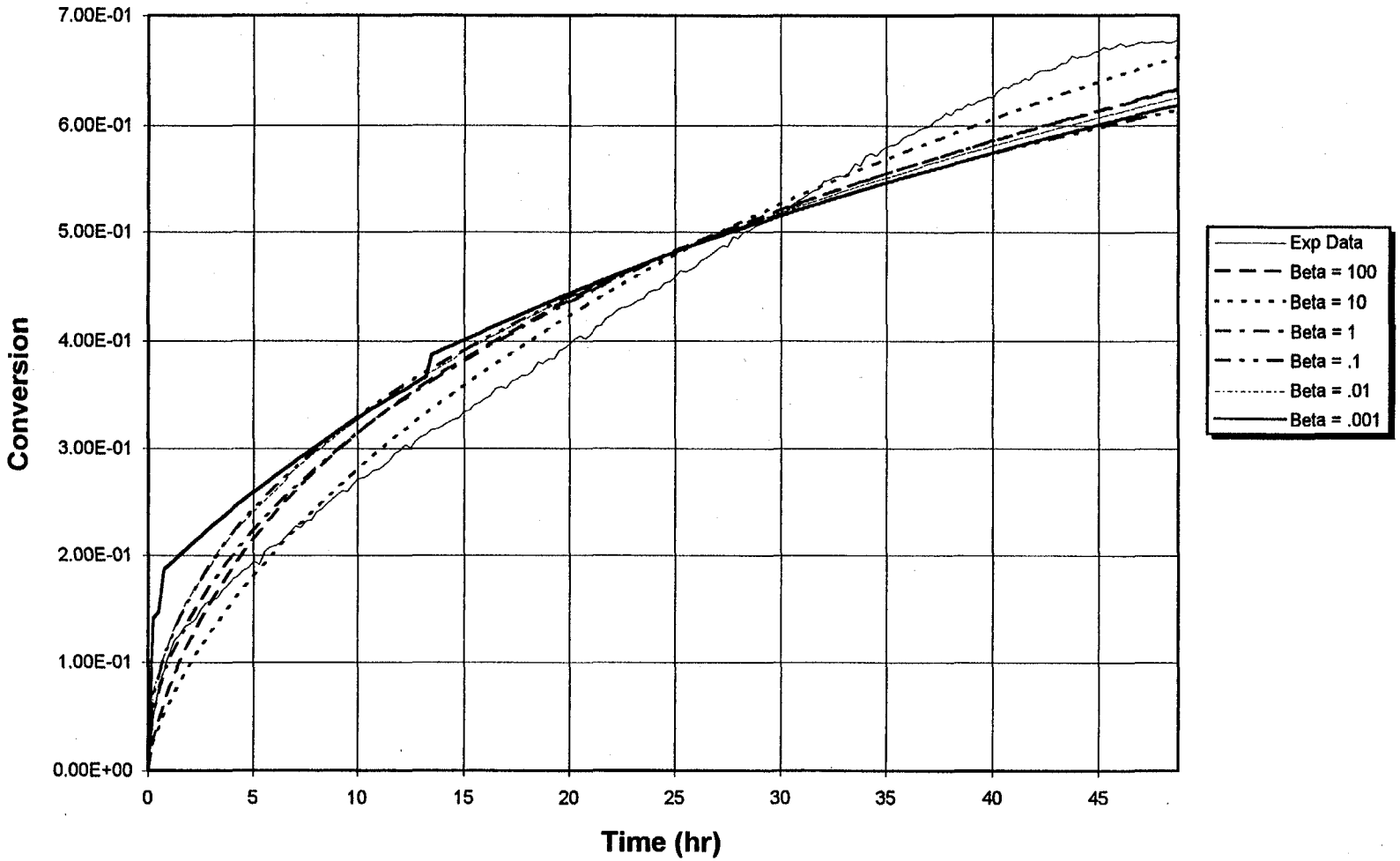

Figure 5.24. Optimized loading curve for run T22 as a function of β holding α at 0.1.

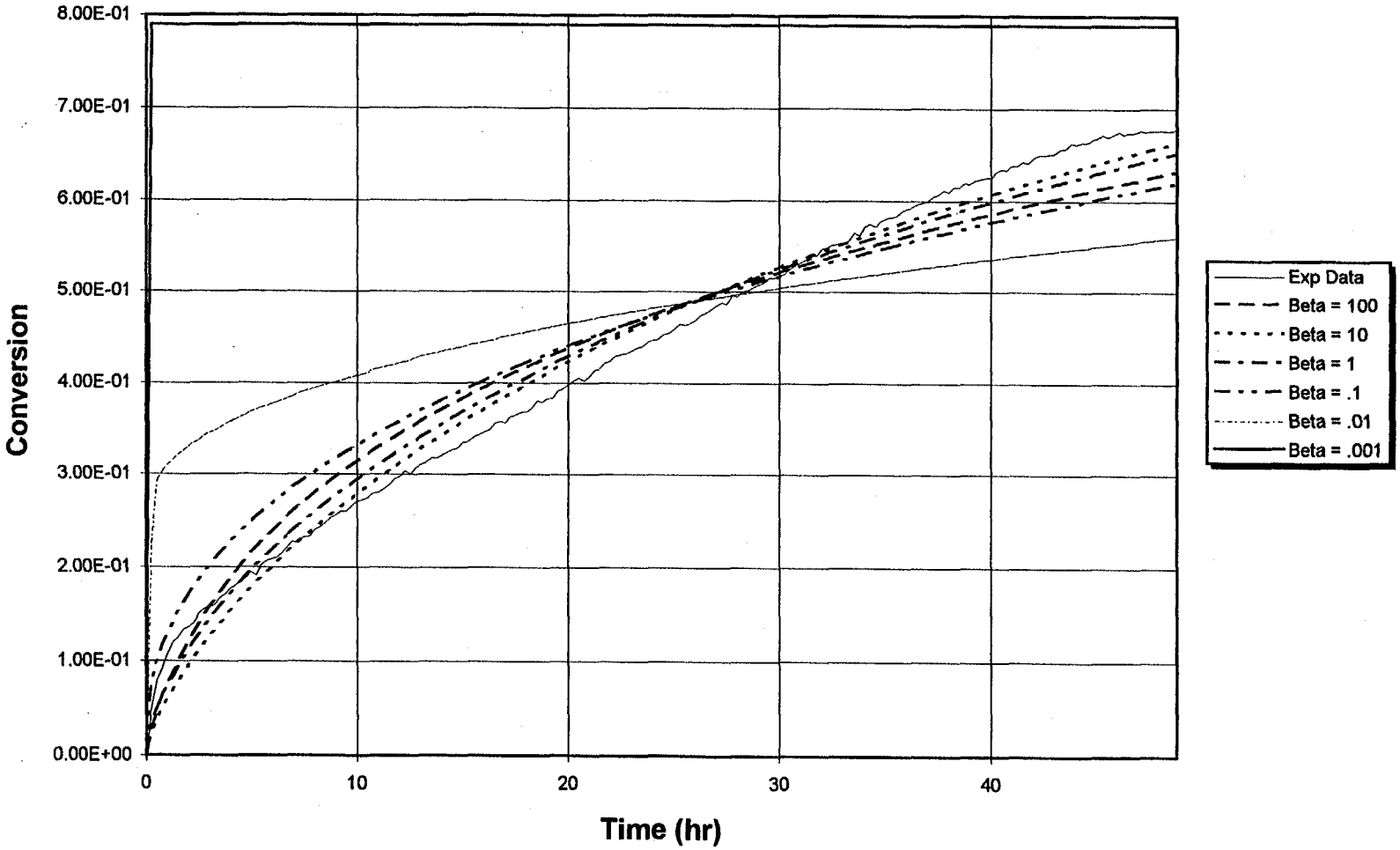

Figure 5.25. Optimized loading curve for run T22 as a function of β holding α at 0.001.

similarities with the values of D_c determined from the evaluation of the slope of the uptake curve plotted as $\ln(1-X_B)$ vs time (Table 5.8). The closest values to the values of D_c determined by the slope method were selected based on the lowest sum of the squares of the errors from the tables of D_c values from the least square curve fitting method. As can be seen from Table 5.10, either the same point in terms of the adjustable parameters α and β or a nearby point yielded virtually the same error term. In most cases the selected values of D_c were associated with α values of 0.001, which indicated primarily micropore diffusion. β values were generally about 10. [Note, however, that an α value of 0.001 is the smallest value evaluated in the table.] Also examined was the "best-fits" obtained using an α value of 0.001 and a β value of 10 for all data sets. The resulting values of D_c, ranged from about 3×10^{-14} cm^2/s to 2×10^{-13} cm^2/s. The total least square error increased about 10%. The relatively very small increase in total error that was observed by selecting common α and β values was not unexpected as there was the possibility of multiple combinations of the parameters that resulted in similar loading curves. The numerical bulk of the added error originated from runs T3 and T26, but the error term for numerous runs increased an order of magnitude.

Ma and Lee (1976) reduced the bimodal-type curve fitting problem to one of a single parameter, the micropore diffusion, D_c, coefficient through the use of calculated values for the macropore diffusion coefficient and the use of experimentally determined values for the other parameters in α and β. For the CaX(Na) zeolite in their study, the macropore diffusivity was estimated based on the Knudsen and molecular diffusivities. A

Table 5.10: Bimodal model minimums based on error surface mapping and values of D_c obtained from the slope of the uptake curve $\ln(1-X_B)$ vs time.

	Best fit by using closest/best match to D_c calculated by slope and $\alpha = 0.001$							
Run No.	D_c (cm^2/s)	α	β	Error[a]	$\beta/3\alpha$	r_a (cm)	r_i (cm)	D_p[b] (cm^2/s)
T3	1.74E-14	0.001	0.100	2.50E-02	33.33333	0.09808	0.0002	4.18E-06
T6	3.30E-14	0.001	1.000	1.40E-02	333.3333	0.09808	0.0002	7.94E-06
T7	4.23E-14	0.001	10.000	3.40E-01	3333.333	0.19715	0.0002	4.11E-05
T8	3.59E-14	0.001	10.000	4.67E-01	3333.333	0.09808	0.0002	8.63E-06
T10	4.64E-14	0.001	1.000	3.54E-01	333.3333	0.09808	0.0002	1.12E-05
T11	1.09E-14	0.001	0.100	1.13E-02	33.33333	0.09808	0.0002	2.62E-06
T12	1.45E-14	0.001	10.000	5.51E-02	3333.333	0.09808	0.0002	3.49E-06
T13	1.23E-14	0.001	1.000	4.81E-01	333.3333	0.09808	0.0002	1.02E-05
T14	2.60E-14	0.001	10.000	2.21E-02	3333.333	0.09808	0.0002	6.25E-06
T15	3.26E-14	0.001	10.000	5.84E-01	3333.333	0.09808	0.0002	7.84E-06
T16	6.27E-14	0.001	10.000	2.02E-01	3333.333	0.09808	0.0002	1.51E-05
T18	2.70E-14	0.001	10.000	1.58E-01	3333.333	0.09808	0.0002	6.49E-06
T19	9.30E-15	0.001	0.100	1.85E-03	33.33333	0.09808	0.0002	2.24E-06
T20	1.47E-14	0.001	0.100	8.99E-03	33.33333	0.19715	0.0002	1.43E-05
T22	1.95E-14	0.001	1.000	1.31E-01	333.3333	0.19715	0.0002	1.89E-05
T26	1.95E-14	0.001	1.000	1.31E-01	333.3333	0.19715	0.0002	1.89E-05
				Error sum: 2.99E+00				

[a]Error terms are the resultant sum of the square of the error between the experimental data and the proposed model.
[b]Calculated from α by Eq.(2.62).

similar analysis was conducted with the data obtained in this study. As shown in Table 4.4, the effective macropore diffusivity for the Ag°Z was about 0.014 cm^2/s and based on the effective Knudsen diffusivity in the mesopores, the overall "macropore" diffusivity was estimated to be in the range of 5×10^{-4} cm^2/s. Finally using the value of D_c obtained from the slope of the plot of $\ln(1-X_B)$ vs time, the effective overall macropore diffusivity along with the physical dimensions, values of α on the order of 5×10^{-6} up to about 8×10^{-5} were obtained. Fairly constant values of all terms should result in a relatively constant value for α; the primary variation in α resulting from the differences in the macrosphere radius. On theoretical grounds there was no obvious basis for significant variations in the macropore diffusivity; but the impacts of the pellet structure were unknown. Based on photographic evidence the values of the crystal radii in the pellet were very similar. The final term in α is the pellet radii, which were well established.

The value of β appeared to be more difficult to establish. Obviously from the definition of β, it was a function of α which in turn was a function of the macropore and mesopore diffusivities. One other significant unknown remained in the β term, which was the value for the adsorption equilibrium constant. This was estimated to be about 3.4×10^5 based on the gas phase CH_3I concentration from run T16 and the highest loading observed on the Ag°Z. The resulting value of β was about 20. At this point, it was felt that the least well established value was that of β, and a third optimization approach was taken to see if some correlation existed between the observed behavior in the early time periods and the value of β with the operational or pretreatment conditions. Table 5.11 is a

Table 5.11: Optimized fit using bimodal model and fixed parameters of D_c based on the slope from the plot of $\ln(1-X_B)$ vs time in the micropore model value and α based on theoretical computed values

Run No.	D_c (cm^2/s)	α	β	Error[a]
T3	2.42E-14	1.28E-05	5.52E-01	4.72E-02
T6	3.15E-14	1.67E-05	8.10E-01	1.77E-02
T7	3.33E-14	7.67E-05	6.80E+00	3.34E-01
T8	3.34E-14	1.77E-05	8.94E+00	4.64E-01
T10	5.67E-14	2.83E-05	1.88E+00	2.56E-01
T11	2.19E-14	1.16E-05	1.02E+00	3.88E-02
T12	9.32E-15	4.94E-06	4.96E+00	5.51E-02
T13	2.58E-14	1.37E-05	4.43E+00	4.70E-01
T14	1.13E-14	5.99E-06	2.46E+00	2.23E-02
T15	2.57E-14	1.36E-05	6.80E+00	5.74E-01
T16	2.98E-14	1.58E-05	2.92E+00	2.02E-01
T18	1.59E-14	8.43E-06	4.24E+00	1.58E-01
T19[b]	2.42E-14	1.28E-05	8.26E-01	6.65E-03
T20[b]	2.42E-14	5.57E-05	4.08E-01	6.41E-03
T22	2.57E-14	5.92E-05	1.98E+00	9.18E-02
T26	1.06E-14	5.81E-06	8.67E-01	2.42E-01
			Total error:	2.99E+00

[a]Error terms are the resultant sum of the square of the error between the experimental data and the proposed model.

[b]Short run D_c from Run T3 was used.

summary of the bimodal model parameters which were obtained through a one-dimensional least square optimization holding D_c to the values established by the slopes of the uptake curve plotted as $\ln(1-X_B)$ vs time and α as calculated using D_c, the calculated effective macropore/mesopore diffusivity, D_p, the measured pellet diameter, and particle diameter determined from the electron microscope images. This in essence moved all of the unknowns and variabilities to the equilibrium term contained in the β expression.

This approach produced relatively good fits to the experimental data. As can be seen by comparing the error terms contained in Table 5.11 with those in Table 5.9 or 5.10, the fits obtained by this method were as good as those obtained from the surface mapping approach to the locating of a global minimum. In several cases, notably T3, slightly higher errors resulted from this approach than in the approach in which multiple parameters were allowed to be adjusted, but the fit with the experimental data was still very good. The overall performance of this model using a single parameter was superior to the shrinking core model with all but one parameter fixed. There was, however, no obvious trend in the resulting values of β. These values ranged from 0.4 to about 9.

Further calculation of other parameters such as the equilibrium constant contained in the β term from the values of the parameters determined as described above was not thought to be valid for several reasons. First, when one parameter is determined from a second fitted parameter, the uncertainties tend to accumulate in the resultant value. Second, in this determination, since the value of D_c was determined from the slope of the uptake curve plotted as $\ln(1-X_B)$ vs time and α was calculated from this value and other

theoretical and measured terms, all of the uncertainties will be accumulated in the single adjustable parameter. Third, as noted from the photographs of the pellets there can be significant variations in the structure which in turn could impact the macropore diffusivity. Since the theoretical value of D_p was used, any variation from this value would end up being observed in the fitted value of β. It will be shown in Sect. 5.3 that moderate variations in the theoretical values of D_p will not have an impact through α on the least squares regression of the data to the proposed model. And finally, the nature of the experiments conducted was not directed toward the determination of terms such as the equilibrium constant. Therefore, it is believed that any such secondary value would be of questionable validity.

5.2.6.2 Analysis of the derived parameters and the resulting data fits

This study has shown that there is a slow (micropore) diffusional process controlling the latter portion of the uptake curve and that the value of the diffusivity associated with this phase of the uptake was consistent over a number of runs. Based on the value of α obtained for the bimodal model, it was also shown that the process can be considered to be occurring in two steps. The time constants for the two processes are such that the macropore diffusion was virtually complete prior to any significant micropore diffusion occurring. Thus there was a shift in time prior to the start of the micropore adsorption. In the case of the bimodal model and this process, this shift can be explained in two ways. The first is that the shift is related to the time over which the adsorption/reaction occurs in the macropores prior to the second step in which the

micropore diffusion controls. The second is tied to the formation of the silver nodules shown in the scanning electron microscope images.

One measure of this time shift was the observed shift in the y-intercept of the line describing the uptake curve plotted as $\ln(1-X_B)$ vs time in the long time period. If no macropore diffusional resistance were observed and all microsphere were subject to a bulk phase gas concentration equal to the bulk gas phase at time = 0, then only the micropore diffusional rate would be observed. In this case, the y-intercept would be the given by $\ln(6/\pi^2)$. However, with macropore diffusional resistance and adsorption occurring in the initial phase, there is some finite time period required at any point in the pellet before the concentration of the CH_3I becomes nonzero and even longer before it reaches the bulk equilibrium concentration. This delay shifts the start of the micropore diffusion and the associated micropore uptake. Thus for any given value of D_c obtained by the slope method, the actual conversion at a given time will be less than that predicted by the micropore diffusion alone utilizing the derived value of D_c.

The quantity and rate at which iodine was adsorbed in the macropores is then a function of the available surface area, the nature of the macropore structure, and the quantity of available silver. Based on photographic evidence, the available surface area and the pore structure was quite variable and could not be predicted by any of the process measurements made during each of the test runs. The available silver may be related to the "nonframework" silver cations in the mordenite structure, to any silver on the surface of the mordenite crystals, and to the silver nodules that appear after the hydrogen

pretreatment. As will be discussed shortly, this may also be quite variable and the magnitude of the variation was unknown for each run. This macropore diffusion control in the initial time period would also appear to explain the appearance of the shrinking core that vanishes by the time 20 to 30% conversion occurs. One other point on this topic is that the term macropore or bimodal, in the case of this material, is a significant simplification. As noted in Sect. 4.1.3, the pore sizes range from 20 Å to 10 μ with a peak in the macropore region occurring about a pore diameter of about 1 μ. Thus a continuum of pore sizes existed.

All of this raises the obvious question of the value of the more theoretical approach used in the determination of α which in turn was used to obtain β. First, considering α, as noted there was the possibility for significant structural variations in the pellet which may have impacted the macropore diffusivity. Ideally, the macropore diffusivity could be determined from experimental data obtained in the very early time periods of the adsorption process prior to any significant micropore diffusional interaction. The use of the flowing gas stream, the balance sensitivity, and the data recording interval used to collect the uptake data did not lend itself to the determination of loading rates over very short time increments. In addition, the experimental data for several runs were clouded slightly in the first few time increments by the possible thermal upsets of the balance. Finally there was also the possibility of wide variations in the macroporous structure of the AgZ pellets. These structural variations are clearly shown in Figs. 4.1–4.9. A separate study is needed to evaluate and determine the macropore diffusivity.

Such a study should be conducted on very well characterized Ag°Z pellets probably utilizing a different experimental configuration such that thermal upsets in the balance system can be avoided. The factors that would appear important would include the quality/uniformity of the mordenite crystals, the macropore structure, and finally, the number, size, and total silver content of the silver nodules.

These structural variations must also be considered in the evaluation of the β value, which addresses the equilibrium uptake ratio for the micropore to macropore. One unanswered question raised by this study is the extent to which the macropore surface area was altered by the structural changes noted in the photomicrographs and what was the resulting impact of the diffusion rates and quantity of CH_3I adsorbed. Certainly higher macropore surface area was expected in the case of the very irregular mordenite crystals shown in Figs. 4.8 and 4.9. Since there was no attempt made in this study to characterize each pellet in the test bed or even to obtain pore size and surface area data from each test bed, it was assumed in this analysis that the data from the specimens analyzed was representative of the beds in general.

Another factor that must be considered in the overall analysis was the formation of the silver nodules and the role that these played in the loading process. The extent to which these entered into the observed loading could not be determined by the data obtained in these studies. Several things were unknown about the silver nodules. The first was the relative quantity of silver contained in the nodules as compared to that remaining within the microporous mordenite structure. Jubin (1980, 1982) reported that following

regeneration of the iodine loaded Ag°Z with 4.5% hydrogen in argon at 500°C, silver nodules >8000 Å diam were observed and that a significant loss in loading capacity was noted for the reused Ag°Z in tests utilizing a fixed bed length and which were terminated when the bed effluent concentration dropped below a per specified target DF. This was believed to be the result of a reduction in the number of readily available silver sites. Some limited data were available in the form of the X-ray fluorescence data described in Sect. 4.1.1. Walker (1994), in the analytical report describing the reading of the images, indicated that the silver nodules observed in the low loading tests, T19 and T20, contained very little or no iodine. It was certainly not known if these nodules contained any type of pore structure or whether iodine loading in the nodules would have been observed at substantially higher loadings. Clearly additional research is still needed to understand the potential positive or negative role played by the silver nodules. Questions which need to be addressed include:

1. Is the silver contained in the nodule reacted at high loadings or is only the surface reacted?

2. If the interior silver is reacted, what is the rate at which it is reacted?

3. Is the reaction of the interior silver associated with a shrinking core behavior or that of a shrinking particle, in which the AgI product "flakes off?"

4. Is all of the silver accessible to the iodine, and if so does the subsequent reaction with the silver in any way result in some type of pore blockage?

This potential impact of the silver is the basis for the second explanation for the shift. This explanation is in many ways similar to the first but focuses the second step entirely on the presence of the silver nodules formed as a result of the hydrogen reduction

step. Certainly the presence of free silver in the midst of the mordenite crystals cannot be completely ignored as silver is a key reactant in this process. It was not known to what extent the available silver in the mordenite structure was reduced by the formation of these nodules but obviously some reduction must have taken place to account for the mass in the nodules. The hypothesized behavior of the system under this explanation could also be described by the use of the same model in which the second step was diffusion of the CH_3I into the silver nodules and subsequent reaction, in which case there may be a possible three-step process occurring. Here the slowest step is the silver nodule diffusion step, and in this model the macropore and micropore diffusion would be combined into a single effective diffusivity. In this case, the apparent time shift prior to the onset of the second diffusion process would be attributed to the time required to complete the adsorption and reaction with the silver contained in the macropores and micropores. This is then followed by the slow step in which the iodine diffuses into the silver nodule and is reacted to form AgI there. A possible indication that this latter explanation was credible is the X-ray fluorescence data from Y-12 (Walker, 1994) that indicated that the silver nodules observed in the low loading tests, T19 and T20, contain very little iodine. This could also mean that for all practical purposes once the silver forms a nodule it has effectively reduced the overall available silver by the amount included in the interior of the nodule and in this case the first explanation is more reasonable. This brings us back to the need for additional research to understand the role played by the silver nodules.

Finally a few words are also needed on run T18, which was conducted with a "dry" air stream. As noted in the previous section, this run exhibited the same type long-term behavior as the other runs and had a comparable value for D_c, indicating that in the long time period the adsorption rate may also be controlled by micropore diffusion. However this run can also be adequately modeled by the shrinking core reaction controlled model. The shrinking core model in this case, accurately described the uptake observed in the initial time period, which was not accomplished with the bimodal model. It was thought that during the initial uptake period, in which the macropore diffusion would normally be controlling in the bimodal model, the reaction rate was controlling the uptake on the pellet due to the low concentration of available water. In the micropore diffusion-controlled region, the second step of the bimodal model, the overall reaction rate increased due to the increased area in the micropores. This resulted in an overall reaction rate that was now faster than the diffusion rate and hence the observed loading rate was controlled by the diffusion process. This analysis assumed that the rate constant, in fact, remained constant. The calculated reaction rate to achieve the same rate of loading in the case of a shift to the microsphere is about 1.2×10^{-4} cm/s. This was compared to the observed rate constant for the macrosphere of about 5.9×10^{-2} cm/s. The reaction rate should be independent of the pellet/particle size and thus it was inferred from this that while the loading in the macropores was reaction rate limited, the uptake in the microspheres in diffusion rate limited. Obviously this conclusion was based on a single run. Additional tests utilizing

both a very dry gas stream and different size pellets as well as possibly a test bed composed of the single crystals should be conducted to verify these conclusions.

This study has determined a consistent "micropore diffusion" rate on the order of 2×10^{-14} cm^2/s. It has also been shown that the bimodal model adequately explains the observed uptake behavior and photographic as well as x-ray evidence. It has further been shown that the adsorption process described by this model can be considered a two-step process. This information is important since it is the rate of the second step that ultimately controls the final bed loading rate if high bed loadings are desired. There are, however, several questions concerning the impact of the many process and structural variables still remaining to be answered. But even without the answers to every new question raised in this study, a significantly deeper fundamental understanding of the CH_3I adsorption processes onto Ag°Z has been achieved.

5.3 SENSITIVITY OF BIMODAL MODEL PARAMETERS AND ESTIMATE OF EXPERIMENTAL ERROR IN THE EXPERIMENTAL DATA

The following discussion examines the sensitivity of the bimodal model to variations in the three adjustable parameters. All of the following comparisons were done utilizing the experimental data from run T22. This run was selected for this analysis because it was not "perfectly" fit by the model as are some runs yet it does not exhibit an "abnormally" shaped loading curve either. The reference values are those determined by optimizing the value of β while utilizing the value of D_c obtained from the slope of the uptake curve plotted as $\ln(1-X_B)$ vs time and the theoretical value of α determined as

described above. In this case the standard or reference values will be D_c value of 2.57×10^{-14} cm^2/s, α of 5.92×10^{-5}, and a β of 1.98.

Figure 5.26 shows the predicted loading curve in terms of conversion for variations in the value of D_c while holding the values of α and β fixed. The value of D_c was changed by ±20% from the reference condition. In this case the shape of the uptake curve clearly showed the change in the diffusion coefficient.

Figure 5.27 shows the predicted loading curve in terms of conversion for variations in the value of β while holding the values of D_c and α fixed. The value of β was changed by ±20% from the reference condition. In this case the shape of the uptake curve exhibited a shift in the conversion, but the uptake curves in the long time region were nearly parallel.

When the value of α was altered in a similar fashion, virtually no change in the uptake curve was observed. In fact, the maximum change in conversion between the +20% and –20% values of α was less than 0.5%. Shifts in α of several orders of magnitude also produced virtually no change. This is consistent with the value noted on the error surface maps. Figure 5.28 shows the predicted loading curve in terms of conversion for variations in the value of α while holding the values of D_c and β fixed. The value of α was increased to 5.9×10^{-3} from the reference condition with virtually no impact. This is easily explained by the physical significance of the α term. When the value is less than 10^{-3}, the process can be considered a two-step process and thus the behavior in the initial time period has virtually no effect on the behavior in the long time periods.

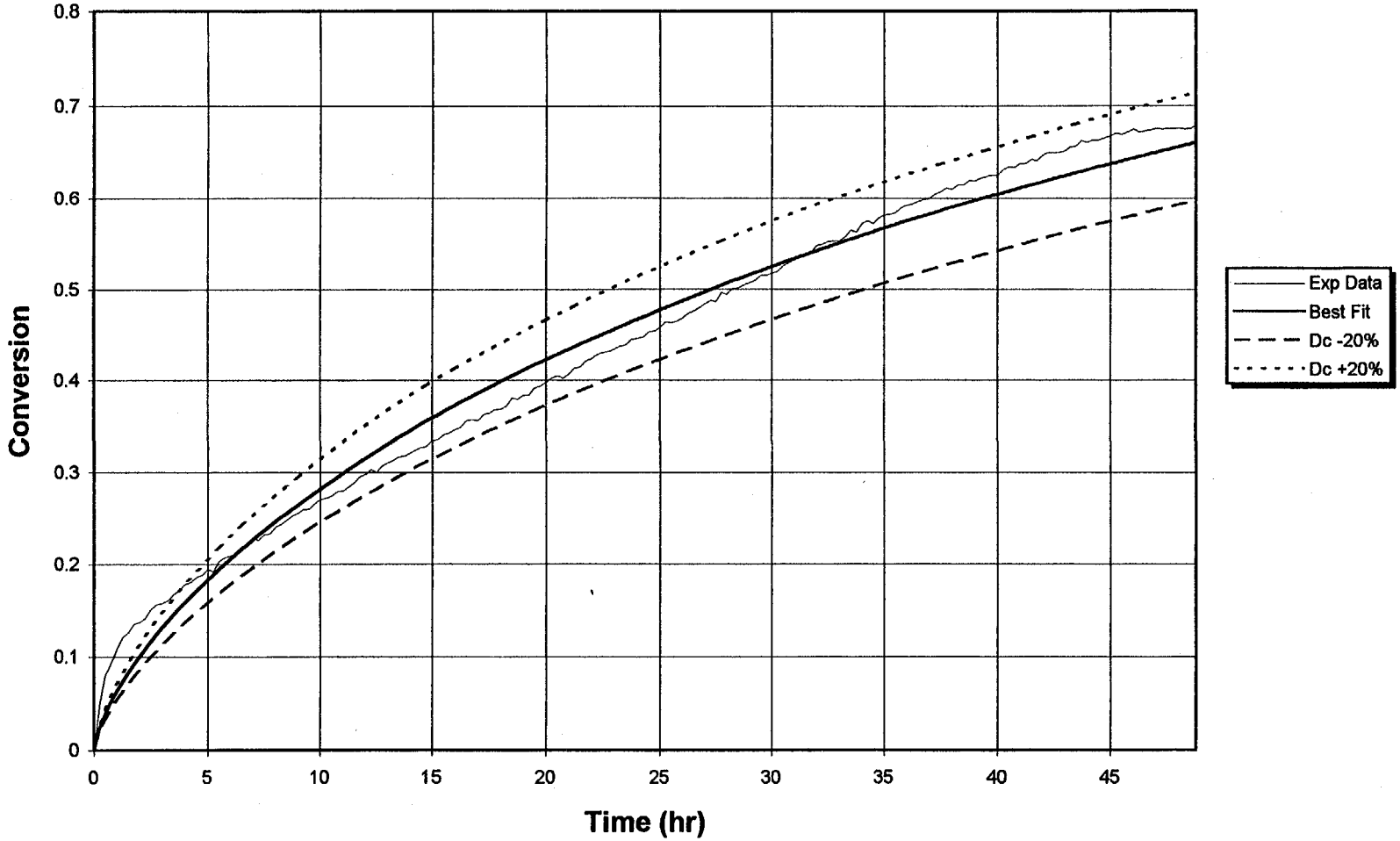

Figure 5.26. Predicted loading curve in terms of conversion for variations in the value of D_c while holding the values of α and β fixed.

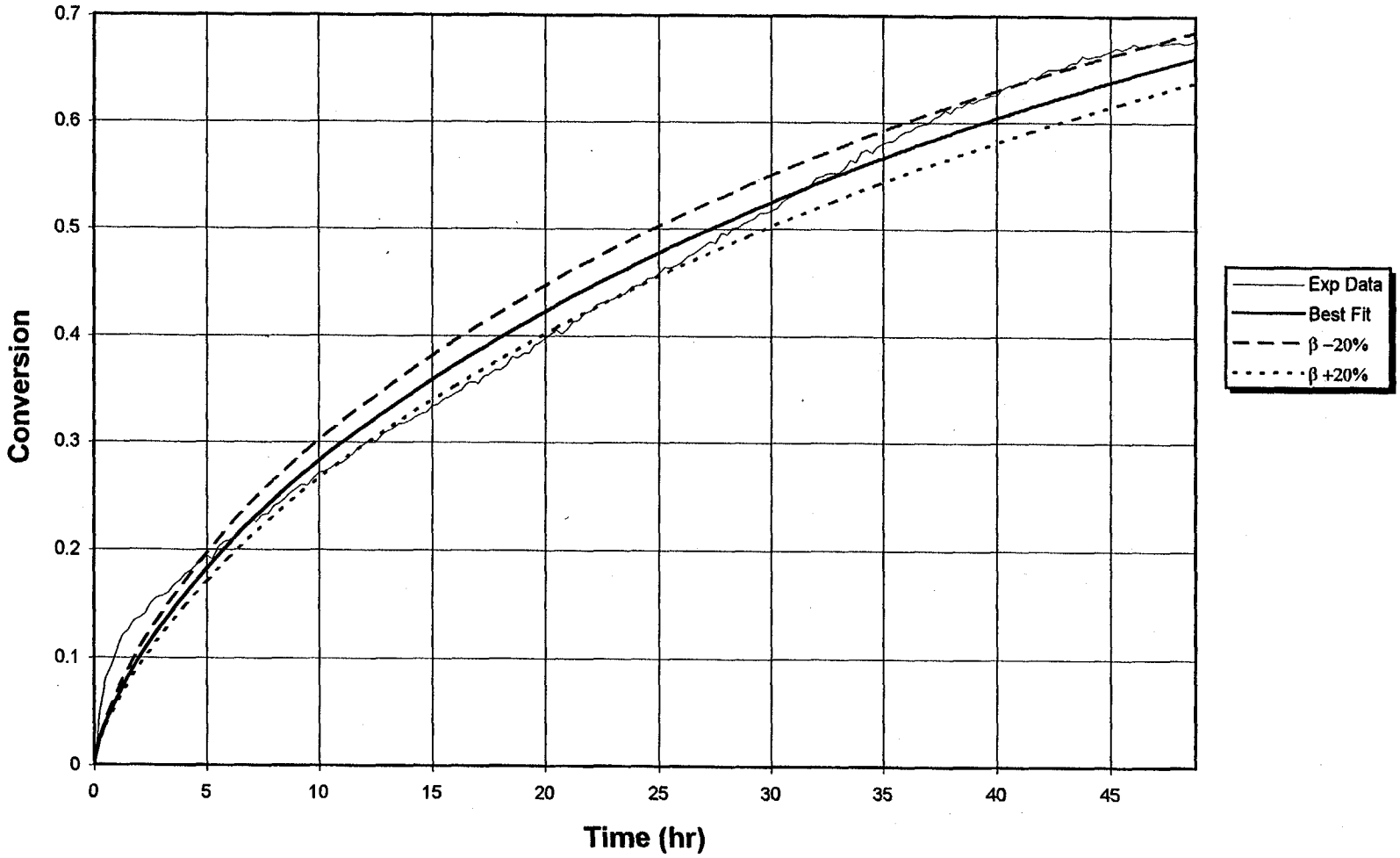

Figure 5.27. Predicted loading curve in terms of conversion for variations in the value of β while holding the values of D_c and α fixed.

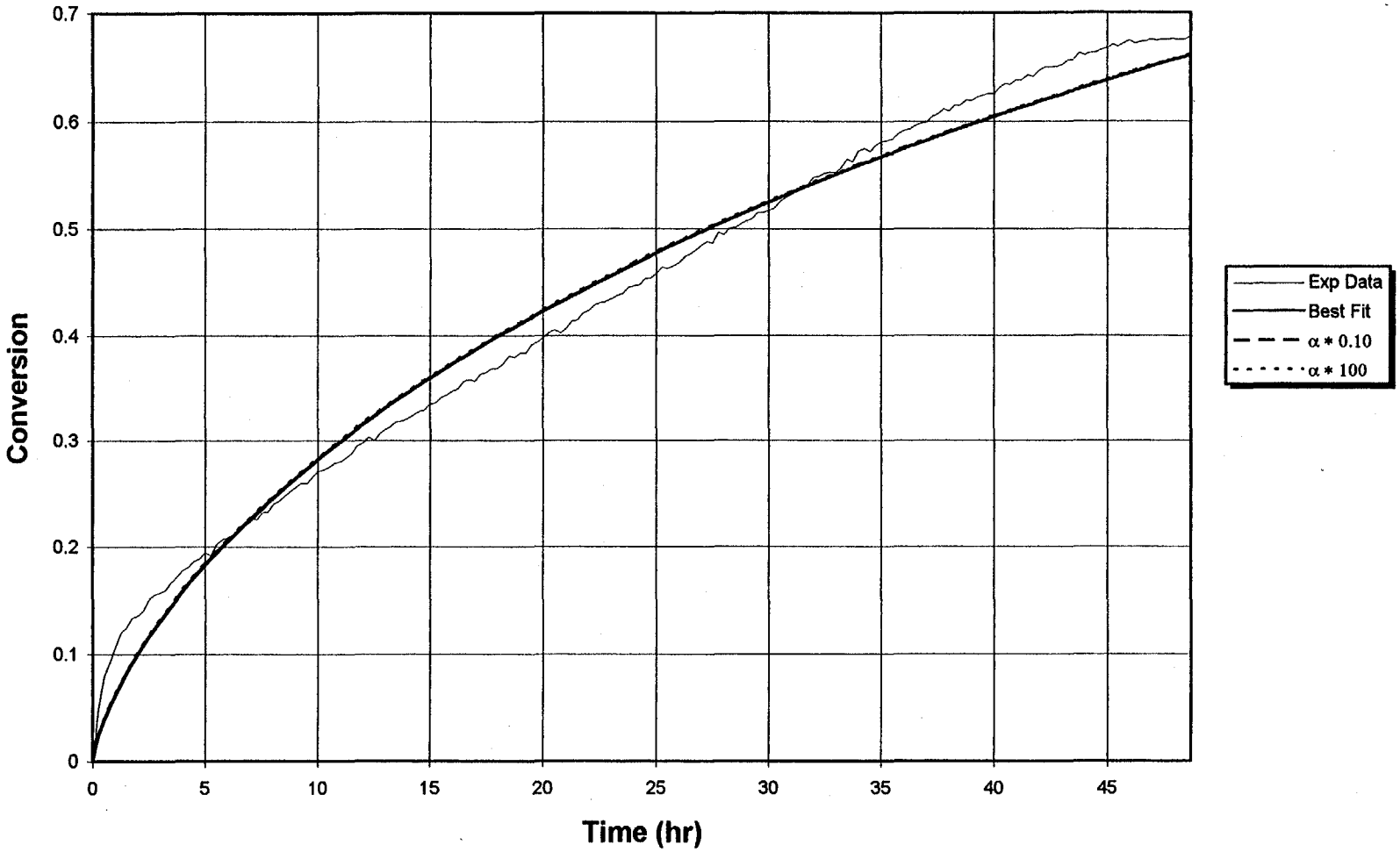

Figure 5.28. Predicted loading curve in terms of conversion for variations in the value of α while holding the values of D_c and β fixed.

The final example of the model sensitivity was conducted by altering D_c ±1 order of magnitude and fixing the value of D_p which resulted in a shift in α by 1 order of magnitude also. The shift in α as just discussed should have no significant effect given the magnitude of the α value. The parameter β was then optimized by the least squares curve fitting. Figure 5.29 shows the predicted loading curve in terms of conversion for optimized value β for each value of D_c. These changes resulted in drastic changes in the overall shape of the uptake curve as a direct result of the very significant shifts in the β required to minimize the least squares error term. For the case of D_c of 2.57×10^{-13}, the β value is 55.9 but as D_c is decreased to 2.57×10^{-15}, the β value drops to 1.05×10^{-4}, which would indicate a very high macropore uptake as indicated by the very level uptake curve following the initial uptake period.

The comparative examination of runs T3 and T6 provided some measure of the experimental accuracy for this study. Both runs exhibited no notable thermal instability in the balance stability. The values of D_c as determined by the slope method were 2.42×10^{-14} and 3.15×10^{-14} cm^2/s for T3 and T6 respectively. The values of the y-intercept, which can be considered an indication of the time shift for the onset of the micropore diffusion, are −0.275 and −0.250 for T3 and T6 respectively. The difference in the values of D_c indicated about a 30% error based on this one set of planned duplicates.

One other factor which may have impacted the overall loading rates is the water uptake. Based on the data shown in Fig. 4.15 the water uptake term could account for as much as a 10 to 20% overestimation of the total observed "iodine" loading.

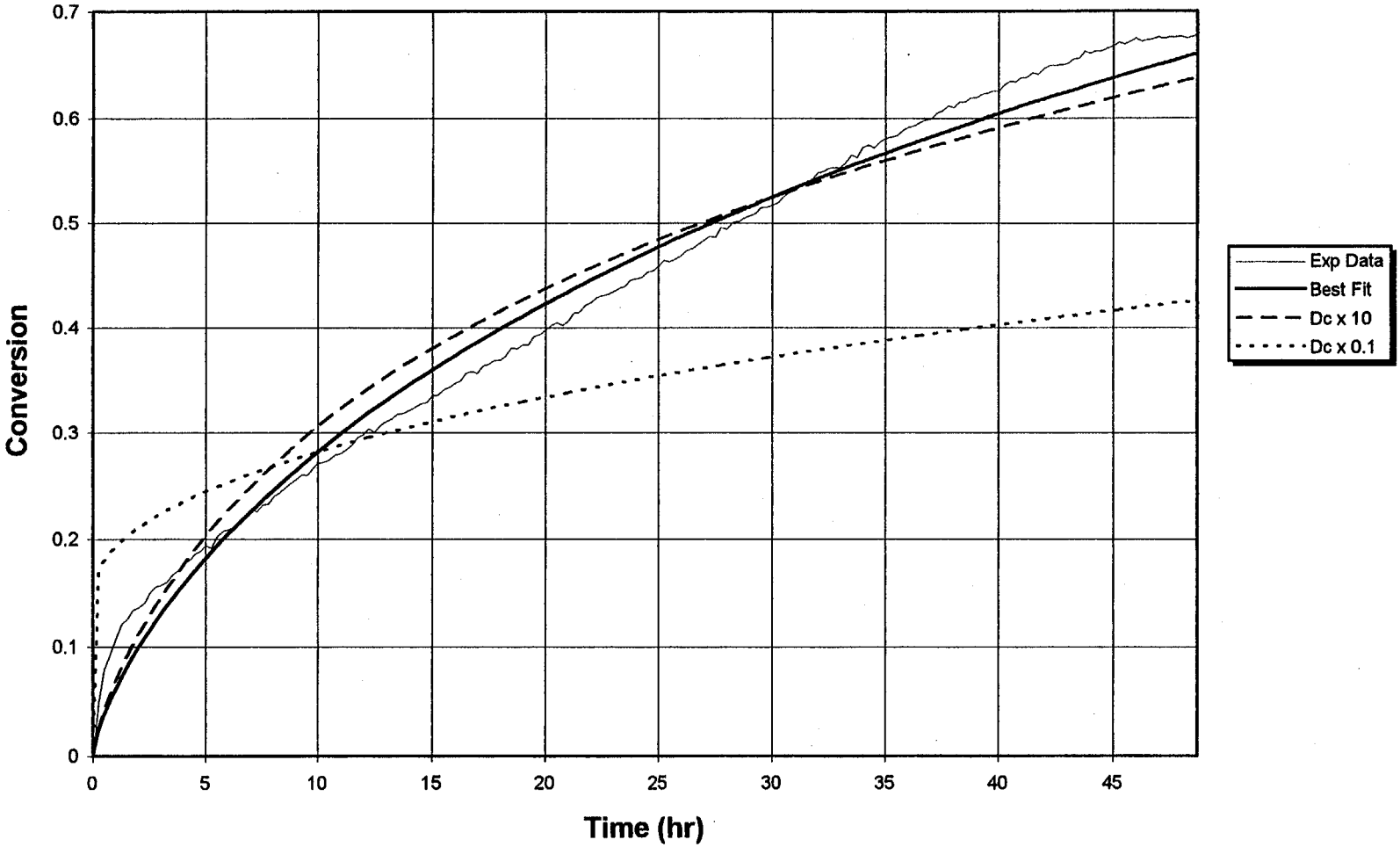

Figure 5.29. Predicted loading curve in terms of conversion for variations in the value of D_c while holding the value of α fixed and optimizing β.

In summary, considering the potential sources for experimental variation and the model sensitivity, the values determined for the bimodal model parameters, D_c, α, and β, are very consistent and clearly appear to adequately model the uptake of CH_3I on Ag°Z over the longer time periods. In addition, the bimodal two-step process seems to explain the appearance of a "ring" or shrinking core in the pellets at low conversion and yet a uniform iodine distribution at higher loadings.

5.4 OTHER ALTERNATE MODELS

Another possible model for this adsorption process is a stage model described in Crank's book (1975), *The Mathematics of Diffusion*, which was developed to account for the "S" shaped loading curve. This model also appears to be consistent with the observed behavior. However, this model is quite empirical compared to any of the ones described. The loading in this model is typified by an initial stage consisting of rapid uptake of material on the surface. The loading curve for this portion is indicative of rapid diffusion. (This could be the macropore diffusion in the present case and reaction on the available surface in the macropores.) This initial phase levels off far short of the ultimate loading and is followed by a more gradual increase to full loading of the bed. The shape of the second stage loading curve is associated with the increase in surface concentration. This could be the micropore diffusion portion of the loading. The model, as described by Crank (1975), was first put forward by Bagley and Long (1955). Long and Richmond (1960) confirmed the work of Bagley and Long and showed that the surface

concentration, C_s, is governed by an equation similar to the one presented below:

$$C_s = C_i + \left(C_e - C_i\right)\left(1 - e^{-\xi t}\right) \tag{5.5}$$

where:

C_i is instantaneous equilibrium concentration

C_e is final equilibrium concentration

t is time, and

ξ is a constant.

In the current case the relationship of C_i to C_e would be linked to the relative surface areas of the macropores to the micropores.

6. CONCLUSIONS

An in-depth examination of the adsorption of CH_3I onto silver-exchanged mordenite has been conducted. The experimental uptake data and other related data were analyzed to determine the controlling mechanism(s) involved. Nine well accepted mass transfer models were evaluated for their ability to adequately explain the observed behavior. It can be concluded from the analysis of the experimental data obtained by the "single-pellet" type experiments and for the process conditions used in this study that the overall mass transfer rate associated with the adsorption of CH_3I onto Ag°Z is affected by both micropore and macropore diffusion. And as such, a bimodal model best describes the observed uptake of CH_3I on the Ag°Z. The micropore diffusivity was determined for the experimental data. In addition, as certain process conditions were varied, the associated decrease in chemical reaction rate was also shown to limit the mass transfer. These results in turn should provide the basis for further studies involving more complex systems containing other process variables as well as additional studies with this system.

The specific conclusions drawn from this study are as follows:

1. It was shown based on both fundamental analysis and based on the results of the least squares curve fitting that the gas film resistance to mass transfer is negligible.

2. Using the same type analysis techniques, it was also shown that the system can be considered virtually isothermal. The maximum calculated delta temperature between the pellet and the bulk fluid was 0.37°C. This is an important determination in that it simplifies the modeling of the process.

3. The micropore diffusivity at 150°C as calculated from the slope of the $\ln(1-X_B)$ vs time curve is in the range of 1.95×10^{-14} to 3.33×10^{-14} cm^2/s. The error in these values as estimated from the duplicate run at the standard conditions is about 30%.

4. The bimodal model which includes the uptake in both the macropores and the micropores provides the most uniform ability to model the behavior of the adsorption of CH_3I onto Ag°Z. The model parameters indicate that the uptake is occurring in a two-step manner, with the macropore uptake being much faster than the micropore uptake. This two-step process can account for the "shrinking core" observed at low conversions and the relatively uniform iodine concentration observed in the pellet at moderate to high concentrations.

5. The uptake in macropores appears to be reaction rate limited when the water vapor concentration is less than the CH_3I gas concentration. The apparent reaction rate constant at 150°C in the single run that became reaction controlled was 5.9×10^{-2} cm/s.

6. Possible thermal effects on measurement equipment in initial 1- to 4-h time periods for several of the runs may result in questionable loading rates in these time periods.

7. The macropore diffusivity could not be accurately determined due to several factors. The initial uptake curve in several runs was subject to erroneous readings from the electronic balance as a result of thermal effects. In addition, the initial uptake rate may have also included water uptake which could significantly alter the derived values from this data.

8. The impact of the free silver observed in the mordenite structure could not be identified.

7. RECOMMENDATIONS

There are several areas in which additional studies should be undertaken to extend the understanding of the mechanisms of CH_3I adsorption onto silver-exchanged mordenite.

7.1 DETERMINATION OF CH_3I-AgZ REACTIONS

In particular, a clearer understanding of the role played by water is needed. From the present studies, the loading rate of the AgZ was shown to be limited by insufficient water in the gas stream. Methyl iodide adsorption rates with a very dry gas stream such as bottled air should be determined. However, this test would be more suited for a sealed system rather than flowing systems considering volume of gas required. Tests at a high water vapor content might also be of interest. It would be expected that too much water would also be detrimental due to possible capillary condensation.

It would also be of interest to compare elemental iodine and methyl iodide diffusion/uptake rates. This test is of interest because none of the elemental iodine reactions presented by Scheele et al. (1983) involve water. Thus no shift to reaction control would be expected.

All of these tests should also include some type of monitor on the effluent or test chamber to detect reaction products. A gas chromatograph is one possibility. An on-line monitor to track the water vapor content of the feed gas should also considered.

7.2 ISOLATION OF THE MICROPORE DIFFUSION BEHAVIOR FROM THE MACROPORE ADSORPTION

This separate determination of micropore diffusion coefficients could possibly be accomplished through the use of an AgZ material based on the Zeolon™ 100 mordenite. Since the Zeolon™ 100 material is a crystalline powder of approximately the same size as the microparticles found in the Zeolon™ 900 mordenite, this would allow the focus to be placed on the micropore diffusion term without the complication of the biporous pellet provided that the bed diffusional resistances could be shown to be negligible. The limitations placed on gas velocity and particle size due to fluidization of the bed in the equipment used in the current study would not permit the use of very small particles or high gas velocities. The use of a sealed microbalance system such as that used by Vaidyanathan (1971) would be useful in further investigations of the micropore diffusion. This type of study would provide verification of the micropore diffusivity determined in this work.

7.3 EXAMINATION THE ADSORPTION ON THE SILVER NODULES FORMED WITHIN THE AgZ MATRIX

Detailed tests should be conducted to evaluate the role played by the silver and silver nodules. This would also include the impact on the observed uptake rates of the pretreatment of AgZ with the key parameters being time, the gas used, and the size and number of silver nodules formed. This study should also determine the degree to which the silver is depleted in the AgZ matrix. Tests would need to be conducted with and without hydrogen pretreatment to form a baseline.

7.4 EXAMINATION OF THE ROLE PLAYED BY STRUCTURAL VARIATIONS

The impact of the structural variations in the pellet are much more difficult to quantify. It appeared in this study that there can be significant variations from pellet to pellet. It might be possible to conduct these tests with a very small number of pellets and characterize them "fully."

7.5 DETERMINATION OF THE MACROPORE DIFFUSIVITY

This effort must focus on the initial period of the CH_3I uptake. These tests should use a different type of apparatus than the one used in the present study and will have to include the characterization of the pellet as described in Sect. 7.4. Since it has been shown that the gas film resistance to mass transfer is not a factor, it would appear possible to use a sealed system similar to those used by Lee or Vaidyanathan. It would also be important

to determine if there is a displacement of water as iodine is adsorbed. The relative quantity of water on the AgZ has an impact on the gravimetric determinations. If the current test equipment were to be used to determine the macropore diffusivities, part of this effort would also involve improving the observed temperature instabilities of the measurement systems. This might include increasing the insulation between the balance and the heater and installing thermocouples inside the balance and recording the temperature data on PC file along with weight data. Other improvements might be made to the inlet gas heater to reduce the overall box temperature.

7.6 EVALUATION OF THE EFFECTS FROM LONG-TERM EXPOSURE TO AIR PRIOR TO LOADING

This evaluation is an extension of the pretreatment analysis noted in Sect. 7.3 and would examine the effects of extended periods of air flow without CH_3I loading. Actual operation of iodine traps utilizing this material will undoubtedly result in long periods of gas flow containing little or no iodine. Of interest is the evaluation of any change in the uptake rate arising from possible reoxidation of the silver.

BIBLIOGRAPHY

BIBLIOGRAPHY

M. H. Abbasi, J. W. Evans, and I. S. Abramson, "Diffusion of Gases in Porous Solids: Monte Carlo Simulations in the Knudsen and Ordinary Diffusion Regimes", *AIChE Journal*, Vol 29, No. 4, pg 617-624, (July 1983).

E. Bagley and F. A. Long, "Two-Stage Sorption and Desorption of Organic Vapors on Cellulose Acetate," *J. Am Chem Soc.*, Vol 77, pg 2172-2178, (1955).

H. K. Beyer and P. A. Jacobs, "Reduction and Reoxidation of Silver Mordenites," *Molecular Sieves-II*, ed. by James R Katzer, ACS Symposium Series No. 40, Am. Chem. Soc., Washington, D.C., pg 493-503, (1977).

R. B. Bird, W. E. Stewart, and E. N. Lightfoot, *Transport Phenomena*, John Wiley & Sons, New York, (1960).

D. W. Breck, *Zeolite Molecular Sieves, Structure, Chemistry, and Use*, John Wiley & Sons, New York, (1974).

L. L. Burger, *Storage of Unreprocessed Fuel, Nuclear Waste Management Quarterly Progress Report April Through June 1977*, ed. by A. M. Platt, Battelle Pacific Northwest Laboratories, BNWL-2377-2, (November 1977).

L. L. Burger and R. E. Burns, *Technical Requirements for the Control of ^{129}Iodine in a Nuclear Fuels Reprocessing Plant*, Pacific Northwest Laboratory, PNL-3186, (November 1979).

L. L. Burger and R. D. Scheele, "Iodine Fixation Studies at the Pacific Northwest Laboratory," *Management Modes for Iodine-129*, W. Hebel and G. Cottone, eds. Harwood Academic Publishers, New York, (1981).

L. L. Burger and R. D. Scheele, *Recycle of Iodine-Loaded Silver Mordenite by Hydrogen Reduction*, Pacific Northwest Laboratory, PNL-4490, (November 1982).

L. L. Burger and R. D. Scheele, *The Status of Radioiodine Control for Nuclear Fuel Reprocessing Plants*, Pacific Northwest Laboratory, PNL-4689, (July 1983).

J. J. Carberry, *Chemical and Catalytic Reaction Engineering*, McGraw-Hill, Inc., New York, (1976).

J. Crank, *The Mathematics of Diffusion, Second Edition*, Oxford University Press Inc., New York, (1975).

C. Donner and T. Tamberg, "Zur Abscheidung von Methyl and Athyljodid an Silverzeolithen," pg 28-29, *Atomwirtschaft*, (Jan 1971).

C. Donner and T. Tamberg, "Zur Abscheidung von Methyljodid an Silverzeolithen," *Z. Naturforsch*, 27, pg 1323-1328, (1972).

M. P. Dudukovic and H. S. Lamba, "Solution of Moving Boundary Problems for Gas-Solid Noncatalytic Reactions by Orthogonal Collocation," *Chemical Engineering Science*, Vol 33, pg 303-314, (1978).

G. E. Forsythe, M.A. Malcolm, and C. B. Moler, *Computer Methods for Mathematical Computations*, Prentice Hall, Inc., Englewood Cliffs, New Jersy, (1977).

Handbook of Chemistry and Physics, 74th Edition, David R. Lide, Editor, CRC Press, Inc., Boca Raton, FL, (1993).

IONEX Reseach Corporation, "IONEX Ag-900 Silver Exchanged Molecular Sieve," Bulletin and Material Safety Data Sheet, (December 1986).

R. T. Jubin, "Organic Iodine Removal from Simulated Off-Gas Streams Using Silver-Exchanged Mordenite," *Proc. 16th DOE Nuclear Air Cleaning Conference*, CONF-801038, pg 519-531 (1980).

R. T. Jubin, "Organic Iodine Removal from Simulated Off-Gas Streams Using Partially Exchanged Silver Mordenite," *Proc. 17th DOE Nuclear Air Cleaning Conference*, CONF-820833, pg. 183-198 (1982).

J. Kärger and D. M. Ruthven, *Diffusion in Zeolites and Other Microporous Solids*, John Wiley & Sons, Inc. New York, (1992).

W. M. Kays and M. E. Crawford, *Convective Heat and Mass Tranfer, Second Edition*, McGraw-Hill, Inc., New York, (1980).

F. Kikuchi, Y. Komori, and K. Takeda, "Experience of Iodine Removal in Tokai Reprocessing Plant," *Proc. 18th DOE Nuclear Airborne Waste Management and Air Cleaning Conference*, CONF-840806, pg 451-460 (1985).

B. D. Kulkarni and L. K. Doraiswamy, "Modeling of Noncatalytic Gas-Solid Reactions," *Handbook of Heat and Mass Transfer, Volume 2: Mass Transfer and Reactor Design*, Nicholas P. Cheremisinoff, Editor, pg. 1107-1135, Gulf Publishing Company, Houston, TX, (1986).

Lap-Keung Lee, "The Kinetics of Sorption in a Biporous Adsorbent Particle," *AIChE Journal*, Vol 24, No 3, pg 531-533, (1978).

Lap-Keung Lee and D. M. Ruthven, "Analysis of Thermal Effects in Adsorption Rate Measurements," *J. Chem. Soc. Faraday I*, Vol 75, pg 2406-2422, (1978).

T. Y. Lee, *Single and Multicomponent Diffusion in Faujasite Pellets*, PhD Dissertation, Worcester Polytechnic Institute, (June 1976).

Lectrodryer, a Division of Ajax Magnethermic Corporation, "The Lectrodryer Dewpoint Apparatus," Bulletin DP-A2, (undated).

O. Levenspiel, *Chemical Reaction Engineering, Second Edition*, John Wiley & Sons, Inc. New York, (1972).

O. Levenspiel, *The Chemical Reactor Omnibook*, OSU Book Store, Inc., Corvallis, Oregon, (1979).

F. A. Long and D. Richman, "Concentration Gradients for Diffusion of Vapors in Glassy Polymers and Their Relation to Time Dependent Diffusion Phenomena," *J. Am Chem Soc.*, Vol 82, pg 513-519, (1960)

Y. H. Ma and T. Y. Lee, "Transient Diffusion in Solids with a Bipore Distribution," *AIChE Journal*, Vol 22, No 1, pg 147-152, (1976).

W. J. Maeck and D. T. Pence, "Application of Metal Zeolites to Radioiodine Air Cleaning Problems," *Proc. 11th AEC Air Cleaning Conference*, CONF-700816, p. 607-618 (1970).

W. J. Maeck, D. T. Pence, and J. H. Keller, *A Highly Efficient Inorganic Adsorber for Airborne Iodine Species (Silver Zeolite Development Studies)*, IN-1224 (1968).

H. A. C. McKay, P. Miquel, and I. F. White, *Management Modes for Iodine-129*, W. Hebel and G. Cottone, eds. Harwood Academic Publishers, New York (1981).

W. M. Meier and D. H.Olson, *Atlas of Zeolite Structure Types, Third Revised Edition*, Butterworth-Heinemann, Stoneham, MA, (1992).

L. P. Murphy, B. A. Staples, and T. R. Thomas, *The Development of Ag°Z for Bulk ^{129}I Removal from Nuclear Fuel Reprocessing Plants and PbX for ^{129}I Storage*, Idaho National Engineering Laboratory, ICP-1135 (December 1977).

T. D. Murphy, Jr., "Design and Analysis of Industrial Experiments," *Chem. Eng.*, Vol 84, pg 168-182, (June 6, 1977).

National Archives of the United States, *Code of Federal Regulations Part 10 Energy* (January 1994).

National Archives of the United States, *Code of Federal Regulations Part 40* (July 1993).

Norton Company, Chemical Process Products Division, *Zeolon Acid Resistant Molecular Sieves*, Bulletin 2-51 (1976).

D. T. Pence, F. A. Duce, and W. J. Maeck, "A Study of the Adsorption Properties of Metal Zeolites for Airborne Iodine Species," *Proc. 11th AEC Air Cleaning Conference*, CONF-700816, pg 581-599 (1970).

D. T. Pence and B. A. Staples, "Solid Adsorbents for Collection and Storage of Iodine-129 from Reprocessing Plants," *Proc. 13th AEC Air Cleaning Conf.*, CONF-740807, pg 758-764 (August 1974).

R. H. Perry, D. W. Green, and J. O. Maloney, *Perry's Chemical Engineers' Handbook*, Sixth Edition, McGraw-Hill, New York (1992).

D. Porey, Personal communication to R. T. Jubin, Dec. 6, 1993.

W. H. Press, S. A. Teukolsky, W. T. Vettering, and B. P. Flannery, *Numerical Recipes in FORTRAN: the Art of Scientific Computing, Second Edition*, Cambridge University Press, New York, (1992a).

W. H. Press, S. A. Teukolsky, W. T. Vettering, and B. P. Flannery, *Numerical Recipes FORTRAN Diskette, Second Edition*, Cambridge, Massachusetts, (1992b).

P. A. Ramachandran and L. K. Doraiswamy, "Modeling of Noncatalytic Gas-Soild Reactions", *AIChE Journal*, Vol 28., No. 6, pg. 881-900, (1982).

P. A. Ramachandran and B. D. Kulkarni, "Approximate Analytical Solution to Gas-Solid Noncatalytic Reaction Problems", *Ind. Eng. Chem. Process Des. Dev.*, Vol 19. pg. 717-719, (1980).

R. C. Reid, J. M. Prausnitz, and T. K. Sherwood, *The Properties of Gases and Liquids, Third Edition*, McGraw-Hill Book Company, New York, (1977).

E. Ruckenstein, A. S. Vaidyanathan, and G. R. Youngquist, "Sorption by Solids with Bidisperse Pore Structures," *Chemical Engineering Science*, Vol 26, pg 1305-1318, (1971).

D. M. Ruthven, *Principles of Adsorption & Adsorption Processes*, John Wiley & Sons, (1984).

D. M. Ruthven, Lap-Keung Lee, and H. Yucel, "Kinetics of Nonisothermal Sorption in Molecular Sieve Crystals," *AIChE Journal*, Vol 26, No. 1, pg 16-23, (July 1980).

D. M. Ruthven and Lap-Keung Lee, "Kinetics of Nonisothermal Sorption: Systems with Bed Diffusion Control," *AIChE Journal*, Vol 27, No. 4, pg 654-663, (July 1981).

C. N. Satterfield and A. J. Frabetti, Jr., "Sorption and Diffusion of Gaseous Hydrocarbons in Synthetic Mordenite," *AIChE Journal*, Vol 13, No. 4, pg 731-738, (July 1967).

C. N. Satterfield and W. G. Margetts, "Diffusion in Sodium Mordenite," *AIChE Journal*, Vol 17, No. 2, pg 295-299, (March 1971).

R. D. Scheele, L. L. Burger, and C. L. Matsuzaki, *Methyl Iodide Sorbtion by Reduced Silver Mordenite*, PNL-4489, Pacific Northwest Laboratory, (1983).

R. D. Scheele, L. L. Burger, and J. K. Soldat, *The Adequacy of Radioiodine Control and Monitoring at Nuclear Fuels Reprocessing Plants*, PNL-5108, Pacific Northwest Laboratory, (June 1984).

R. D. Scheele and L. L. Burger, *Evaluation of Silver Mordenite for Radioiodine Retention at the Purex Precess Facility Modification*, PNL-6261, Pacific Northwest Laboratory, (July 1987).

R. D. Scheele, L. L. Burger, and B. T. Halko, *Comparison of Silver Sorbents for Application to Radioiodine Retention at the Purex Precess Facility Modification*, PNL-6607, Pacific Northwest Laboratory, (September 1988).

T. K. Sherwood, R. L. Pigford, and C. R. Wilke, *Mass Transfer*, McGraw-Hill, Inc., New York, (1975).

H. Shiomi, Y. Yuasa, A Tani, M. Ohki, and T. Nakagawa, "A Parametric Study on Removal Efficiency of Impregnated Activated Charcoal and Silver Zeolite for Radioactive Methyl Iodide," *Proc. 17th DOE Nuclear Air Cleaning Conference*, CONF-820833, pg 199-222, (1982).

C. M. Slansky, editor, *LWR Fuel Reprocessing and Recycle Progress Report for January 1-March 31, 1977*, Idaho National Engineering Laboratory, ICP-1116 (1977).

B. A. Staples, L. P. Murphy, and T. R. Thomas, "Airborne Elemental Iodine Loading Capacities of Metal Zeolites and a Dry Method for Recycling Silver Zeolite," *Proc. 14th ERDA Air Cleaning Conference*, CONF-760822, pg 363-380 (1976).

T. R. Thomas, B. A. Staples, L. P. Murphy, and J. T. Nichols, *Airborne Elemental Iodine Loading Capacities of Metal Exchanged Zeolites and a Method for Recycling Silver Zeolite*, Idaho National Engineering Laboratory, ICP-1119 (July 1977).

T. R. Thomas, B. A. Staples, and L. P. Murphy, "The Development of Ag°Z for Bulk ^{129}I Removal from Nuclear Fuel Reprocessing Plants and PbX for ^{129}I Storage," *Proc. 15th DOE Air Cleaning Conference*, CONF-780819, pg 394-415, (1978).

R. E. Treybal, *Mass-Transfer Operations, 3rd Edition*, McGraw Hill, Inc., New York. (1980).

K. Tsutsumi and H. Takahashi, "The Formation of Metallic Silver in Silver Form Zeolites," *Bull. Chem. Soc. Jpn.*, 45(8), pg. 2332-2337, (1977).

U.S. Department of Energy, Office of Environmental Management, Office of Technology Development, "Underground Storage Tank Demonstration (UST-ID)," DOE/EM-0122P (February 1994).

A. S. Vaidyanathan, *Theoretical and Experimental Investigation of Sorption in Bidisperse Porous Particles*, PhD Dissertation, Clarkson College of Technology, (September 1971).

D. E. W. Vaughan, "The Synthesis and Manufacture of Zeolites," *Chemical Engineering Progress*, Vol 84, No 2, pg 25-31, (Feb 1988).

N. Wakao and T. Funazkri, "Effect of Fluid Dispersion Coefficients on Particle-to-Fluid Mass Transfer Coefficients in Packed Beds - Correlation of Sherwood Numbers," *Chemical Engineering Science*, 33, pg 1375-1384 (1978).

L. R. Walker to R. T. Jubin, "Chemical Report Sheet", Internal Correspondence, (March 14, 1994).

R. T. Yang, *Gas Separation by Adsorption Processes*, Butterworth Publishers, Stoneham, Massachusetts, 1987.

D. J. C. Yates, "The Stability of Metallic Cations in Zeolites," *J. Phys. Chem.*, 69, pg 1676-1683 (1965).

APPENDIXES

APPENDIX A.1
SUPPORTING PHYSICAL PROPERTY DATA AND SPECIFIC DIMENSIONAL MEASUREMENTS

A.1.1 RELEVANT PHYSICAL PROPERTY DATA

A.1.1.1 Molecular Weight

Compound	Molecular weight (g/mol)	Source
Air	28.97	Bird et al. (1960)–Table B.1
CH_3I	141.939	Reid et al. (1977)
Water	18.015	Reid et al. (1977)

A.1.1.2 Viscosity

The viscosity of air was estimated from Fig. 3.42 in *Perry's Chemical Engineer's Handbook 6th Edition* (Perry et al., 1992).

Temperature (°C)	Viscosity (centipoise)
150	0.023
200	0.025

The viscosity of the CH_3I-air mixture was assumed to be that of air alone as the mole fraction of CH_3I ranged from 0.000039 to 0.000237 (250 to 1500 mg CH_3I/m^3).

A.1.1.3 Heat Capacity and Thermal Conductivity

The heat capacity and thermal conductivity of air was obtained from Table A-1 in the text by Kays and Crawford (1980) by linear interpolation.

Temperature (°K)	C_p (kJ/kg°K)	k_f(W/m°K)
423	1.016	34.56×10^{-3}
473	1.024	37.79×10^{-3}

These values, which are for air, were used for the CH_3I mixture as the mole fraction of CH_3I ranged from 0.000039 to 0.000237 (250 to 1500 mg CH_3I/m^3).

The heat capacity of the Ag°Z was estimated to be 0.176 cal/g°K from Fig. 9.10 in the text by Breck (1974). This value is given for commercially available type 5A molecular sieve.

A.1.1.4 Lennard Jones Parameters for Calculation of Molecular Diffusivity

Compound	σ_{AB} (Å)	ε_{AB}/K (°K)	Source
Air	3.711	78.6	Sherwood et. al. (1975) (Table 2.3)
CH_3I	4.791	396.0	Estimated (see comments that follow)

Note that the values of the Lennard-Jones potential parameters for CH_3I were estimated using Eqs. (A1.1) and (A1.2) from Sherwood et. al. (1975) which defines a relationship for σ_{AB} and ε_{AB}/K to the component's critical values by

$$\frac{\varepsilon_{AB}}{K} = 0.75(T_c) \qquad \text{(A1.1)}$$

and

$$\sigma_{AB} = \frac{5}{6} V_c^{1/3} \quad . \tag{A1.2}$$

A.1.1.5 Critical Values

Compound	T_c(°K)	V_c(cm^3/g-mol)	Source
CH_3I	528.0	190	Reid et. al. (1977)

A.1.2 DIMENSIONAL DATA FOR 1/16-in. DIAMETER AgZ PELLETS

Calculation of equivalent spherical radius was based upon the 190 individual pellets used in run T-17. These pellets had a total weight of 2.5416 g.

In the absence of measured density data in the early stages of data analysis, the equivalent spherical radius was calculated using an approximated density from a selected single pellet which was 0.5 cm long and 0.16 cm diam and had a weight of 0.0187 g. In the batch of pellets from test T17 the individual pellet lengths ranged from approximately 0.159 to 0.953 cm. It follows that the weight per unit length of the pellet is:

0.0187 g/0.5 cm = 0.0374 g/cm.

And that the total length of pellets used was

2.5416 g/0.0374 g/cm = 67.957 cm.

Therefore, the average pellet length was

67.957 cm/190 pieces = 0.358 cm.

Average pellet volume: 0.007198 cm^3

Average pellet surface area: 0.220163 cm^2

Equivalent spherical particle radius as defined by Kärger and Ruthven (1992) is the radius of a sphere having the same external surface area to volume ratio as the actual particle geometry. Equivalent spherical radius was computed to be 0.09808 cm.

The calculations were later repeated using the bulk density obtained from Y-12. Using a bulk density of 1.73, the computed equivalent radius was 0.09931 cm.

A.1.3 DIMENSIONAL DATA FOR 1/8-in. DIAMETER AgZ PELLETS

Calculation of equivalent spherical radius was based upon the 36 individual pellets used in run T-20. These pellets had a total weight of 3.0342 g.

In the absence of measured density data in the early stages of data analysis, the equivalent spherical radius was calculated using the combined length when the pellets were placed end to end. The measured length was 27.5 cm, and the pellets were 0.318 cm diam. In the batch of pellets from test T20, the individual pellet lengths ranged from approximately 0.318 to 1.27 cm. It follows that the average pellet length was:

27.5 cm/36 pieces = 0.764 cm.

Average pellet volume: 0.060479 cm^3

Average pellet surface area: 0.920291 cm^2

Equivalent spherical particle radius as defined by Kärger and Ruthven (1992) is the radius of a sphere having the same external surface area to volume ratio as the actual particle geometry. Equivalent spherical radius was computed to be 0.19715 cm.

The calculations were later repeated using the bulk density obtained from Y-12. Using a bulk density of 1.66 and the same number of pellets and pellet diameter, the computed equivalent radius was 0.19251 cm.

APPENDIX A.2
SUMMARY DATA SHEETS FOR
CH_3I LOADING

Table A.2.1: Test T3 summary data sheet.

Case description	Over weekend loading - test 1 - base case
Data file name	load3
Air rate (L/min)	11.315
H_2/Ar rate (L/min)	0
CH_3I rate (L/min)	0.085
Total gas rate (L/min)	11.4
CH_3I concentration (mg/m^3)	1000
Temperature (°C)	150
Pellet size diam (in.)	0.063
Stability code (K/L/M/N)	N
Run date	07-09-1993
Run start time	13:45:04
This sorbents run will last	252000 s
281 readings will be recorded at intervals of 900 s.	
Silver content (%)	18.000
Bed weight (g)	2.988
Moles of Ag avaliable (gmol)	4.99E-03
Max. Theoretical I Load (g)	0.633
Weight at start of H_2 treatment	149.726
Weight at end of H_2 treatment	149.668
Weight change (g)	0.058
Calculated moles of oxygen	3.63E-03
CH_3I concentration	
Cylinder volume (L)	43.8
Liquid density (g/mL)	2.279
CH_3I loaded in cylinder (mL)	20
Initial charge pressure (psig)	101
CH_3I conc. in cylinder (g/L)	0.132216
Available gas (L)	344.7388
Total gas rate	11.4
Based on cylinder pressure drop/time	
Initial run pressure (psig)	101
Final run pressure (psig)	0
Flow time (s)	153900
CH_3I flow rate (g/min)	0.01777

Table A.2.1: (continued)

Based on cylinder concentration and flow rate	
Flow rate (L/min)	0.085
Total gas Rrte (L/min)	11.4
CH_3I flow rate (g/min)	0.011238
CH_3I conc. (g/L) - flow rate	0.000986
CH_3I conc. (g/L) - ΔP	0.001559
Weight at start of CH_3I loading	149.6027
Weight at end of CH_3I loading	150.0577
Weight change (g)	0.455
Calculated moles of iodine	3.59E-03
Weight at start of air flush	150.0577
Weight at end of air flush	150.05
Weight change (g)	0.0077
Calculated moles of iodine	6.07E-05
Iodine remaining (g)	0.4473
Iodine remaining (gmol)	3.52E-03
Final percent Ag utilization	70.69

Table A.2.2: Test T5 summary data sheet.

Case description	CH_3I loading following nitrogen purge and cool down
Data file name	t5ch3i.dat
Air rate (L/min)	11.315
H_2/Ar rate (L/min)	0
CH_3I rate (L/min)	0.085
Total gas rate (L/min)	11.4
CH_3I concentration (mg/m^3)	1000
Temperature (°C)	150
Pellet size diam (in.)	0.125
Stability code (K/L/M/N)	N
Run date	7/22/93
Run start time	13:26:36
This sorbents run will last	259200 s
289 readings will be recorded at intervals of 900 s.	
Silver content (%)	19.000
Bed weight (g)	2.636
Moles of Ag avaliable (gmol)	4.64E-03
Max Theoretical I Load (g)	0.589
Weight at start of H_2 treatment	149.6387
Weight at end of H_2 treatment	149.628
Weight change (g)	0.0107
Calculated moles of oxygen	6.69E-04
CH_3I concentration	
Cylinder volume (L)	43.8
Liquid density (g/mL)	2.279
CH_3I loaded in cylinder (mL)	20
Initial charge pressure (psig)	102
CH_3I conc. in cylinder (g/L)	0.131083
Available gas (L)	347.7184
Total gas rate	11.4

Based on cylinder pressure drop/time		Intermediate values based on pressure drop	
Initial run pressure (psig)	102	102	102
Final run pressure (psig)	0	72	52
Flow time (s)	188100	56160	87240
CH_3I flow rate (g/min)	0.014539	0.014323	0.015367

Table A.2.2: (continued)

Based on cylinder concentration and flow rate			
Flow rate (L/min)	0.085		
Total gas rate (L/min)	11.4		
CH_3I flow rate (g/min)	0.011142		
CH_3I conc. (g/L) - flow rate	0.000977	Intermediate values based on pressure drop	
CH_3I conc. (g/L) - ΔP	0.001275	0.001256	0.001348
Weight at start of CH_3I loading	149.5733		
Weight at end of CH_3I loading	150.05		
Weight change (g)	0.4767		
Calculated moles of iodine	3.76E-03		
Weight at start of air flush	150.05		
Weight at end of air flush	150.041		
Weight change (g)	0.009		
Calculated moles of iodine	7.09E-05		
Iodine remaining (g)	0.4677		
Iodine remaining (gmol)	3.69E-03		
Final percent Ag utilization	79.38		

Table A.2.3: Test T6 summary data sheet.

Case description	CH_3I loading after n2 cool down
Data file name	t6ch3i
Air rate (L/min)	11.315
H_2/Ar rate (L/min)	0
CH_3I rate (L/min)	0.085
Total gas rate (L/min)	11.4
CH_3I concentration (mg/m^3)	1000
Temperature (°C)	150
Pellet size diam (in.)	0.0625
Stability code (K/L/M/N)	N
Run date	8/2/93
Run start time	8:07:23
This sorbents run will last	360000 s
401 readings will be recorded at intervals of 900 s.	
Silver content (%)	18.000
Bed weight (g)	2.331
Moles of Ag avaliable (gmol)	3.89E-03
Max Theoretical I Load (g)	0.494
Weight at start of H_2 treatment	149.2003
Weight at end of H_2 treatment	149.188
Weight change (g)	0.0123
Calculated moles of oxygen	7.69E-04
CH_3I concentration	
Cylinder volume (L)	43.8
Liquid density (g/mL)	2.279
CH_3I loaded in cylinder (mL)	20
Initial charge pressure (psig)	100
CH_3I conc. in cylinder (g/L)	0.133369
Available gas (L)	341.7592
Total gas rate	11.4

Based on cylinder pressure drop/time		Intermediate values based on pressure drop	
Initial run pressure (psig)	100	100	100
Final run pressure (psig)	4	59	40
Flow time (s)	153000	67500	97200
CH_3I flow rate (g/min)	0.01716	0.016611	0.016881

Table A.2.3: (continued)

Based on cylinder concentration and flow rate			
Flow rate (L/min)	0.085		
Total gas rate (L/min)	11.4		
CH_3I flow rate (g/min)	0.011336		
CH_3I conc. (g/L) - flow rate	0.000994	Intermediate values based on pressure drop	
CH_3I conc. (g/L) - ΔP	0.001505	0.001457	0.001481
Weight at start of CH_3I loading	149.044		
Weight at end of CH_3I loading	149.418		
Weight change (g)	0.374		
Calculated moles of iodine	2.95E-03		
Weight at start of air flush	149.418		
Weight at end of air flush	149.416		
Weight change (g)	0.002		
Calculated moles of iodine	1.58E-05		
Iodine remaining (g)	0.372		
Iodine remaining (gmol)	2.93E-03		
Final percent Ag utilization	75.37		

Table A.2.4: Test T7 summary data sheet.

Case description	CH_3I loading following n2 treatment
Data file name	t7ch3i
Air rate (L/min)	11.315
H_2/Ar rate (L/min)	0
CH_3I rate (L/min)	0.085
Total gas rate (L/min)	11.4
CH_3I concentration (mg/m^3)	1000
Temperature (°C)	150
Pellet size diam (in.)	0.125
Stability code (K/L/M/N)	N
Run date	8/10/93
Run start time	15:15:19
This sorbents run will last	259200 s
289 readings will be recorded at intervals of 900 s.	
Silver content (%)	19.000
Bed weight (g)	2.865
Moles of Ag avaliable (gmol)	5.05E-03
Max Theoretical I Load (g)	0.640
Weight at start of H_2 treatment	149.682
Weight at end of H_2 treatment	149.666
Weight change (g)	0.016
Calculated moles of oxygen	1.00E-03
CH_3I concentration	
Cylinder volume (L)	43.8
Liquid density (g/mL)	2.279
CH_3I loaded in cylinder (mL)	20
Initial charge pressure (psig)	100
CH_3I conc. in cylinder (g/L)	0.133369
Available gas (L)	341.7592
Total gas rate	11.4

Based on cylinder pressure drop/time		Intermediate values based on pressure drop	
Initial run pressure (psig)	100	100	100
Final run pressure (psig)	4	58	8
Flow time (s)	151200	63900	145800
CH_3I flow rate (g/min)	0.017364	0.017975	0.017257

Table A.2.4: (continued)

Based on cylinder concentration and flow rate			
Flow rate (L/min)	0.085		
Total gas rate (L/min)	11.4		
CH_3I flow rate (g/min)	0.011336		
CH_3I conc. (g/L) - flow rate	0.000994	Intermediate values based on pressure drop	
CH_3I conc. (g/L) - ΔP	0.001523	0.001577	0.001514
Weight at start of CH_3I loading	149.518		
Weight at end of CH_3I loading	149.901		
Weight change (g)	0.383		
Calculated moles of iodine	3.02E-03		
Weight at start of air flush	149.901		
Weight at end of air flush	149.8737		
Weight change (g)	0.0273		
Calculated moles of iodine	2.15E-04		
Iodine remaining (g)	0.3557		
Iodine remaining (gmol)	2.80E-03		
Final percent Ag utilization	55.54		

Table A.2.5: Test T8 summary data sheet.

Case description	Loading at half normal gas flow
Data file name	t8ch3i
Air rate (L/min)	5.7
H_2/Ar rate (L/min)	0
CH_3I rate (L/min)	0.042
Total gas rate (L/min)	5.742
CH_3I concentration (mg/m^3)	1000
Temperature (°C)	150
Pellet size diam (in.)	0.0625
Stability code (K/L/M/N)	N
Run date	8/19/93
Run start time	11:53:05
This sorbents run will last	432000 s
481 readings will be recorded at intervals of 900 s.	
Silver content (%)	18.000
Bed weight (g)	2.699
Moles of Ag avaliable (gmol)	4.50E-03
Max Theoretical I Load (g)	0.572
Weight at start of H_2 treatment	149.3127
Weight at end of H_2 treatment	149.234
Weight change (g)	0.0787
Calculated moles of oxygen	4.92E-03
CH_3I concentration	
Cylinder volume (L)	43.8
Liquid density (g/mL)	2.279
CH_3I loaded in cylinder (mL)	20
Initial charge pressure (psig)	100
CH_3I conc. in cylinder (g/L)	0.133369
Available gas (L)	341.7592
Total gas rate	5.7

Based on cylinder pressure drop/time		Intermediate values based on pressure drop
Initial run pressure (psig)	100	100
Final run pressure (psig)	15.5	72
Flow time (s)	242100	81000
CH_3I flow rate (g/min)	0.009545	0.009454

Table A.4.5: (continued)

Based on cylinder concentration and flow rate		
Flow rate (L/min)	0.043	
Total gas rate (L/min)	11.4	
CH_3I flow rate (g/min)	0.005735	
CH_3I conc. (g/L) - flow rate	0.001006	Intermediate values based on pressure drop
CH_3I conc. (g/L) - ΔP	0.001675	0.001659
Weight at start of CH_3I loading	149.1677	
Weight at end of CH_3I loading	149.405	
Weight change (g)	0.2373	
Calculated moles of iodine	1.87E-03	
Weight at start of air flush	149.4797	
Weight at end of air flush	149.4807	
Weight change (g)	-0.001	
Calculated moles of iodine	-7.88E-06	
Iodine remaining (g)	0.2383	
Iodine remaining (gmol)	1.88E-03	
Final percent Ag utilization	41.69	

Table A.2.6: Test T10 summary data sheet.

Case description	Loading
Data file name	t10lod.dat
Air rate (L/min)	11.315
H_2/Ar rate (L/min)	0
CH_3I rate (L/min)	0.085
Total gas rate (L/min)	11.4
CH_3I concentration (mg/m^3)	1000
Temperature (°C)	200
Pellet size diam (in.)	0.0625
Stability code (K/L/M/N)	N
Run date	9/10/93
Run start time	11:05:00
This sorbents run will last	252000 s
281 readings will be recorded at intervals of 900 s.	
Silver content (%)	18.000
Bed weight (g)	2.416
Moles of Ag avaliable (gmol)	4.03E-03
Max Theoretical I Load (g)	0.512
Weight at start of H_2 treatment	149.2823
Weight at end of H_2 treatment	149.2053
Weight change (g)	0.077
Calculated moles of oxygen	4.81E-03
CH_3I concentration	
Cylinder volume (L)	43.8
Liquid density (g/mL)	2.279
CH_3I loaded in cylinder (mL)	20
Initial charge pressure (psig)	103
CH_3I conc. in cylinder (g/L)	0.129969
Available gas (L)	350.698
Total gas rate	11.4

Based on cylinder pressure drop/time		Intermediate values based on pressure drop
Initial run pressure (psig)	103	103
Final run pressure (psig)	0	61
Flow time (s)	201600	80100
CH_3I flow rate (g/min)	0.013565	0.013922

Table A.2.6: (continued)

Based on cylinder concentration and flow rate		
Flow rate (L/min)	0.085	
Total gas rate (L/min)	11.4	
CH_3I flow rate (g/min)	0.011047	
CH_3I conc. (g/L) - flow rate	0.000969	Intermediate values based on pressure drop
CH_3I conc. (g/L) - ΔP	0.00119	0.001221
Weight at start of CH_3 loading	149.112	
Weight at end of CH_3I loading	149.582	
Weight change (g)	0.47	
Calculated moles of iodine	3.70E-03	
Weight at start of air flush	149.582	
Weight at end of air flush	149.5803	
Weight change (g)	0.0017	
Calculated moles of iodine	1.34E-05	
Iodine remaining (g)	0.4683	
Iodine remaining (gmol)	3.69E-03	
Final percent Ag utilization	91.53	

Table A.2.7: Test T11 summary data sheet.

Case description	Loading methyl iodide
Data file name	t11lod
Air rate (L/min)	11.272
H_2/Ar rate (L/min)	0
CH_3I rate (L/min)	0.128
Total gas rate (L/min)	11.4
CH_3I concentration (mg/m^3)	1500
Temperature (°C)	150
Pellet size diam (in.)	0.063
Stability code (K/L/M/N)	N
Run date	9/16/93
Run start time	13:09:12
This sorbents run will last	86400 s
97 readings will be recorded at intervals of 900 s.	
Silver content (%)	18.000
Bed weight (g)	2.799
Moles of Ag avaliable (gmol)	4.67E-03
Max Theoretical I Load (g)	0.593
Weight at start of H_2 treatment	149.488
Weight at end of H_2 treatment	149.396
Weight change (g)	0.092
Calculated moles of oxygen	5.75E-03
CH_3I concentration	
Cylinder volume (L)	43.8
Liquid density (g/mL)	2.279
CH_3I loaded in cylinder (mL)	20
Initial charge pressure (psig)	101.5
CH_3I conc. in cylinder (g/L)	0.131647
Available gas (L)	346.2286
Total gas rate	11.4
Based on cylinder pressure drop/time	
Initial run pressure (psig)	101.5
Final run pressure (psig)	0
Flow time (s)	146822
CH_3I flow rate (g/min)	0.018627

Table A.2.7: (continued)

Based on cylinder concentration and flow rate	
Flow rate (L/min)	0.128
Total gas rate (L/min)	11.4
CH_3I flow rate (g/min)	0.016851
CH_3I conc. (g/L) - flow rate	0.001478
CH_3I conc. (g/L) - ΔP	0.001634
Weight at start of CH_3I loading	149.3133
Weight at end of CH_3I loading	149.6803
Weight change (g)	0.367
Calculated moles of iodine	2.89E-03
Weight at start of air flush	149.6803
Weight at end of air flush	149.6673
Weight change (g)	0.013
Calculated moles of iodine	1.02E-04
Iodine remaining (g)	0.354
Iodine remaining (gmol)	2.79E-03
Final percent Ag utilization	59.72

Table A.2.8: Test T12 summary data sheet.

Case description	Methyl iodide loading test
Data file name	T12CH3I
Air rate (L/min)	11.357
H_2/Ar rate (L/min)	0
CH_3I rate (L/min)	0.043
Total gas rate (L/min)	11.4
CH_3I concentration (mg/m^3)	500
Temperature (°C)	150
Pellet size diam (in.)	0.063
Stability code (K/L/M/N)	N
Run date	9/24/93
Run start time	11:22:06
This sorbents run will last	244800 s
273 readings will be recorded at intervals of 900 s.	
Silver content (%)	18.000
Bed weight (g)	2.624
Moles of Ag avaliable (gmol)	4.38E-03
Max Theoretical I Load (g)	0.556
Weight at start of H_2 treatment	149.3127
Weight at end of H_2 treatment	149.234
Weight change (g)	0.0787
Calculated moles of oxygen	4.92E-03
CH_3I concentration	
Cylinder volume (L)	43.8
Liquid density (g/mL)	2.279
CH_3I loaded in cylinder (mL)	20
Initial charge pressure (psig)	100
CH_3I conc. in cylinder (g/L)	0.133369
Available gas (L)	341.7592
Total gas rate	11.4
Based on cylinder pressure drop/time	
Initial run pressure (psig)	100
Final run pressure (psig)	15.5
Flow time (s)	242100
CH_3I flow rate (g/min)	0.009545

Table A.2.8: (continued)

Based on cylinder concentration and flow rate	
Flow rate (L/min)	0.043
Total gas rate (L/min)	11.4
CH_3I flow rate (g/min)	0.005735
CH_3I conc. (g/L) - flow rate	0.000503
CH_3I conc. (g/L) - ΔP	0.000837
Weight at start of CH_3I loading	149.1677
Weight at end of CH_3I loading	149.405
Weight change (g)	0.2373
Calculated moles of iodine	1.87E-03
Weight at start of air flush	149.4797
Weight at end of air flush	149.4807
Weight change (g)	-0.001
Calculated moles of iodine	–7.88E-06
Iodine remaining (g)	0.2383
Iodine remaining (gmol)	1.88E-03
Final percent Ag utilization	42.89

Table A.2.9: Test T13 summary data sheet.

Case description	Humid air at 1 L/min room temp
Data file name	t13load
Air rate (L/min)	11.315
H_2/Ar rate (L/min)	0
CH_3I rate (L/min)	0.085
Total gas rate (L/min)	11.4
CH_3I concentration (mg/m^3)	1000
Temperature (°C)	150
Pellet size diam (in.)	0.063
Stability code (K/L/M/N)	N
Run date	10/1/93
Run start time	16:03:55
This sorbents run will last	237600 s
265 readings will be recorded at intervals of 900 s.	
Silver content (%)	18.000
Bed weight (g)	2.514
Moles of Ag avaliable (gmol)	4.20E-03
Max Theoretical I Load (g)	0.532
Weight at start of H_2 treatment	149.108
Weight at end of H_2 treatment	149.02
Weight change (g)	0.088
Calculated moles of oxygen	5.50E-03
CH_3I concentration	
Cylinder volume (L)	43.8
Liquid density (g/mL)	2.279
CH_3I loaded in cylinder (mL)	20
Initial charge pressure (psig)	100.5
CH_3I conc. in cylinder (g/L)	0.13279
Available gas (L)	343.249
Total gas rate	11.4
Based on cylinder pressure drop/time	
Initial run pressure (psig)	100.5
Final run pressure (psig)	0
Flow time (s)	175500
CH_3I flow rate (g/min)	0.015583

Table A.2.9: (continued)

Based on cylinder concentration and flow rate	
Flow rate (L/min)	0.085
Total gas rate (L/min)	11.4
CH_3I flow rate (g/min)	0.011287
CH_3I conc. (g/L) - flow rate	0.00099
CH_3I conc. (g/L) - ΔP	0.001367
Weight at start of CH_3I loading	148.956
Weight at end of CH_3I loading	149.2617
Weight change (g)	0.3057
Calculated moles of iodine	2.41E-03
Weight at start of air flush	149.2617
Weight at end of air flush	149.2577
Weight change (g)	0.004
Calculated moles of iodine	3.15E-05
Iodine remaining (g)	0.3017
Iodine remaining (gmol)	2.38E-03
Final percent Ag utilization	56.67

Table A.2.10: Test T14 summary data sheet.

Case description	Methyl iodide loading no water addition
Data file name	t14load
Air rate (L/min)	11.358
H_2/Ar rate (L/min)	0
CH_3I rate (L/min)	0.043
Total gas rate (L/min)	11.4
CH_3I concentration (mg/m^3)	250
Temperature (°C)	150
Pellet size diam (in.)	0.063
Stability code (K/L/M/N)	N
Run date	10-08-1993
Run start time	14:35:49
This sorbents run will last	241200 s
269 readings will be recorded at intervals of 900 s.	
Silver content (%)	18.000
Bed weight (g)	2.859
Moles of Ag avaliable (gmol)	4.77E-03
Max Theoretical I Load (g)	0.605
Weight at start of H_2 treatment	149.434
Weight at end of H_2 treatment	149.3317
Weight change (g)	0.1023
Calculated moles of oxygen	6.39E-03
CH_3I concentration	
Cylinder volume (L)	43.8
Liquid density (g/mL)	2.279
CH_3I loaded in cylinder (mL)	10
Initial charge pressure (psig)	102
CH_3I conc. in cylinder (g/L)	0.065542
Available gas (L)	347.7184
Total gas rate	11.4

Based on cylinder pressure drop/time		Intermediate values based on pressure drop	
Initial run pressure (psig)	102	102	102
Final run pressure (psig)	3	26	18
Flow time (s)	327840	235800	265740
CH_3I flow rate (g/min)	0.004048	0.004321	0.004238

Table A.2.10: (continued)

Based on cylinder concentration and flow rate			
Flow rate (L/min)	0.043		
Total gas rate (L/min)	5.7		
CH_3I flow rate (g/min)	0.002818		
CH_3I conc. (g/L) - flow rate	0.000247	Intermediate values based on pressure drop	
CH_3I conc. (g/L) - ΔP	0.000355	0.000379	0.000372
Weight at start of CH_3I loading	149.3067		
Weight at end of CH_3I loading	149.6747		
Weight change (g)	0.368		
Calculated moles of iodine	2.90E-03		
Weight at start of air flush	0		
Weight at end of air flush	0		
Weight change (g)	0		
Calculated moles of iodine	0.00E+00		
Iodine remaining (g)	0.368		
Iodine remaining (gmol)	2.90E-03		
Final percent Ag utilization	60.79		

Table A.2.11: Test T15 summary data sheet.

Case description	Methyl iodide loading test with flow rates 20 % of normal rate of 11.4 L/min
Data file name	t15load
Air rate (L/min)	2.263
H_2/Ar rate (L/min)	0
CH_3I rate (L/min)	0.017
Total gas rate (L/min)	2.28
CH_3I concentration (mg/m^3)	1000
Temperature (°C)	150
Pellet size diam (in.)	0.063
Stability code (K/L/M/N)	N
Run date	10/22/93
Run start time	15:57:45
This sorbents run will last	291600 s
325 readings will be recorded at intervals of 900 s.	
Silver content (%)	18.000
Bed weight (g)	2.570
Moles of Ag avaliable (gmol)	4.29E-03
Max Theoretical I Load (g)	0.544
Weight at start of H_2 treatment	149.112
Weight at end of H_2 treatment	149.042
Weight change (g)	0.07
Calculated moles of oxygen	4.38E-03
CH_3I concentration	
Cylinder volume (L)	43.8
Liquid density (g/mL)	2.279
CH_3I loaded in cylinder (mL)	20
Initial charge pressure (psig)	101
CH_3I conc. in cylinder (g/L)	0.132216
Available gas (L)	344.7388
Total gas rate	2.28

Table A.2.11: (continued)

Based on cylinder pressure drop/time		Intermediate values based on pressure drop			
Initial run pressure (psig)	101	101	101	101	101
Final run pressure (psig)	42.5	65	57.5	55.5	54
Flow time (s)	492600	338700	406200	424200	432300
CH_3I flow rate (g/min)	0.003216	0.002878	0.0029	0.002904	0.002944
Based on cylinder concentration and flow rate					
Flow rate (L/min)	0.017				
Total gas rate (L/min)	2.28				
CH_3I flow rate (g/min)	0.002248				
CH_3I conc. (g/L) - flow rate	0.000986	Intermediate values based on pressure drop			
CH_3I conc. (g/L) - ΔP	0.00141	0.001262	0.001272	0.001274	0.001291
Weight at start of CH_3I loading	149.098				
Weight at end of CH_3I loading	149.604				
Weight change (g)	0.506				
Calculated moles of iodine	3.99E-03				
Weight at start of air flush	149.604				
Weight at end of air flush	149.598				
Weight change (g)	0.006				
Calculated moles of iodine	4.73E-05				
Iodine remaining (g)	0.5				
Iodine remaining (gmol)	3.94E-03				
Final percent Ag utilization	91.87				

Table A.2.12: Test T16 summary data sheet.

Case description	Loading at 10% of normal flow rate
Data file name	t16load
Air rate (L/min)	1.1315
H_2/Ar rate (L/min)	0
CH_3I rate (L/min)	0.0085
Total gas rate (L/min)	1.14
CH_3I concentration (mg/m^3)	1000
Temperature (°C)	150
Pellet size diam (in.)	0.063
Stability code (K/L/M/N)	N
Run date	11/3/93
Run start time	15:30:58
This sorbents run will last	604800 s

673 readings will be recorded at intervals of 900 s.

Silver content (%)	18.000
Bed weight (g)	2.646
Moles of Ag avaliable (gmol)	4.41E-03
Max Theoretical I Load (g)	0.560
Weight at start of H_2 treatment	149.2213
Weight at end of H_2 treatment	149.184
Weight change (g)	0.0373
Calculated moles of oxygen	2.33E-03

Table A.2.12: (continued)

CH_3I concentration										
Cylinder volume (L)	43.8									
Liquid density (g/mL)	2.279									
CH_3I loaded in cylinder (mL)	20									
Initial charge pressure (psig)	101									
CH_3I conc. in cylinder (g/L)	0.132216									
Available gas (L)	344.7388									
Total gas rate	1.14									
Based on cylinder pressure drop/time										
Initial run pressure (psig)	44.2	44.2	44.2	44.2	44.2	44.2	44.2	44.2	44.2	44.2
Final run pressure (psig)	2	41	38.5	33.5	32	14	9	6	4.5	2
Flow time (s)	604800	58500	90900	146700	175500	404100	490500	522000	576900	604800
CH_3I flow rate (g/min)	0.001889	0.001481	0.001698	0.001975	0.001882	0.002024	0.001943	0.001982	0.001863	0.001889
Based on cylinder concentration and flow rate										
Flow rate (L/min)	0.0085									
Total gas rate (L/min)	1.14									
CH_3I flow rate (g/min)	0.001124									
CH_3I conc. (g/L) - flow rate	0.000986									
CH_3I conc. (g/L) - ΔP	0.001657	0.001299	0.001489	0.001732	0.001651	0.001775	0.001705	0.001738	0.001635	0.001657
Weight at start of CH_3I loading	149.188									
Weight at end of CH_3I loading	149.748									

Table A.2.12: (continued)

Weight change (g)	0.56
Calculated moles of iodine	4.41E-03
Weight at start of air flush	149.716
Weight at end of air flush	149.712
Weight change (g)	0.004
Calculated moles of iodine	3.15E-05
Iodine remaining (g)	0.556
Iodine remaining (gmol)	4.38E-03
Final percent Ag utilization	99.24

Table A.2.13: Test T18 summary data sheet.

Case description	ch3i loading (system reset after holiday)
Data file name	t18loadb.dat, t18loadc.dat
Air rate (L/min)	1.13
H_2/Ar rate (L/min)	0
CH_3I rate (L/min)	0.0083
Total gas rate (L/min)	1.14
CH_3I concentration ($mg/m^{3)}$	1000
Temperature (°C)	150
Pellet size diam (in.)	0.063
Stability code (K/L/M/N)	N
Run date	11/29/93
Run start time	16:18:05
This sorbents run will last	259200 s
289 readings will be recorded at intervals of 900 s.	
Silver content (%)	18.000
Bed weight (g)	2.691
Moles of Ag avaliable (gmol)	4.49E-03
Max Theoretical I Load (g)	0.570
Weight at start of H_2 treatment	149.314
Weight at end of H_2 treatment	149.26
Weight change (g)	0.054
Calculated moles of oxygen	3.38E-03
CH_3I concentration	
Cylinder volume (L)	43.8
Liquid density (g/mL)	2.279
CH_3I loaded in cylinder (mL)	20
Initial charge pressure (psig)	101
CH_3I conc. in cylinder (g/L)	0.132216
Available gas (L)	344.7388
Total gas rate	1.14

Based on cylinder pressure drop/time		Intermediate values based on pressure drop				
Initial run pressure (psig)	86	86	86	86	86	86
Final run pressure (psig)	56.4	84	79	75	71.5	57
Flow time (s)	577800	60300	146700	229500	320400	577800
CH_3I flow rate (g/min)	0.001387	0.000898	0.001292	0.001298	0.001225	0.001359

Table A.2.13: (continued)

Based on cylinder concentration and flow rate						
Flow rate (L/min)	0.0085					
Total gas rate (L/min)	1.14					
CH_3I flow rate (g/min)	0.001124					
CH_3I conc. (g/L) - flow rate	0.000986					
CH_3I conc. (g/L) - ΔP	0.001217	0.000788	0.001133	0.001138	0.001075	0.001192
Weight at start of CH_3I loading	149.2567					
Weight at end of CH_3I loading	149.762					
Weight change (g)	0.5053					
Calculated moles of iodine	3.98E-03					
Weight at start of air flush	149.76					
Weight at end of air flush	149.74					
Weight change (g)	0.02					
Calculated moles of iodine	1.58E-04					
Iodine remaining (g)	0.4853					
Iodine remaining (gmol)	3.82E-03					
Final percent Ag utilization	85.18					

Table A.2.14: Test T19 summary data sheet.

Case description	Short-term loading with high CH_3I concentration
Data file name	t19load.dat
Air rate (L/min)	11.255
H_2/Ar rate (L/min)	0
CH_3I rate (L/min)	0.145
Total gas rate (L/min)	11.4
CH_3I concentration (mg/m^3)	1750
Temperature (°C)	150
Pellet size diam (in.)	0.0625
Stability code (K/L/M/N)	N
Run date	12/9/93
Run start time	16:15:12
This sorbents run will last	54000 s
61 readings will be recorded at intervals of 900 s.	
Silver content (%)	18.000
Bed weight (g)	2.897
Moles of Ag avaliable (gmol)	4.83E-03
Max Theoretical I Load (g)	0.614
Weight at start of H_2 treatment	149.4933
Weight at end of H_2 treatment	149.414
Weight change (g)	0.0793
Calculated moles of oxygen	4.96E-03
CH_3I concentration	
Cylinder volume (L)	43.8
Liquid density (g/mL)	2.279
CH_3I loaded in cylinder (mL)	20
Initial charge pressure (psig)	101
CH_3I conc. in cylinder (g/L)	0.132216
Available gas (L)	344.7388
Total gas rate	11.4

Based on cylinder pressure drop/time		Intermediate values based on pressure drop
Initial run pressure (psig)	56	56
Final run pressure (psig)	31	54
Flow time (s)	27900	3600
CH_3I flow rate (g/min)	0.024263	0.015043

Table A.2.14: (continued)

Based on cylinder concentration and flow rate		
Flow rate (L/min)	0.17	
Total gas rate (L/min)	11.4	
CH_3I flow rate (g/min)	0.022477	
		Intermediate values based on pressure drop
CH_3I conc. (g/L) - flow rate	0.001972	
CH_3I conc. (g/L) - ΔP	0.002128	0.00132
Weight at start of CH_3I loading	149.3057	
Weight at end of CH_3I loading	149.4763	
Weight change (g)	0.1706	
Calculated moles of iodine	1.34E-03	
Weight at start of air flush	149.4763	
Weight at end of air flush	149.4763	
Weight change (g)	0	
Calculated moles of iodine	0.00E+00	
Iodine remaining (g)	0.1706	
Iodine remaining (gmol)	1.34E-03	
Final percent Ag utilization	27.81	

Table A.2.15: Test T20 summary data sheet.

Case description	Short loading of large pellets
Data file name	t20load.dat
Air rate (L/min)	11.24
H_2/Ar rate (L/min)	0
CH_3I rate (L/min)	0.16
Total gas rate (L/min)	11.4
CH_3I concentration (mg/m^3)	1700
Temperature (°C)	150
Pellet size diam (in.)	0.125
Stability code (K/L/M/N)	N
Run date	12/15/93
Run start time	14:26:28
This sorbents run will last	90000 s

101 readings will be recorded at intervals of 900 s.

Silver content (%)	19.000
Bed weight (g)	3.017
Moles of Ag avaliable (gmol)	5.31E-03
Max Theoretical I Load (g)	0.674
Weight at start of H_2 treatment	149.7203
Weight at end of H_2 treatment	149.108
Weight change (g)	0.6123
Calculated moles of oxygen	3.83E-02

CH_3I concentration

Cylinder volume (L)	43.8
Liquid density (g/mL)	2.279
CH_3I loaded in cylinder (mL)	20
Initial charge pressure (psig)	101
CH_3I conc. in cylinder (g/L)	0.132216
Available gas (L)	344.7388
Total gas rate	11.4

Based on cylinder pressure drop/time		Intermediate values based on pressure drop		
Initial run pressure (psig)	31	31	31	31
Final run pressure (psig)	0	25.5	23	0
Flow time (s)	45000	5700	9300	45000
CH_3I flow rate (g/min)	0.018653	0.026127	0.023292	0.018653

Table A.2.15: (continued)

Based on cylinder concentration and flow rate				
Flow rate (L/min)	0.17			
Total gas rate (L/min)	11.4			
CH_3I flow rate (g/min)	0.022477			
		Intermediate values based on pressure drop		
CH_3I conc. (g/L) - flow rate	0.001972			
CH_3I conc. (g/L) - ΔP	0.001636	0.002292	0.002043	0.001636
Weight at start of CH_3I loading	149.6023			
Weight at end of CH_3I loading	149.872			
Weight change (g)	0.2697			
Calculated moles of iodine	2.13E-03			
Weight at start of air flush	149.874			
Weight at end of air flush	149.8663			
Weight change (g)	0.0077			
Calculated moles of iodine	6.07E-05			
Iodine remaining (g)	0.262			
Iodine remaining (gmol)	2.06E-03			
Final percent Ag utilization	38.85			

Table A.2.16: Test T22 summary data sheet.

Case description	Loading methyl iodide test
Data file name	t22lod
Air rate (L/min)	11.272
H_2/Ar rate (L/min)	0
CH_3I rate (L/min)	0.128
Total gas rate (L/min)	11.4
CH_3I concentration (mg/m^3)	1500
Temperature (°C)	150
Pellet size diam (in.)	0.125
Stability code (K/L/M/N)	N
Run date	2/11/94
Run start time	10:29:16
This sorbents run will last	259200 s
289 readings will be recorded at intervals of 900 s.	
Silver content (%)	19.000
Bed weight (g)	2.866
Moles of Ag avaliable (gmol)	5.05E-03
Max Theoretical I Load (g)	0.641
Weight at start of H_2 treatment	149.6087
Weight at end of H_2 treatment	149.576
Weight change (g)	0.0327
Calculated moles of oxygen	2.04E-03
CH_3I concentration	
Cylinder volume (L)	43.8
Liquid density (g/mL)	2.279
CH_3I loaded in cylinder (mL)	20
Initial charge pressure (psig)	98
CH_3I conc. in cylinder (g/L)	0.135736
Available gas (L)	335.8
Total gas rate	11.4
Based on cylinder pressure drop/time	
Initial run pressure (psig)	98
Final run pressure (psig)	0
Flow time (s)	175500
CH_3I flow rate (g/min)	0.015583

Table A.2.16: (continued)

Based on cylinder concentration and flow rate	
Flow rate (L/min)	0.128
Total gas rate (L/min)	11.4
CH_3I flow rate (g/min)	0.017374
CH_3I conc. (g/L) - flow rate	0.001524
CH_3I conc. (g/L) - ΔP	0.001367
Weight at start of CH_3I loading	149.5073
Weight at end of CH_3I loading	149.942
Weight change (g)	0.4347
Calculated moles of iodine	3.43E-03
Weight at start of air flush	149.942
Weight at end of air flush	149.9277
Weight change (g)	0.0143
Calculated moles of iodine	1.13E-04
Iodine remaining (g)	0.4204
Iodine remaining (gmol)	3.31E-03
Final percent Ag utilization	65.62

Table A.2.17: Test T26 summary data sheet.

Case description	Loading at low temperature
Data file name	t26stlod
Air rate (L/min)	11.315
H_2/Ar rate (L/min)	0
CH_3I rate (L/min)	0.085
Total gas rate (L/min)	11.4
CH_3I concentration (mg/m^3)	1000
Temperature (°C)	125
Pellet size diam (in.)	0.063
Stability code (K/L/M/N)	N
Run date	8/3/94
Run start time	21:06:46
This sorbents run will last	126000 s
141 readings will be recorded at intervals of 900 s.	
Silver content (%)	19.000
Bed weight (g)	2.585
Moles of Ag avaliable (gmol)	4.55E-03
Max Theoretical I Load (g)	0.578
Weight at start of H_2 treatment	149.2313
Weight at end of H_2 treatment	149.264
Weight change (g)	-0.0327
Calculated moles of oxygen	-2.04E-03
CH_3I concentration	
Cylinder volume (L)	43.8
Liquid density (g/mL)	2.279
CH_3I loaded in cylinder (mL)	20
Initial charge pressure (psig)	106
CH_3I conc. in cylinder (g/L)	0.126739
Available gas (L)	359.6367
Total gas rate	11.4

Based on cylinder pressure drop/time		Intermediate values based on pressure drop	
Initial run pressure (psig)	106	106	106
Final run pressure (psig)	46.5	90	46.5
Flow time (s)	127200	45000	127200
CH_3I flow rate (g/min)	0.012068	0.009173	0.012068

Table A.2.17: (continued)

Based on cylinder concentration and flow rate			
Flow rate (L/min)	0.085		
Total gas rate (L/min)	11.4		
CH_3I flow rate (g/min)	0.010773		
		Intermediate values based on pressure drop	
CH_3I conc. (g/L) - flow rate	0.000945		
CH_3I conc. (g/L) - ΔP	0.001059	0.000805	0.001059
Weight at start of CH_3I loading	149.1937		
Weight at end of CH_3I loading	149.4213		
Weight change (g)	0.2276		
Calculated moles of iodine	1.79E-03		
Weight at start of air flush	149.4213		
Weight at end of air flush	149.4213	Note: air flush data not recorded	
Weight change (g)	0		
Calculated moles of iodine	0.00E+00		
Iodine remaining (g)	0.2276		
Iodine remaining (gmol)	1.79E-03		
Final percent Ag utilization	39.38		

APPENDIX A.3
QuickBasic PROGRAM USED TO INTERFACE WITH SARTORIOUS BALANCE AND RECORD WEIGHT/TIME DATA

```
'-------------------------------------------------------------
'-                                                           -
'-                      Weight Analysis                      -
'-                                                           -
'-------------------------------------------------------------
'
'
'
'
'                   NOMENCLATURE FOR THIS PROGRAM
'
'       RTIME     -       Total run time for the experiment:
'                         must be given in seconds
'       TINTV     -       Time interval between samples weighed:
'                         must be given in seconds
'       BL$       -       String representation of the mass recorded
'                         from the MC1 scale at a specific instant in
'                         time
'       T$(NRUN)  -       Array that represents the time at which the
'                         corresponding Y(NRUN) masses are recorded
'       X(NRUN)   -       Array that represents the elapsed time at which
'                         the corresponding Y(NRUN) masses are recorded
'       Y(NRUN)   -       Array that represents the mass at which the
'                         corresponding X(NRUN) times are recorded
'       X(NRUN)   -       Array that represents the time at which the
'                         corresponding Y(NRUN) masses are recorded
'       BL2$(6)   -       Array that represents the mass at 10 second
'                         intervals during the final minute of each weighing
'                         period
'       TI        -       A counter used in the for next loops
'       TI2       -       A counter used in the average weight for next loops
'       REALMASS  -       Numerical representation for BL$
'       INSTRATE  -       Rate at which the iodine is loaded for the
'                         specified time intervals TINTV
'       AVETIME&  -       1/3 of the run time:  represents the time
'                         intervals representing the trends in the
'                         loading of the bed
'       ANR       -       Represents the number of runs that occur
'                         between and during an AVETIME& period
'       AVERATE   -       Rate at which the iodine is loaded for the
'                         specified time interval AVETIME&
'       GTIME     -       The time interval to be used on the graph
'                         determined by the user, may be in minutes
'                         or seconds pending the length of time
'       OD        -       Initial date that the current run was
'                         started.
'       CD        -       Current date in the current run.
'       TIM$      -       Current time as a string.
'       OTIME&    -       Initial time that the run was started in seconds
'                         since midnight of run start day.
'       CTIME&    -       Current elapsed time since run was started in
'                         seconds since midnight of initial day.
'       ELAPD     -       Elapsed days or date changes since initial day
'       RATE30    -       Average rate of loading over last 30 minutes
'       RATE60    -       Average rate of loading over last 60 minutes
'       RATE120   -       Average rate of loading over last 120 minutes

'*************************************************************************
'*                                                                       *
'*      Clears previously created results printed to the screen          *
'*                                                                       *
'*************************************************************************

CLS
P$ = CHR$(27) + "P"
T$ = CHR$(27) + "T"
K$ = CHR$(27) + "K"
```

```
L$ = CHR$(27) + "L"
M$ = CHR$(27) + "M"
N$ = CHR$(27) + "N"

'************************************************************************
'*                                                                      *
'*      Allows for communication between the balance and computer       *
'*                                                                      *
'************************************************************************

OPEN "COM1:1200,O,,,CS,DS" FOR RANDOM AS #1

'************************************************************************
'*                                                                      *
'*                              Set up case                             *
'*                                                                      *
'************************************************************************

INPUT "This run will last (in hours)    - "; RTIMEH!
INPUT "Sampling time intervals (min)    - "; TINTVM!
INPUT "Enter air rate (L/MIN)           - "; AIRR$
INPUT "Enter H2/Ar rate (L/MIN)         - "; H2R$
INPUT "Enter CH3I rate (L/MIN)          - "; CH3IR$
INPUT "Enter TOTAL gas rate (L/MIN)     - "; TOTALR$
INPUT "Enter CH3I concentration (MG/M3) - "; CH3I$
INPUT "Enter Temperature (C)            - "; TEMP$
INPUT "Pellet size - diameter (in)      - "; PELLET$
RTIME& = INT(RTIMEH! * 60 * 60)
TINTV = INT(TINTVM! * 60)
REM PRINT RTIME&, RTIMEH!, TINTVM!, TINTV
DO UNTIL TARE$ = "Y" OR TARE$ = "N"
   LOCATE 10, 1
   INPUT "Tare Balance (Y/N)              - "; TARE$
   IF TARE$ = "y" THEN
      TARE$ = "Y"
   END IF
   IF TARE$ = "n" THEN
      TARE$ = "N"
   END IF
LOOP
DO UNTIL AMB$ = "K" OR AMB$ = "L" OR AMB$ = "M" OR AMB$ = "N"
   LOCATE 11, 1
   INPUT "Stability Code (K/L/M/N)         - "; AMB$
   IF AMB$ = "k" THEN
      AMB$ = "K"
   END IF
   IF AMB$ = "l" THEN
      AMB$ = "L"
   END IF
   IF AMB$ = "m" THEN
      AMB$ = "M"
   END IF
   IF AMB$ = "n" THEN
      AMB$ = "N"
   END IF
LOOP
INPUT "Enter file name for output (ex - A:\TEST_1.DAT)"; OUTFILE$
INPUT "Enter case description"; CASEDESC$

OPEN OUTFILE$ FOR OUTPUT AS #2

OD = VAL(RIGHT$(LEFT$(DATE$, 5), 2))
TIM$ = TIME$
OTIME& = VAL(LEFT$(TIM$, 2)) * 3600 + VAL(RIGHT$(TIM$, 2))
OTIME& = OTIME& + VAL(RIGHT$(LEFT$(TIM$, 5), 2)) * 60
ELAPD = 0
```

```
NRUN = INT(RTIME& / TINTV) + 1
DIM T$(NRUN)
DIM X(NRUN)
DIM Y(NRUN)
DIM Z(NRUN)
DIM BL2(6)

'*************************************************************************
'*                                                                       *
'*      Returns the number of characters of unused space in the input    *
'*      buffer.  As long as the number of characters is greater than     *
'*      255, this command remains inoperable.  It usually fluctuates     *
'*      around 512 characters.                                           *
'*                                                                       *
'*************************************************************************

IF LOF(1) < 255 THEN INPUT #1, BL$: PRINT TIME$, BL$:  GOSUB DAT

'*************************************************************************
'*                                                                       *
'*            Initiate actual recording of data from balance             *
'*                                                                       *
'*************************************************************************

PRINT #2, "21  "; NRUN
PRINT #2, "Case Description - : "; CASEDESC$
PRINT #2, "Data file name                - "; OUTFILE$
PRINT #2, "Air rate (L/MIN)              - "; AIRR$
PRINT #2, "H2/Ar rate (L/MIN)            - "; H2R$
PRINT #2, "CH3I rate (L/MIN)             - "; CH3IR$
PRINT #2, "TOTAL gas rate (L/MIN)        - "; TOTALR$
PRINT #2, "CH3I concentration (MG/M3)    - "; CH3I$
PRINT #2, "Temperature (C)               - "; TEMP$
PRINT #2, "Pellet size - diameter (mm)   - "; PELLET$
PRINT #2, "Stability Code (K/L/M/N)      - "; AMB$
PRINT #2, "Run date                      - "; DATE$
PRINT #2, "Run start time                - "; TIME$
PRINT #2, "This sorbents run will last - "; RTIME&; " seconds"
PRINT #2, NRUN; "readings will be recorded at intervals of"; TINTV; "seconds."
PRINT #2, " "
PRINT #2, "-------------------------------------------------------------------"
PRINT #2, "Point #    Clock      Elapsed Time    Loaded Weight   Loading Rate "
PRINT #2, "           Time          (sec)          (grams)       (grams/sec) "
PRINT #2, "-------------------------------------------------------------------"

CLS
LOCATE 1, 1
PRINT "This sorbents run will last - "; RTIME&; " seconds"
PRINT NRUN; "readings will be recorded at intervals of"; TINTV; "seconds."
PRINT " "
IF AMB$ = "K" THEN
   PRINT #1, K$:
   PRINT TIME$; "      Stability Set to VERY STABLE"
   PRINT #2, TIME$; "      Stability Set to VERY STABLE"
END IF
IF AMB$ = "L" THEN
   PRINT #1, L$:
   PRINT TIME$; "      Stability Set to STABLE"
   PRINT #2, TIME$; "      Stability Set to STABLE"
END IF
IF AMB$ = "M" THEN
   PRINT #1, M$:
   PRINT TIME$; "      Stability Set to UNSTABLE"
   PRINT #2, TIME$; "      Stability Set to UNSTABLE"
END IF
IF AMB$ = "N" THEN
   PRINT #1, N$:
```

```
   PRINT TIME$; "      Stability Set to VERY UNSTABLE"
   PRINT #2, TIME$; "      Stability Set to VERY UNSTABLE"
END IF
IF TARE$ = "Y" THEN
   PRINT #1, T$:
   PRINT TIME$; "      Balanced Tared"
   PRINT #2, TIME$; "      Balanced Tared"
ELSE
   PRINT #2, TIME$; "      Balanced NOT Tared"
END IF
CLOSE #2

LOCATE 5, 1
PRINT "-------------------------------------------------------------------------"
PRINT "Point #    Clock      Elapsed Time    Loaded Weight   Loading Rate "
PRINT "           Time          (sec)          (grams)       (grams/sec) "
PRINT "-------------------------------------------------------------------------"
'     0         1         2         3         4         5         6
'     01234567890123456789012345678901234567890123456789012345678901234567890123456
'*************************************************************************
'*                                                                       *
'*      Read initial weight from balance by calling subroutine DAT       *
'*                                                                       *
'*************************************************************************

TI = 1
GOSUB DAYTIME
GOSUB DAT

'*************************************************************************
'*                                                                       *
'*      For-next loop that calls up the subroutine DAT every interval    *
'*      of time specified above by the user:  Also begins time count.    *
'*                                                                       *
'*************************************************************************

FOR TI = 2 TO NRUN
  IF TINTV < 180 THEN
     DO
        GOSUB DAYTIME
     LOOP WHILE CTIME& < OTIME& + (TINTV * (TI - 1))
  END IF
  IF TINTV >= 180 THEN
     DO
        GOSUB DAYTIME
     LOOP WHILE CTIME& < OTIME& + (TINTV * (TI - 1) - 60)
  END IF
  GOSUB DAT
NEXT TI

CLOSE #1

END
```

```
'*************************************************************************
'*                                                                       *
'*                          SUBROUTINE DAYTIME                           *
'*                       Calculates elapsed time                         *
'*                                                                       *
'*************************************************************************

DAYTIME:

TIM$ = TIME$
CTIME& = VAL(LEFT$(TIM$, 2)) * 3600 + VAL(RIGHT$(TIM$, 2))
CTIME& = CTIME& + VAL(RIGHT$(LEFT$(TIM$, 5), 2)) * 60
CD = VAL(RIGHT$(LEFT$(DATE$, 5), 2))
IF CD <> OD THEN
   ELAPD = ELAPD + 1
   OD = VAL(RIGHT$(LEFT$(DATE$, 5), 2))
END IF
ELAPS1& = 3600
ELAPS2& = 24 * ELAPD
ELAPS& = ELAPS1& * ELAPS2&
CTIME& = CTIME& + ELAPS&

' PRINT TIM$, ELAPD, ELAPS&, CTIME&, OTIME& + (TINTV * (TI - 1))

RETURN
```

```
'*************************************************************************
'*                                                                       *
'*                          SUBROUTINE DAT                               *
'*     Reads data from scale, displays on monitor and stores in file     *
'*                                                                       *
'*************************************************************************

DAT:
REALMAS6 = 0!
REALMASS = 0!
IF TINTV >= 180 THEN
   FOR TI2 = 1 TO 6
     DO
        GOSUB DAYTIME
        LOOP WHILE CTIME& < OTIME& + (TINTV * (TI - 1) - (60 - TI2 * 10))
        PRINT #1, P$
        INPUT #1, BL$
        BL2(TI2) = VAL(BL$)
        REALMAS6 = REALMAS6 + VAL(BL$)
   NEXT TI2

   REALMASS = REALMAS6 / 6

END IF

IF TINTV < 180 THEN
   PRINT #1, P$
   INPUT #1, BL$
   REALMASS = VAL(BL$)
END IF

' Stores time and mass into arrays x and y

X(TI) = TINTV * (TI - 1)
Y(TI) = REALMASS
T$(TI) = TIM$
' compute instantaneous rate of change
IF TI > 1 THEN
   INSTRATE = (Y(TI) - Y(TI - 1)) / TINTV
   Z(TI) = INSTRATE
ELSE
   INSTRATE = 0
   Z(TI) = INSTRATE
END IF

LOCATE 9, 1
LC = 9
IF TI > 6 THEN
   FOR TIC = TI - 5 TO TI
      ' PRINT TIC, T$(TIC), X(TIC), Y(TIC), Z(TIC)
      LOCATE LC, 1
      PRINT TIC
      LOCATE LC, 12
      PRINT T$(TIC)
      LOCATE LC, 24
      PRINT USING "#######."; X(TIC)
      LOCATE LC, 40
      PRINT USING "####.####"; Y(TIC)
      LOCATE LC, 56
      PRINT USING "##.##^^^^"; Z(TIC)
      LC = LC + 1
   NEXT TIC
ELSE
   FOR TIC = 1 TO TI
      ' PRINT TIC, T$(TIC), X(TIC), Y(TIC), Z(TIC)
      LOCATE LC, 1
      PRINT TIC
```

```
      LOCATE LC, 12
      PRINT T$(TIC)
      LOCATE LC, 24
      PRINT USING "#######."; X(TIC)
      LOCATE LC, 40
      PRINT USING "####.####"; Y(TIC)
      LOCATE LC, 56
      PRINT USING "##.##^^^^"; Z(TIC)
      LC = LC + 1
   NEXT TIC
END IF

' Display Initial weight and total weight change
LOCATE 17, 1
PRINT "Initial Weight (grams)      - "
LOCATE 17, 32
PRINT USING "####.###"; Y(1)
LOCATE 18, 1
PRINT "Total Weight Change (grams) - "
LOCATE 18, 32
PRINT USING "####.###"; Y(TI) - Y(1)
'     0         1         2         3         4         5         6
'     01234567890123456789012345678901234567890123456789012345678980123456

' compute longer term rates of change
LOCATE 20, 1
IF INT(X(TI) / 60) >= 30 THEN
   ZTOTAL = 0
   ZCOUNT = 0
   TICS = TI - INT(30 * 60 / TINTV)
   FOR TIC = TI - INT(30 * 60 / TINTV) TO TI
      ZTOTAL = Z(TIC) + ZTOTAL
      ZCOUNT = ZCOUNT + 1
   NEXT TIC
   ' RATE30 = (ZTOTAL / ZCOUNT) * 60
   RATE30 = (Y(TI) - Y(TICS)) / 30
   PRINT "Average loading rate over last 30 minutes (grams/min): "
   LOCATE 20, 57
   PRINT USING "##.##^^^^"; RATE30
END IF
LOCATE 21, 1
IF INT(X(TI) / 60) >= 60 THEN
   ZTOTAL = 0
   ZCOUNT = 0
   TICS = TI - INT(60 * 60 / TINTV)
   FOR TIC = TI - INT(60 * 60 / TINTV) TO TI
      ZTOTAL = Z(TIC) + ZTOTAL
      ZCOUNT = ZCOUNT + 1
   NEXT TIC
   ' RATE60 = (ZTOTAL / ZCOUNT) * 60
   RATE60 = (Y(TI) - Y(TICS)) / 60
   PRINT "Average loading rate over last 60 minutes (grams/min): "
   LOCATE 21, 57
   PRINT USING "##.##^^^^"; RATE60
END IF
LOCATE 22, 1
IF INT(X(TI) / 60) >= 120 THEN
   ZTOTAL = 0
   ZCOUNT = 0
   TICS = TI - INT(120 * 60 / TINTV)
   FOR TIC = TI - INT(120 * 60 / TINTV) TO TI
      ZTOTAL = Z(TIC) + ZTOTAL
      ZCOUNT = ZCOUNT + 1
   NEXT TIC
   ' RATE120 = (ZTOTAL / ZCOUNT) * 60
   RATE120 = (Y(TI) - Y(TICS)) / 120
   PRINT "Average loading rate over last 120 minutes (grams/min): "
```

```
    '     0         1         2         3         4         5         6
    '     01234567890123456789012345678901234567890123456789012345678901234567890123456
    LOCATE 22, 57
    PRINT USING "##.##^^^^"; RATE120
END IF

OPEN OUTFILE$ FOR APPEND AS #2
WRITE #2, TI, TIM$, INT(TINTV * (TI - 1)), REALMASS, INSTRATE
CLOSE #2

RETURN
```

APPENDIX A.4
SUMMARY RESULTS FROM BIMODAL MODEL ANALYSIS USED TO GENERATE ERROR SURFACE MAPS

Table A.4.1: Test T3 summary data from bimodal model curve fitting.

α	β	D_c (cm^2/s)	Error
1.00E+02	1.00E+02	2.44E-12	1.17E-02
1.00E+02	1.00E+01	1.89E-12	1.16E-02
1.00E+02	1.00E+00	1.83E-12	1.16E-02
1.00E+02	1.00E-01	1.82E-12	1.16E-02
1.00E+02	1.00E-02	1.82E-12	1.16E-02
1.00E+02	1.00E-03	1.82E-12	1.16E-02
1.00E+01	1.00E+02	8.14E-13	1.72E-02
1.00E+01	1.00E+01	2.51E-13	1.08E-02
1.00E+01	1.00E+00	1.89E-13	1.09E-02
1.00E+01	1.00E-01	1.83E-13	1.15E-02
1.00E+01	1.00E-02	1.82E-13	1.15E-02
1.00E+01	1.00E-03	1.82E-13	1.15E-02
1.00E+00	1.00E+02	6.56E-13	2.48E-02
1.00E+00	1.00E+01	1.03E-13	6.93E-02
1.00E+00	1.00E+00	2.95E-14	7.81E-03
1.00E+00	1.00E-01	1.93E-14	1.12E-02
1.00E+00	1.00E-02	1.83E-14	1.15E-02
1.00E+00	1.00E-03	1.82E-14	1.15E-02
1.00E-01	1.00E+02	6.40E-13	2.62E-02
1.00E-01	1.00E+01	9.27E-14	1.43E-01
1.00E-01	1.00E+00	2.23E-14	1.10E-02
1.00E-01	1.00E-01	3.46E-15	3.29E-02
1.00E-01	1.00E-02	1.95E-15	1.40E-02
1.00E-01	1.00E-03	1.75E-15	5.90E-02
1.00E-02	1.00E+02	6.39E-13	2.63E-02
1.00E-02	1.00E+01	9.18E-14	1.56E-01
1.00E-02	1.00E+00	2.70E-14	5.37E-02
1.00E-02	1.00E-01	9.44E-15	3.92E-01
1.00E-02	1.00E-02	3.46E-16	1.72E-01
1.00E-02	1.00E-03	1.56E-16	1.28E+00
1.00E-03	1.00E+02	6.40E-13	2.63E-02
1.00E-03	1.00E+01	9.17E-14	1.58E-01
1.00E-03	1.00E+00	2.77E-14	7.03E-02
1.00E-03	1.00E-01	1.73E-14	2.50E-02
1.00E-03	1.00E-02	7.36E-15	9.53E-01
1.00E-03	1.00E-03	1.54E-17	1.89E+01

Table A.4.2: Test T6 summary data from bimodal model curve fitting.

α	β	D_c (cm^2/s)	Error
1.00E+02	1.00E+02	3.02E-12	7.16E-02
1.00E+02	1.00E+01	2.34E-12	7.40E-02
1.00E+02	1.00E+00	2.27E-12	7.44E-02
1.00E+02	1.00E-01	2.26E-12	7.44E-02
1.00E+02	1.00E-02	2.26E-12	7.44E-02
1.00E+02	1.00E-03	2.26E-12	7.44E-02
1.00E+01	1.00E+02	1.00E-12	5.08E-02
1.00E+01	1.00E+01	3.09E-13	4.97E-02
1.00E+01	1.00E+00	2.35E-13	7.04E-02
1.00E+01	1.00E-01	2.27E-13	7.41E-02
1.00E+01	1.00E-02	2.26E-13	7.44E-02
1.00E+01	1.00E-03	2.26E-13	7.44E-02
1.00E+00	1.00E+02	8.06E-13	4.16E-02
1.00E+00	1.00E+01	1.23E-13	1.55E-02
1.00E+00	1.00E+00	3.62E-14	5.19E-02
1.00E+00	1.00E-01	2.40E-14	7.39E-02
1.00E+00	1.00E-02	2.27E-14	7.46E-02
1.00E+00	1.00E-03	2.26E-14	7.45E-02
1.00E-01	1.00E+02	7.87E-13	4.05E-02
1.00E-01	1.00E+01	1.09E-13	4.87E-02
1.00E-01	1.00E+00	2.74E-14	3.78E-02
1.00E-01	1.00E-01	4.40E-15	1.64E-01
1.00E-01	1.00E-02	2.43E-15	9.17E-02
1.00E-01	1.00E-03	2.24E-15	1.64E-01
1.00E-02	1.00E+02	7.85E-13	4.04E-02
1.00E-02	1.00E+01	1.08E-13	5.60E-02
1.00E-02	1.00E+00	3.22E-14	1.40E-02
1.00E-02	1.00E-01	1.34E-14	7.75E-01
1.00E-02	1.00E-02	4.64E-16	4.46E-01
1.00E-02	1.00E-03	2.19E-16	1.53E+00
1.00E-03	1.00E+02	7.84E-13	4.04E-02
1.00E-03	1.00E+01	1.08E-13	5.68E-02
1.00E-03	1.00E+00	3.30E-14	1.83E-02
1.00E-03	1.00E-01	2.17E-14	1.25E-01
1.00E-03	1.00E-02	1.13E-14	1.41E+00
1.00E-03	1.00E-03	1.54E-17	1.67E+01

Table A.4.3: Test T7 summary data from bimodal model curve fitting.

α	β	D_c (cm^2/s)	Error
1.00E+02	1.00E+02	9.02E-13	6.60E-01
1.00E+02	1.00E+01	6.96E-13	6.66E-01
1.00E+02	1.00E+00	6.75E-13	6.67E-01
1.00E+02	1.00E-01	6.73E-13	6.67E-01
1.00E+02	1.00E-02	6.73E-13	6.67E-01
1.00E+02	1.00E-03	6.73E-13	6.67E-01
1.00E+01	1.00E+02	3.10E-13	5.91E-01
1.00E+01	1.00E+01	9.61E-14	6.00E-01
1.00E+01	1.00E+00	7.03E-14	6.59E-01
1.00E+01	1.00E-01	6.75E-14	6.66E-01
1.00E+01	1.00E-02	6.73E-14	6.66E-01
1.00E+01	1.00E-03	6.72E-14	6.67E-01
1.00E+00	1.00E+02	2.53E-13	5.54E-01
1.00E+00	1.00E+01	4.52E-14	4.19E-01
1.00E+00	1.00E+00	1.12E-14	6.39E-01
1.00E+00	1.00E-01	7.14E-15	6.67E-01
1.00E+00	1.00E-02	6.76E-15	6.67E-01
1.00E+00	1.00E-03	6.73E-15	6.67E-01
1.00E-01	1.00E+02	2.48E-13	5.50E-01
1.00E-01	1.00E+01	4.25E-14	3.48E-01
1.00E-01	1.00E+00	8.71E-15	5.78E-01
1.00E-01	1.00E-01	1.20E-15	7.20E-01
1.00E-01	1.00E-02	7.09E-16	6.99E-01
1.00E-01	1.00E-03	6.18E-16	8.81E-01
1.00E-02	1.00E+02	2.47E-13	5.49E-01
1.00E-02	1.00E+01	4.23E-14	3.40E-01
1.00E-02	1.00E+00	1.15E-14	4.50E-01
1.00E-02	1.00E-01	1.82E-15	1.24E+00
1.00E-02	1.00E-02	1.19E-16	1.09E+00
1.00E-02	1.00E-03	1.54E-17	4.50E+00
1.00E-03	1.00E+02	2.47E-13	5.49E-01
1.00E-03	1.00E+01	4.23E-14	3.40E-01
1.00E-03	1.00E+00	1.20E-14	4.27E-01
1.00E-03	1.00E-01	6.09E-15	7.72E-01
1.00E-03	1.00E-02	9.67E-17	2.35E+00
1.00E-03	1.00E-03	1.54E-17	4.14E+01

Table A.4.4: Test T8 summary data from bimodal model curve fitting.

α	β	D_c (cm^2/s)	Error
1.00E+02	1.00E+02	7.60E-13	8.65E-01
1.00E+02	1.00E+01	5.86E-13	8.73E-01
1.00E+02	1.00E+00	5.68E-13	8.75E-01
1.00E+02	1.00E-01	5.66E-13	8.75E-01
1.00E+02	1.00E-02	5.66E-13	8.75E-01
1.00E+02	1.00E-03	5.66E-13	8.75E-01
1.00E+01	1.00E+02	2.61E-13	7.79E-01
1.00E+01	1.00E+01	8.10E-14	7.93E-01
1.00E+01	1.00E+00	5.92E-14	8.64E-01
1.00E+01	1.00E-01	5.69E-14	8.73E-01
1.00E+01	1.00E-02	5.66E-14	8.73E-01
1.00E+01	1.00E-03	5.66E-14	8.73E-01
1.00E+00	1.00E+02	2.14E-13	7.32E-01
1.00E+00	1.00E+01	3.83E-14	5.70E-01
1.00E+00	1.00E+00	9.44E-15	8.41E-01
1.00E+00	1.00E-01	6.01E-15	8.74E-01
1.00E+00	1.00E-02	5.69E-15	8.73E-01
1.00E+00	1.00E-03	5.66E-15	8.73E-01
1.00E-01	1.00E+02	2.09E-13	7.26E-01
1.00E-01	1.00E+01	3.60E-14	4.79E-01
1.00E-01	1.00E+00	7.35E-15	7.67E-01
1.00E-01	1.00E-01	1.01E-15	9.37E-01
1.00E-01	1.00E-02	5.91E-16	9.13E-01
1.00E-01	1.00E-03	5.20E-16	1.13E+00
1.00E-02	1.00E+02	2.09E-13	7.25E-01
1.00E-02	1.00E+01	3.59E-14	4.68E-01
1.00E-02	1.00E+00	9.77E-15	6.08E-01
1.00E-02	1.00E-01	1.51E-15	1.54E+00
1.00E-02	1.00E-02	9.98E-17	1.41E+00
1.00E-02	1.00E-03	1.54E-17	5.49E+00
1.00E-03	1.00E+02	2.09E-13	7.25E-01
1.00E-03	1.00E+01	3.59E-14	4.67E-01
1.00E-03	1.00E+00	1.02E-14	5.79E-01
1.00E-03	1.00E-01	5.10E-15	1.00E+00
1.00E-03	1.00E-02	8.00E-17	2.73E+00
1.00E-03	1.00E-03	1.54E-17	4.87E+01

Table A.4.5: Test T10 summary data from bimodal model curve fitting.

α	β	D_c (cm^2/s)	Error
1.00E+02	1.00E+02	4.59E-12	6.49E-01
1.00E+02	1.00E+01	3.55E-12	6.52E-01
1.00E+02	1.00E+00	3.45E-12	6.52E-01
1.00E+02	1.00E-01	3.44E-12	6.52E-01
1.00E+02	1.00E-02	3.44E-12	6.52E-01
1.00E+02	1.00E-03	3.44E-12	6.52E-01
1.00E+01	1.00E+02	1.51E-12	6.28E-01
1.00E+01	1.00E+01	4.65E-13	6.22E-01
1.00E+01	1.00E+00	3.56E-13	6.47E-01
1.00E+01	1.00E-01	3.45E-13	6.51E-01
1.00E+01	1.00E-02	3.44E-13	6.52E-01
1.00E+01	1.00E-03	3.44E-13	6.52E-01
1.00E+00	1.00E+02	1.21E-12	6.14E-01
1.00E+00	1.00E+01	1.74E-13	4.01E-01
1.00E+00	1.00E+00	5.41E-14	5.85E-01
1.00E+00	1.00E-01	3.64E-14	6.51E-01
1.00E+00	1.00E-02	3.46E-14	6.52E-01
1.00E+00	1.00E-03	3.44E-14	6.52E-01
1.00E-01	1.00E+02	1.18E-12	6.12E-01
1.00E-01	1.00E+01	1.51E-13	3.08E-01
1.00E-01	1.00E+00	4.08E-14	5.93E-01
1.00E-01	1.00E-01	7.19E-15	1.23E+00
1.00E-01	1.00E-02	3.73E-15	7.07E-01
1.00E-01	1.00E-03	3.44E-15	6.76E-01
1.00E-02	1.00E+02	1.17E-12	6.12E-01
1.00E-02	1.00E+01	1.49E-13	2.97E-01
1.00E-02	1.00E+00	4.57E-14	3.83E-01
1.00E-02	1.00E-01	2.58E-14	1.38E+00
1.00E-02	1.00E-02	8.05E-16	2.09E+00
1.00E-02	1.00E-03	3.39E-16	1.10E+00
1.00E-03	1.00E+02	1.17E-12	6.12E-01
1.00E-03	1.00E+01	1.49E-13	2.96E-01
1.00E-03	1.00E+00	4.64E-14	3.54E-01
1.00E-03	1.00E-01	3.37E-14	7.16E-01
1.00E-03	1.00E-02	2.31E-14	1.62E+00
1.00E-03	1.00E-03	6.19E-16	6.52E+00

Table A.4.6: Test T11 summary data from bimodal model curve fitting.

α	β	D_e (cm^2/s)	Error
1.00E+02	1.00E+02	1.62E-12	5.91E-03
1.00E+02	1.00E+01	1.25E-12	5.37E-03
1.00E+02	1.00E+00	1.21E-12	5.29E-03
1.00E+02	1.00E-01	1.20E-12	5.23E-03
1.00E+02	1.00E-02	1.20E-12	5.23E-03
1.00E+02	1.00E-03	1.20E-12	5.23E-03
1.00E+01	1.00E+02	5.57E-13	1.28E-02
1.00E+01	1.00E+01	1.71E-13	5.16E-03
1.00E+01	1.00E+00	1.26E-13	4.90E-03
1.00E+01	1.00E-01	1.21E-13	4.98E-03
1.00E+01	1.00E-02	1.20E-13	4.67E-03
1.00E+01	1.00E-03	1.20E-13	4.67E-03
1.00E+00	1.00E+02	4.55E-13	2.06E-02
1.00E+00	1.00E+01	7.90E-14	2.63E-02
1.00E+00	1.00E+00	2.00E-14	4.11E-03
1.00E+00	1.00E-01	1.28E-14	4.65E-03
1.00E+00	1.00E-02	1.21E-14	4.59E-03
1.00E+00	1.00E-03	1.20E-14	4.58E-03
1.00E-01	1.00E+02	4.47E-13	2.19E-02
1.00E-01	1.00E+01	7.44E-14	5.75E-02
1.00E-01	1.00E+00	1.55E-14	4.74E-03
1.00E-01	1.00E-01	2.16E-15	7.35E-03
1.00E-01	1.00E-02	1.27E-15	5.58E-03
1.00E-01	1.00E-03	1.10E-15	4.88E-02
1.00E-02	1.00E+02	4.44E-13	2.21E-02
1.00E-02	1.00E+01	7.42E-14	6.36E-02
1.00E-02	1.00E+00	2.03E-14	2.27E-02
1.00E-02	1.00E-01	3.60E-15	9.53E-02
1.00E-02	1.00E-02	1.98E-16	1.14E-01
1.00E-02	1.00E-03	1.54E-17	1.36E+00
1.00E-03	1.00E+02	4.44E-13	2.21E-02
1.00E-03	1.00E+01	7.41E-14	6.42E-02
1.00E-03	1.00E+00	2.12E-14	3.02E-02
1.00E-03	1.00E-01	1.09E-14	1.13E-02
1.00E-03	1.00E-02	1.11E-15	5.00E-01
1.00E-03	1.00E-03	1.54E-17	2.16E+01

Table A.4.7: Test T12 summary data from bimodal model curve fitting.

α	β	D_c (cm^2/s)	Error
1.00E+02	1.00E+02	2.25E-13	1.80E-01
1.00E+02	1.00E+01	1.71E-13	1.93E-01
1.00E+02	1.00E+00	1.66E-13	1.96E-01
1.00E+02	1.00E-01	1.65E-13	1.97E-01
1.00E+02	1.00E-02	1.65E-13	1.97E-01
1.00E+02	1.00E-03	1.65E-13	1.97E-01
1.00E+01	1.00E+02	8.68E-14	1.14E-01
1.00E+01	1.00E+01	2.53E-14	1.70E-01
1.00E+01	1.00E+00	1.74E-14	1.96E-01
1.00E+01	1.00E-01	1.66E-14	2.02E-01
1.00E+01	1.00E-02	1.66E-14	2.10E-01
1.00E+01	1.00E-03	1.65E-14	2.10E-01
1.00E+00	1.00E+02	7.44E-14	8.74E-02
1.00E+00	1.00E+01	1.39E-14	1.04E-01
1.00E+00	1.00E+00	2.80E-15	1.97E-01
1.00E+00	1.00E-01	1.75E-15	2.10E-01
1.00E+00	1.00E-02	1.67E-15	2.13E-01
1.00E+00	1.00E-03	1.66E-15	2.13E-01
1.00E-01	1.00E+02	7.36E-14	8.43E-02
1.00E-01	1.00E+01	1.44E-14	6.12E-02
1.00E-01	1.00E+00	2.33E-15	1.74E-01
1.00E-01	1.00E-01	2.82E-16	2.28E-01
1.00E-01	1.00E-02	1.63E-16	2.59E-01
1.00E-01	1.00E-03	4.85E-17	7.48E-01
1.00E-02	1.00E+02	7.36E-14	8.40E-02
1.00E-02	1.00E+01	1.45E-14	5.56E-02
1.00E-02	1.00E+00	3.53E-15	1.03E-01
1.00E-02	1.00E-01	2.96E-16	3.20E-01
1.00E-02	1.00E-02	1.54E-17	1.41E+00
1.00E-02	1.00E-03	1.54E-17	1.10E+01
1.00E-03	1.00E+02	7.36E-14	8.39E-02
1.00E-03	1.00E+01	1.45E-14	5.51E-02
1.00E-03	1.00E+00	3.78E-15	8.81E-02
1.00E-03	1.00E-01	1.30E-15	2.88E-01
1.00E-03	1.00E-02	3.28E-17	7.36E-01
1.00E-03	1.00E-03	1.54E-17	7.36E+01

Table A.4.8: Test T13 summary data from bimodal model curve fitting.

α	β	D_c (cm^2/s)	Error
1.00E+02	1.00E+02	9.63E-13	9.98E-01
1.00E+02	1.00E+01	7.44E-13	1.01E+00
1.00E+02	1.00E+00	7.22E-13	1.01E+00
1.00E+02	1.00E-01	7.20E-13	1.01E+00
1.00E+02	1.00E-02	7.19E-13	1.01E+00
1.00E+02	1.00E-03	7.19E-13	1.01E+00
1.00E+01	1.00E+02	3.26E-13	9.08E-01
1.00E+01	1.00E+01	1.01E-13	9.15E-01
1.00E+01	1.00E+00	7.50E-14	9.96E-01
1.00E+01	1.00E-01	7.23E-14	1.01E+00
1.00E+01	1.00E-02	7.20E-14	1.01E+00
1.00E+01	1.00E-03	7.19E-14	1.01E+00
1.00E+00	1.00E+02	2.65E-13	8.51E-01
1.00E+00	1.00E+01	4.59E-14	6.26E-01
1.00E+00	1.00E+00	1.19E-14	9.62E-01
1.00E+00	1.00E-01	7.64E-15	1.01E+00
1.00E+00	1.00E-02	7.24E-15	1.01E+00
1.00E+00	1.00E-03	7.20E-15	1.01E+00
1.00E-01	1.00E+02	2.59E-13	8.43E-01
1.00E-01	1.00E+01	4.26E-14	4.99E-01
1.00E-01	1.00E+00	9.15E-15	8.79E-01
1.00E-01	1.00E-01	1.30E-15	1.09E+00
1.00E-01	1.00E-02	7.67E-16	1.05E+00
1.00E-01	1.00E-03	6.68E-16	1.18E+00
1.00E-02	1.00E+02	2.58E-13	8.42E-01
1.00E-02	1.00E+01	4.24E-14	4.82E-01
1.00E-02	1.00E+00	1.18E-14	6.77E-01
1.00E-02	1.00E-01	2.35E-15	1.89E+00
1.00E-02	1.00E-02	1.21E-16	1.24E+00
1.00E-02	1.00E-03	3.45E-17	3.72E+00
1.00E-03	1.00E+02	2.58E-13	8.42E-01
1.00E-03	1.00E+01	4.23E-14	4.81E-01
1.00E-03	1.00E+00	1.23E-14	6.38E-01
1.00E-03	1.00E-01	6.66E-15	1.14E+00
1.00E-03	1.00E-02	1.47E-15	2.79E+00
1.00E-03	1.00E-03	1.54E-17	3.39E+01

Table A.4.9: Test T14 summary data from bimodal model curve fitting.

α	β	D_c (cm^2/s)	Error
1.00E+02	1.00E+02	5.01E-13	8.21E-02
1.00E+02	1.00E+01	3.85E-13	8.64E-02
1.00E+02	1.00E+00	3.73E-13	8.73E-02
1.00E+02	1.00E-01	3.72E-13	8.71E-02
1.00E+02	1.00E-02	3.72E-13	8.71E-02
1.00E+02	1.00E-03	3.72E-13	8.71E-02
1.00E+01	1.00E+02	1.77E-13	5.08E-02
1.00E+01	1.00E+01	5.44E-14	6.33E-02
1.00E+01	1.00E+00	3.90E-14	8.43E-02
1.00E+01	1.00E-01	3.74E-14	8.70E-02
1.00E+01	1.00E-02	3.72E-14	8.79E-02
1.00E+01	1.00E-03	3.72E-14	8.79E-02
1.00E+00	1.00E+02	1.47E-13	4.21E-02
1.00E+00	1.00E+01	2.70E-14	2.10E-02
1.00E+00	1.00E+00	6.24E-15	8.04E-02
1.00E+00	1.00E-01	3.95E-15	8.85E-02
1.00E+00	1.00E-02	3.74E-15	8.85E-02
1.00E+00	1.00E-03	3.72E-15	8.83E-02
1.00E-01	1.00E+02	1.44E-13	4.14E-02
1.00E-01	1.00E+01	2.60E-14	1.98E-02
1.00E-01	1.00E+00	4.96E-15	5.89E-02
1.00E-01	1.00E-01	6.54E-16	1.07E-01
1.00E-01	1.00E-02	3.89E-16	1.14E-01
1.00E-01	1.00E-03	3.37E-16	4.23E-01
1.00E-02	1.00E+02	1.44E-13	4.13E-02
1.00E-02	1.00E+01	2.60E-14	2.18E-02
1.00E-02	1.00E+00	6.84E-15	2.47E-02
1.00E-02	1.00E-01	8.60E-16	2.73E-01
1.00E-02	1.00E-02	5.52E-17	6.84E-01
1.00E-02	1.00E-03	1.54E-17	5.48E+00
1.00E-03	1.00E+02	1.44E-13	4.13E-02
1.00E-03	1.00E+01	2.60E-14	2.21E-02
1.00E-03	1.00E+00	7.20E-15	2.21E-02
1.00E-03	1.00E-01	3.22E-15	1.45E-01
1.00E-03	1.00E-02	6.29E-17	5.54E-01
1.00E-03	1.00E-03	1.54E-17	5.56E+01

Table A.4.10: Test T15 summary data from bimodal model curve fitting.

α	β	D_c (cm^2/s)	Error
1.00E+02	1.00E+02	6.57E-13	1.20E+00
1.00E+02	1.00E+01	5.07E-13	1.22E+00
1.00E+02	1.00E+00	4.92E-13	1.22E+00
1.00E+02	1.00E-01	4.90E-13	1.22E+00
1.00E+02	1.00E-02	4.90E-13	1.22E+00
1.00E+02	1.00E-03	4.90E-13	1.22E+00
1.00E+01	1.00E+02	2.29E-13	1.01E+00
1.00E+01	1.00E+01	7.09E-14	1.10E+00
1.00E+01	1.00E+00	5.13E-14	1.21E+00
1.00E+01	1.00E-01	4.92E-14	1.23E+00
1.00E+01	1.00E-02	4.91E-14	1.23E+00
1.00E+01	1.00E-03	4.90E-14	1.23E+00
1.00E+00	1.00E+02	1.88E-13	9.13E-01
1.00E+00	1.00E+01	3.43E-14	7.85E-01
1.00E+00	1.00E+00	8.21E-15	1.19E+00
1.00E+00	1.00E-01	5.20E-15	1.23E+00
1.00E+00	1.00E-02	4.93E-15	1.23E+00
1.00E+00	1.00E-03	4.91E-15	1.23E+00
1.00E-01	1.00E+02	1.84E-13	9.00E-01
1.00E-01	1.00E+01	3.27E-14	6.11E-01
1.00E-01	1.00E+00	6.46E-15	1.08E+00
1.00E-01	1.00E-01	8.67E-16	1.32E+00
1.00E-01	1.00E-02	5.19E-16	1.32E+00
1.00E-01	1.00E-03	4.69E-16	1.88E+00
1.00E-02	1.00E+02	1.83E-13	8.99E-01
1.00E-02	1.00E+01	3.26E-14	5.87E-01
1.00E-02	1.00E+00	8.72E-15	8.21E-01
1.00E-02	1.00E-01	1.17E-15	1.98E+00
1.00E-02	1.00E-02	9.26E-17	2.39E+00
1.00E-02	1.00E-03	1.54E-17	7.64E+00
1.00E-03	1.00E+02	1.83E-13	8.99E-01
1.00E-03	1.00E+01	3.26E-14	5.84E-01
1.00E-03	1.00E+00	9.13E-15	7.66E-01
1.00E-03	1.00E-01	4.37E-15	1.45E+00
1.00E-03	1.00E-02	6.63E-17	2.89E+00
1.00E-03	1.00E-03	1.54E-17	5.52E+01

Table A.4.11: Test T16 summary data from bimodal model curve fitting.

α	β	D_e (cm^2/s)	Error
1.00E+02	1.00E+02	1.56E-12	7.36E-01
1.00E+02	1.00E+01	1.21E-12	7.47E-01
1.00E+02	1.00E+00	1.17E-12	7.49E-01
1.00E+02	1.00E-01	1.17E-12	7.50E-01
1.00E+02	1.00E-02	1.17E-12	7.50E-01
1.00E+02	1.00E-03	1.17E-12	7.50E-01
1.00E+01	1.00E+02	5.22E-13	6.36E-01
1.00E+01	1.00E+01	1.62E-13	6.50E-01
1.00E+01	1.00E+00	1.21E-13	7.36E-01
1.00E+01	1.00E-01	1.17E-13	7.49E-01
1.00E+01	1.00E-02	1.17E-13	7.52E-01
1.00E+01	1.00E-03	1.17E-13	7.52E-01
1.00E+00	1.00E+02	4.22E-13	5.79E-01
1.00E+00	1.00E+01	6.94E-14	3.34E-01
1.00E+00	1.00E+00	1.91E-14	6.89E-01
1.00E+00	1.00E-01	1.24E-14	7.51E-01
1.00E+00	1.00E-02	1.17E-14	7.53E-01
1.00E+00	1.00E-03	1.17E-14	7.53E-01
1.00E-01	1.00E+02	4.14E-13	5.71E-01
1.00E-01	1.00E+01	6.32E-14	2.18E-01
1.00E-01	1.00E+00	1.45E-14	6.08E-01
1.00E-01	1.00E-01	2.15E-15	8.78E-01
1.00E-01	1.00E-02	1.25E-15	8.02E-01
1.00E-01	1.00E-03	1.14E-15	1.08E+00
1.00E-02	1.00E+02	4.13E-13	5.70E-01
1.00E-02	1.00E+01	6.27E-14	2.04E-01
1.00E-02	1.00E+00	1.81E-14	3.82E-01
1.00E-02	1.00E-01	4.95E-15	1.99E+00
1.00E-02	1.00E-02	2.00E-16	1.38E+00
1.00E-02	1.00E-03	9.30E-17	4.36E+00
1.00E-03	1.00E+02	4.13E-13	5.70E-01
1.00E-03	1.00E+01	6.27E-14	2.02E-01
1.00E-03	1.00E+00	1.86E-14	3.42E-01
1.00E-03	1.00E-01	1.09E-14	9.08E-01
1.00E-03	1.00E-02	3.57E-15	3.35E+00
1.00E-03	1.00E-03	1.54E-17	3.31E+01

Table A.4.12: Test T18 summary data from bimodal model curve fitting.

α	β	D_c (cm^2/s)	Error
1.00E+02	1.00E+02	5.14E-13	4.90E-01
1.00E+02	1.00E+01	3.94E-13	5.07E-01
1.00E+02	1.00E+00	3.82E-13	5.10E-01
1.00E+02	1.00E-01	3.81E-13	5.12E-01
1.00E+02	1.00E-02	3.81E-13	5.12E-01
1.00E+02	1.00E-03	3.81E-13	5.12E-01
1.00E+01	1.00E+02	1.81E-13	3.63E-01
1.00E+01	1.00E+01	5.59E-14	4.41E-01
1.00E+01	1.00E+00	4.00E-14	5.05E-01
1.00E+01	1.00E-01	3.83E-14	5.15E-01
1.00E+01	1.00E-02	3.82E-14	5.22E-01
1.00E+01	1.00E-03	3.82E-14	5.22E-01
1.00E+00	1.00E+02	1.51E-13	3.02E-01
1.00E+00	1.00E+01	2.78E-14	2.67E-01
1.00E+00	1.00E+00	6.41E-15	4.97E-01
1.00E+00	1.00E-01	4.05E-15	5.23E-01
1.00E+00	1.00E-02	3.84E-15	5.25E-01
1.00E+00	1.00E-03	3.82E-15	5.24E-01
1.00E-01	1.00E+02	1.48E-13	2.94E-01
1.00E-01	1.00E+01	2.70E-14	1.72E-01
1.00E-01	1.00E+00	5.10E-15	4.34E-01
1.00E-01	1.00E-01	6.68E-16	5.70E-01
1.00E-01	1.00E-02	3.96E-16	5.91E-01
1.00E-01	1.00E-03	3.82E-16	1.18E+00
1.00E-02	1.00E+02	1.48E-13	2.93E-01
1.00E-02	1.00E+01	2.70E-14	1.59E-01
1.00E-02	1.00E+00	7.04E-15	2.80E-01
1.00E-02	1.00E-01	8.75E-16	9.18E-01
1.00E-02	1.00E-02	6.17E-17	1.61E+00
1.00E-02	1.00E-03	1.54E-17	7.15E+00
1.00E-03	1.00E+02	1.48E-13	2.93E-01
1.00E-03	1.00E+01	2.70E-14	1.58E-01
1.00E-03	1.00E+00	7.41E-15	2.49E-01
1.00E-03	1.00E-01	3.30E-15	6.67E-01
1.00E-03	1.00E-02	5.79E-17	1.38E+00
1.00E-03	1.00E-03	1.54E-17	5.83E+01

Table A.4.13: Test T19 summary data from bimodal model curve fitting.

α	β	D_c (cm^2/s)	Error
1.00E+02	1.00E+02	1.57E-12	2.47E-04
1.00E+02	1.00E+01	1.20E-12	1.44E-04
1.00E+02	1.00E+00	1.16E-12	1.34E-04
1.00E+02	1.00E-01	1.16E-12	1.75E-04
1.00E+02	1.00E-02	1.16E-12	1.75E-04
1.00E+02	1.00E-03	1.16E-12	1.75E-04
1.00E+01	1.00E+02	5.89E-13	3.00E-03
1.00E+01	1.00E+01	1.75E-13	4.50E-04
1.00E+01	1.00E+00	1.21E-13	1.88E-04
1.00E+01	1.00E-01	1.16E-13	2.62E-04
1.00E+01	1.00E-02	1.15E-13	4.82E-04
1.00E+01	1.00E-03	1.15E-13	4.82E-04
1.00E+00	1.00E+02	5.05E-13	5.70E-03
1.00E+00	1.00E+01	9.37E-14	3.71E-03
1.00E+00	1.00E+00	1.95E-14	2.32E-04
1.00E+00	1.00E-01	1.22E-14	4.06E-04
1.00E+00	1.00E-02	1.16E-14	5.53E-04
1.00E+00	1.00E-03	1.15E-14	5.53E-04
1.00E-01	1.00E+02	4.98E-13	6.15E-03
1.00E-01	1.00E+01	9.48E-14	9.29E-03
1.00E-01	1.00E+00	1.60E-14	4.57E-04
1.00E-01	1.00E-01	1.98E-15	4.94E-04
1.00E-01	1.00E-02	1.16E-15	1.12E-03
1.00E-01	1.00E-03	6.98E-16	3.46E-02
1.00E-02	1.00E+02	4.97E-13	6.20E-03
1.00E-02	1.00E+01	9.55E-14	1.05E-02
1.00E-02	1.00E+00	2.37E-14	3.75E-03
1.00E-02	1.00E-01	2.28E-15	3.17E-03
1.00E-02	1.00E-02	8.68E-17	8.87E-02
1.00E-02	1.00E-03	1.54E-17	1.24E+00
1.00E-03	1.00E+02	4.97E-13	6.21E-03
1.00E-03	1.00E+01	9.55E-14	1.06E-02
1.00E-03	1.00E+00	2.53E-14	5.26E-03
1.00E-03	1.00E-01	9.30E-15	1.85E-03
1.00E-03	1.00E-02	1.72E-16	3.67E-02
1.00E-03	1.00E-03	1.54E-17	1.11E+01

Table A.4.14: Test T20 summary data from bimodal model curve fitting.

α	β	D_c (cm^2/s)	Error
1.00E+02	1.00E+02	2.24E-12	1.60E-03
1.00E+02	1.00E+01	1.72E-12	2.04E-03
1.00E+02	1.00E+00	1.67E-12	2.12E-03
1.00E+02	1.00E-01	1.66E-12	2.18E-03
1.00E+02	1.00E-02	1.66E-12	2.18E-03
1.00E+02	1.00E-03	1.66E-12	2.18E-03
1.00E+01	1.00E+02	7.81E-13	1.86E-03
1.00E+01	1.00E+01	2.40E-13	1.41E-03
1.00E+01	1.00E+00	1.74E-13	2.08E-03
1.00E+01	1.00E-01	1.67E-13	2.34E-03
1.00E+01	1.00E-02	1.66E-13	2.68E-03
1.00E+01	1.00E-03	1.66E-13	2.68E-03
1.00E+00	1.00E+02	6.46E-13	4.50E-03
1.00E+00	1.00E+01	1.16E-13	8.79E-03
1.00E+00	1.00E+00	2.77E-14	2.06E-03
1.00E+00	1.00E-01	1.76E-14	2.65E-03
1.00E+00	1.00E-02	1.67E-14	2.81E-03
1.00E+00	1.00E-03	1.66E-14	2.79E-03
1.00E-01	1.00E+02	6.34E-13	5.00E-03
1.00E-01	1.00E+01	1.10E-13	2.10E-02
1.00E-01	1.00E+00	2.18E-14	1.71E-03
1.00E-01	1.00E-01	2.95E-15	4.04E-03
1.00E-01	1.00E-02	1.74E-15	5.02E-03
1.00E-01	1.00E-03	1.48E-15	5.50E-02
1.00E-02	1.00E+02	6.32E-13	5.06E-03
1.00E-02	1.00E+01	1.09E-13	2.37E-02
1.00E-02	1.00E+00	2.95E-14	7.17E-03
1.00E-02	1.00E-01	4.28E-15	3.29E-02
1.00E-02	1.00E-02	2.59E-16	1.04E-01
1.00E-02	1.00E-03	1.54E-17	9.72E-01
1.00E-03	1.00E+02	6.32E-13	5.06E-03
1.00E-03	1.00E+01	1.09E-13	2.39E-02
1.00E-03	1.00E+00	3.09E-14	9.92E-03
1.00E-03	1.00E-01	1.47E-14	8.99E-03
1.00E-03	1.00E-02	3.29E-16	1.44E-01
1.00E-03	1.00E-03	1.54E-17	1.34E+01

Table A.4.15: Test T22 summary data from bimodal model curve fitting.

α	β	D_c (cm^2/s)	Error
1.00E+02	1.00E+02	1.66E-12	3.42E-01
1.00E+02	1.00E+01	1.28E-12	3.46E-01
1.00E+02	1.00E+00	1.24E-12	3.47E-01
1.00E+02	1.00E-01	1.24E-12	3.47E-01
1.00E+02	1.00E-02	1.24E-12	3.47E-01
1.00E+02	1.00E-03	1.24E-12	3.47E-01
1.00E+01	1.00E+02	5.55E-13	2.97E-01
1.00E+01	1.00E+01	1.71E-13	2.91E-01
1.00E+01	1.00E+00	1.29E-13	3.39E-01
1.00E+01	1.00E-01	1.24E-13	3.47E-01
1.00E+01	1.00E-02	1.24E-13	3.48E-01
1.00E+01	1.00E-03	1.24E-13	3.48E-01
1.00E+00	1.00E+02	4.48E-13	2.74E-01
1.00E+00	1.00E+01	7.23E-14	1.22E-01
1.00E+00	1.00E+00	2.02E-14	3.05E-01
1.00E+00	1.00E-01	1.31E-14	3.47E-01
1.00E+00	1.00E-02	1.25E-14	3.48E-01
1.00E+00	1.00E-03	1.24E-14	3.48E-01
1.00E-01	1.00E+02	4.38E-13	2.71E-01
1.00E-01	1.00E+01	6.56E-14	8.88E-02
1.00E-01	1.00E+00	1.53E-14	2.63E-01
1.00E-01	1.00E-01	2.29E-15	4.41E-01
1.00E-01	1.00E-02	1.32E-15	3.74E-01
1.00E-01	1.00E-03	1.20E-15	5.42E-01
1.00E-02	1.00E+02	4.37E-13	2.70E-01
1.00E-02	1.00E+01	6.50E-14	8.73E-02
1.00E-02	1.00E+00	1.89E-14	1.46E-01
1.00E-02	1.00E-01	5.65E-15	1.28E+00
1.00E-02	1.00E-02	2.18E-16	7.77E-01
1.00E-02	1.00E-03	9.95E-17	3.03E+00
1.00E-03	1.00E+02	4.37E-13	2.70E-01
1.00E-03	1.00E+01	6.50E-14	8.72E-02
1.00E-03	1.00E+00	1.95E-14	1.31E-01
1.00E-03	1.00E-01	1.17E-14	4.40E-01
1.00E-03	1.00E-02	4.19E-15	2.30E+00
1.00E-03	1.00E-03	1.54E-17	2.97E+01

Table A.4.16: Test T26 summary data from bimodal model curve fitting.

α	β	D_c (cm^2/s)	Error
1.00E+02	1.00E+02	7.81E-13	9.75E-02
1.00E+02	1.00E+01	6.00E-13	8.99E-02
1.00E+02	1.00E+00	5.82E-13	8.87E-02
1.00E+02	1.00E-01	5.80E-13	8.86E-02
1.00E+02	1.00E-02	5.80E-13	8.86E-02
1.00E+02	1.00E-03	5.80E-13	8.86E-02
1.00E+01	1.00E+02	2.79E-13	1.59E-01
1.00E+01	1.00E+01	8.39E-14	1.13E-01
1.00E+01	1.00E+00	6.07E-14	9.09E-02
1.00E+01	1.00E-01	5.83E-14	8.88E-02
1.00E+01	1.00E-02	5.80E-14	8.86E-02
1.00E+01	1.00E-03	5.80E-14	8.86E-02
1.00E+00	1.00E+02	2.27E-13	1.98E-01
1.00E+00	1.00E+01	4.11E-14	2.10E-01
1.00E+00	1.00E+00	9.72E-15	9.59E-02
1.00E+00	1.00E-01	6.17E-15	8.88E-02
1.00E+00	1.00E-02	5.85E-15	8.86E-02
1.00E+00	1.00E-03	5.81E-15	8.86E-02
1.00E-01	1.00E+02	2.23E-13	2.03E-01
1.00E-01	1.00E+01	3.83E-14	2.98E-01
1.00E-01	1.00E+00	7.72E-15	1.27E-01
1.00E-01	1.00E-01	1.07E-15	8.22E-02
1.00E-01	1.00E-02	6.19E-16	8.58E-02
1.00E-01	1.00E-03	5.83E-16	8.44E-02
1.00E-02	1.00E+02	2.23E-13	2.04E-01
1.00E-02	1.00E+01	3.83E-14	3.14E-01
1.00E-02	1.00E+00	1.05E-14	2.20E-01
1.00E-02	1.00E-01	1.74E-15	4.04E-02
1.00E-02	1.00E-02	1.06E-16	1.28E-02
1.00E-02	1.00E-03	5.50E-17	2.54E-02
1.00E-03	1.00E+02	2.22E-13	2.04E-01
1.00E-03	1.00E+01	3.83E-14	3.16E-01
1.00E-03	1.00E+00	1.10E-14	2.47E-01
1.00E-03	1.00E-01	5.53E-15	7.85E-02
1.00E-03	1.00E-02	5.54E-16	1.49E-01
1.00E-03	1.00E-03	1.54E-17	1.67E+00

VITA

Robert T. (Bob) Jubin was born in 1953 in Akron, Ohio. He graduated from Akron's East High School in 1972 and went on to undergraduate studies at the University of Akron where, in 1977, he received a Bachelor of Science degree in Chemical Engineering. In 1981, he received a Master of Science degree from the University of Tennessee in Engineering Administration with emphasis on Chemical Engineering as a part-time student. He has continued his studies toward his doctorate in Chemical Engineering on a part-time student basis.

He has been a full-time employee of the Oak Ridge National Laboratory, operated by Union Carbide Nuclear Division (now Martin Marietta Energy Systems, Inc.) for the U.S. Department of Energy since the receipt of his Bachelor of Science degree in 1977. Initial work assignments focused on development of processes for the removal of radioactive iodine from nuclear fuel reprocessing plant gaseous effluents. Subsequent work includes extensive development efforts on liquid-liquid extraction equipment as well as work in process modeling and flow sheet design.

Bob is married to the former Sandra Sweeney, also of Akron, Ohio. They have two children, Julie and Michael.

INTERNAL DISTRIBUTION

1. J. F. Birdwell
2. A. G. Croff
3. M. H. Ehinger
4. D. C. Haley
5. W. R. Hamel
6. J. H. Hannah
7-9. J. N. Herndon
10. D. E. Hobson
11-20. R. T. Jubin
21. L. N. Klatt
22. L. M. Kyker
23. B. E. Lewis
24. S. R. Martin
25. S. A. Meacham
26. R. E. Norman
27. C. E. Oliver
28. K. E. Plummer
29. J. D. Randolph
30. S. L. Schrock
31. S. P. Singh
32. B. B. Spencer
33. J. G. Stradley
34. L. R. Walker
35. J. S. Watson
36. H. R. Yook
37-38. Laboratory Records
39. Laboratory Records ORNL-RC
40. RPSD Publications Office
41. ORNL Patent Section
42. Central Research Library
43. Document Reference Section

EXTERNAL DISTRIBUTION

44. P. Baron, Chef du SEC, Comissariat A L'Energie Atomique, Direction du Cycle du Combustible, Department du Retraitment des Dechets et du Demantelement, Service d'Etudes et de Modelisation des Procedes, Centre Fontenay-aux-Roses, B.P. 6, 92265 Fontenay-aux-Roses, Cedex, France.

45. R. M. Counce, The University of Tennessee, Chemical Engineering Department, 419 Dougherty Engineering Building, Knoxville, Tennessee 37996-2000.

46. W. Davis, The University of Tennessee, Civil Engineering Department, Perkins Hall, Knoxville, Tennessee 37996.

47. W. D. Holland, Tennessee Technological University, Chemical Engineering Office, Cookeville, Tennessee 38501.

48. C. Madic, Docteur es Science-Professeur a I'Instn, Adjoint au Chef du SEMP, Comissariat A L'Energie Atomique, Direction du Cycle du Combustible, Department du Retraitment des Dechets et du Demantelement, Service d'Etudes et de Modelisation des Procedes, Centre Fontenay-aux-Roses, B.P. 6, 92265 Fontenay-aux-Roses, Cedex, France

49. J. Perona, The University of Tennessee, Chemical Engineering Department, 419 Dougherty Engineering Building, Knoxville, Tennessee 37996-2000.

50. Office of Assistant Manager for Energy Research and Development, Oak Ridge Operations Office, Department of Energy, P.O. Box 2008, Oak Ridge, Tennessee 37831-6269.

51. Office of Scientific and Technical Information, P.O. Box 62, Oak Ridge, Tennessee 37831.